Università degli Studi di Padova

University of Padua, Department of Physics and Astronomy "G. Galilei"

Master Thesis in Astrophysics and Cosmology

Assessing the effects of stellar binarity on Neptunian exoplanets

Alessandro Matteo Rossi
ID 2166016

Supervisor
Prof. Luca Malavolta
University of Padua

Co-supervisor
Dr. Monica Rainer
INAF-OAB

Co-supervisor
Dr. Silvano Desidera
INAF-OAPd

Co-supervisor
Dr. Francesco Borsa
INAF-OAB

Academic Year 2025/2026

A mio papà,
che il tempo ha portato via prima di questo giorno,
ma che non mi ha mai lasciato.

Contents

Abstract ix

1 Exoplanets 1

1.1 An historical digression 1
1.1.a The dawn of exoplanet research 1
1.1.b The first detections 2
1.2 Exoplanet demographics and classification schemes 3
1.2.a Jupiters 3
1.2.b Neptunes 5
1.2.c Earths 5
1.3 How to detect your planet 6
1.3.a Radial velocity 6
Notable spectrographs 9
1.3.b Transit method 9
CoRoT 11
Kepler and K2 11
TESS 12
PLATO 12
Ariel 13
1.3.c Astrometry 13
HIPPARCOS and Tycho 15
Gaia 16
1.3.d Direct imaging 17
Notable instruments 17
1.3.e Other methods 18
Microlensing 18
Transit time variation (TTV) 19

2 Obliquities in exoplanetary systems 21

2.1 Rossiter–McLaughlin effect 22
2.1.a Reloaded Rossiter–McLaughlin 28
2.1.b Rossiter–McLaughlin revolutions 28
2.1.c Doppler shadow 29

2.2 Obliquity distribution 29
2.3 The effect of binarity 33

3 Probing for stellar companions: imaging and radial velocity 35
3.1 Direct imaging 35
3.1.a ExoFOP archive and data selection 37
3.1.b From projected to physical separation 39
3.2 Catalogs of binaries 41
3.2.a PMa and PM acceleration catalogs 42
3.2.b Astrometric catalogs 42
3.2.c Binary catalogs 43
3.3 Radial velocity 44

4 Detecting companions through astrometric anomalies 47
4.1 Tycho-2, the second reduction of the *Hipparcos* star mapper 47
4.2 Proper motion anomaly 48
4.2.a Astrometric smearing γ 50
4.2.b Baseline efficiency ζ 51
4.2.c Geometric projection η 52
4.3 Systematics correction 54
4.3.a Parallax zero-point calibration and chromaticity 54
4.3.b Distance estimation 56
4.3.c Epoch backpropagation and perspective acceleration . . . 56
4.3.d Error inflation 57
4.3.e Reference frame alignment 59
4.3.f Light travel time 60
4.4 PMa calculation 61
4.4.a Methodological Robustness and Assumptions 63
4.5 Benchmarking 64
4.5.a Binary detection 64
4.5.b Companion mass estimation 67

5 A homogeneous and multi-technique analysis 75
5.1 Neptunian sample 76
5.2 Results 84
5.2.a No new binaries in a larger Neptunian sample 84
5.2.b No correlation between obliquity and binarity 85
5.2.c Neptunian alignment in compact systems 87
5.2.d A dichotomous Neptunian population? 89

Conclusions 99

A Discussion of individual targets 103
A.1 AU Mic b 104
A.2 DS Tuc A b 105
A.3 GJ 436 b 107

A.4 GJ 3470 b . . . 108
A.5 HAT-P-11 b . . . 109
A.6 HD 63433 b . . . 110
A.7 HD 89345 b . . . 112
A.8 HIP 67522 b . . . 113
A.9 K2-25 b . . . 113
A.10 K2-33 b . . . 114
A.11 K2-105 b . . . 115
A.12 K2-290 b . . . 116
A.13 K2-329 b . . . 117
A.14 Kepler-9 b . . . 119
A.15 Kepler-25 c . . . 120
A.16 Kepler-30 b . . . 121
A.17 Kepler-63 b . . . 122
A.18 Kepler-1656 b . . . 122
A.19 TOI-942 b . . . 123
A.20 TOI-1135 b . . . 124
A.21 TOI-1268 b . . . 124
A.22 TOI-1694 b . . . 125
A.23 TOI-1759 A b . . . 125
A.24 TOI-1842 b . . . 126
A.25 TOI-2076 b . . . 126
A.26 TOI-2364 b . . . 127
A.27 TOI-2374 b . . . 127
A.28 TOI-3884 b . . . 128
A.29 TOI-5398 b . . . 128
A.30 WASP-69 b . . . 129
A.31 WASP-107 b . . . 129
A.32 WASP-131 b . . . 130
A.33 WASP-148 b . . . 133
A.34 WASP-166 b . . . 133

B Gaia DR3 zero-point correction **135**

C Sensitivity analysis: exclusion of TOI-1710 A **137**

References **141**

List of Figures **155**

List of Tables **159**

Acknowledgments **161**

Abstract

Recent literature regarding exoplanets has focused increasingly on intermediate-sized planets, commonly referred to as Neptunians (or sub-Saturns). An area of particular interest involves their architecture, specifically the inclination between the host star's spin axis and the planet's orbital axis. It is possible to infer the projected angle between the two, commonly referred to as the projected spin-orbit obliquity λ, by modeling the Rossiter–McLaughlin (RM) effect, which consists of an apparent shift in the radial velocity (RV) during a planetary transit. Knowing the rotation period of the star P_{rot} it is possible to deproject this quantity from the plane of the sky into a physical tridimensional angle. This quantity is known as the true spin-orbit obliquity Ψ, and it is regarded as a fundamental tracer of the dynamical history of the planet. During my B.Sc. thesis, I conducted a systematic analysis of the RM effect, producing the largest catalog of true spin-orbit obliquities to date, which we later published in A&A (Rossi et al. 2026). We highlighted that Neptunian planets exhibit a dichotomous distribution of true obliquities, sharply divided into a cluster of aligned planets (orbiting along the equator of the star, similar to Solar System members) and a second cluster of perpendicular planets (orbiting the poles of their host stars, a peculiar but not uncommon occurrence). We also underscored how the small sample size could be a major factor hindering the characterization of the real true obliquity distribution. Another key factor that could perturb the architecture of a planetary system is the presence of binary companions, as numerous studies have highlighted.

This thesis aims to investigate the effect of stellar binarity on the architecture of Neptunian exoplanets. Using a comprehensive multi-technique approach, I have conducted a systematic search for binary companions around Neptunian hosts to identify potential correlations with orbital misalignment. I updated the sample from Rossi et al. (2026) by adding six newly characterized targets, bringing the total to 38 Neptunian planets with measured Ψ, a 20% increase over the previous record. The methodological cornerstone of this work is the development of an original astrometric pipeline. By cross-calibrating the historical Tycho-2 catalog, the second reduction of the *Hipparcos* star mapper, with modern *Gaia* DR3 data, I exploited a 24.5 year temporal lever arm to compute the proper motion anomaly. This framework represents a significant scale-up in multiplicity studies, opening the possibility to infer binarity for 2.5 million targets, a potential that has remained largely untapped until now. To ensure a thorough vetting of the stellar environment, this astrometric search was integrated with high-resolution imaging analysis (speckle and adaptive optics) from the Exoplanet Follow-up Observing Program and a search for linear RV drifts in the Data Analysis Center for Exoplanets database, covering the entire range of physical separations from a few au to hundreds of au. Furthermore, the analysis

was bolstered by a dedicated literature review for every target and a comprehensive search across eleven multiplicity catalogs, providing a complete census of the stellar environment across all accessible scales.

The results demonstrate that stellar binarity plays a neutral role in shaping Neptunian architecture. No statistically significant difference was found between the obliquity populations of planets in single and binary systems, suggesting that Neptunian misalignments are likely not driven by external stellar perturbations. Conversely, the presence of a compact companion seems to induce alignment, as suggested by recent literature. Most importantly, this work provides evidence that the previously claimed Neptunian dichotomy is starting to collapse with an increase in sample size. Bootstrap smoothed model selections strongly favor a unimodal distribution with a prominent alignment peak and an isotropic tail, yielding a combined winning rate of almost 90% for single-peaked models.

1 Exoplanets

1.1 An historical digression

The night sky has fascinated humankind since the Ancient Greeks. They first noted the existence of some $\pi\lambda\alpha\nu\eta\tau\eta\varsigma\ \alpha\sigma\tau\epsilon\varrho\eta\varsigma$ — wandering stars — scintillating in the night sky and having a higher proper motion (PM) than the fixed stars of the background sky. Their fascination for the night sky led several philosophers to discuss whether other worlds could exist and what their features could be. The atomists Leucippus and Democritus argued that atoms could combine in ways different than the ones we are used to, and form worlds with none or multiple Suns and Moons, while Epicurus stated that infinite other worlds existed, with several degrees of similarity to ours. Among the opposers to this idea we find Aristotle, whose beliefs on planets beyond Earth and on the role and position of Earth in the universe shaped human culture for centuries to come. This did not stop other brilliant thinkers of the past from discussing the topic of the celestial bodies we now know as extra-solar planets, or exoplanets in short (see Dick 1982, for a review).

1.1.a The dawn of exoplanet research

Struve (1952) proposed a pioneering approach that could lead to the detection of the first planets. Considering that stellar companions can exist even at $0.02\,\mathrm{au}$, he argued that a Jupiter-mass planet orbiting this close to its host star could have a period as short as a single day and cause a radial velocity (RV) displacement of $\pm 0.2\ \mathrm{km\,s^{-1}}$. Moreover, he theorized that the planet could partially eclipse the host star's disk, hence generating a detectable decrease in the observed flux. In doing so, he laid the conceptual foundation of the RV and the transit methods for discovery and characterization of exoplanets, the primary techniques used today.

1.1.b The first detections

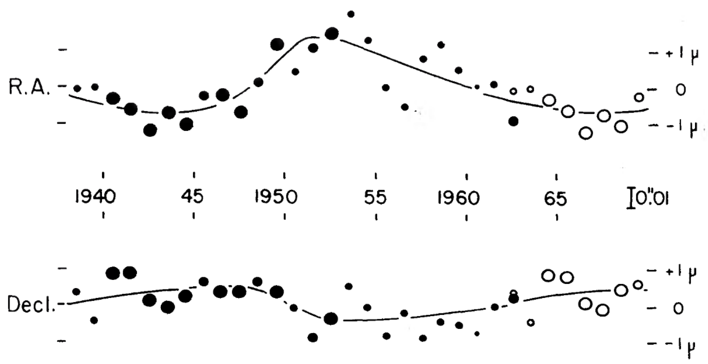

Figure 1.1: Barnard's star yearly mean positions from Van de Kamp (1963)

In the following years several astronomers reported potential detections. Van de Kamp (1963) and Van de Kamp (1982) claimed the discovery of a $1.6\,\mathrm{M_{Jup}}$ planet orbiting Barnard's Star (Barnard 1916) — a well known star notable for its exceptionally high PM — after 25 years of astrometric measurements (fig. 1.1). This conclusion was later disputed and attributed to systematic measurement errors (Gatewood & Eichhorn 1973). However, in recent years debate sparked around this object, resulting in four non-transiting planets being confirmed to orbit Barnard's star (Ribas et al. 2018; González Hernández et al. 2024; Basant et al. 2025; Stefanov, A. K. et al. 2025). Campbell, Walker & Yang (1988) suggested the existence of three Jovian planets around three K-type stars, while Latham et al. (1989) argued that HD 114762 hosted a substellar companion with a mass slightly lower than the hydrogen ignition mass of $\sim 13\,\mathrm{M_{Jup}}$. Furthermore, Wolszczan & Frail (1992) reported the detection of a planetary system with two Earth-mass planets around the millisecond pulsar PSR1257+12 using the 300-m class Arecibo radio telescope, now decommissioned after a devastating earthquake. These discoveries marked significant milestones towards the discovery of a planetary system hosted by a conventional star, as the one announced by Mayor & Queloz (1995), a Jupiter-mass planet orbiting the solar-type star 51 Pegasi. Despite its short orbital period of $P \sim 4.23\,\mathrm{d}$, previously thought impossible for a planet, the field of exoplanetology took off after this discovery.

1.2 Exoplanet demographics and classification schemes

Mayor and Queloz were awarded the Nobel Prize in Physics in 2019, for their contribution (Mayor & Queloz 1995) to the establishment of exoplanetology as a new field of astronomy. Since their discovery, more than 6000 exoplanets have been confirmed[1](Nature Astronomy editorial 2025), with over a thousand additional candidates awaiting confirmation. Comprehensive data on these objects are maintained in several online databases, such as NASA Exoplanet Archive[2] (Christiansen et al. 2025; NASA Exoplanet Science Institute 2020) or exoplanet.eu[3] (Schneider et al. 2011). The vast population of exoplanets can be categorized following different conventions. This thesis adopts the framework presented by M. Perryman (2018), an encyclopedic reference on the subject whose origins date back to the early era of the field when the number of known planets was still the dozens (M. A. C. Perryman 2000). Specifically, the mass-based distinction follows the scheme proposed by Stevens & Gaudi (2013) as illustrated in Figure 1.2. Within this framework, certain categories are of particular relevance to the scope of this work.

1.2.a Jupiters

As the name suggests, these are exoplanets comparable to Jupiter in radius, mass, and bulk composition. The large magnitude of these quantities facilitates their detection. Indeed, these *giant planets* were the first exoplanets to be discovered, via both RV and transits, methods that will be discussed in detail in the following sections (e.g., Queloz et al. 2000b; Charbonneau et al. 1999; G. W. Marcy et al. 2001; Pepe et al. 2002). For the scope of this thesis, I define Jupiters as those planets with a mass $100 < M_{\rm p}/{\rm M}_{\oplus} < 1000$[4]. Objects with $1000\,{\rm M}_{\oplus} < M < 12\,{\rm M}_{\rm Jup}$ are classified as super-Jupiters, while those exceeding the deuterium-burning limit ($M \sim 12\,{\rm M}_{\rm Jup}$) are categorized as brown dwarfs (BDs).

Early detections revealed that these massive planets tend to be dramatically close to their host stars (e.g., Mayor & Queloz 1995, with 51 Peg b being closer than 10 times the orbit of Mercury). While in-situ formation of such hot Jupiters (HJs) is difficult to reconcile with standard gravitational instability models, core accretion may provide a viable pathway under specific circumstances (see Daw-

[1]According to the NASA Exoplanet Archive (Christiansen et al. 2025). These figures may vary across different catalogs due to the inherent arbitrariness in defining the boundaries of an exoplanet, particularly regarding mass and radius limits.

[2]`https://exoplanetarchive.ipac.caltech.edu/index.html`

[3]`https://exoplanet.eu`

[4]Where ${\rm M}_{\rm Jup} \approx 317.8\,{\rm M}_{\oplus}$, with ${\rm M}_{\oplus} \approx 6 \cdot 10^{24}$ kg

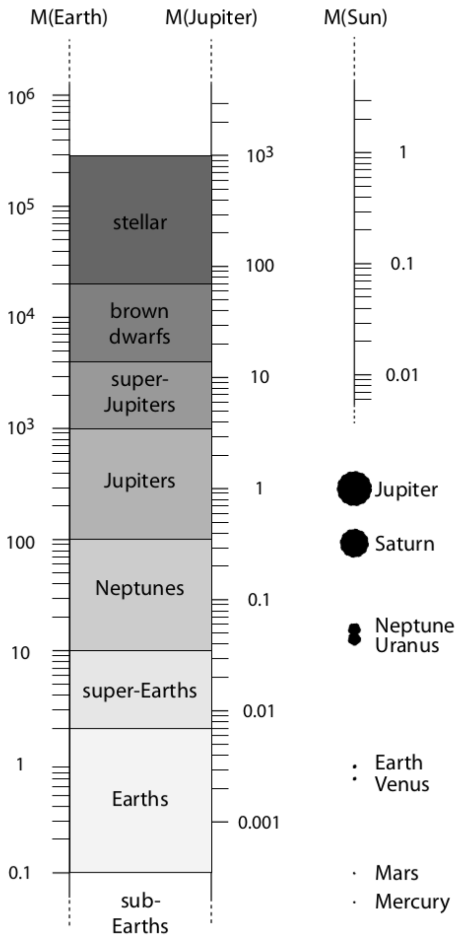

Figure 1.2: Stevens & Gaudi (2013) classification of exoplanets according to their mass. Source: M. Perryman (2018).

son & Johnson 2018, for a review). However, ex-situ formation followed by migration is the preferred pathway. This occurs either through disk migration or through high eccentricity tidal migration (S. Albrecht et al. 2012). A comprehensive review is offered by S. H. Albrecht, Dawson & Winn (2022). The latter mechanism is particularly relevant to this work, as it justifies the existence of misaligned orbits (that will be discussed in Chapter 2), with mechanisms such as planet–planet scattering (Weidenschilling & Marzari 1996; Ford & Rasio 2006), von Zeipel–Kozai–Lidov cycles (von Zeipel 1910; Kozai 1962; Lidov 1962), or secular interactions (Wu & Lithwick 2011; Petrovich 2015). Depending on the distance from their host star, we can distinguish between HJs ($a/R_\star < 10$) and warm/cold Jupiters (S. H. Albrecht, Dawson & Winn 2022).

1.2.b Neptunes

Neptune-sized planets have historically received less attention than Jupiters, primarily because they have only recently gained statistical representation[5] in the available measurements. Because their RV signals and transit depths are significantly shallower than those of Jupiters, their detection required high-precision modern instrumentation. According to Stevens & Gaudi (2013) classification, Neptunian planets are defined as having masses in the range $10 < M_{\rm p}/{\rm M}_{\oplus} < 100$.

1.2.c Earths

Earths are defined, for the scope of this thesis, as a broader category including super-Earths ($2 < M_{\rm p}/{\rm M}_{\oplus} < 10$), Earths ($0.1 < M_{\rm p}/{\rm M}_{\oplus} < 2$), and sub-Earths ($M_{\rm p} < 0.1\,{\rm M}_{\oplus}$). The technical challenges regarding signal-to-noise ratio (SNR) — and the resulting statistical under-representation of this subsample[6]— are even more pronounced for these planets. Nevertheless, certain systems have emerged for their peculiar features, such as TRAPPIST-1, a resonant chain of seven Earth-sized planets with semi-major axes smaller than the orbit of Mercury (Gillon et al. 2017; Luger et al. 2017).

[5]Filtering NEA planets for Neptunian masses, after setting `default parameter set` to 1 (the parameter indicating the NEA preferred orbital solution) yielded 655 planets out of the 6061 available in Dec, 2025.

[6]As of Dec, 2025 only 638 planets out of 6061 on NEA are Earths

1.3 How to detect your planet

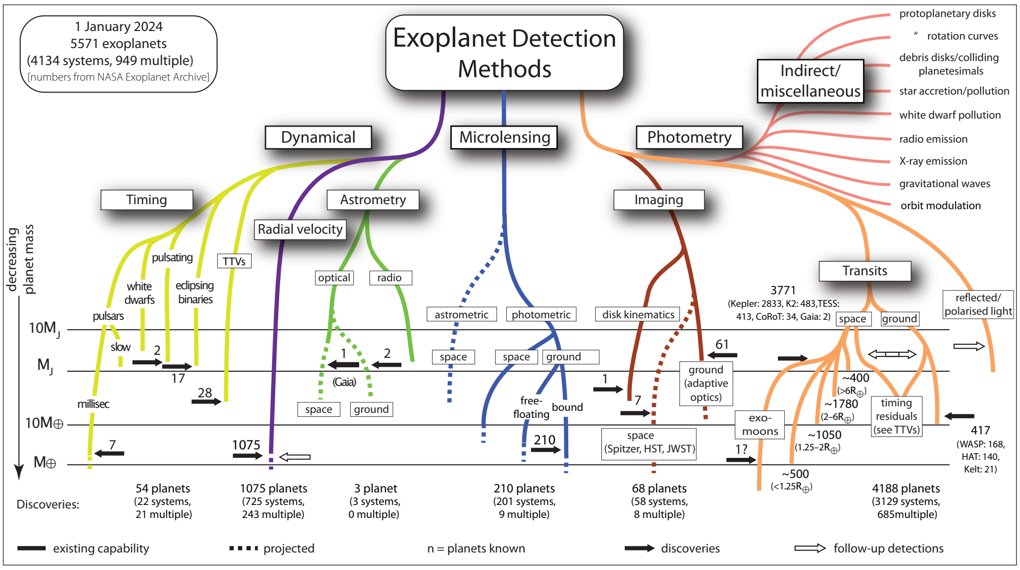

Figure 1.3: "Perryman Tree" plot of exoplanet detection methods updated on Jan, 1st 2024. Among ∼ 5500 known two years ago, the vast majority were discovered via transits, followed by RV. As of 2024, astrometry still plays a marginal role in the total count. Source: Micheal Perryman[7]

Various detection methods have been developed to observe and confirm exoplanets, each characterized by different ranges of applicability and different rates of success (fig. 1.3). This section focuses on the detection methods most relevant to the scope of this work, while providing only a brief overview of alternative methods. Each method description is complemented by an introduction to the most relevant surveys or instruments based on it.

1.3.a Radial velocity

The first planetary detection was performed via RV (Mayor & Queloz 1995), and it is safe to say that before the turn of the century all detections were performed in RV from ground-based facilities. Notable examples include D. A. Fischer et al. (2008) and Tamuz et al. (2008), as well as reviews by Udry & Santos (2007), Lovis & D. Fischer (2010), Hatzes (2016), and Wright (2018). The fundamental principle of RV lies in the measurement of the velocity variation along the line of sight connecting the observer (a ground or space based facility) with the target star. This measurement is made possible by the Doppler effect

[7] https://www.michaelperryman.co.uk/exoplanets

$$\lambda = \lambda_0 \left(1 + \frac{v}{c}\right) \tag{1.1}$$

where λ_0 is the wavelength emitted by a star moving with a velocity v along the line of sight, resulting in a measured λ wavelength. In a spectroscopic observation, the gravitational pull of an orbiting planet causes the star to wobble around the system's barycenter[8], resulting in a periodic shift of the stellar spectral lines (a sinusoidal curve for circular orbits).

This motion can be derived by applying Kepler's laws to a two-body system (in a first approximation). Specifically, considering a target star and a planet orbiting their mutual barycenter, the third law becomes:

$$P_{\rm orb}^2 = \frac{4\pi^2}{G(M_\star + M_{\rm p})} (a_{\rm s} + a_{\rm p})^3 \tag{1.2}$$

where P is the planet's orbital period, $M_\star$ is the stellar mass, $M_{\rm p}$ is the planet's mass, while $a_{\rm s}$ and $a_{\rm p}$ represent the distance of the star and the planet from the barycenter, and star and the planet, respectively. Assuming a circular orbit with a velocity

$$v_s = \frac{2\pi a_{\rm s}}{P_{\rm orb}} \tag{1.3}$$

as well as $a_p \gg a_s$ and $M_\star \gg M_{\rm p}$, and imposing the definition of the system's barycenter

$$M_\star \, a_{\rm s} = M_{\rm p} \, a_{\rm p} \tag{1.4}$$

it is possible to solve Equation (1.2) for $a_{\rm p}$. Substituting Equation (1.3) and the expression for $a_{\rm s}$ from Equation (1.4) we get

$$v = \left(\frac{2\pi G}{M_\star^2 P_{\rm orb}}\right)^{\frac{1}{3}} M_{\rm p} \tag{1.5}$$

In a more rigorous derivation that also accounts for the orbital inclination $i_{\rm orb}$ and the eccentricity e, the observable quantity is the RV semi-amplitude

$$K = \left(\frac{2\pi G}{P_{\rm orb}}\right)^{\frac{1}{3}} \frac{M_{\rm p} \sin i_{\rm orb}}{M_\star^{2/3}} \frac{1}{\sqrt{1-e^2}} \tag{1.6}$$

Even the simplified RV analytical framework demonstrates that the RV method is sensitive to the masses of the bodies involved. Specifically, this method is

[8] A nice pedagogical visualization is given in https://science.nasa.gov/resource/radial-velocity/

sensitive to the lower limit of planetary mass, which degenerates with the orbital inclination (fig. 1.4).

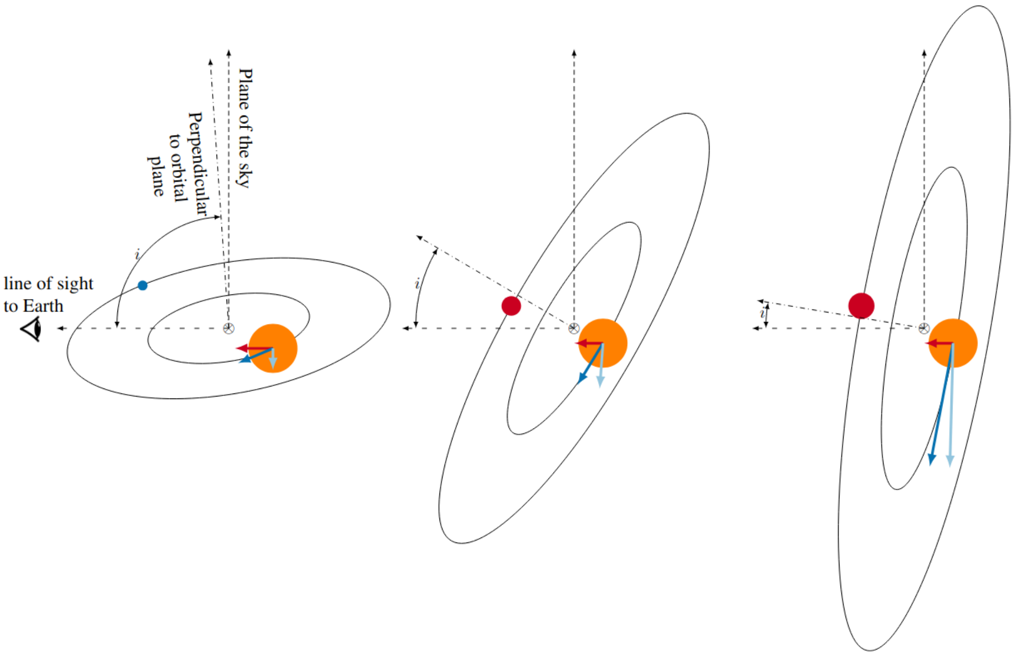

Figure 1.4: Sketch of the RV method. Based on Doppler effect, it measures the gravitational influence of an orbiting body (blue and red solid circles) on its host star (orange solid circle). Depending on the inclination i—also named $i_{\rm orb}$ in the text—the RV (red vector) can have the same intensity although the inclination i dramatically changes, as well as the tangential (light blue vector) and true (blue vector) velocity. Source: Trifonov (2026)

This method favors more massive planets around lighter stars, with short orbital periods. This explains why the first discovered planets were HJs. To put the required precision into perspective, the RV signals for Solar System planets as they would be measured by an external observer are

$$v_{\oplus} = 0.089 \text{ m s}^{-1} \qquad v_{\rm Jup} = 12.4 \text{ m s}^{-1} \qquad v_{\rm Nep} = 0.281 \text{ m s}^{-1} \tag{1.7}$$

Such small signals highlight the need for extremely precise and, above all, long-term stable instrumentation to ensure a sufficient SNR. The primary challenges in detecting low-mass planets (like Earth-analogs) include maintaining instrumental stability and accounting for ”stellar jitter”, the noise induced by stellar activity, such as starspots and granulation (M. Perryman 2018; Trifonov 2026), that can cause spurious detections (Trifonov 2026).

Notable spectrographs A plethora of spectrographs, ranging from low to high resolution, have been developed throughout the last three decades to study exoplanets. While low-resolution spectroscopy is usually performed to probe for the presence of stellar contaminants around a target, high-resolution studies are conducted to infer the mass of the planetary companion. The latter is usually performed by the state-of-the-art Echelle high resolution spectrographs (HRS, thoroughly described in e.g., Y. Zhang et al. 2022) such as HARPS (Mayor et al. 2003) at the ESO 3.6m telescope, HARPS-N (Cosentino et al. 2012) mounted on the TNG in La Palma, ESPRESSO mounted on the VLT at Paranal (Pepe et al. 2021), and ANDES (Marconi et al. 2022) for the upcoming E-ELT.

1.3.b Transit method

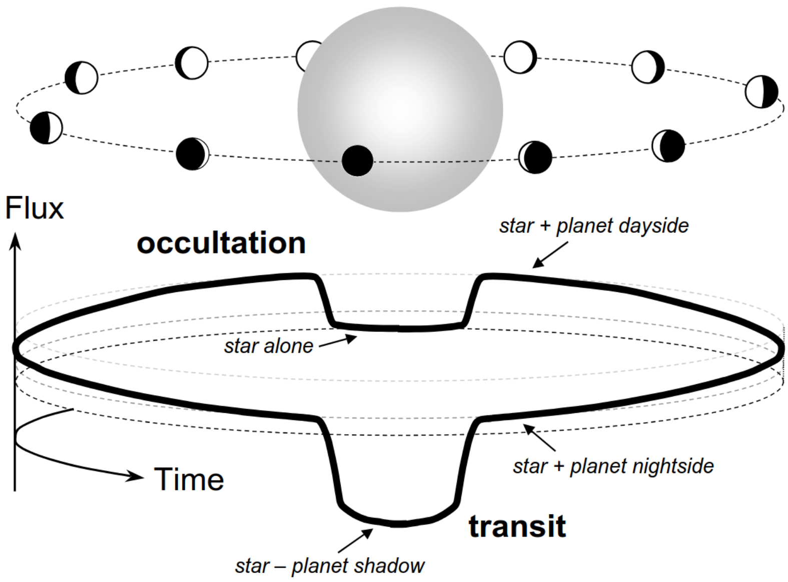

Figure 1.5: Illustration of the stellar flux varying according to transits and occultations. When the planet is occulted behind the star (star alone) we have a conspicuous amount of flux, which further increases when the planet appears from behind the star (star + planet dayside). As the planet proceeds to show its nightside (star + planet nightside) the flux reduces, plummeting when it transits in front of the star (star – planet shadow). Source: Winn (2010)

The transit method currently accounts for the vast majority of exoplanet detections. This method relies on the serendipitous alignment between the orbiting planet and the host star, hence allowing the planet to *transit* across its host stars' disk. Along with RV, it was one of the first methods used to detect planets (G. Marcy et al. 2000; Briot & Schneider 2018), following the initial breakthrough of

RV surveys.

The fundamental principle of transits is to detect the flux drop caused by a transiting planet masking a portion of the host star's disk. A comprehensive model of a transit event can be seen in Figure 1.5. Beyond the primary transit, a high-precision light curve can reveal additional features: the phase curve reflects the changing contribution of the planet's irradiated dayside as it orbits the star, while the occultation (or secondary eclipse) occurs when the planet is hidden behind the star (Winn 2010). A detailed theoretical treatment of transits and occultations is provided by Winn (2010). For the scope of this thesis, it is worth noting that only few planetary systems are transiting, due to the low transit probability. In the fortuitous case of a circular $e = 0$ orbit, this probability is given by Eq. 11 of Winn (2010):

$$p = \frac{R_\star}{a} \approx 0.005 \left(\frac{R_\star}{\mathrm{R}_\odot}\right) \left(\frac{a}{1\,\mathrm{au}}\right)^{-1} \tag{1.8}$$

where $R_\star$ is the stellar radius, a is the planetary semi-major axis, $\mathrm{R}_\odot$ represents the solar radius, and with the reasonable assumption of a planetary radius significantly smaller than the stellar radius $R_\mathrm{p} \ll R_\star$.

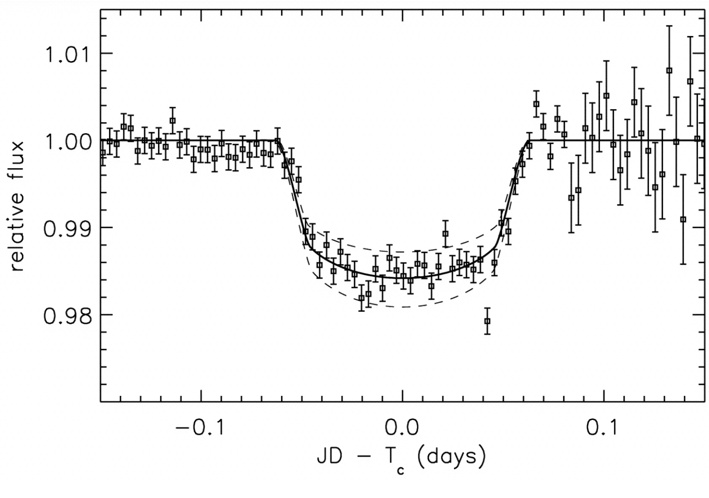

Figure 1.6: Light curve of HD 209458 from the discovery paper by Charbonneau et al. (1999). The typical shallow decrease of flux is due to limb darkening, which is a geometrical effect that causes the boundaries of the star to be darker than the center, due to the viewing angle (see e.g. Espinoza & Jordán 2015; Agol, Luger & Foreman-Mackey 2020).

Several packages have been developed for transit analysis, such as `batman`[9]

[9] https://github.com/lkreidberg/batman

(Kreidberg 2015) and `PyTransit`[10] (Parviainen 2015). Analyzing the light curve usually results in a profile similar to fig. 1.6, which displays the characteristic flux dip. The detection of the occultation, or secondary transit, is significantly more challenging, as it produces a much shallower signal. Similarly to the previous section, I list some of the most notable surveys which have shaped the exoplanet legacy so far. Planets detected by these surveys, and later confirmed with ground based observations, are the basis of Rossi et al. (2026), the largest catalog of exoplanetary true obliquities to date, which will be discussed in the framework of this work in the next section.

CoRoT The Convection, internal Rotation and Transiting (CoRoT) satellite was a space mission launched in 2006 and decommissioned six years later due to a computer malfunction. Its research fields included asteroseismology and pioneering studies of exoplanetary transits for solar-like and F-type stars via photometric measurements (Deleuil & Fridlund 2018). Its legacy comprises $177,454$ light curves, with durations ranging from a few days to $\sim$ 150 days and the discovery of 39 exoplanets and brown dwarfs (BDs) (Deleuil & Fridlund 2018). One of the most outstanding results is the detection of CoRoT-7b, the first telluric planet (a super-Earth) ever found (Léger et al. 2009).

Kepler and K2 The Kepler Mission (Borucki et al. 2010) was launched in 2009 after the discoveries of CoRoT. It detected over 4500 planetary candidates, with 75% validated from later studies (see Lissauer et al. 2012, for a complete description of the statistical validation method), during its four years of transit monitoring on $190,000$ stars. Its main goal was addressing the key questions left by CoRoT, the frequency of telluric planets, their size and semi-major axis distribution, and their existence in multi-planet systems similar to the Solar System (Borucki 2018). The targets were solar-like stars (F-, G- and K- type). They live longer, they have relatively low stellar activity and we have a broader knowledge about them - compared to other types - because of their similarity with our Sun. Thus, they allow an easier detection of an exoplanetary signal. Conversely, a planet in the habitable zone (HZ), the range of distances in which a planet can host liquid water, has an orbital period $P_{\rm orb}$ in the order of years, requiring a longer time to detect a transit.

Kepler observed continuously for 4 years the same star-dense region, close to the Cygnus constellation, following a stable heliocentric orbit thanks to 4 reaction wheels (Borucki 2018). After four years of operations, two of them failed and the mission was repurposed as K2. Instead of a stable long-term monitoring

[10] https://github.com/hpparvi/PyTransit

of a single field, K2 was continuously drifting while observing on the ecliptic plane. The same objects were able to stay in the field-of-view of the telescope for no more than 83 days, which limited the possibility to detect planets with long orbital periods (Howell et al. 2014). Still, $310,000$ more stars (and even exotic objects) were observed before the satellite ran out of fuel in 2018. Both the missions combined covered approximately 6% of the visible sky. The major difference between the two surveys is the observation time. Kepler's stability was able to detect transits by planets with longer orbital periods, opposite to K2. The 2014 (Lissauer et al. 2014; Rowe et al. 2014) and 2016 (Morton et al. 2016) sudden increase in fig. 1.7 corresponds with the bulk of exoplanets announced by Kepler.

TESS The Transiting Exoplanet Satellite Survey (TESS) is the successor of Kepler. It was launched in 2018, with the goal of observing stars brighter than Kepler, to facilitate transiting planet confirmation, but in all directions, without a fixed target region (Ricker et al. 2014). Considering that TESS cannot match Kepler sensitivity to longer orbital periods and lower magnitudes, it is meant to be an all-sky survey (Winn 2024). It is currently monitoring brighter stars than Kepler, primarily F- to M- type, very abundant in the Solar neighborhood, with M-types rarely observed by Kepler, having reached its third three-year extension. Although several missions have been proposed to increase our knowledge of exoplanets, such as the Habitable World Observatory (HWO Feinberg et al. 2024) and the Large Interferometer For Life (LIFE Quanz et al. 2022), the next breakthrough steps will be taken by PLATO and ARIEL, which will start performing science within the 2030s.

PLATO The PLAnetary Transits and Oscillations of stars (PLATO, Rauer et al. 2014; Rauer et al. 2025) mission is the third medium-class mission in the ESA Cosmic Vision program, designed to detect and characterize terrestrial exoplanets orbiting bright solar-type stars, with a particular focus on planets in the HZ. PLATO consists of 26 small-aperture telescopes that provide a wide field of view ($\sim 2232\,\mathrm{deg}^2$) and high photometric precision for bright targets. A key strength of the mission is the synergy between transit photometry and asteroseismology, which enables precise determination of stellar parameters (mass, radius, and age), and consequently accurate planetary radii and bulk densities when combined with ground-based RV follow-up (Miglio et al. 2017). By targeting bright and nearby stars (Nascimbeni et al. 2022; Nascimbeni et al. 2025), PLATO will provide a benchmark sample of exoplanets with well-determined parameters, playing a crucial role in advancing our understanding of planetary system formation, evolution, and the occurrence of habitable worlds.

Ariel The Atmospheric Remote-sensing Infrared Exoplanet Large-survey (ARIEL, Tinetti et al. 2018; Tinetti et al. 2022) is designed for the investigation of at least one thousand transiting exoplanetary atmospheres (Zingales et al. 2018) in order to infer population-level results and produce the first homogeneous spectroscopic dataset[11] suitable for comparative exoplanetology (Mugnai et al. 2020). By targeting a large and diverse sample of transiting exoplanets, ranging from HJs to warm Neptunes and super-Earths orbiting F–M type stars, ARIEL aims to establish direct links between atmospheric composition, planetary bulk properties, and formation and evolutionary pathways (Puig et al. 2018). The mission is based on transit and eclipse spectroscopy over a broad wavelength range ($\sim 0.5 - 7.8\,\mu\mathrm{m}$), enabled by a $\sim 1\,\mathrm{m}$ class telescope feeding both photometric and spectroscopic channels, allowing simultaneous constraints on molecular abundances, thermal structure, and scattering processes such as clouds and hazes (Puig et al. 2018). Its statistical approach will enable robust measurements of key trends such as the mass–metallicity relation, atmospheric diversity, and the prevalence of aerosols, thereby providing empirical constraints on planet formation models and migration histories (Zellem et al. 2019). In this context, ARIEL complements high-precision facilities such as JWST by trading depth for breadth, delivering a population-level framework necessary to interpret detailed atmospheric studies within a broader astrophysical context (Puig et al. 2018; Zellem et al. 2019).

1.3.c Astrometry

Astrometry concerns the measurement of positions and motions of celestial objects (M. Perryman 2018). Early star maps date back to antiquity, created by the Greek Hipparchus (Gysembergh, J. Williams & Zingg 2022) and the Chinese Shi Shen (Ho 2000). While astrometry is the oldest branch of astronomy, yet it has only recently entered its golden age in the context of exoplanetary science. Unlike the RV method, it consists of the precise measurement of the two-dimensional stellar position and its motion on the plane of the sky (e.g. Unwin et al. 2008). The presence of a planetary companion induces a periodic displacement of the host star around the system's common barycenter. When projected onto the sky, this motion appears as a small elliptical "wobble" superimposed on the star's PM and parallax (Sahlmann et al. 2011; M. Perryman 2018). The fundamental observable in astrometric surveys is the astrometric signature α

[11] https://github.com/arielmission-space/Mission_Candidate_Sample/

(usually expressed in arcseconds), which represents the angular semi-major axis of the star's orbit around the barycenter

$$\alpha = \frac{M_\mathrm{p}}{M_\star}\frac{a}{d} \tag{1.9}$$

where M_p and $M_\star$ are the planetary and stellar masses, a is the semi-major axis of the planet's orbit, and d is the distance of the system from the observer. The astrometric signal increases linearly with the orbital separation a. This makes astrometry the ideal technique for detecting long-period (cold) Jupiters and characterizing the outer architecture of planetary systems (Sozzetti et al. 2014). One of the most significant advantages of astrometry is its ability to fully determine the orbital inclination i_orb and the longitude of the ascending node Ω. By resolving the 3-D geometry of the orbit, astrometry breaks the $M_\mathrm{p} \sin i$ degeneracy inherent in RV measurements, allowing for the determination of the planet's true mass rather than just a lower limit (Quirrenbach 2010).

Despite its potential, astrometric detection from the ground is extremely challenging due to atmospheric turbulence, which historically limited precision to the milli-arcsecond (mas) regime, insufficient for most planetary detections (Sozzetti 2005). Significant breakthroughs were achieved only via space-based missions. While the *Hipparcos* mission (M. A. C. Perryman et al. 1997) was the first large scale mission dedicated to astrometry, the current revolution is led by the ESA *Gaia* mission (Gaia Collaboration et al. 2016). With the release of *Gaia* Data Release 3 (DR3), the scientific community gained access to the first large-scale catalog of non single stars (NSS), containing thousands of solutions for binary and planetary-candidate systems (Gaia Collaboration et al. 2023a). It is expected that by the end of its mission, *Gaia* will have discovered tens of thousands of new exoplanets (M. Perryman et al. 2014; Feng 2026). Furthermore, the combination of *Gaia* astrometry with long-baseline RV data is proving to be one of the most powerful tools for precisely weighing exoplanets and brown dwarfs, providing a comprehensive view of their dynamical properties (e.g. Snellen & A. G. A. Brown 2018; Feng et al. 2022).

Legacy astrometric missions, such as $Hipparcos$, can still be valuable for the large baseline they provide when combined with $Gaia$. Specifically, the proper motion anomaly (PMa) is a powerful astrometric technique that can be applied to detect astrometric signature of stellar and substellar companions (including, but not limited to, Kervella et al. 2019; Brandt 2021; Kervella, Arenou & Thévenin 2022). As this will be foundational for this work, it will be discussed in great detail in the following sections.

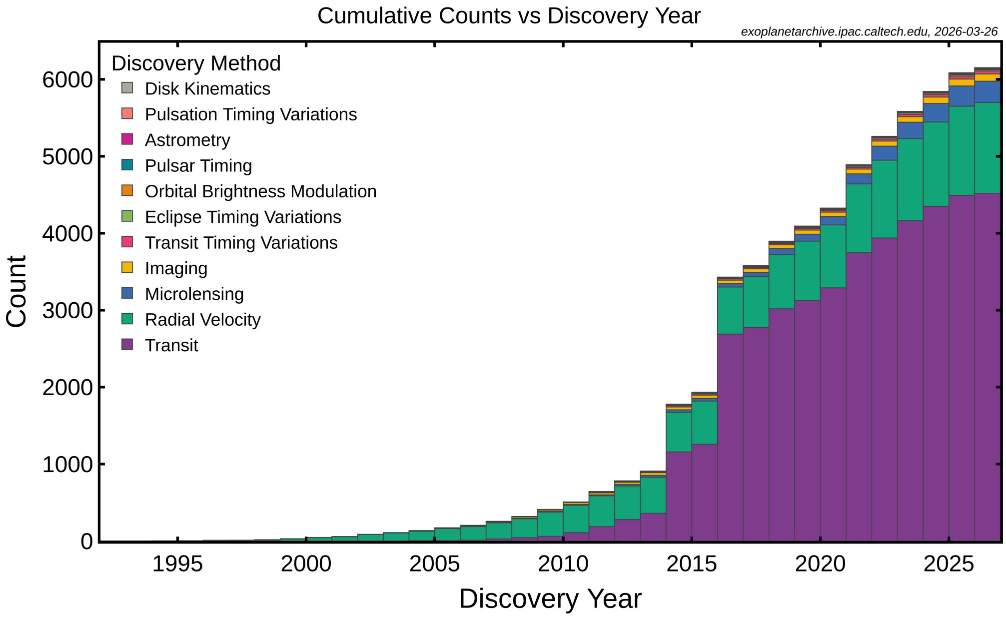

Figure 1.7: Cumulative histogram of discovered planet, by year. The colorcoding represents the discovery method. It is clear the preponderant role played by transits and RV.

HIPPARCOS and Tycho The HIgh Precision PARallax COllecting Satellite ($Hipparcos$, M. A. C. Perryman et al. 1997) was the first astrometric space survey by ESA, also named after the famous Greek astronomer Hipparchus, marking the beginning of modern astrometry. It was launched in 1989 and allowed the detection of over one hundred thousand stars with an unprecedented mas precision providing the first high-precision optical realization of the International Celestial Reference System (ICRS), known as the Hipparcos Celestial Reference Frame (HCRF) (ESA 1997). A new reduction was performed in 1997, yielding more precise data (van Leeuwen 2007a; van Leeuwen 2007b). An auxiliary star mapper, Tycho, was mounted on the probe, and provided astrometry for 2.5 million stars, although with lower precision (Høg et al. 1997; Høg et al. 1998). Similarly, Tycho data was also re-reduced to improve data quality (Høg et al. 2000b).

While the original Tycho-1 catalog contained approximately one million stars, the Tycho-2 Catalog (Høg et al. 2000b) significantly expanded this to 2.5 million stars. The primary innovation of Tycho-2 was not just the increased density, but the methodology used for proper motions. Unlike the main $Hipparcos$ catalog, which derived proper motions from a ∼3.5-year mission baseline, Tycho-2 incorporated ground-based observations from the previous century, including the Astrographic Catalog (AC, see Urban et al. 1998). This provided a tempo-

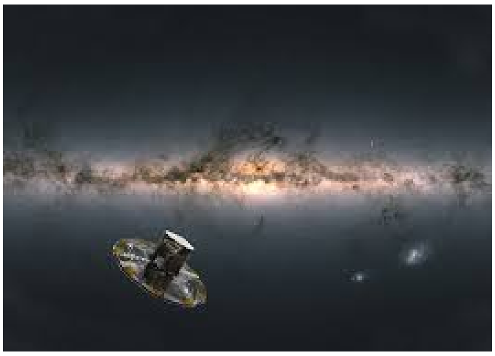

Figure 1.8: Artist's impressions of the *Hipparcos* (left) and *Gaia* (right) satellites. Sources: NASA (https://science.nasa.gov/mission/hipparcos/), ESA (https://www.esa.int/Science_Exploration/Space_Science/Gaia)

ral baseline of nearly 100 years, resulting in a PM precision of approximately $2.5\,\mathrm{mas\,yr^{-1}}$ (Høg et al. 2000b). Despite these differences in data fusion, the astrometric reference frame of Tycho-2 was explicitly anchored to the *Hipparcos* solution. Specifically:

- The global zero-point of positions and proper motions in Tycho-2 is defined by the *Hipparcos* stars present in the catalog (Høg et al. 2000b).
- Any global rotation or systematic distortion present in the *Hipparcos* Main Catalog is, by construction, inherited by Tycho-2 (Høg et al. 2000b).

Gaia The legacy of *Hipparcos* was enhanced by the subsequent *Gaia* mission (Lindegren & M. A. C. Perryman 1996; Gaia Collaboration et al. 2016), the billion-star surveyor. *Gaia* parallaxes reached an unprecedented resolution of μas (e.g., Sozzetti et al. 2016), becoming the most precise astrometric probe ever created, yielding breakthrough discoveries such as the Gaia-Sausage merger (Helmi et al. 2018). The most recent available data release is DR3 (European Space Agency (ESA) & DPAC Consortium 2022; Gaia Collaboration et al. 2023b), with the next DR4 forthcoming in a few months. The whole Gaia legacy will be included in DR5, containing the whole 66 months of observations, and it is expected in the early 2030s[12].

[12] https://www.cosmos.esa.int/web/gaia/release

1.3.d Direct imaging

Direct imaging represents the most intuitive yet technically demanding method of exoplanet detection. Unlike indirect methods, which rely on the planet's gravitational or photometric effect on the host star, imaging allows for the direct detection of a planetary companion (Traub & Oppenheimer 2010; Bowler 2016), whose orbital motion can also be tracked over time[13]. The primary challenge of this technique is the extreme contrast ratio (C) between the host star and its planetary companion. In the visible spectrum, a Jupiter-like planet is approximately 10^9 times fainter than its host star; this ratio improves to 10^6–10^7 in the near-infrared, where young, self-luminous planets emit the residual heat from their formation (Traub & Oppenheimer 2010). To overcome this contrast and the diffraction limit of the telescope, two key technologies are essential: Adaptive optics (AO) to correct for atmospheric turbulence in real-time, and coronagraphy to suppress the stellar diffraction pattern (e.g. Macintosh et al. 2014). The sensitivity of direct imaging is complementary to RV and transits, as it is most effective for detecting massive planets ($M \gtrsim 1\,\mathrm{M_{Jup}}$) around young stars at wide orbital separations ($a \gtrsim 10\,\mathrm{au}$), where the angular separation is sufficient to resolve the planet from the star's residual speckle noise (Bowler 2016). The first confirmed image of a planetary-mass companion was obtained around the brown dwarf 2M1207 using VLT/NACO (Chauvin et al. 2004), followed by the discovery of a multi-planetary system orbiting the A-type star HR 8799 (Marois et al. 2008; Marois et al. 2010).

Notable instruments Instruments for direct imaging can be divided into speckle interferometers and AO instruments. The first set employs fixed mirrors to obtain a large amount of low exposure frames which are capable of freezing the atmospheric turbulence around a target, which is later removed by comparing the different frames. While these instruments can reach the diffraction limit and provide information very close to the host star, their dynamic range is limited. Consequently, their sensitivity is typically restricted to the detection of stellar companions rather than planetary-mass objects. The second set of instruments works in the opposite direction: by modifying the shape of the mirrors with micromovements generated by a set of high-frequency actuators, the atmospheric contribution can be removed almost in its entirety. The two techniques also differ in their range of projected separations. Speckle imagers are able to reach the diffraction limit, but are limited in dynamic range, hence, they can provide information closer to the star but at lower contrast.

[13] https://science.nasa.gov/universe/exoplanets/a-four-planet-system-in-orbit-directly-imaged-and-remarkable/

Conversely, AO provides deeper contrast curves at larger separations.

Examples of speckle imagers include Alopeke, NESSI (Scott & Howell 2018), and Zorro (Scott 2019), while renowned AO instruments include SPHERE (Beuzit et al. 2019), Gemini Planet Imager (GPI, Macintosh et al. 2006), NIRC2 (e.g., Xuan et al. 2018) and PHARO (Hayward et al. 2001).

A further essential category is that of space-based telescopes, most notably JWST and the upcoming Nancy Grace Roman Space Telescope. As they operate outside the Earth's atmosphere, these facilities do not require AO systems to compensate for turbulence. Instead, they exploit the extreme stability of the point spread function (PSF) and utilize coronagraphs to achieve the highest possible contrast levels close to the star.

1.3.e Other methods

The exploration of the parameter space of exoplanets involves several more methods, as can be seen in Figure 1.7. Although their usage is beyond the scope of this work, I list the most prominent ones below, highlighting some the of most remarkable results obtained.

Microlensing Gravitational lensing arises from the curvature of spacetime induced by mass, which deflects the path of electromagnetic radiation as predicted by General Relativity; its first observational confirmation was obtained by Dyson, Eddington & C. (1920) during the 1919 solar eclipse. When light emitted by a background source is bent by a sufficiently massive foreground object acting as a gravitational lens, the observed image can be magnified, distorted, or even multiplied, depending on the alignment between source, lens, and observer. In the strong lensing regime, which was first observed in 1979 (Bernstein, Tyson & Kochanek 1993), this effect produces multiple images, arcs, or Einstein rings, typically involving high-redshift galaxies or clusters as lenses (Saha et al. 2024), and is relatively rare in the nearby universe due to the scarcity of such massive structures. In contrast, weak lensing does not generate multiple images but instead induces coherent distortions in the shapes of background sources along preferred directions, without requiring precise alignment, allowing lower-mass galaxies or clusters to act as lenses (Saha et al. 2024); as a result, it is inherently statistical in nature. Both regimes are extensively used to probe mass-density profiles, mass-to-light ratios, and large-scale mass distributions, as exemplified by the *Euclid mission*, launched in July 2023, which combines strong and weak lensing to study over 200,000 high-redshift galaxies (Atek et al. 2024). Microlensing is particularly relevant for studying exoplanets. In this regime, the lens mass is stellar and it could be a planet, a star or an exoplanetary system. Therefore, the mass is too small to produce an observable displacement or distortion of light (Cloutier 2026). When a foreground exoplanetary system, the lens, aligns with a background star, it produces a tiny and temporary increase in the apparent brightness of the lensed star. This phenomenon, also known as magnification, is observed as a peculiar light curve. Unlike the previous regimes, this phenomenon is statistically rare, so it is unlikely for a single object observation to detect this effect. For this reason, large-scale surveys are conducted in star-dense regions, such as the galactic bulge, to observe thousands of star simultaneously (M. Perryman 2018). This method allows for the detection of long-period and free-floating planets, because the measurement is instantaneous (and unrepeatable) and it does not require an observation lasting a full orbital period (Gaudi 2012). It is also sensitive to exomoons, because the geometry of the lens and the light curve are closely tied (Gaudi 2010). This is, currently[14] the only method capable of detecting planets far beyond our galactic neighborhood. As with astrometry, few planets have been discovered via microlensing to date.

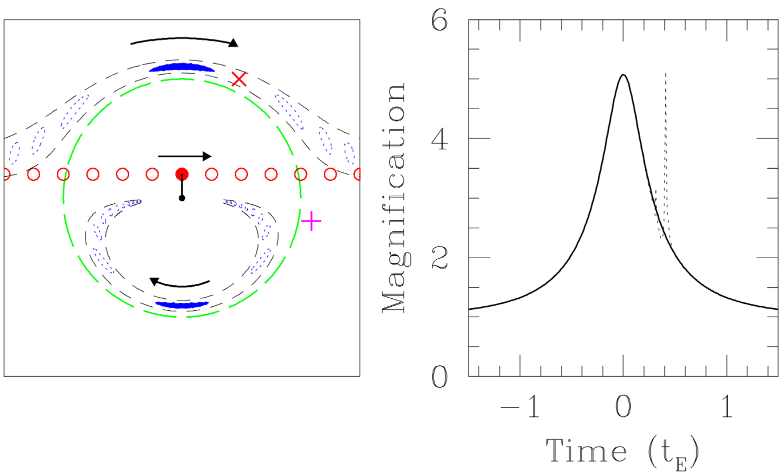

Figure 1.9: Plot of microlensing of an exoplanetary system. **Left**: Blue dotted ovals represent the images of the lensed system (red circles), relative to the position of the lens (solid black dot). If the lens has an exoplanet orbiting it in the position marked by a red cross, the light curve will show a smooth deviation. If the planet is in the position marked by the pink plus, no microlensing is detected. Solid blue ovals correspond to the images produced by the solid red circle. **Right**: Lens light profile, with the perturbation caused by the planet drawn as a dotted peak. Source: Gaudi (2010).

Transit time variation (TTV) The TTV (Holman & Murray 2005) is a dynamical effect observed in a transiting exoplanet due to the presence of additional non-

[14] A possible exception may be Gaia future detections, which are not available yet.

transiting companion(s). Given at least three transits it is possible to detect a variation from the linear ephemeris

$$TT_{\mathrm{N,lin}} = TT_{\mathrm{ref}} + P_{\mathrm{orb}} \cdot N \tag{1.10}$$

where P_{orb}, TT_{ref}, and N represent the planet orbital period, a reference ephemeris and the number of elapsed transits, respectively, after which we compute the expected transit time $TT_{\mathrm{N,lin}}$, under the assumption of the transit being governed by a linear law. In the case this law is not fulfilled, and the observed transit time differs by a significant margin from the expected time (fig. 1.10), we have a TTV and we are therefore able to extract valuable data about the non-transiting planet causing this variation. This technique has been extensively used (e.g., Holman et al. 2010; Lithwick, Xie & Wu 2012; Borsato et al. 2014; Holczer et al. 2016; Hadden & Lithwick 2017; Naponiello 2026; Maciejewski 2026) and it accounts for the discovery of roughly 300 planets. It is worth noting that the amplitude of the TTV is enhanced when the planets are close to a mean-motion resonance (MMR).

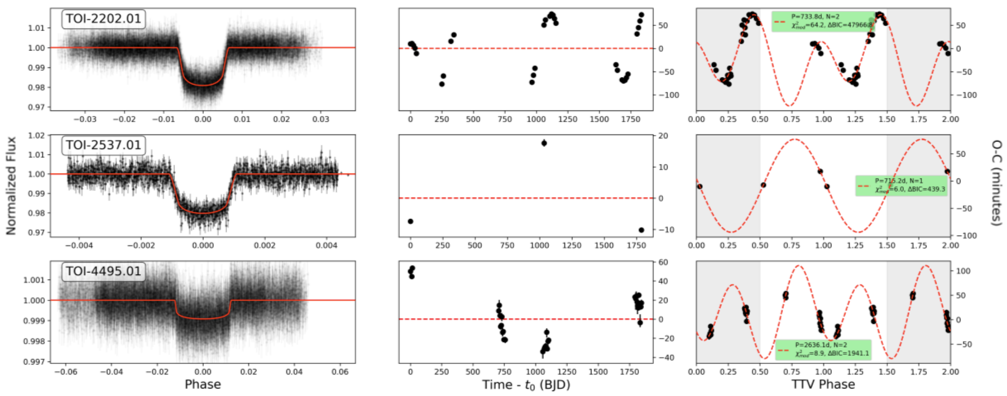

Figure 1.10: Three-panel diagnostic plot for TTV candidates. Left: TTV-corrected transit light curves with best fit model. Middle: observed-computed (O-C) measurements. Right: O-C plot folded to best fit the TTV period. Adapted from Naponiello (2026).

2 Obliquities in exoplanetary systems

Obliquities are a key parameter in understanding the formation and evolution of planetary systems. The low mutual inclination between Solar System planets and our Sun's spin axis (Beck & Giles 2005) is not always the rule, and indeed exoplanetary systems show a wide range of spin-orbit inclinations (e.g., S. Albrecht et al. 2012; S. H. Albrecht et al. 2021; Bourrier et al. 2023; Espinoza-Retamal et al. 2024; Zak et al. 2024; Espinoza-Retamal et al. 2025; Rossi et al. 2026). This diversity is extremely interesting, as it reflects the different dynamical histories of various exoplanets. The first models of planet formation were developed based on the observational results gathered from our Solar System. Indeed, the standard model of planet formation consists of a disk of dust, gas, and debris forming after a gas cloud collapses into a protostar. The rotational motion of the disk causes dust to aggregate into pebbles, eventually forming planets[1], whose orbits are clearly equatorial with respect to the stellar rotation (see e.g., Lissauer 1993, for a review). However, this standard process may vary depending on several factors, and this can have consequences on the architecture of the planetary system, including the obliquity of the planetary orbits. High-resolution observations with ALMA have revealed complex geometries, including warped or broken disks (Facchini, Lodato & Price 2013; Bi et al. 2020). Such architectures can be caused by magnetic torques between the young star and inner disk (Lai, Foucart & Lin 2011), even in the case of binaries (Foucart & Lai 2013), or by the interaction with a distant binary companion (Batygin 2012). In the case of HJs, the obliquity can be affected by the photoevaporation rate in the inner cavity of a protoplanetary disk as well as the migration type of the planet (Zanazzi

[1]The model presented here is clearly oversimplified, the process is not fully understood yet and it is an interesting topic of debate.

& Lai 2018). Neptune-sized planets can be influenced by the outer planetary disk and have their orbits tilted rapidly after formation due to the presence of a massive outer disk (Handley & Batygin 2026). Orbital architectures can be shaped by a plethora of factors even after planet formation. These include more violent mechanisms that can also take place, such as planet-planet scattering (Rasio & Ford 1996; Weidenschilling & Marzari 1996; Chatterjee et al. 2008) or stellar fly-bys, whose strong gravitational interaction can induce a tilt of the planetary orbit. Often, the Kozai-Lidov (Kozai 1962; Lidov 1962) mechanism is invoked to explain misalignment coupled with an increase in eccentricity, caused by an external companion. However, in the latter case, the planet is in a regime of maximum tidal interaction with its host star, hence the eccentricity can be dissipated and the orbit circularized (D. Fabrycky & Tremaine 2007). Clearly, nothing prevents two or more of these mechanisms from occurring at the same time, hence the picture of planetary alignment is quite complex.

2.1 Rossiter–McLaughlin effect

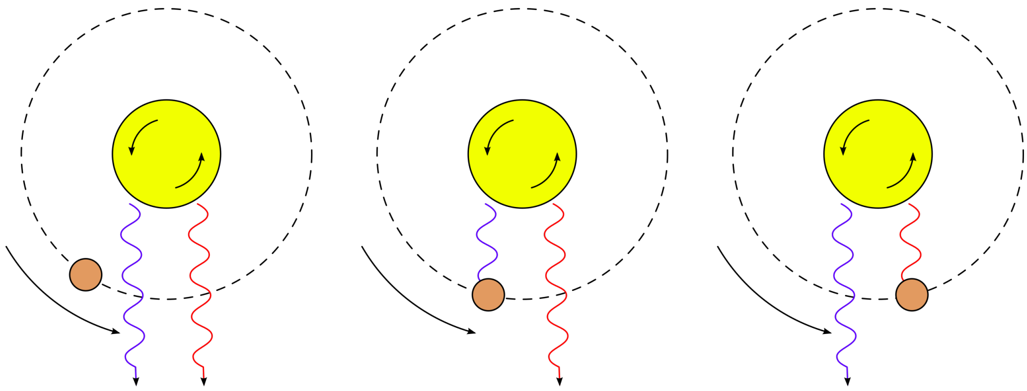

Figure 2.1: Extremely simplified model showing a counterclockwise-rotating star with a planet orbiting it. During its counterclockwise orbit, the planet sequentially blocks blue-shifted and red-shifted light (light coming from the approaching and receding side respectively). Source: Autiwa (2010).

Exoplanets, both as singles or as a population, can be studied to understand their dynamical history based on their current architecture by exploiting the Rossiter–McLaughlin (RM) effect. At the end of the 19$^{\text{th}}$ century, Holt (1893) theorized that a star's rotation rate could affect spectral line broadening, because different parts of the star have different radial velocities relative to the observer. At the time, it was not possible to observe this broadening directly, as the broadening caused by the resolution of the available instruments was larger than this effect. In order to prove the presence of rotational broadening, he suggested spectroscopic observations of the eclipsing binary star Algol. Holt (1893) argued that, during an eclipse by its companion, a sufficiently sensitive instrument could, in principle, detect an apparent change in radial velocity, due to the companion blocking the light of the receding or approaching hemisphere (fig. 2.1). This was the theoretical foundation for the discovery of the actual effect, which was reported independently by Rossiter (1924) and McLaughlin (1924), who observed it in two binary star systems, βLyrae and the aforementioned Algol, respectively. Indeed, RM effect can be applied to study the inclination of binary stars (S. Albrecht et al. 2009; Triaud et al. 2013; Triaud et al. 2017; Spejcher et al. 2025).

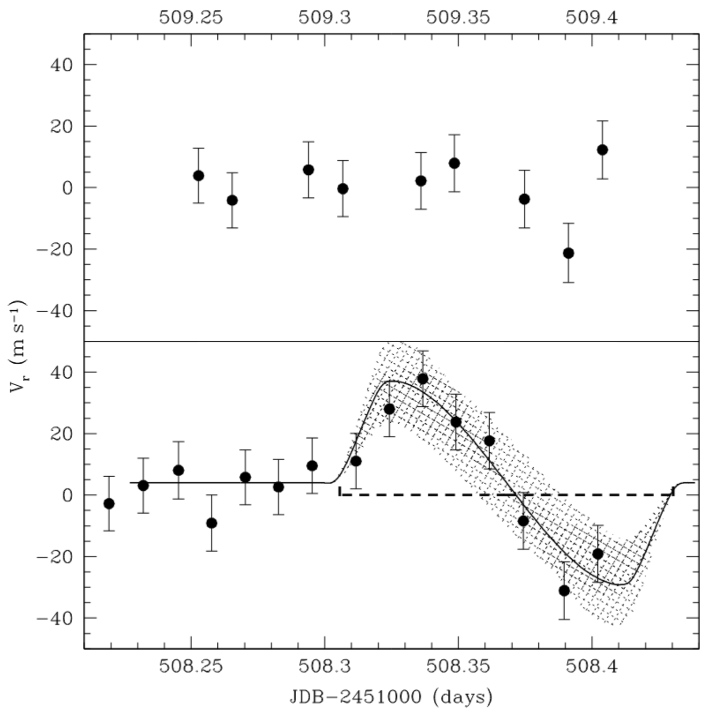

Figure 2.2: Two sequences of RV measurements of HD 209458 from Queloz et al. (2000a). The top panel shows the out-of-transit RV curve, whereas the bottom panel, showing the in-transit RV curve, highlights the peculiar shape of RM effect.

In a similar way, it can be used to measure the obliquity of a transiting planet: Queloz et al. (2000a) were the first team to perform a RV measurement of the RM effect on the transiting exoplanet HD 209458 b. The result is shown in fig. 2.2.

Figure 2.4 offers a detailed visualization of the quantities involved in the RM effect. The final goal of RM observations is to measure the true spin-orbit obliquity Ψ—the angle between the planet orbital axis i_{orb} and the stellar spin axis

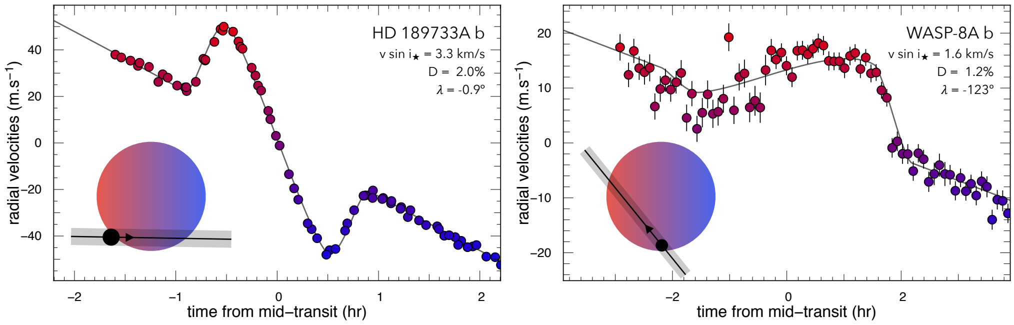

Figure 2.3: The RM effect on the HJs HD 189733A b (left) and WASP-8A b (right). The RV points are color-coded according to Doppler shift. It is possible to note how aligned planets (left) show a more symmetrical RV curve, as opposed to misaligned ones (right). Source: Triaud (2018)

$i_\star$. However, knowledge of this quantity necessarily requires the measurement of λ[2], the projected (on the plane of the sky) spin-orbit obliquity. This measurement can be performed by observing the apparent RV variation caused by the transiting planet, whose amplitude can be quantified as

$$A_{\rm RM} \simeq \frac{2}{3}\left(\frac{R_{\rm p}}{R_\star}\right)^2 v \sin i_\star \sqrt{1-b^2} \tag{2.1}$$

where $D = (R_{\rm p}/R_\star)^2$—the ratio of planetary and stellar radii squared, respectively —is the transit depth, $v \sin i_\star$is the equatorial velocity v projected onto the line of sight — defined by the angle $i_\star$ — and b is the impact parameter (Triaud 2018). The shape of the RM curve is determined by the λ value itself (fig. 2.3), as well as the motion of the planet relative to the stellar spin (either prograde or retrograde) (Triaud 2018).

The mathematical framework useful to transform λ into Ψ can be discussed following the argument by D. C. Fabrycky & Winn (2009). Let $\hat{\boldsymbol{n}}_o$ and $\hat{\boldsymbol{n}}_\star$ be the unit vectors in the directions of the planet orbital angular momentum and the stellar rotational angular momentum, respectively, as shown in fig. 2.4. As mentioned earlier, the angle between these vectors is Ψ, and it is not directly measurable. It is useful to introduce the coordinates systems shown in fig. 2.5. The XYZ system in the left panel is characterized by $\hat{\boldsymbol{Z}}$ pointing towards the observer, $\hat{\boldsymbol{X}}$ pointing to the line of nodes of the planetary orbit, and $\hat{\boldsymbol{Y}}$ completing the right-handed triad. As a result, $\hat{\boldsymbol{n}}_o$ lies in the $Y-Z$ plane and its inclination is

$$i_o = \arccos\left(\hat{\boldsymbol{n}}_o \cdot \hat{\boldsymbol{Z}}\right) \tag{2.2}$$

[2]In this thesis, I will adopt the Ohta, Taruya & Suto (2005) convention described above, with λ measured from $i_{\rm orb}$ to $i_\star$. Some authors measure this angle oppositely as calling it $\beta = -\lambda$

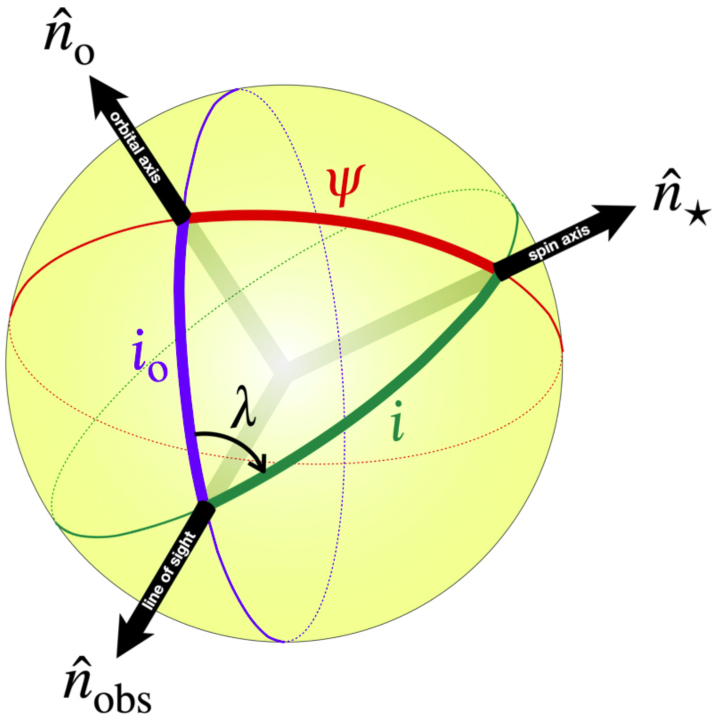

Figure 2.4: Tridimensional visualization of vectors and angles useful to study the system. The vectors $\mathbf{n}_\star$, $\mathbf{n_o}$, $\mathbf{n_{obs}}$ represent the stellar rotational axis, the planetary orbital axis and the LOS, respectively. i_o is the orbital obliquity, i is the stellar inclination, λ is the spin-orbit inclination projected on the LOS defined from the orbital obliquity to the stellar obliquity, and Ψ is the true obliquity, or 3-D inclination. Source: S. H. Albrecht, Dawson & Winn (2022).

ranging from 0 to π. Similarly, the stellar inclination is given by

$$i_\star = \arccos\left(\hat{\boldsymbol{n}}_\star \cdot \hat{\boldsymbol{Z}}\right) \tag{2.3}$$

Similar geometrical considerations, which also include the sky-projected spin-orbit angle λ, lead to the following definition of $\hat{\boldsymbol{n}}_o$ and $\hat{\boldsymbol{n}}_\star$ in the observer-oriented coordinate system

$$\hat{\boldsymbol{n}}_o = \hat{\boldsymbol{Y}}\ \sin i_o + \hat{\boldsymbol{Z}}\ \cos i_o \tag{2.4}$$

$$\hat{\boldsymbol{n}}_\star = \hat{\boldsymbol{X}} \sin i_\star \sin\lambda + \hat{\boldsymbol{Y}} \sin i_\star \cos\lambda + \hat{\boldsymbol{Z}} \cos i_\star \tag{2.5}$$

It is important to note that a two-fold degeneracy exists due to symmetry: a configuration (i_o, λ) is indistinguishable from its opposite $(\pi - i_o, -\lambda)$. Therefore, it is a suitable choice to restrict i_o and λ to the ranges $[0, \pi/2]$ and $[-\pi, \pi]$, respectively.

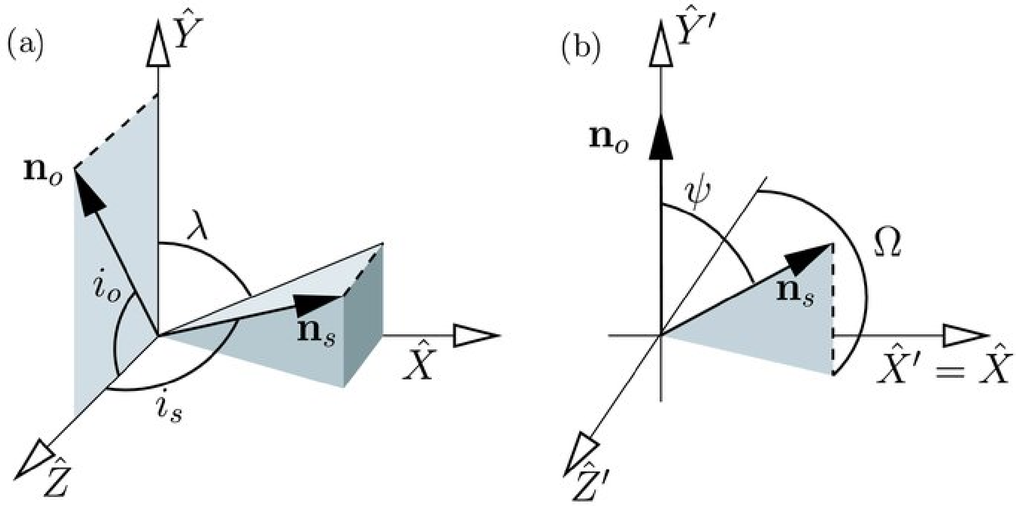

Figure 2.5: Coordinate systems for theoretical description of RM effect. **Left**: an observer-oriented coordinate system, with $\hat{\boldsymbol{Z}}$ pointing towards the LOS and the $\hat{\boldsymbol{X}} - \hat{\boldsymbol{Y}}$ plane coinciding with the sky plane. **Right**: an orbit-oriented coordinate system, with $\hat{\boldsymbol{Y}'}$ coinciding with the planet orbital axis and the $\hat{\boldsymbol{X}'} - \hat{\boldsymbol{Z}'}$ plane being the orbital plane. The systems are tied by a rotation of $\pi/2 - i_o$ around $\hat{\boldsymbol{X}} \equiv \hat{\boldsymbol{X}'}$. Source: D. C. Fabrycky & Winn (2009).

It is possible to introduce an orbit-oriented coordinate system $X'Y'Z'$, shown in the right panel of fig. 2.5. In this orbit-oriented frame, $\hat{\boldsymbol{Y}'} \equiv \hat{\boldsymbol{n}}_o$. Therefore, $X'Y'Z'$ is tied to XYZ by a $\pi/2 - i_o$ rotation about the X-axis.

It is possible to define Ψ as the polar angle and Ω as the azimuthal angle and, without further geometrical analysis, note that

$$\hat{\boldsymbol{n}}_\star = \hat{\boldsymbol{X}'} \sin\Psi \sin\Omega + \hat{\boldsymbol{Y}'} \cos\Psi - \hat{\boldsymbol{Z}'} \sin\Psi \cos\Omega = 0 \tag{2.6}$$

Considering the aforementioned rotation, the equations tying the different coordinate systems are

$$\hat{\boldsymbol{X}'} = \hat{\boldsymbol{X}} \tag{2.7}$$

$$\hat{\boldsymbol{Y}'} = \hat{\boldsymbol{Y}} \sin i_o + \hat{\boldsymbol{Z}} \cos i_o \tag{2.8}$$

$$\hat{\boldsymbol{Z}'} = -\hat{\boldsymbol{Y}} \cos i_o + \hat{\boldsymbol{Z}} \sin i_o \tag{2.9}$$

which can be employed to write eq. (2.5) in the orbit-oriented frame, without the need for Ψ and Ω, as

$$\mathbf{n}_s = \hat{\boldsymbol{X}}' \sin i_\star \sin\lambda + \hat{\boldsymbol{Y}}'(\sin i_\star \cos\lambda \sin i_o + \cos i_\star \cos i_o) + \hat{\boldsymbol{Z}}'(\cos i_\star \sin i_o - \sin i_\star \cos\lambda \cos i_o) \tag{2.10}$$

Since eq. (2.5) and eq. (2.10) represent the same vector, the following three relations naturally arise

$$\sin i_\star \sin\lambda = \sin\Psi \sin\Omega \tag{2.11}$$

$$\cos\Psi = \sin i_\star \cos\lambda \sin i_o + \cos i_\star \cos i_o \tag{2.12}$$

$$\sin\Psi \cos\Omega = \sin i_\star \cos\lambda \cos i_o - \cos i_\star \sin i_o \tag{2.13}$$

Assuming a realistic scenario, in which λ has been measured via RM observations, it is possible to infer constraints on the expected Ψ by combining observations of multiple systems (D. C. Fabrycky & Winn 2009). With these definitions, it is clear that

$$\hat{\boldsymbol{n}}_\star \cdot \hat{\boldsymbol{n}}_o = \cos\Psi = \cos i \cos i_o + \sin i \sin i_o \cos\lambda \tag{2.14}$$

$$(\hat{\boldsymbol{n}}_\star \times \hat{\boldsymbol{n}}_o) \cdot \hat{\boldsymbol{n}}_{obs} = \sin i \sin i_o \sin\lambda \tag{2.15}$$

The quantities populating eqs. (2.14) and (2.15) can be challenging to obtain from a single measurement done via a single technique, because different methods are mostly sensitive to different parameter ranges. Moreover, the light our instruments detect is an integration of the star flux and spectrum over the whole visible hemisphere. Conversely, some spectral features depend on the star's orientation. Thus, the determination of Ψ requires a combination of different observation techniques (S. H. Albrecht, Dawson & Winn 2022). In the end this framework allows for the de-projection of λ via the spherical cosine law as given by eq. (2.14).

It is important to underline the importance of a correct inference of $\sin i_\star$ (Masuda & Winn 2020), without resorting on incorrect numerical or Monte Carlo (MC) computations. Indeed, a quantitatively consistent result for $i_\star$, as well as the other parameters involved, can be obtained following the footsteps of several authors (S. H. Albrecht et al. 2021; S. H. Albrecht, Dawson & Winn 2022; Bourrier et al. 2023; Bowler et al. 2023; Morgan et al. 2024; Rossi et al. 2026). Assuming a rigid body rotation of the star—instead of the more physically correct differential rotation—it is possible to perform the following assumption

$$\sin i_\star = v \sin i_\star (v)^{-1} = v \sin i_\star \left(\frac{2\pi R_\star}{P_{\text{rot}}} \right)^{-1} \tag{2.16}$$

where $v = 2\pi R_\star / P_{\text{rot}}$ is the stellar equatorial velocity and P_{rot} is the stellar rotation period. Hence, we can rewrite eq. (2.14) as

$$\begin{aligned} \cos \Psi = {} & v \sin i_\star \left(\frac{2\pi R_\star}{P_{\text{rot}}} \right)^{-1} \cos \lambda \sin i_{\text{orb}} \\ & + \cos \left(\arcsin \left(v \sin i_\star \left(\frac{2\pi R_\star}{P_{\text{rot}}} \right)^{-1} \right) \right) \cos i_{\text{orb}} \end{aligned} \tag{2.17}$$

and sample uniformly on $R_\star$, λ, P_{rot} and isotropically on $\sin i_\star$ via Markov chain Monte Carlo (MCMC). Several Python packages can be used, for example `emcee` (Foreman-Mackey et al. 2013) or `PyMC` (Abril-Pla et al. 2023). The inference of λ can be performed using other methods to model the RM.

2.1.a Reloaded Rossiter–McLaughlin

Cegla et al. (2016) proposed a method known as the reloaded Rossiter–McLaughlin (RRM) effect. This method allows RM modeling through a direct measurement of the cross-correlation function (CCF) and RV of the stellar surface occulted by the planet during its transit. This approach reduces the reliance on traditional RM assumptions, namely:

- The local CCF is directly measured without prior assumptions on the local or disk-integrated profile.
- The rigid-body rotator approximation is not required, allowing one to solve $i_\star$ without relying on $v_{\text{eq}} \sin i_\star$.

However, high resolution spectra from highly stable instruments are needed to analyze the light (e.g., ESPRESSO, HARPS, HARPS-N), as well as a robust knowledge of stellar photosphere via accurate stellar models.

2.1.b Rossiter–McLaughlin revolutions

Bourrier et al. (2021) argued that Rossiter–McLaughlin revolutions (RMR) could be useful to extract more information from spectral data compared to classical RM, particularly for small-sized planets. This is possible because the entire series of spectral profiles is used. It also allows for the detection of mutual inclinations in multi-planet systems. However, multiparameter fits for each transit observation are computationally expensive compared to a traditional RM fit.

2.1.c Doppler shadow

Miller et al. (2010) were among the first to analyze the spectral signature left during the planetary transit, and tomographically reconstruct the planet trajectory on the stellar disk, in order to infer λ and $v \sin i_\star$, without traditional RM biases, such as the displacement of the CCF centroid. This method is able to lift the degeneracy between the two quantities (D. J. A. Brown et al. 2012).

2.2 Obliquity distribution

Measuring the RM effect is observationally expensive in terms of telescope time, in addition to the prerequisite of a transiting configuration (Winn et al. 2005; Cloutier & Triaud 2016). Besides NEA and `exoplanet.eu`, specialized databases exist that are dedicated to tracking measured obliquities. Among these, the most famous is certainly TEPCat[3] (Southworth 2011; Southworth 2026). Considering the plethora of factors that can influence the orbital architecture, it comes as no surprise that the dynamics of a planetary system play a key role in our understanding of exoplanets as a population, as well as the conditions under which they formed. In recent years, several conclusions have been drawn regarding the obliquity distribution of planets or planet types. Winn et al. (2010) noted how HJs orbiting stars with effective temperatures higher than $\sim 6250\,\mathrm{K}$ can be misaligned. They concluded that this threshold is related to the so called Kraft break (Kraft 1967), a threshold beyond which the convective envelope of the star becomes negligible[4]. S. H. Albrecht et al. (2021), using a sample of 57 planets, suggested that planets tend to cluster on either aligned or perpendicular orbits, with a deficit of planets in between, as in Figure 2.6.

In a later work, Siegel, Winn & S. H. Albrecht (2023) pondered this conclusion demonstrating that gravity darkening (GD) is a method inherently biased towards the detection of perpendicular orbits. The team also suggested how a non-uniform sample of stellar inclinations $i_\star$ could have biased the former interpretation. This finding was later supported by Dong & Foreman-Mackey (2023),

[3] `https://www.astro.keele.ac.uk/jkt/tepcat/`

[4] This physical boundary is critical because stars cooler than the Kraft break possess thick convective envelopes that facilitate efficient tidal dissipation. In these systems, the tidal interaction between the star and the planet leads to orbital realignment on timescales typically shorter than the age of the system. Conversely, for hotter stars ($T_{\mathrm{eff}} > 6250\,\mathrm{K}$) with primarily radiative envelopes, tidal dissipation is orders of magnitude weaker, resulting in realignment timescales that often exceed the stellar lifetime, thus preserving the primordial misalignments.

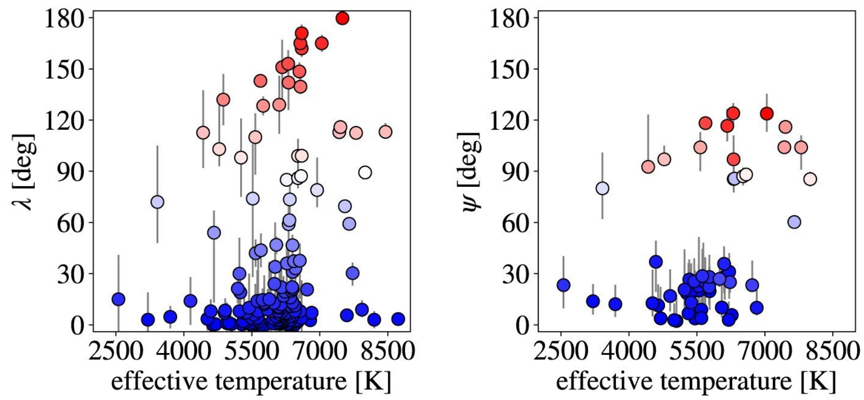

Figure 2.6: Dichotomous distribution of exoplanetary obliquities according to S. H. Albrecht et al. (2021). Starting from ~ 150 projected obliquities λ, as seen in the left panel, the authors proved a dichomotous behavior of the whole exoplanetary population, as seen in the right panel.

who used a hierarchical Bayesian framework to prove that a sample of uniformly drawn synthetic planets would result in an obliquity distribution composed of a strong peak of aligned planets followed by an isotropic tail of misalignments, with no peculiar clustering, as in Figure 2.7. Lastly, Rossi et al. (2026) proved using a data-driven approach on the largest sample of true obliquities available to date, surpassing other catalogs (S. H. Albrecht, Dawson & Winn 2022; Knudstrup et al. 2024), how the behavior of predominantly aligned planets can start to emerge with more robust statistics and a more uniform distribution of $i_\star$. Small-sized exoplanets are being increasingly studied as their mass and size, dramatically lower than their gas giants counterparts, may lead them to different formation and evolution pathways. On this topic, Rossi et al. (2026) falls into the ongoing discussion regarding Neptunian exoplanets: compact[5] multi-planet systems tend to be aligned (Radzom et al. 2024; Handley et al. 2026), whereas isolated systems tend to be misaligned (Radzom et al. 2024; Polanski et al. 2025), polar Neptunians are stable to tides (Louden & Millholland 2024). Most of all, Neptunians seem to show a dichotomous behavior (Petrovich et al. 2020; Espinoza-Retamal et al. 2024; Rossi et al. 2026). Figure 2.8 presents the most updated catalog of Neptunian true obliquities, which suggests the existence of a dichotomy, although Rossi et al. (2026) underscored how low statistics and an anisotropic $i_\star$ distribution surely play a role. Ongoing research from several teams is helping to undermine this dichotomy, thanks to new obliquity measurements (J. I. Espinoza-Retamal 2026, private communication). Nonethe-

[5]where we define compact a system where the two planets have an orbital period ratio $P_2/P_1 < 4$ according to Radzom et al. (2024) definition

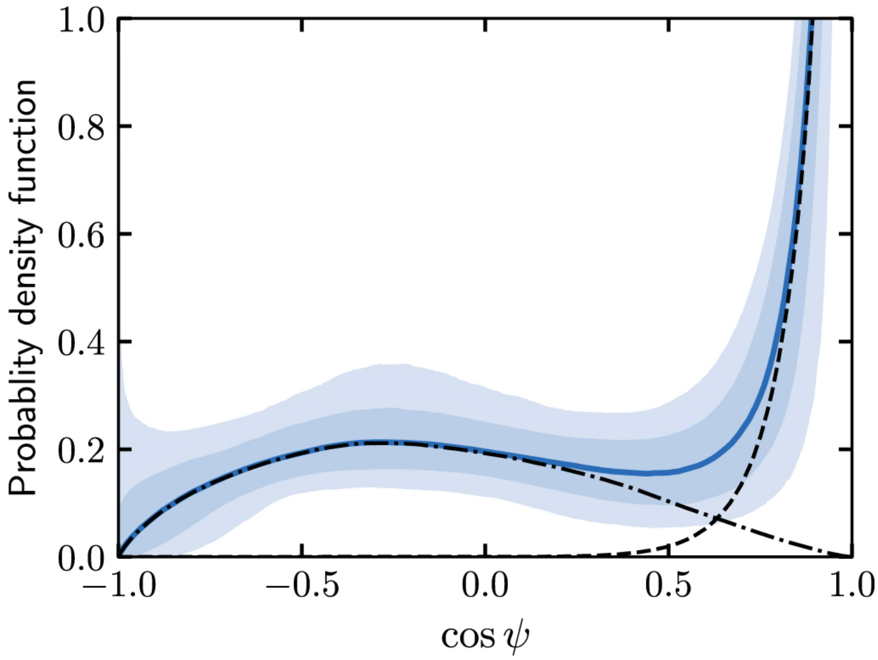

Figure 2.7: Hierarchical Bayesian framework (HBA) from Dong & Foreman-Mackey (2023) probing the obliquity trend of the exoplanetary population. The overall population, as well as the overrepresented Jupiter-sized subpopulation, should present a peak of aligned orbits, followed by an isotropic tail of misalignments.

less, mechanisms to ensure Neptunians stay in polar orbits have been recently proposed (Handley & Batygin 2026), although the applicability of such mechanisms seems limited to a few planets in specific configurations (L. Handley 2026, private communication).

Although Rossi et al. (2026) disproved that the whole exoplanetary population shows a preferential alignment for either equatorial or polar orbits, the team highlighted how the subpopulation of Neptunians[6] still presents a peculiar Ψ distribution. The small sample size highlighted by Rossi et al. (2026) is primarily caused by the technical difficulty in detecting such small planets, with a RV signal being as much as an order of magnitude smaller than that produced by a Jupiter-mass planet. PLATO (Rauer et al. 2025) is expected to overcome these difficulties, injecting thousands of planets into the overall sample, with many of them scheduled for follow-up measurements with high-resolution spectrographs. Its unmatched sensitivity will be foundational to detect and characterize the first Earth-twin, but data analysis by astronomers will necessarily take

[6]Recall that Neptunians (sometimes referred to as sub-Saturns) are defined as those planets having a mass $10 < M/\mathrm{M}_\oplus < 100$. Boundaries used to define this category are not unique and different authors may adopt different mass limits.

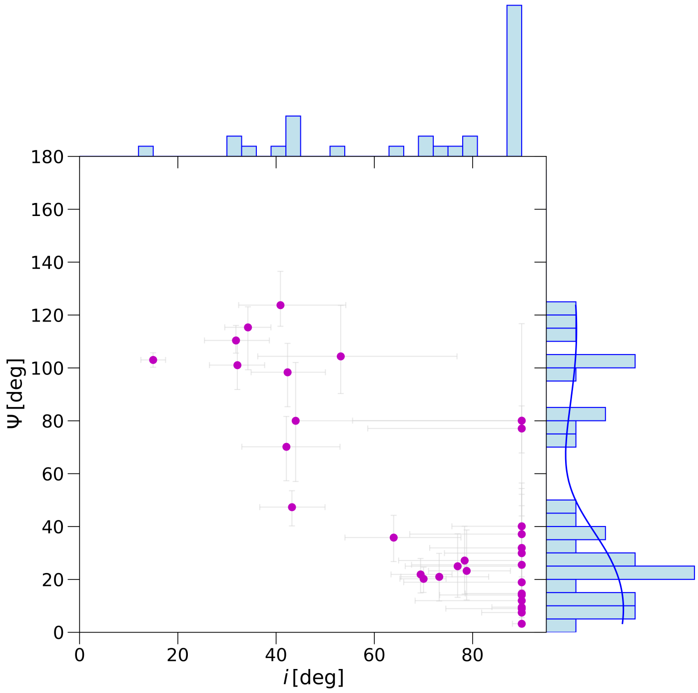

Figure 2.8: True obliquity distribution of Neptunian exoplanets from Rossi et al. (2026) dataset. The marginal on the y axis represents an histogram of Ψ values binned every $5°$. The KDE computed on the histogram highlights the dichotomous behavior. The marginal on the x axis highlights the uneven distribution of stellar inclination $i_\star$.

several years. Neptunes are also expected to have formed differently from gas giants. While Jupiters can be formed by a relatively fast runaway gas accretion after formation beyond the snow line, Neptunians are probably the result of a core accretion failure halted by disk dissipation. As a consequence, their migration processes also differ from their Jovian counterparts. The gas giants usually experience Type II migration, opening a gap in the protoplanetary disk, whereas lighter Neptunians undergo Type I migration and are more influenced by the disk itself (see Kley & Nelson 2012, for a review). In the end, if the planet ends up in a misaligned orbit, the tidal effects are also dramatically different because of the different planet-to-star mass ratio $q = M_p/M_\star$, which is correlated to the tidal quality factor

$$\tau_{\text{tidal}} \propto q^{-2} \tag{2.18}$$

This basically implies that Neptunians have longer realignment timescales, often exceeding the age of the universe, hence they are doomed to reside in misaligned orbits if previous processes moved them to such configurations.

2.3 The effect of binarity

Considering the complex and evolving picture of Neptunian architectures, the goal of this work is to expand our knowledge of their orbital distribution. Since stellar companions can influence the evolution of planetary systems, the goal of this thesis is to systematically study the Neptunians presented by Rossi et al. (2026) to probe for the presence of stellar companions, and then understand whether their presence correlates with the sample orbital distribution. This task will be accomplished in a multi-technique fashion, combining RV, direct imaging, and PMa to constrain the presence of binaries. A binary companion can substantially alter planetary alignment through two main channels: primordially, by exerting torques on the protoplanetary disk that lead to a spin-disk misalignment before planet formation is complete (Batygin 2012), or dynamically, through the Kozai-Lidov mechanism. In the latter, the gravitational perturbations from the distant companion induce large-scale oscillations in the planet's inclination and eccentricity, which, coupled with tidal dissipation, can result in the planet settling into a highly inclined or even retrograde orbit (D. Fabrycky & Tremaine 2007).

3 Probing for stellar companions: imaging and radial velocity

Historically, direct imaging and RV modeling have been key to detecting the presence of binary companions. The former can be used to identify contaminants that may hinder the photometric analysis of nearby target stars, with examples including Furlan et al. (2017) and Ziegler et al. (2020), whereas a detection with RV implies that the two stars are most likely gravitationally bound (e.g., Knutson et al. 2014). To confirm a true physical association, these techniques are often complemented by astrometric data. Specifically, comparing the parallax and PM of the two sources allows one to determine if they are comoving, thereby distinguishing bound binaries from background contaminants. Another technique to discover stellar companions is the photometric monitoring, that allows one to identify eclipsing binaries. As these objects are typically very close to the central stars, similarly to the planetary companions studied in this thesis, I do not consider this technique. The case of planets in circumbinary configuration is different from the dynamical point of view and is not discussed in this thesis.

3.1 Direct imaging

Different techniques have different ranges of applicability, as shown in Figure 3.1. The first I am going to introduce is direct imaging, which is capable of probing for the presence of companions in wide orbits; indeed, several binaries have been discovered this way, starting with BDs even before the discovery of 51 Peg b (Becklin & Zuckerman 1988). The fundamental challenge of direct imaging analysis of binary stars lies in the projection effects of the data. Specifically, the information that can be retrieved is limited to the projected angular separation of the target from its possible companion. Converting the projected separation ρ into the physical semi-major axis $a_{\rm rel}$, conventionally measured in au, is a

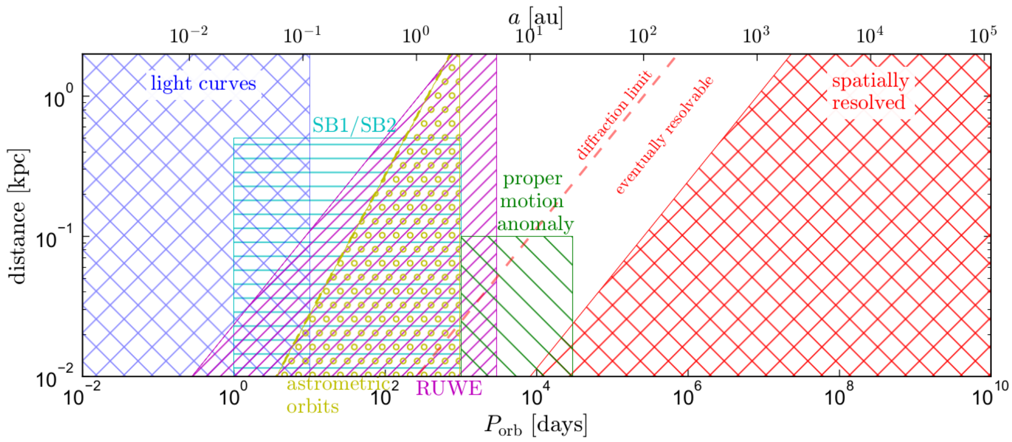

Figure 3.1: Discovery space for binary star detection methods. The plot shows the sensitivity regions of various observational techniques as a function of orbital period $P_{\rm rot}$ (or semi-major axis a)) on the x-axis, and distance from Earth on the y-axis. Colored regions indicate where methods such as light curves (photometry), SB1/SB2 (spectroscopy), Gaia RUWE, PMa, and direct imaging (spatially resolved) are most effective. It is clear that PMa works best for targets within ~ 100 pc and prospective companions around 10 au. Source: El-Badry (2024).

non-trivial task due to the unknown orbital inclination and phase (Torres 1999). The separation in au is typically estimated using a conversion factor c that ties projected and physical separation, accounting for the distance d of the system

$$a_{\rm rel} = c\,\rho\,d \tag{3.1}$$

The choice of the proper c is a debated topic in the literature, and a comprehensive dissertation on this topic is presented in the Appendix of Dupuy & M. C. Liu (2011). In their work, the authors argue that a median value for an unbiased sample of binaries is around $c = 1.1$. D. A. Fischer & G. W. Marcy (1992), after running a Monte Carlo (MC) simulation based on thousands of synthetic orbits, concluded that the proper factor should be $c = 1.27$. The results from the two works differ because of different statistical assumptions. Dupuy & M. C. Liu (2011) extensively analyze different eccentricity and mass distributions, finding a set of median values where $c = 1.1$ is the one applicable under the assumption of a uniform eccentricity distribution. Conversely, D. A. Fischer & G. W. Marcy (1992) limit the analysis to a geometrical calculation, reporting an average value (and not a median) for the overall sample, being inherently more sensitive to outlying orbits. In view of these considerations, I adopt the conservative $c = 1.27$ from D. A. Fischer & G. W. Marcy (1992) to derive upper limits for the presence of binary companions. This choice is specifically intended to avoid overestimating the detection capabilities at small orbital distances, ensuring that any exclusion of potential companions is based on a robust statistical framework.

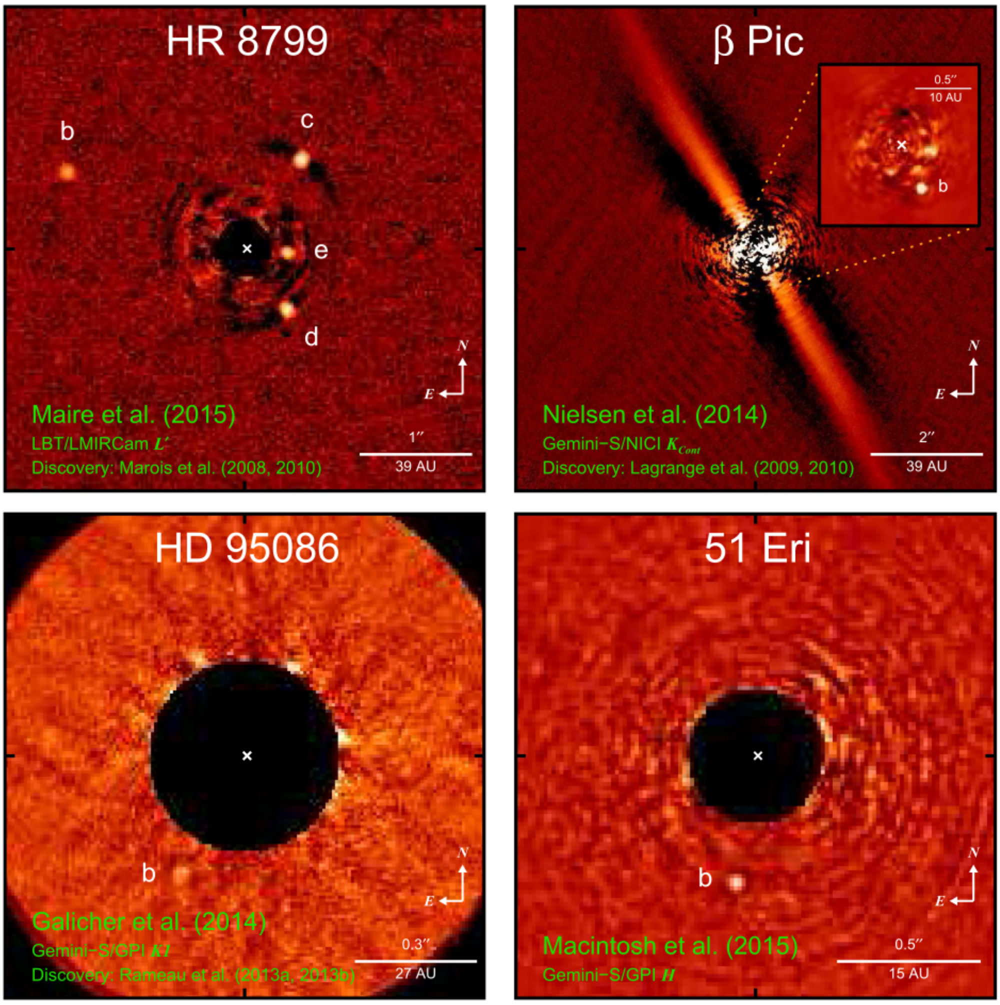

Figure 3.2: Pictures of imaged planets within 100 au. Source: Bowler (2016).

Several authors have studied binaries in planetary systems (e.g., Furlan et al. 2017; Ziegler et al. 2020). Bowler (2016) offers a review of the direct imaging of extrasolar planets, with some results highlighted in Figure 3.2.

3.1.a ExoFOP archive and data selection

In order to provide robust constraints on the multiplicity of the Rossi et al. (2026) sample, the starting point was the Exoplanet Follow-up Observing Program (ExoFOP) (Christiansen et al. 2025). This database includes a vast amount of follow-up observations of NASA missions, namely TESS, Kepler, and K2, including time series, imaging, and RVs, along with stellar and planetary parameters. Specifically, I targeted the imaging products for this part of the work. Imaging entries for a given target star are composed of several details described in Figure 3.3. They include information about the contributor, the equipment used, the estimated PSF, the pixel scale of the image, and the observation date. Every observation is assigned a unique tag identifier referring to all the files uploaded regarding it. The most important quantity for the scope of this work is the estimated contrast, as it describes the maximum magnitude difference the instrument is able to detect at a given distance. This is crucial considering that exoplanets (and BDs) and stars are characterized by differences in emission, and thus the former require a deeper contrast to be detected compared to the latter (Bowler 2016; Fontanive et al. 2019). Another key parameter is the observation filter, as the different temperatures of the aforementioned objects shift the peak emission to redder bands for exoplanets, according to Planck's law. In order to discern between the several filters used on different instruments, the Spanish virtual observatory filter profile service (SVO FPS)[1] was employed as the primary reference to crossmatch the different filters.

User	Telescope	Instrument	Filter	Image Type	Pixel scale (arcsec)	Estimated PSF (arcsec)	Estimated Contrast	Observation date (UT)		Ec	Group	Tag
furlan	Gemini (8 m)	'Alopeke	562: 562 (54) nm	Speckle	0.01	0.02	Δ 4.47 mag @ 0.5"	2021-02-02			tfopwg	94611
furlan	Gemini (8 m)	'Alopeke	832: 832 (40) nm	Speckle	0.01	0.02	Δ 6.36 mag @ 0.5"	2021-02-02			tfopwg	94611
giacalone	Shane (3 m)	ShARCS	Ks: 2.150 (0.320)...	AO	0.033			2020-11-30			tfopwg	6266
safonov	SAI-2.5m (2.5 m)	Speckle Polarimeter	I	Speckle	0.02049	0.083	Δ 6.1 mag @ 1"	2020-11-29			tfopwg	93065
ciardi	Palomar (5 m)	PHARO	Brgamma	AO	0.025	0.132155	Δ 5.481 mag @ 0.5"	2020-01-08			tfopwg	8620
dressing	Shane (3 m)	ShARCS	Ks	AO	0.033			2019-11-12			tfopwg	7276
dressing	Shane (3 m)	ShARCS	J	AO	0.033			2019-11-12			tfopwg	7276

Figure 3.3: ExoFOP direct imaging entry. Columns include information about the contributor, the telescope used along with the instrument and the filter, the type of observations (AO meaning adaptive optics, or speckle imaging), pixel scale, PSF, contrast, observation date and unique tag identifier for the data products associated with the observation.

Hence, the selection criteria for the imaging data prioritized (i) the deepest contrast limits, (ii) longer wavelength filters (redder bands), and (iii) the smallest PSF values. It is worth noting that most observations available for my targets clearly showed a correlation between optimal contrast and telescope aperture, as expected. Unfortunately, not all targets had imaging observations available on ExoFOP; this will be detailed in Chapter 5.

[1] https://svo2.cab.inta-csic.es/theory/fps/

3.1.b From projected to physical separation

Estimating an upper limit for the mass and the location of a companion, commonly referred to as sensitivity, essentially corresponds to evaluating Equation (3.1) over a range of projected separations. In order to achieve this, I applied some relevant corrections that will be described in Section 4.3 (namely the zero-point correction and parallax uncertainties inflation). I then applied the distance modulus

$$M_{\text{abs}} = (m_\star + \Delta\text{mag}) - 5\,\text{Log}\,D + 5 \tag{3.2}$$

with $m_\star$ being the target apparent magnitude, Δmag the contrast as a function of projected separation, and D the distance. In the case of young targets, the availability of age constraints from Rossi et al. (2026) allowed for the adoption of age-dependent evolutionary models (BHAC15, Baraffe et al. 2015). These models[2] provide information about luminosity at a given mass and age (and vice versa). Thanks to this, it is possible to use the luminosity in a given band, matching the observation band, to retrieve the mass of the target knowing its age. Specifically, I perform a linear interpolation in log-mass space using the provided look-up tables to produce sensitivity plots similar to Figure 3.4. Plots for some of the most notable targets with available observations are available in Chapter A. Plots have been created assuming the central value of age to be the real value.

For main sequence (MS) targets, empirical tracks were preferred over theoretical models to minimize the impact of age uncertainties, which are particularly significant for field stars. Commonly referred to as Mamajek tracks (Pecaut & Mamajek 2013), these models are broadly applicable to MS stars, for which the change in luminosity is negligibly dependent on age compared to young objects. These well known models[3] are similar to BHAC15, with the only two exceptions being their age independence, and the fact that they are compiled from observations. The use of these tracks allowed for greater precision for MS targets, as they usually present large uncertainties in age that would make BHAC15 models, used with the central value, rather imprecise and thus uninformative.

A critical aspect of this analysis is the strong dependence of evolutionary and empirical models on the specific passbands of the observations. To ensure a consistent comparison between the data and the models, it was necessary to match the observation filters (typically the $832\,\text{nm}$ filter and the Brγ narrow-band

[2] BHAC15 models are available at https://perso.ens-lyon.fr/isabelle.baraffe/BHAC15dir/

[3] Mamajek models are available at https://www.pas.rochester.edu/~emamajek/EEM_dwarf_UBVIJHK_colors_Teff.txt

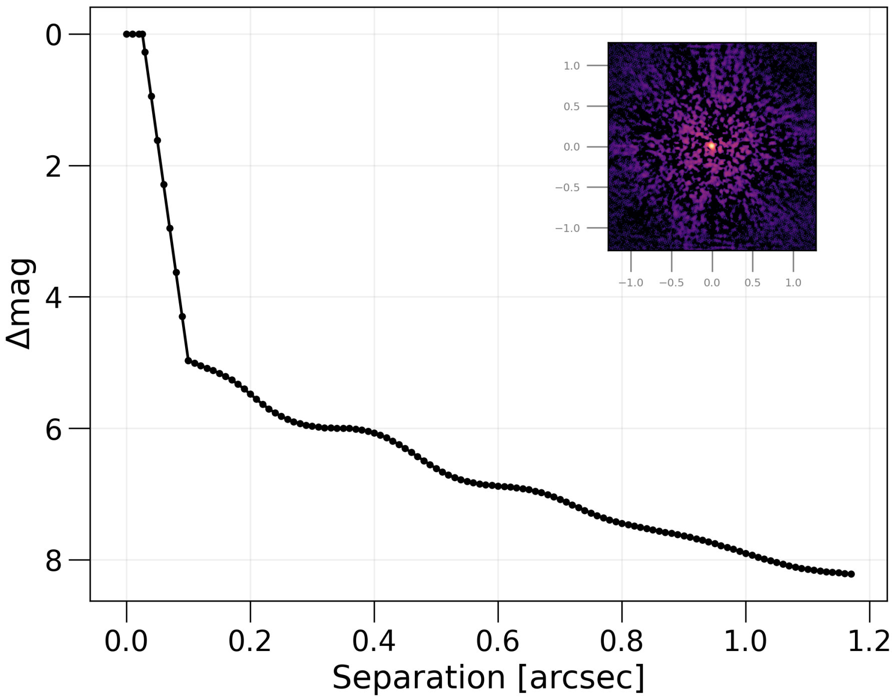

Figure 3.4: Imaging contrast curve of AU Mic. The inset is shown on a logarithmic scale to improve visibility.

filter), with the corresponding magnitudes of the primary star. I crossmatched my targets with the SIMBAD and 2MASS databases[4] to retrieve the most accurate photometry for each system. In the case of the Mamajek tracks, which provide a limited set of standard filter outputs, I employed color indexes to convert the available photometry into the required passband when an exact match was not present. In contrast, BHAC15 models are more versatile, providing magnitudes for several sets of photometric filters, such as *Gaia*, 2MASS, and JWST. This allowed a more direct mapping of the contrast curves (Figure 3.4) into the mass-separation space (Figure 3.5).

By extracting mass limits at specific physical separations (3, 5, 10, 30, 50, 100, and 300 au)[5], I characterized the system's dynamical environment. The direct imaging instruments have typically a field of view of a few arcseconds. At wider separation, bound companions can be identified in the *Gaia* catalog

[4] https://irsa.ipac.caltech.edu/Missions/2mass.html

[5] This choice allows for the integration of information from both speckle and AO direct imaging in a single visualization. Clearly, speckle frames are not suited for providing information at large separations but, conversely, this regime will be covered by AO, which is instead limited in probing close separations.

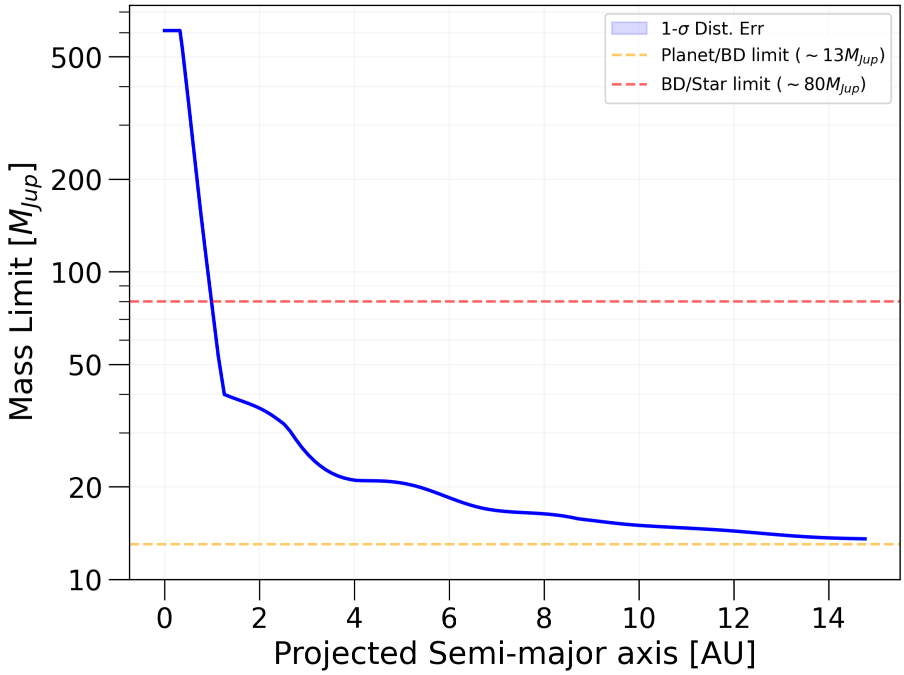

Figure 3.5: Imaging mass sensitivity plot of AU Mic. The plot represents the mass limits placed by direct imaging with respect to the physical separation from the primary star. It is useful to note that such stringent limits on masses can be placed only in the most favorable cases. Indeed, AU Mic is a young and nearby star for which I am able to exclude any companions with masses in the planetary regime.

(e.g. DR3), looking for stars with similar parallax and proper motion (and RV, when available) with respect to the target. Following the logic discussed by Ziegler et al. (2020), the absence of massive companions at these scales suggests a stable formation history for any detected planets. The exclusion of any stellar companion (then with mass much larger than the close-in planetary objects) within $50 - 100\,\mathrm{au}$ is essential for validating the orbital stability and the derived parameters (such as the radius) of transiting planets in these systems, as it rules out significant transit depth dilution and severe dynamical scattering.

3.2 Catalogs of binaries

As mentioned in the introduction to this chapter, these techniques have already been exploited multiple times to search for binary companions, consequently, a plethora of catalogs has been developed throughout the decades to track multiple systems, starting long before the dawn of exoplanetology. In this subsection, I describe the primary catalogs available today, which have all been used to get a comprehensive view of the Neptunian-hosting stars introduced by Rossi et al. (2026). The catalog classification adopted is customary, and does not reflect the usual classification of binaries divided into visual binaries (two resolved components), astrometric binaries (detected through the astrometric non-linear motion across the sky), spectroscopic binaries (detected via Doppler shifts of the lines of one star, also known as SB1, or of the lines of both stars visible in the same spectrum, also known as SB2), and eclipsing binaries.

3.2.a PMa and PM acceleration catalogs

The formalism of the PMa computation will be introduced in the next chapter, along with its application to the Tycho-2 catalog. For the moment, I will limit the discussion to a brief introduction of the technique, whose range of applicability is shown in Figure 3.1. Although limited in the range of orbital periods, it is able to probe a region of the distance-period parameter space with minimal to no overlap with other methods. It basically relies on the assumption that a single star moves linearly in the sky, with a defined PM, across different decades, whereas the presence of a binary companion would cause the target star to move around the barycenter of the system, hence generating a difference in PMs across decades, thus a PMa. This methodology has been applied by Kervella and collaborators in two different works: Kervella et al. (2019)[6] applied it to compute PMa between *Hipparcos* and *Gaia* DR2, whereas Kervella, Arenou & Thévenin (2022)[7] extended their work to *Gaia* EDR3, with some changes in the results due to the improvement in DR3 data compared to DR2. Both catalogs include almost the whole sample of $\sim 100,000$ *Hipparcos* stars[8]. In a similar fashion, Brandt developed the Hipparcos-Gaia Catalog of Accelerations (HGCA) basing the binarity inference on the astrometric acceleration of stars, which, for a similar argument, is noticeable on stars with a companion. The HGCA has been developed both for *Gaia* DR2 (Brandt 2018) and DR3 (Brandt 2021)[9], with only the latter being used in this work.

3.2.b Astrometric catalogs

For the first time in the history of astrometric missions, the *Gaia* DPAC will provide raw astrometric data along with the fourth data release (DR4) in December

[6] http://cdsarc.u-strasbg.fr/viz-bin/qcat?J/A+A/623/A72

[7] https://cdsarc.cds.unistra.fr/viz-bin/cat/J/A+A/657/A7

[8] The *Hipparcos* dataset has been trimmed in magnitude and distance to ensure reliability of the final product. For further details, refer to Kervella et al. (2019) and Kervella, Arenou & Thévenin (2022) and references therein.

[9] https://cdsarc.cds.unistra.fr/viz-bin/cat/J/ApJS/254/42

2026, along with a plethora of astrometric binaries, for which astronomers are eagerly waiting. This represents a milestone, as astronomers will have the capability to fit their own astrometric solutions to the data, without necessarily relying on the ones provided by the DPAC. Indeed, each astrometric mission has always provided a catalog, along with a user manual, that may include a sub-catalog of double stars. Specifically, the mission pipeline solves the star treating it as a double solution to include it in this sub-catalog if the result is positive. This is the case of the visual binaries included in Tycho Double Star Catalog (TDSC)[10] (Fabricius et al. 2002), as well as Tycho[11] (Høg et al. 1997), Tycho-2[12] (Høg et al. 2000b), and the second data reduction of *Hipparcos*[13] (van Leeuwen 2007b). *Gaia* DR3 lists its double star solution in the non single stars (NSS) catalog[14] (Gaia Collaboration et al. 2023a), and it includes astrometric, spectroscopic and eclipsing binaries with even some orbital solutions. *Gaia* DR3 has also been exploited to produce a catalog of a million *Gaia* stars with $> 90\%$ probability of being bound with visible targets (El-Badry, Rix & Heintz 2021). Another useful, and consulted, catalog based on astrometric accelerations and jerks was produced by Makarov & Kaplan (2005)[15].

3.2.c Binary catalogs

Plenty of catalogs of visual binaries have been produced over time. Listing and consulting all of them would be a gargantuan task, but a selection that encompasses the most successful ones can be utilized for the aim of this thesis. The choice made includes the catalog of eclipsing binaries by Malkov et al. (2006)[16] and the Washington Double Star Catalog[17] (WDS, Mason et al. 2001). The latter is the evolution of the Index Catalog of Visual Double Stars (Jeffers, van den Bos & Greeby 1963) and it is intended to include all the binary stars for which at least one observation has been performed in at least one passband. The binaries are listed as components (B, C, etc.) of a primary system located at a certain sky position at epoch J2000.0. The only differences between two entries of the same system are their projected separation and the magnitude of the component. Since this is an ensemble of measurements collected throughout the decades

[10] https://cdsarc.cds.unistra.fr/viz-bin/cat/I/276
[11] https://cdsarc.cds.unistra.fr/viz-bin/cat/I/239
[12] https://cdsarc.cds.unistra.fr/viz-bin/cat/I/259
[13] https://cdsarc.cds.unistra.fr/viz-bin/cat/I/311
[14] https://cdsarc.cds.unistra.fr/viz-bin/cat/I/357
[15] https://cdsarc.cds.unistra.fr/viz-bin/cat/J/AJ/129/2420
[16] https://cdsarc.cds.unistra.fr/viz-bin/cat/J/A+A/446/785
[17] https://cdsarc.cds.unistra.fr/cgi-bin/cat/B/wds

with different instruments and filters, it is highly inhomogeneous and due to its nature of catalog of visual binaries, it often includes visual contaminants. However, it is improbable for a visual companion detected via other means to not be present in the catalog (with the only exception of *Gaia* comoving objects). These peculiarities were also exploited to create the TDSC (Fabricius et al. 2002).

3.3 Radial velocity

The detection and characterization of long-period companions, ranging from giant planets and brown dwarfs to stellar binaries, rely heavily on the temporal baseline of the observations. While short-period planets can be identified within weeks or months, uncovering the full architecture of a planetary system requires long-term RV monitoring, often spanning several decades (e.g., Duquennoy, Mayor & Halbwachs 1991; Moe & Di Stefano 2017). It is worth mentioning that shorter period binaries would be detected with a lower temporal coverage; however, they are not present in my sample as the presence of such a companion would have a major dynamical effect on the system during its formation, likely halting the birth of planets.

According to Kepler's third law, the orbital period of a companion increases with its semi-major axis ($P \propto a^{3/2}$). Consequently, companions located beyond the snow line (typically $> 5\,\mathrm{au}$) have periods exceeding a decade, similar to Jupiter's orbit. As noted by Wittenmyer et al. 2020, long-baseline surveys, such as the Anglo-Australian Planet Search (AAPS) are essential to distinguish between a truly isolated planet and a member of a wider hierarchical system. Even when the observational baseline is shorter than the orbital period, long-term radial velocity (RV) data often reveal a linear trend or a significant curvature in the residuals, that can be combined with direct imaging information to probe for the presence of stellar or substellar companions (Montet et al. 2014).

RV is the second observational pillar of this work to identify binary companions. I conducted a comprehensive search in two primary databases, namely the Survey of Surveys (SoS) and Data Analysis Center for Exoplanets (DACE). The former is a catalog constructed by Tsantaki et al. (2022) containing more than 23 million stars in the current release (Turchi et al. 2025), obtained by combining several surveys (APOGEE, GALAH, RAVE, and LAMOST). Although its primary goal is stellar science, the availability of already corrected and normalized RVs makes it a valuable asset for this thesis. The latter is an exoplanet data archival and visualization tool established by the University of Geneva, that among the various planetary parameters, also provides access to RVs from ESO facilities such as HARPS, HARPS-N, NIRPS, CORALIE, and ESPRESSO. This catalog comprises 378 TB of data, mostly composed of CHEOPS and TESS lightcurves, and high-resolution spectra with RV. Models, opacities, atmospheric spectra, and few high-resolution images are also available.

I queried both SoS[18] and DACE[19] using their web interfaces. Despite the depth of these archives, the results highlight a significant gap in the current archival coverage for my specific planetary host sample. SoS provides no measurements for my planetary sample, while DACE RV time-series are often restricted to older targets of my list, that were still usable for the purpose of this work. Consequently, the analysis focused on DACE.

The RV analysis was performed using the following criteria to ensure the robustness of the detected signals:

1. I exclusively selected data points that passed the internal quality checks of the respective reduction pipelines (e.g., the HARPS DRS). An initial cleaning phase was performed to remove blatant outliers. In instances where entire observational runs were affected by instrumental systematics, they were excluded to maintain the integrity of the time series.

2. Given that many targets were observed using multiple instruments or different versions of the same pipeline, I included relative instrumental offsets as free parameters in the fit. This is essential to prevent artificial jumps in the RV from being misinterpreted as astrophysical signals.

3. For each known planet in the system, a Keplerian orbit was fitted using the standard orbital parameters[20] Initial starting points were retrieved from the Rossi et al. (2026) catalog. In cases where parameters were missing, I performed a literature search to retrieve values from the papers on which Rossi et al. (2026) based their inference.

4. The model performance was monitored via the reduced chi-squared χ^2_r of the fit. No detrending was performed for stellar activity. I also refrained from adding stellar jitter to obtain a marginal improvement of the fit, as the only purpose of this was to enlarge the errorbars and reduce the chi-squared, probably masking velocity drifts over time.

5. Finally, I fitted a linear RV trend to the datapoints, and it was considered significant only if exceeded a threshold of 3σ from zero, and if it also improved the chi-squared.

Nonetheless, only few targets had enough observations to robustly fit linear drifts: it is clear that future work will require a deeper analysis of RV databases

[18] https://gaiaportal.ssdc.asi.it/SoS/query/form

[19] https://dace.unige.ch/

[20] Specifically, the orbital period $P_{\rm orb}$, the RV semiamplitude K, the eccentricity e, the argument of periastron ω, and the time of inferior conjunction T_c in case of a transiting planet, as all my planets are transiting.

combined with new observations for those targets lacking long-term information. This gap highlights the necessity for new dedicated observations and reinforces the importance of the complementary use of the Tycho-2 catalog and direct imaging as the primary drivers of this thesis work.

4 Detecting companions through astrometric anomalies

In this chapter, I will introduce the pipeline I developed to compute the PMa between Tycho-2 and *Gaia* data. It includes all the necessary corrections and implementations to ensure that the code is capable of consistently retrieving the PMa for each target. Compared to the previous two techniques, this can be regarded as a non-standard method, as no Tycho-2–*Gaia* PMa computation has ever been reported in the literature. The goal of this thesis, constraining the presence of binaries across the Rossi et al. (2026) Neptunian subsample, aligns well with a PMa analysis, which is a complementary technique to study stellar binarity, as shown in Figure 3.1. Its sensitivity, which spans a rather specific range of distances, is the only technique available for that parameter space (El-Badry 2024).

4.1 Tycho-2, the second reduction of the *Hipparcos* star mapper

The Tycho-2 catalog (Høg et al. 2000b) is a primary astrometric reference providing positions and PMs for the 2.5 million brightest stars in the sky. It resulted from a sophisticated re-reduction of the *Hipparcos* Star Mapper data, providing a significant improvement over the original Tycho-1 catalog (Høg et al. 1997; Høg et al. 1998). While its typical PM precision of $2.5\,\mathrm{mas/yr}$ is comparatively low by modern *Gaia* standards, Tycho-2 remains a useful tool for contemporary astrometry for several reasons:

- The combination of Tycho-2 (mean observation epoch ≈ J1991.5) and *Gaia* DR3 (epoch J2016.0) positions provides a ≈ 24.75 years baseline. This long lever arm allows for the calculation of long-term PMs, which are essential for identifying dynamical perturbations. The main limitation lies in the inherent uncertainties of a $\sim$30 year old catalog.

- At the time of this work, no comprehensive, official cross-calibration focusing specifically on the Tycho-2 vs. *Gaia* DR3 baseline for the entire catalog has been produced, leaving room for targeted studies on specific planetary hosts.
- It provides a critical data-point for bright stars that often lack high-precision historical measurements outside the $Hipparcos$ mission.

Tycho-2 can be queried in multiple ways[1], including the CDS VizieR service[2]. A standard Tycho-2 entry consists of a region number (TYC1), an internal running number (TYC2), and a component number (TYC3), usually unitary, resulting in e.g., TYC 9339-551-1, which corresponds to DS Tucanae. Most of the catalog contains positions and PMs, along with uncertainties, at a mean observational epoch of J1991.5, as thoroughly detailed in Høg et al. (2000a). The actual observation epochs for right ascension α and declination δ in the Tycho-2 catalog are often distinct, and generally neither refers exactly to the epoch J1991.5, as the positional measurements were collected over approximately three years. Tycho-2 is a re-reduction of the original Tycho catalog (Høg et al. 1997), designed to provide higher precision and a larger sample of targets, specifically 2.5 million instead of the original million (Høg et al. 2000b). In this second version of the catalog[3], most of the positions have been normalized to the J2000.0 epoch by means of PMs, which have been collected using several photographic plates of measurements collected throughout the 20$^{\text{th}}$ century. Crucially, these are not instantaneous measurements, but rather represent a PM averaged over roughly a century. Using these normalized positions would shorten the temporal baseline (e.g., comparing J2000.0 to Gaia instead of J1991.5 to Gaia), thereby averaging out the orbital curvature and reducing the detectable amplitude of the PMa. This would ultimately hinder the detection of binary systems.

4.2 Proper motion anomaly

The PMa, usually denoted as $\Delta\boldsymbol{\mu}$, is a vector quantity representing the deviation of a star's observed PM from the uniform linear motion of the system's barycen-

[1]For a complete description refer to https://www.cosmos.esa.int/web/hipparcos/tycho-2#

[2]For the CDS catalog version refer to https://cdsarc.cds.unistra.fr/viz-bin/ReadMe/I/259?format=html&tex=true

[3]The full documentation for Tycho-2 catalog can be found following the links in https://www.astro.ku.dk/~erik/Tycho-2/. It contains all the information provided in these paragraphs with no references.

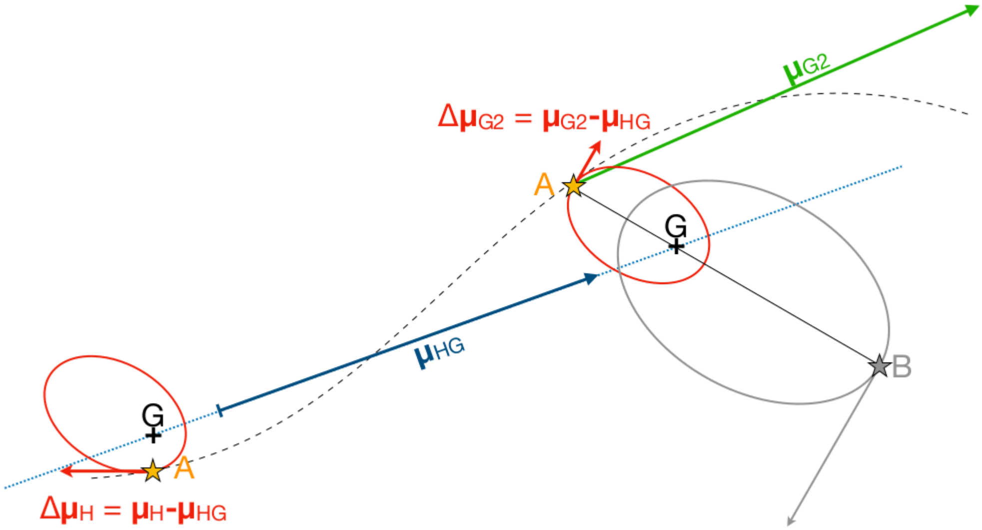

Figure 4.1: Principle of PMa determination from Kervella et al. (2019). In their work, they analyzed the PMa between *Hipparcos* and *Gaia* DR2. The *Hipparcos* position is represented by the yellow star A, while the *Gaia* DR2 position is shown by the same star on the right. If we assume that a secondary star B is orbiting A, and that the photocenter of the system is reasonably close to A, we find that the difference between the long term PM $\boldsymbol{\mu}_{\mathrm{HG}}$ and the Gaia instantaneous PM $\boldsymbol{\mu}_{\mathrm{G2}}$ is non-zero, suggesting the presence of a second object orbiting star A.

ter. While in an isolated and single-star system, the stellar motion is purely inertial, the presence of an unseen companion (e.g., a planet, BD or stellar companion) induces a reflex motion of the host star around the common center of mass. Mathematically, the PMa is defined as the difference between two velocity vectors measured over different timescales

$$\Delta\boldsymbol{\mu} = \boldsymbol{\mu}_{\mathrm{inst}} - \boldsymbol{\mu}_{\mathrm{LT}} \tag{4.1}$$

where $\boldsymbol{\mu}_{\mathrm{inst}}$ represents the velocity projected on the plane of the sky and measured in $\mathrm{mas\,yr^{-1}}$, over a short observational baseline (for example, the ~ 3 years mission span included in the *Gaia* DR3 release), whereas $\boldsymbol{\mu}_{\mathrm{LT}}$ is the mean velocity computed from the difference in barycentric positions between two widely separated epochs, such as the ~ 25 year interval between the *Hipparcos*/Tycho-2 era and *Gaia*. A schematic visualization is given in Figure 4.1. The kinematic meaning of the PMa lies in the geometry of the orbital motion projected onto the tangential plane of the sky. Considering that the stellar motion throughout the sky is equivalent to motion on a sphere, a quasi-instantaneous measurement (e.g., *Gaia*) provides the tangent to the orbit at a specific epoch. Conversely, the long-term PM, calculated by comparing positions from Tycho-2 and *Gaia*, represents the chord connecting two different points on the sphere (Kervella et al. 2019). In a single-star — and also ideal — scenario, the tangent coincides with the direction of the chord, resulting in a null PMa. The presence of a companion results in a non-null difference between the two vectors, providing evidence of the gravitational pull of a stellar companion or, for very precise astrometric measurements, substellar companion (Kervella et al. 2019; Kervella, Arenou & Thévenin 2022). Finally, combining the measured anomaly with Kepler's third law and the conservation of linear momentum, it is possible to estimate the companion mass, with respect to its distance, without the need to observe a full orbital revolution. The relation is given by

$$\frac{m_2}{\sqrt{r}} = \sqrt{\frac{M_1}{G}} \left(\frac{\Delta\mu}{\varpi} \times 4740.470 \right) \tag{4.2}$$

where m_2 is the companion mass at a distance r, and the other terms are the parallax ϖ, the absolute value of the PMa $\Delta\mu$, the primary star mass M_1, and 4740.470 is a normalization constant ensuring that m_2 is expressed in solar masses $\mathrm{M}_\odot$. However, reality is far from simple, and this relation must be corrected for several effects (Kervella et al. 2019).

4.2.a Astrometric smearing γ

The PM measurements provided by astrometric missions are, unfortunately, not instantaneous snapshots of a star's velocity, but rather the result of a fit to a series of individual transits collected over a specific mission duration, which for the part of *Gaia* included in DR3 is $\delta t \approx 2.83\,\mathrm{yr}$ (Gaia Collaboration et al. 2021). When the orbital period P_{orb} of a companion is comparable to or shorter than this window, the star's orbital oscillation is smeared within the measurement, resulting in a significant suppression of the detected PMa. To account for this, I implemented the analytical correction factor γ according to Eq. 12 of Kervella et al. (2019)

$$\gamma(P, \delta t) = \frac{P}{\pi \delta t \sqrt{2}} \sqrt{1 - \cos \frac{2\pi\delta t}{P}} \tag{4.3}$$

It is evident that a period much larger than the observing window results in a unitary correction, hence a reasonably instantaneous measurement, while this correction gets closer to zero as the orbital period decreases. Accounting for this unavoidable phenomenon is crucial for a correct inference.

4.2.b Baseline efficiency ζ

If the orbital period of the companion is significantly larger compared to the long-term baseline, in this work $24.5\,\mathrm{yr}$, the PMa calculation of Equation (4.1) results in part of the orbital velocity being subtracted from the long-term PM vector $\boldsymbol{\mu}_{\mathrm{LT}}$. This bias is difficult to determine analytically, as the long-term baseline depends on the ratio between the orbital period and the time elapsed between the two catalogs. If the period is much longer, the difference between the tangent and the chord approaches zero, making the signal harder to distinguish from noise. To overcome these analytical challenges, I adopted a numerical MC approach: for each period ratio $x = P/\delta t$, I simulated 50000 random orbits sampling uniformly on the orbital elements e, Ω, ω, M_0 and i. This last parameter is correctly sampled following the prescriptions of previous works (Morgan et al. 2024; Rossi et al. 2026), which require an isotropic inclination distribution to be extracted from a uniform sampling on its cosine.

These parameters are then inserted into a set of Thiele-Innes constants (Thiele 1883; Innes 1907; Wright & Howard 2009)

$$A = \cos\omega\cos\Omega - \sin\omega\sin\Omega\cos i \tag{4.4}$$
$$B = \cos\omega\sin\Omega + \sin\omega\cos\Omega\cos i \tag{4.5}$$
$$F = -\sin\omega\cos\Omega - \cos\omega\sin\Omega\cos i \tag{4.6}$$
$$G = -\sin\omega\sin\Omega + \cos\omega\cos\Omega\cos i \tag{4.7}$$

assuming a unitary semi-major axis, which maps the tridimensional Keplerian plane onto its bidimensional projection $(\Delta\alpha, \Delta\delta)$

$$\Delta\alpha = AX + FY \tag{4.8}$$
$$\Delta\delta = BX + GY \tag{4.9}$$

where the auxiliary coordinates X and Y are given by

$$X = \cos E - e \tag{4.10}$$
$$Y = \sqrt{1-e^2}\,\sin E \tag{4.11}$$

for which the E value is extracted by numerically integrating Kepler's equation. The efficiency ζ is then simply

$$\zeta = \frac{|\mathbf{v}_{\mathrm{Gaia,inst}} - (\mathbf{r}_{\mathrm{Gaia}} - \mathbf{r}_{\mathrm{Tycho}})/\Delta t|}{|\mathbf{v}_{\mathrm{Gaia,inst}}|} \tag{4.12}$$

where $\mathbf{v}_{\mathrm{Gaia,inst}}$ is the *Gaia* "instantaneous" velocity, while $\mathbf{r}_{\mathrm{Gaia}}$ and $\mathbf{r}_{\mathrm{Tycho}}$

represent $Gaia$ and Tycho-2 positions, respectively. This is equivalent to the PM version given in Eq. 14 by Kervella et al. (2019)

$$\zeta\left(\frac{P}{\delta t}\right) = \left|\frac{\boldsymbol{\mu}_{\text{Gaia}} - \boldsymbol{\mu}_{\text{LT}}}{\boldsymbol{\mu}_{\text{orb}}}\right| \tag{4.13}$$

The result is shown in Figure 4.2, and it is fully consistent with the findings of Kervella et al. (2019).

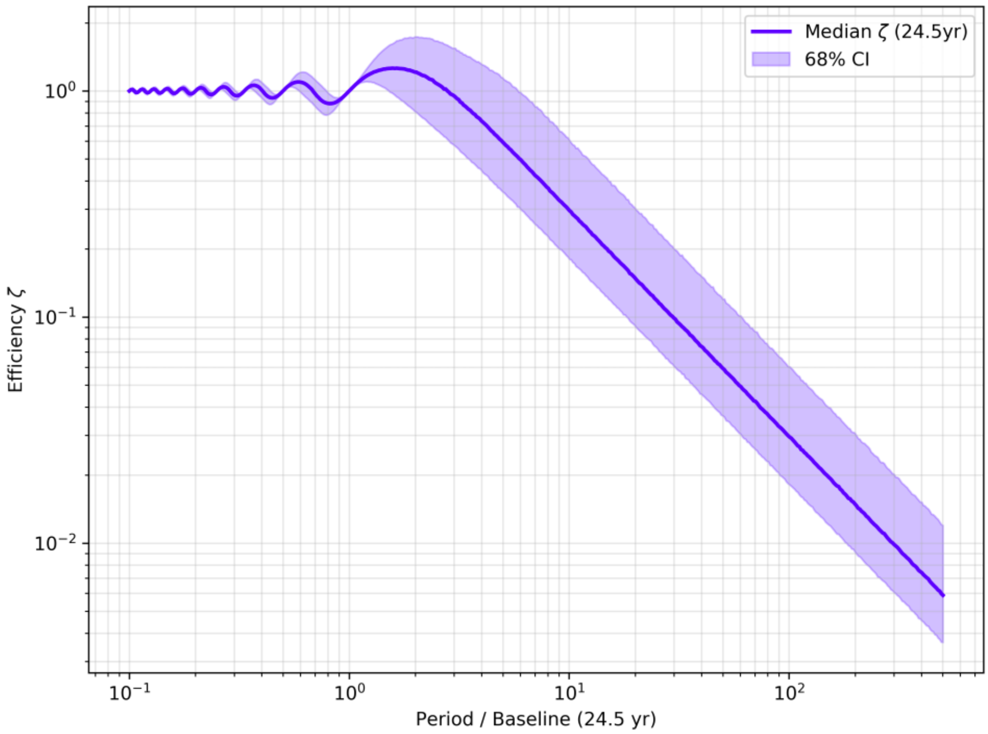

Figure 4.2: Efficiency function ζ as a function of the orbital period normalized to the observational baseline. The plot reproduces the results of Kervella et al. (2019), showing how the sensitivity of the PM anomaly technique varies with the ratio $P/\Delta t$. The blue solid line represents the median efficiency, while the shaded area indicates the 68% confidence interval derived from MC simulations of orbital parameters. The characteristic $1/P$ decay is visible for periods much longer than the $24.5\,\text{yr}$ Tycho-2-$Gaia$ baseline.

4.2.c Geometric projection η

The most significant source of uncertainty in converting an angular anomaly to a mass is the unknown geometry of the tridimensional orbit. Using the same Keplerian framework, I ran a MC simulation with one million samples, to compute the ratio of the two-to-three dimensional velocities

$$\eta = \frac{|\mathbf{v}_{2D}|}{|\mathbf{v}_{3D}|} \tag{4.14}$$

whose result is shown in Figure 4.3, with a median of $0.87^{+0.12}_{-0.32}$, once again in full agreement with previous works (e.g., Tokovinin & Kiyaeva 2016; Kervella et al. 2019). These corrections can be added to Equation (4.2), resulting in

$$m_2 = \frac{\Delta\mu}{\varpi}\sqrt{r \cdot M_1} \cdot \frac{1}{\gamma\,\zeta\,\eta} \tag{4.15}$$

MC techniques can also be exploited to propagate not only these uncertainties, but also the errors on the quantities and corrections that I will introduce in the next subsections.

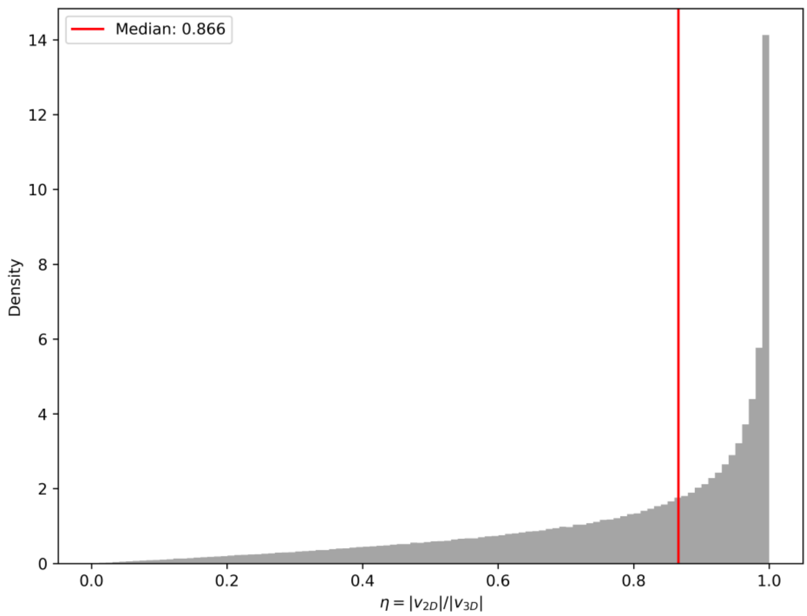

Figure 4.3: Probability density distribution of the geometric projection factor η. The factor is defined as the ratio between the projected tangential velocity ($|v_{2D}|$) and the true 3D orbital velocity ($|v_{3D}|$). The distribution is obtained from a MC simulation of 10^6 orbits with random orientations and eccentricities. The red vertical line indicates the median value of 0.866, which is used to statistically correct for projection effects when converting observed PM anomalies into physical orbital velocities.

It is necessary to emphasize the significant difference in precision between the two eras. Tycho-2 positional errors for bright stars ($V < 11$) are typically in the range of $60\,\mathrm{mas}$, growing to more than $100\,\mathrm{mas}$ for fainter targets (Høg et al. 2000b), which is orders of magnitude larger than the sub-milliarcsecond precision of *Gaia* DR3, where positional uncertainties for similar sources are frequently as low as $0.02 - 0.05\,\mathrm{mas}$ (Lindegren et al. 2021b). Furthermore, Tycho-2 entries include a correlation coefficient between right ascension (RA) and declination (Dec) measurements. This correlation arises from the one-dimensional nature of the *Hipparcos* satellite's scanning geometry, where observations along different great circles were combined into a single solution (ESA 1997; Michalik et al. 2014). Proper management of this covariance matrix is indispensable for a statistically rigorous inference of the PMa. Unlike *Hipparcos*, Tycho-2 does not provide a full covariance matrix for its astrometric solutions, thus, I will place more conservative—and stringent—limits on the detection of binaries. For the modern epoch, *Gaia* provides extensive astrometric data, iteratively refined through successive data releases. I queried the *Gaia* archive[4] using the `astroquery` package (Ginsburg et al. 2019), as well as the query interface[5], a part of `astropy` (Astropy Collaboration et al. 2013). Among the quantities available[6], I used an ADQL query to retrieve sky positions in the J2016.0 reference frame (RA and Dec), parallaxes, and PMs, along with all the correlations between the aforementioned quantities.

4.3 Systematics correction

Both *Gaia* and Tycho-2 are known to suffer from systematics, and accounting for them is crucial to ensure a robust inference. While the parameters discussed in the previous subsections, namely γ, ζ, and η are useful for a physically sound inference of companion masses, the following corrections need to be applied to ensure that the PMa itself is computed robustly.

4.3.a Parallax zero-point calibration and chromaticity

A fundamental requirement for an accurate PMa analysis is the determination of the stellar distance ($d = 1/\varpi$). However, trigonometric parallaxes in the *Gaia* DR3 catalog are known to be affected by a small but complex systematic bias, commonly referred to as the zero-point offset. This bias primarily originates from the satellite's basic angle variations and other instrumental systematics encountered during the scanning process.

Following the methodology prescribed by Lindegren et al. (2021a) and Lindegren et al. (2021b), the zero-point offset is not a constant value but rather follows

[4] https://gea.esac.esa.int/archive/

[5] https://gaia.aip.de/query/

[6] https://gaia.aip.de/metadata/gaiadr3/gaia_source/

a multi-dimensional dependence on the source's magnitude (G), its color (represented by either the effective wavenumber $\nu_{\rm eff}$, or the reconstructed pseudocolor), and its celestial position (characterized by the ecliptic latitude β). This correction is fundamentally dependent on the type of astrometric solution employed for each specific source, categorized into five-parameter (5p) and six-parameter (6p) solutions, corresponding to the `astrometric_params_solved` flag (`31` for 5p, `95` for 6p):

- Five-parameter (5p) solutions: They consist of the standard astrometric solution including positions, PMs, and parallax. These are typically applied to brighter sources ($G \lesssim 19$) with reliable BP and RP photometry. For these sources, the color information required for the astrometric calibration is represented by the effective wavenumber ($\nu_{\rm eff}$), derived directly from the calibrated BP/RP spectra (Lindegren et al. 2021a).
- Six-parameter (6p) solutions: For fainter sources or those in crowded fields where BP and RP information might be degraded or missing, the astrometric pipeline solves for an additional parameter known as the pseudocolor. This parameter serves as an astrometrically estimated color to compensate for the chromatic effects of the telescope's PSF (Lindegren et al. 2021b; Riello et al. 2021).

The pseudocolor is computed when the information about the color $G_{BP} - G_{RP}$ is not reliable enough, which conversely introduces a chromaticity bias, as the photocenter of the star is not determined with sufficient precision. Although the offset typically averages around -0.02 mas, its variation can reach amplitudes comparable to the formal uncertainties for many sources in the *Gaia* catalog. To mitigate this effect, the zero-point offset $\Delta\varpi(G, \nu_{\rm eff}, \beta)$ was calculated using the `gaiadr3_zeropoint`[7][8] tool, which accounts for the specific astrometric solution type (5-parameter or 6-parameter). The observed parallaxes were corrected as $\varpi_{corr} = \varpi_{obs} - \Delta\varpi$ before being utilized to define the Cartesian positions and to account for the perspective acceleration. Within my MC framework, for sources with a 6-parameter solution, the pseudocolor uncertainty was explicitly sampled[9], ensuring that a dynamic zero-point correction was computed and

[7] https://gitlab.com/icc-ub/public/gaiadr3_zeropoint

[8] This correction varies depending on the data reduction used for the specific DR, indeed DR2 needed a correction of $+29\,\mu$as with respect to the catalog value (Arenou et al. 2018; Lindegren et al. 2018).

[9] It should be noted that the zero-point correction is a non-linear function of the input parameters. To optimize computational performance, this iterative sampling was restricted to 6-parameter solutions only, where the pseudocolor uncertainty significantly impacts the resulting zero-point correction, whereas for 5-parameter solutions, the photometric $\nu_{\rm eff}$ is sufficiently precise to allow for a single-point correction without loss of statistical significance.

applied iteratively to each realization. This approach guarantees a rigorous propagation of the chromatic uncertainties.

Finally, it is worth noting the chromatic difference between the two epochs. Tycho-2 positions are defined in the V_T band, similar to Johnson V, while *Gaia* DR3 utilizes a much broader G band that extends into the near-infrared. Since the correction is typically in the μas range, it is negligible compared to the Tycho-2 positional uncertainties of tens of mas. No correction is applied for this effect on Tycho-2 data[10].

4.3.b Distance estimation

The estimation of geometric distances from parallaxes is often treated as a Bayesian inference problem. Bailer-Jones et al. (2021) is widely regarded as the standard reference for *Gaia* DR3 distances, employing a Markov Chain Monte Carlo (MCMC) approach to account for the nonlinearity of the $r = 1/\varpi$ inversion and the Galactic distribution of stars. However, for sources with high-precision parallaxes, where the relative uncertainty is $\sigma_\varpi/\varpi < 0.1$, the direct inversion

$$r_{\rm pc} = \frac{1000}{\varpi_{\rm corr}} \tag{4.16}$$

is statistically sound and avoids potential biases introduced by the choice of a distance prior (Luri et al. 2018). As the targets in my sample consistently fall within this high-SNR regime, I adopt the direct inversion of the corrected parallax to compute stellar distances. A larger sample, covering a broader distance regime, would require, however, a fully Bayesian inference of distances (Luri et al. 2018).

4.3.c Epoch backpropagation and perspective acceleration

The perspective acceleration correction was implemented using the methodology detailed in Kervella et al. (2019), which I am briefly introducing following Section 3.3 of their work. The projection of the spatial velocity vector of a star varies with time due to the change in geometrical perspective introduced by its space motion. I transform the 6D position-velocity vector of the star (α, δ, ϖ, μ_α, μ_δ, $v_{\rm rad}$) into Cartesian coordinates (x, y, z, v_x, v_y, v_z). Both this 6D transformation and the subsequent epoch propagation were performed using the `apply_space_motion` routine from the `Astropy` package (Astropy Collaboration et al. 2013). This approach rigorously handles the non-linear correlations

[10] A finer work would require a proper estimation of the impact of color on Tycho-2 data. It is questionable whether this would have a major impact on the inference.

between the RV and the transverse PM components induced by perspective changes. Considering that Tycho-2 does not include parallax measurements, and that using Tycho-1 parallaxes would be unjustified considering their large uncertainties, I employed *Gaia* parallaxes for both *Gaia* and Tycho-2 6D vectors.

The calculation of the long-term PM requires comparing the positions of Tycho-2 and *Gaia* at their respective mean epochs of observation. Although Tycho-2 positions are formally reported at the J2000.0 epoch, the actual mean epoch of the observations is approximately J1991.5. To ensure a correct dynamical baseline, I back-propagate the Tycho-2 6D vector from J2000.0 to its true observational epoch using the aforementioned `apply_space_motion` routine. The long-term velocity vector $\boldsymbol{v}_{\rm mean}$ is then computed as:

$$\boldsymbol{v}_{\rm mean} = \frac{\mathbf{r}_{\rm Gaia} - \mathbf{r}_{\rm Tycho}}{\Delta t} \tag{4.17}$$

where Δt is the baseline of approximately $24.5\,{\rm yr}$. The PMa is finally derived as the difference between the instantaneous *Gaia* velocity and this long-term average. All uncertainties, including the lack of information on Tycho-2 parallax and the errors in *Gaia* RV, are rigorously propagated through my MC framework. By performing MC sampling from the full multivariate normal distribution defined by the covariance matrix, I ensure that the resulting PMa significance accounts for both the measurement noise and the geometric projection effects.

4.3.d Error inflation

The reliability of the calculated PMa largely depends on the accuracy of the underlying noise model. Relying exclusively on raw uncertainties leads to a statistically over-sensitive SNR statistic, where instrumental systematics are frequently misidentified as physical orbital signals (Brandt 2018). To ensure scientific integrity and provide a robust threshold for stellar companion detection, I adopted the error inflation framework established by Brandt (2021) for the *Gaia* EDR3 edition of the HGCA. Following Section 6.2 of Brandt (2021), I first applied a multiplicative inflation factor of $a = 1.37$ to *Gaia* astrometric uncertainties (except parallaxes, treated separately according to the description below) to account for unmodeled noise in the bright-star observations. Crucially, while previous iterations of the HGCA (Brandt 2018) suggested an additional additive jitter term of $0.2\,{\rm mas\,yr^{-1}}$ to stabilize the residuals, the more recent analysis of $Gaia$ EDR3 data indicates that such a term is no longer required for the positional difference baseline. $Gaia$ DR2, which was foundational for the work of Brandt (2018), was plagued by systematic uncertainties beyond the formal ones, dubbed the degrees of freedom (DOF) bug. One possible way used by the $Gaia$ team to measure the goodness of fit of a single-star model to a certain target relies on the `astrometric_chi2_al` parameter, provided in the *Gaia* archive. In particular, the unit weight error u is computed as this quantity divided by the DOF

$$u = \frac{1}{\nu} \sum_{l} \frac{R_l^2}{\sigma_{\eta,l}^2 + \epsilon_a(t_l)^2} \tag{4.18}$$

where ν represents the DOF, R_l the along-scan (AL) residual of the l-th observation, $\sigma_{\eta,l}$ its formal uncertainty and $\epsilon_a(t_l)$ the excess attitude noise as a function of time (clearly constant for observations taken at a given time). In DR2, the latter presented an unexpected behavior, being on average different from the expected 1.0 (Figure 4.4). Specifically, the excess source noise ϵ_i was underestimated for most targets, with 80% having a zero value, thereby producing a low u value for sources brighter than $G \sim 13$. This bug impacted the formal uncertainties only, with negligible impact on the measurements themselves.

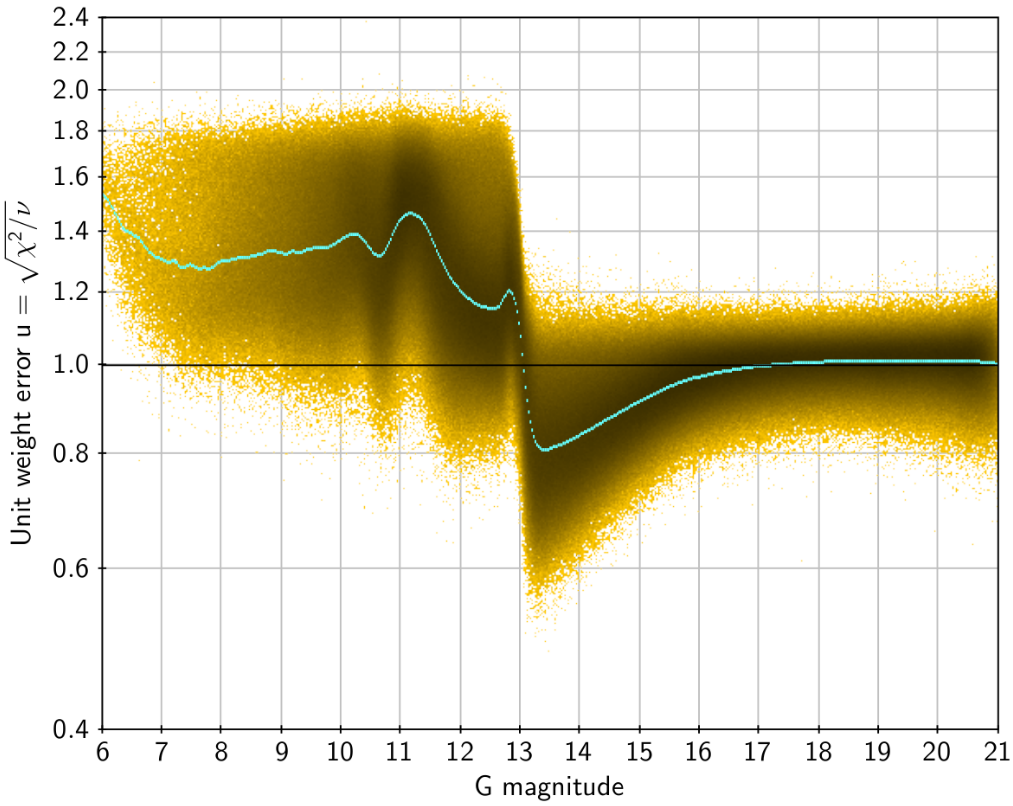

Figure 4.4: DOF bug plaguing *Gaia* DR2. It is evident how the unit weight error u behaves erratically around a magnitude $G = 13$, as shown both by the yellow datapoints and their median lightblue curve. Source: Lindegren et al. (2018).

This bug has been fixed in the (not for long) current data release, leaving only a minimal residual impact on formal uncertainties that I am treating in this subsection. Hence, according to the best-fit model described by Brandt (2021) (Equation 8 and Section 6.2), the additive term is found to be effectively zero ($b = 0$). The multiplicative factor a is included in the covariance matrix used in the MC sampling, which will be discussed thoroughly in the next section, to correct the positions and PMs. Regarding parallaxes, El-Badry, Rix & Heintz (2021) carefully analyzed a sample of roughly a million binaries with a high probability of being bound, located within $1\,\mathrm{kpc}$ from the Sun. They concluded that $Gaia$ DR3 parallax uncertainties, while reliable for fainter targets ($G \gtrsim 18$), are generally underestimated for brighter targets. This underestimation can be corrected by taking into account the target magnitude as shown in Eq. 16 of El-Badry, Rix & Heintz (2021)

$$f(G) = A \,\exp\left[-\frac{(G-G_0)^2}{b^2}\right] + p_0 + p_1 G + p_2 G^2 \tag{4.19}$$

where their best fit coefficients correspond to $A = 0.21$, $G_0 = 12.65$, $b = 0.90$, $p_0 = 1.141$, $p_1 = 0.0040$, $p_2 = -0.00062$. This correction is suited for sources with $7 < G < 21$ and a renormalized unit weight error (RUWE) < 1.4. For the purposes of this work, a RUWE larger than this threshold is considered a signal of potential binarity (Lindegren et al. 2018), thus this category of targets will be treated separately.

Similarly for Tycho-2, I accounted for systematic errors on the instrument coincidence with the ICRS reference frame, and on the computed PMs, amounting to $0.6\,\mathrm{mas}$ and $0.25\,\mathrm{mas\,yr^{-1}}$ [11], respectively (Høg et al. 2000a), by adding them in quadrature to the uncertainties of those quantities[12]. By implementing this error inflation, I avoid overweighting measurements with unrealistically low uncertainties, while providing a robust statistical threshold.

4.3.e Reference frame alignment

The assessment of PMa requires a highly inertial reference frame, common to both $Gaia$ DR3 and Tycho-2. While the *Gaia* reference frame is inherently tied to the extragalactic International Celestial Reference Frame (ICRF) via over 1.6 million quasars (Gaia Collaboration et al. 2022), the alignment for bright stars ($G \lesssim 13$) in the EDR3 and the subsequent DR3 was historically anchored to the

[11] https://cdsarc.cds.unistra.fr/viz-bin/ReadMe/I/259?format=html&tex=true

[12] The different treatment of Tycho-2 errors arises from the conceptual difference between independent errors and the $Gaia$ counterpart, for which the added uncertainty component is inherent in every stellar measurement.

$Hipparcos$ positions (Lindegren et al. 2021b). Consequently, the bright-star PMs inherited the residual rotation (spin) of the $Hipparcos$ realization of the ICRF. It is essential to correct for this effect to avoid spurious orbital accelerations. Initially modeled as a rigid-body rotation of approximately $|\omega| \approx 0.15\,\mathrm{mas\,yr^{-1}}$ (Lindegren et al. 2018), subsequent analyses by Cantat-Gaudin & Brandt (2021) and Brandt (2021) demonstrated that this bias is magnitude-dependent. This systematic effect originates from the different readout modes (Window Class 0) and gatings used by the *Gaia* satellite to observe bright sources without saturating. The residual spin $\vec{\omega}$ reaches amplitudes of up to $80\,\mu\mathrm{as\,yr^{-1}}$ in the $G = 11 - 13$ magnitude range, a value significantly larger than the formal EDR3 uncertainties. In this work, to ensure that the detected anomalies are physical and not artifacts of the reference frame, I applied the magnitude-dependent correction prescribed by Cantat-Gaudin & Brandt (2021). The observed PMs in the *Gaia* system ($\vec{\mu}_G$) were aligned to the inertial ICRF by removing the rotation vector $\vec{\omega}(G)$ as follows:

$$\begin{pmatrix} \Delta\mu_{\alpha*} \\ \Delta\mu_{\delta} \end{pmatrix} = \begin{pmatrix} -\sin\delta\cos\alpha & -\sin\delta\sin\alpha & \cos\delta \\ \sin\alpha & -\cos\alpha & 0 \end{pmatrix} \begin{bmatrix} \omega_X(G) \\ \omega_Y(G) \\ \omega_Z(G) \end{bmatrix} \tag{4.20}$$

where the components $(\omega_X, \omega_Y, \omega_Z)$ are defined in discrete magnitude bins. Accounting for this spin is critical for the robust detection of substellar companions, as it eliminates a systematic bias in the long-term baseline between the Tycho-2 (mean epoch ≈J1991.5) and *Gaia* (epoch J2016.0) measurements. While Cantat-Gaudin & Brandt (2021) also mention a potential color-dependent residual rotation of the reference frame (on the order of $\sim\ 10\,\mu\mathrm{as\,yr^{-1}}$, they recommend applying only the magnitude-dependent correction. Given that the magnitude of this chromatic spin is significantly below the systematic noise floor of the Tycho-2 catalog ($0.25\,\mu\mathrm{as}$), I neglected this higher-order effect to avoid potential overcorrection of the signal, as already discussed above, focusing instead on the dominant magnitude-dependent systematics. I report the code ready-to-use in chapter B. It is also available in the Appendix of Cantat-Gaudin & Brandt (2021).

4.3.f Light travel time

$Gaia$ and Tycho-2 collected photons at different epochs, implying that the star could have moved along the line of sight, resulting in a different light propagation time. Besides the fact that no available pipeline corrects for this effect, using a corrected reference frame for both epochs is functionally equivalent to working in an equally aberrated frame (Kervella et al. 2019). Moreover, Butkevich & Lindegren (2014) quantifies this effect to be on the order of μas for most *Hipparcos* stars, with few of them reaching the 0.1 mas level only on a timespan of 100 years. This is negligible for the purposes of this work, given the ~ 24.5 yr time separation between the two astrometric missions.

4.4 PMa calculation

To identify the gravitational influence of unresolved companions, I calculated the PMa by combining historical astrometric data from the Tycho-2 catalog with modern *Gaia* DR3 measurements, following a mathematical approach that is formally analogous to that described by Kervella et al. (2019) and Kervella, Arenou & Thévenin (2022). The PMa is defined as the vector difference between the instantaneous PM measured by *Gaia* at epoch t_G and the long-term PM derived from the positional difference, averaged over the time baseline, between the Tycho and *Gaia* epochs. It could be equivalently defined as the difference between the "instantaneous" PM "measured by" Tycho-2 and the long-term PM. However, Tycho-2 did not measure any instantaneous PMs, as described in Chapter 4. Trying to compute two distinct PMas, namely, Tycho-2 PM with respect to the long-term PM and *Gaia* DR3 PM with respect to the long-term PM, similarly to the methodology of Kervella et al. (2019) and Kervella, Arenou & Thévenin (2022) is not feasible, as once again, the Tycho-2 PM is not a direct and almost instantaneous measurement. The determination of the PMa significance relies on a rigorous propagation of uncertainties from the raw catalog observables to the final velocity anomaly vector. Unlike simplified approaches that treat RA and Dec errors as independent, my framework accounts for the full correlation structure provided by the *Gaia* DR3 and Tycho-2 catalogs. For each target, I construct a global 11×11 covariance matrix Σ_{tot} which represents the joint probability distribution of all input parameters. The state vector $\boldsymbol{S}$ is defined as:

$$\mathbf{S} = [\alpha_G, \delta_G, \varpi_G, \mu_{\alpha,G}, \mu_{\delta,G}, \hat{\nu}_{\text{eff}}, v_{\text{rad}}, \alpha_T, \delta_T, \mu_{\alpha,T}, \mu_{\delta,T}] \tag{4.21}$$

where α is the RA, δ the Dec, ϖ the parallax, μ_α the PM along the RA coordinate, μ_δ the PM along Dec, $\hat{\nu}_{\text{eff}}$ the *Gaia* pseudocolor, and v_{rad} the RV. The subscripts G and T denote *Gaia* and Tycho-2, respectively. As mentioned before, Tycho-2 does not provide RV or parallaxes, but the impact of their absence is completely negligible and will be discussed later. The matrix $\Sigma_{\text{tot}} \in \mathbb{R}^{11} \times \mathbb{R}^{11}$ is structured in blocks:

- A 5×5 (or 6×6 for 6p solutions, including the pseudocolor $\hat{\nu}_{\text{eff}}$) block for *Gaia* astrometry, scaled by the Brandt (2021) inflation factor $a = 1.37$, except for the parallax uncertainty, which is inflated following El-Badry, Rix & Heintz (2021), and including all formal correlation coefficients ρ_{ij}.

- A variance term for the RV v_{rad}.
- Two 2×2 blocks for Tycho-2 positions and PMs, where the first includes a correlation term between the Tycho-2 positional coordinates[13].

In the end, the matrix is

$$\Sigma_{\text{tot}} = \left(\begin{array}{cccccc|c|cc|cc}
1 & \rho_{\alpha\delta} & \rho_{\alpha\varpi} & \rho_{\alpha\mu_\alpha} & \rho_{\alpha\mu_\delta} & \rho_{\alpha\hat{\nu}} & 0 & 0 & 0 & 0 & 0 \\
\rho_{\alpha\delta} & 1 & \rho_{\delta\varpi} & \rho_{\delta\mu_\alpha} & \rho_{\delta\mu_\delta} & \rho_{\delta\hat{\nu}} & 0 & 0 & 0 & 0 & 0 \\
\rho_{\alpha\varpi} & \rho_{\delta\varpi} & 1 & \rho_{\varpi\mu_\alpha} & \rho_{\varpi\mu_\delta} & \rho_{\varpi\hat{\nu}} & 0 & 0 & 0 & 0 & 0 \\
\rho_{\alpha\mu_\alpha} & \rho_{\delta\mu_\alpha} & \rho_{\varpi\mu_\alpha} & 1 & \rho_{\mu_\alpha\mu_\delta} & \rho_{\mu_\alpha\hat{\nu}} & 0 & 0 & 0 & 0 & 0 \\
\rho_{\alpha\mu_\delta} & \rho_{\delta\mu_\delta} & \rho_{\varpi\mu_\delta} & \rho_{\mu_\alpha\mu_\delta} & 1 & \rho_{\mu_\delta\hat{\nu}} & 0 & 0 & 0 & 0 & 0 \\
\rho_{\alpha\hat{\nu}} & \rho_{\delta\hat{\nu}} & \rho_{\varpi\hat{\nu}} & \rho_{\mu_\alpha\hat{\nu}} & \rho_{\mu_\delta\hat{\nu}} & 1 & 0 & 0 & 0 & 0 & 0 \\
\hline
0 & 0 & 0 & 0 & 0 & 0 & 1 & 0 & 0 & 0 & 0 \\
\hline
0 & 0 & 0 & 0 & 0 & 0 & 0 & 1 & \rho_T & 0 & 0 \\
0 & 0 & 0 & 0 & 0 & 0 & 0 & \rho_T & 1 & 0 & 0 \\
\hline
0 & 0 & 0 & 0 & 0 & 0 & 0 & 0 & 0 & 1 & 0 \\
0 & 0 & 0 & 0 & 0 & 0 & 0 & 0 & 0 & 0 & 1
\end{array}\right) \tag{4.22}$$

To propagate these uncertainties through the non-linear transformations required by the 3D Cartesian PMa derivation described throughout this chapter, along with the various systematic corrections, I employed a MC approach with $N = 5 \cdot 10^4$ [14] realizations. For each realization k, a sample vector $\boldsymbol{S}_k$ is drawn from a multivariate normal distribution:

$$\mathbf{S}_k \sim \mathcal{N}(\mathbf{S}_{\text{obs}}, \mathbf{\Sigma}_{\text{total}}) \tag{4.23}$$

The full pipeline is then executed for every sample, producing a distribution of PMa vectors between Gaia and the long-term PM $\Delta\boldsymbol{\mu}_k$. Crucially, rather than relying on an analytical Jacobian, which would present a significant mathematical hurdle prone to linearization errors, the final 2×2 covariance matrix C_{PMa} is derived numerically from the sample covariance of the MC distribution

$$\mathbf{C}_{\text{PMa}} = \text{cov}(\Delta\boldsymbol{\mu}_{\alpha^*,k}, \Delta\boldsymbol{\mu}_{\delta,k}) \tag{4.24}$$

---

[13] PMs are reasonably uncorrelated as their measurement consists in much more than a set of observations performed by a defined instrument in a defined set of time.

[14] roughly corresponding to a statistical precision of $1/\sqrt{N} \approx 0.45\%$, ensuring that the final covariance matrix is a precise representation of the 11-dimensional uncertainty volume. This matches the level of precision employed in works from the Gaia collaboration (e.g., Gaia Collaboration et al. 2023a)

This matrix $\mathbf{C}_{\mathrm{PMa}}$ captures the effective noise, including the cross-terms induced by the coupling of distance and velocity uncertainties during the 3D to 2D projection. Finally, the statistical significance of the anomaly is evaluated using the Mahalanobis distance (Mahalanobis 1936), expressed as a χ^2 statistic with two degrees of freedom

$$\chi^2 = \Delta\bar{\boldsymbol{\mu}}^{\intercal}\mathbf{C}_{\mathrm{PMa}}^{-1}\Delta\bar{\boldsymbol{\mu}} \tag{4.25}$$

where $\Delta\bar{\boldsymbol{\mu}}$ is the median PMa vector. I quantify the detection strength using the Delta statistic

$$\Delta = \sqrt{\chi^2} \tag{4.26}$$

from Brandt (2018) and Kervella et al. (2019, and consecutive works)[15]. Although previous works place a detection threshold for binary companions at $\Delta = 3$, remaining unaccounted errors from Tycho-2 may influence the robustness of the inference. Hence, I consider this threshold only as a tentative detection, while a more conservative $\Delta = 5$ represents a genuine binarity signal.

4.4.a Methodological Robustness and Assumptions

It is essential to highlight the sound theoretical, computational and statistical foundation of this approach. A possible argument regarding the correctness of a Gaussian-based analysis would not hold in light of the nature of the uncertainties involved (e.g., *Gaia* measurements are the combination of consecutive measurements). Moreover, Section 9 of Brandt (2018) and the work of Brandt (2021) highlight how this numerical treatment ensures proper Gaussianity of the results as well. By adopting the Δ framework, I explicitly account for the non-spherical geometry of the error distributions. Under the assumption of negligible third and fourth moments (i.e., assuming the uncertainties are strictly governed by a multivariate Gaussian distribution) this approach is equivalent to quantifying the anomaly in units of the standard deviation along the specific direction of the PM vector. This effectively transforms the correlated observational space into a standardized space where the detection significance $\Delta = \sqrt{\chi^2}$ directly represents the distance from the null-hypothesis in units of direction-dependent σ.

Regarding the use of *Gaia* parallaxes ϖ and RVs, this does not compromise my inference. The PMa is essentially an angular anomaly; hence, an approximated treatment of the line-of-sight dimension plays a negligible role. It is clear that it can enlarge the number of false negative binaries, but it does not create any

[15] The choice of computing the Delta statistic using the covariance matrix extracted from the sampled distribution follows the specific choice of using a proper metric for a highly dimensional space whose uncertainty space is a non-trivial combination of correlations.

false positives[16]. Parallaxes, however, may pose a threat to the prospective acceleration. Once again, this is negligible as the contribution from this correction (which has been formally and computationally included) is on the order of μas, while Tycho-2 floor errors reside in the $0.6\,\mathrm{mas}$ level (Butkevich & Lindegren 2014). The correction only exceeds the $0.1\,\mathrm{mas}$ level for a few nearby $Hipparcos$ stars on a 100 year timespan, well beyond the aim of this work (Butkevich & Lindegren 2014). Moreover, Kervella et al. (2019) provides the example of the fast moving Kapteyn's star ($v_r \approx 245\ \mathrm{km\,s^{-1}}$): even in this case, the error is negligible, accounting for just 7.2 days on a ~ 25 year baseline, a 0.08% error clearly lower than Tycho-2 relative errors and comparable to the MC statistical error.

In conclusion, this inference is not intended to be the definitive answer to stellar binarity in general. Its primary goal is to leverage the 2.5 million stars of Tycho-2, a major leap forward with respect to the $100,000$ stars of $Hipparcos$, to extract as many binaries as possible, while acknowledging the inherent limitations arising from its construction. The only sensitive argument may be the reliability of Tycho-2 astrometric measurements close to the fainter end of the catalog ($V_T \sim 11.5 - 12.0$). To avoid a potentially dangerous magnitude region, that may present unmitigated effects that were not specifically addressed in this work, I avoid blindly relying on PMa analysis for the faintest targets. A comprehensive analysis of such effects will be part of a future project.

4.5 Benchmarking

Although the framework I developed is in full agreement with state-of-the-art prescriptions regarding PMa (Brandt 2018; Kervella et al. 2019; Brandt 2021; Cantat-Gaudin & Brandt 2021; El-Badry, Rix & Heintz 2021; Kervella, Arenou & Thévenin 2022), it is mandatory to benchmark it to validate its reliability for the analysis of the Rossi et al. (2026) Neptunian sample.

4.5.a Binary detection

Considering that the Tycho-2 uncertainties are roughly one order of magnitude larger than those of $Hipparcos$ for positions and PMs, it is reasonable to expect a lower sensitivity to astrometric motion induced by companions compared

[16] Assuming a high $100\ \mathrm{km\,s^{-1}}$ RV difference between Tycho-2 and Gaia, and a star located far away with a parallax of $\varpi = 0.01''$, the error due to the incorrect, but necessary, treatment of RV would be almost an order of magnitude less than Tycho-2 floor errors. Specifically, $\dot{\mu} = -2\mu\frac{v_r}{d}$ can be applied assuming a constant acceleration and this estimation can be performed for whichever parameters.

to Kervella et al. (2019) and Kervella, Arenou & Thévenin (2022). This lower resolution is further hampered by the unavailability of RVs and parallaxes in the Tycho-2 catalog with respect to *Hipparcos*. As already discussed, this lack of parameters favors a higher rate of false negatives, without introducing false positives. One could argue that Tycho-2 is not a reliable source for PMa analysis, and this argument may be true in terms of recall[17]. However, the 2.5 million targets present in Tycho-2 represent a significant advancement compared to the roughly $100,000$ targets in *Hipparcos*: Tycho-2 may not be able to resolve companions in the substellar regime, but its capabilities can be valuable for probing stellar-sized companions, and even BD-sized companions in the most favorable cases.

I selected the first 100 targets from the Kervella, Arenou & Thévenin (2022) sample in order to compare my code with the results from the *Gaia* EDR3-*Hipparcos* PMa analysis, and then retrieved information on them from Tycho-2 and *Gaia* DR3. Four of these targets were identified as binary companions in Tycho-2 of other targets already in the sample[18]. Considering that binary solutions may be directly computed from the primary, and in general they have undergone a post-processing analysis, I decided to conservatively exclude these targets to mitigate unwanted and uncontrolled effects. This does not compromise my inference, as my Neptunian sample is not composed of targets regarded as binaries by Tycho-2. I ran my code sampling every multivariate Gaussian for $50,000$ iterations to avoid statistical flukes, and the results, shown in Figure 4.5 match the expectations for a well constructed and well behaved code. Due to data availability[19] for these 100 targets, the PMa calculation was performed on 96 targets only.

Results plotted in Figure 4.5 show that the framework is systematically "blinder" compared to Kervella, Arenou & Thévenin (2022), exactly as expected.

[17] defined here as the ability to consistently detect true binaries, without incurring false negatives.

[18] Tycho-2 bases its determination of binarity for *Hipparcos* stars partially on the Catalog of Components of Double and Multiple stars (CCDM, Dommanget & Nys 1995) via the `CCDM` flag. Specifically, a double star solution is divided into a principal and brighter component A and a secondary and fainter component B. The resolution limit of the star mapper of *Hipparcos* was $0.8''$, implying that both photocenter and double star solutions could not probe deeper than this projected separation threshold. Moreover, companion stars B are often referred to the same identifier, with no possibility to associate this secondary component to a different (and obviously unique) *Gaia* entry to perform PMa analysis. Kervella et al. (2019) and Kervella, Arenou & Thévenin (2022) treat these kind of solutions in a similar fashion, that I will not be describing here for the sake of brevity. However, this kind of issue is not present in the Rossi et al. (2026) sample, so this approximation is sound for the purposes of this thesis.

[19] Not all Tycho-2 targets have positions computed at epoch J2000.0, and some Tycho-2 targets are the second component of a two-body system, as already introduced in the text.

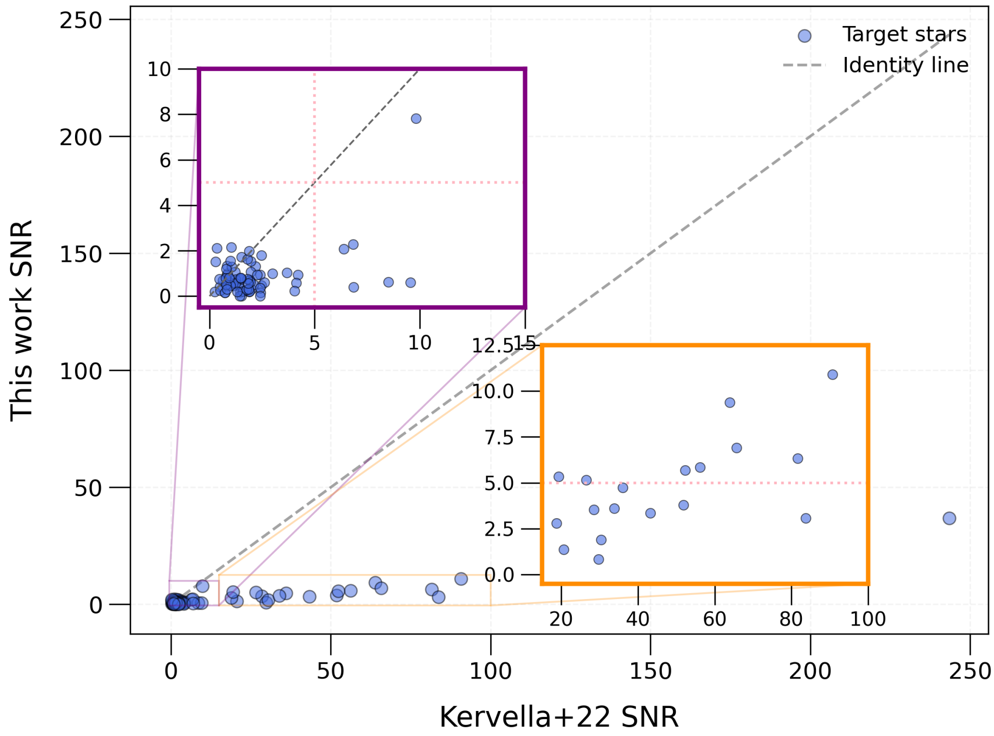

Figure 4.5: Benchmarking of the PMa framework. The majority of the 96 stars show no sign of binarity both in Kervella, Arenou & Thévenin (2022) and in this work. However, some targets are false negatives, as shown in the purple zoom (SNR > 5 on the x-axis but lower than SNR $= 5$ on the y-axis, both represented by dotted pink lines) and in the orange zoom (same as purple).

Given that the binarity estimator is a SNR computed from the PMa, if one takes into account the necessary and available correlations and considers that Tycho-2 is at least one order of magnitude less precise than $Hipparcos$, it is to be expected that some PMa signals would be obscured by Tycho-2 noise, while $Hipparcos$ may be able to detect them with a significant SNR.

I performed some statistical tests to quantitatively assess the robustness of my inference. A Pearson test yielded a linear correlation coefficient of 0.93, with a p-value rejecting the null hypothesis of data not being linearly correlated below the 10^{-4} level[20]. This implies a strong linear correlation between the analysis of this work and Kervella, Arenou & Thévenin (2022). I also performed a Cohen's κ test (Cohen 1960) to understand the performance of the pipeline. Assuming a

[20] A clear outlying point is visible on the right of Figure 4.5. Removing it from the Pearson test still yielded a comparable p-value with just a lower Pearson coefficient of 0.82, confirming that the inference is robust.

conservative threshold for detection of $\text{SNR} > 5$, compared to Kervella, Arenou & Thévenin (2022) $\text{SNR} > 3$, I retrieve a $\kappa = 0.50$, corresponding to a moderate agreement between the two analyses (Figure 4.6). Defining precision as

$$\text{Precision} = \frac{TP}{TP + FP} \tag{4.27}$$

where TP and FP are true positives and false positives, respectively, and recall as

$$\text{Recall} = \frac{TP}{TP + FN} \tag{4.28}$$

where FN means false negatives, I find that my precision is unitary, being able to systematically retrieve real binaries, without finding binarity for single stars. The recall is positively low at 0.40. One would desire both a high recall and precision, but due to the Tycho-2 uncertainties discussed above, this is an expected phenomenon. If I reduce the threshold to $\text{SNR} > 3$, the results improve (Figure 4.7), with a $\kappa = 0.63$ (corresponding to a substantial agreement), a precision still 1.00, and a recall improving to 0.55. I still avoid this less stringent threshold for the discussion developed throughout this section. The only argument that can affect my inference is that a larger benchmark sample is needed, although I am defining a binary detection at $\text{SNR} > 5$, instead of $\text{SNR} > 3$. This represents future work that will be addressed. Confusion matrices for the conservative ($\Delta = 5$), and tentative detection thresholds ($\Delta = 3$) are provided in Figures 4.6 and 4.7, respectively[21].

4.5.b Companion mass estimation

I discussed how Equation (4.15) is a useful tool to characterize the mass of the companion of a given target. I also discussed how imposing the same parallax and RV for both astrometric epochs plays no role in creating false positives. However, estimating the mass is inherently tied to an extremely precise determination of the PMa. A non detection simply produces a mass–separation curve that can be regarded as an upper limit, excluding companions with masses above that threshold, since lower PMas cannot be detected with the current available data from Tycho-2. On the contrary, a detection highlights the space of parameters, namely companion mass M_2 and distance, where the companion star can be located. Results are highly encouraging also in this realm. I compared my mass–distance inference at distances of $3, 5, 10, 30\,\text{au}$ from the primary star,

[21]Confusion matrices are a valuable tool for evaluating the performance of a classification task. In this analysis, the results obtained from my selection (x-axis) are compared against the reference detections provided by Kervella, Arenou & Thévenin (2022) (y-axis), which serve as the benchmark for assessing the accuracy of my methodology.

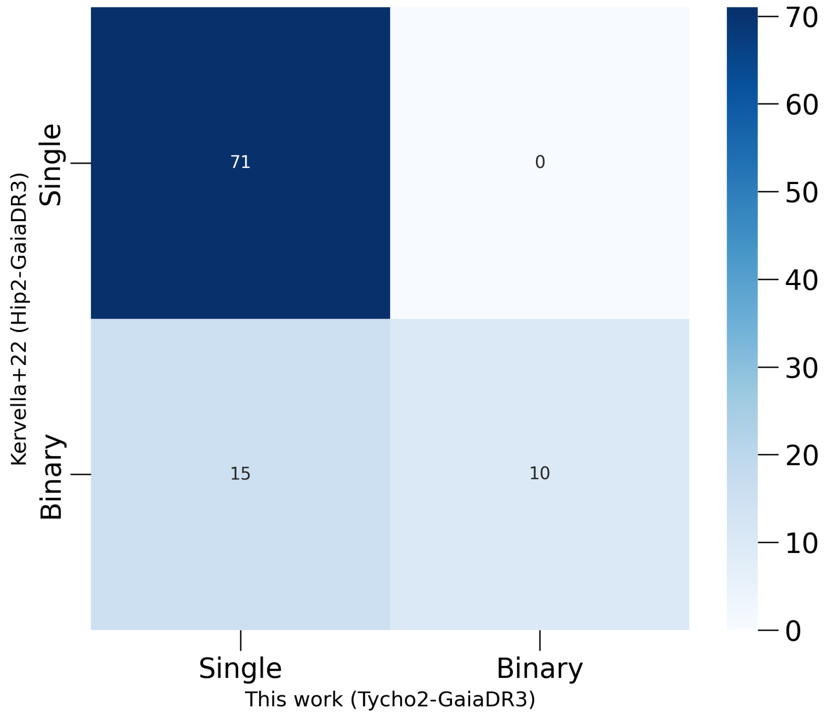

Figure 4.6: Confusion matrix of the astrometric framework benchmark, assuming a detection threshold of $\mathrm{SNR} > 5$. Among the 96 targets sample, I obtain a precision of 1.00 with a low recall of 0.40. This is in agreement with the theoretical discussion regarding the expected performance of the framework.

in agreement with Kervella, Arenou & Thévenin (2022) work, and I am able to place robust limits for both detections and non-detections. Specifically, non-detections show higher upper mass limits for the companions, as expected for a catalog limited by its own noise. Detections, however, are expected to be solid in terms of mass-distance relations, as Equation (4.15) explicitly depends on the PMa determination, and indeed these estimates closely match with Kervella, Arenou & Thévenin (2022). I stress the fact that SNRs are lower because of the noise, but PMa determinations are clearly reliable. The results can be seen in Figures 4.8 to 4.11, where I show the behavior of the mass-distance relation between my analysis and the one provided in Kervella, Arenou & Thévenin (2022). The plots represent mass estimations at fixed distances: non-detections ($\Delta < 3$) represent only an upper limit above which I am able to exclude the presence of a binary companion with a mass higher than this limit, tentative ($3 < \Delta < 5$) and solid ($\Delta > 5$) detections represent instead the value of the mass causing the PMa, along with its uncertainties, at that specific distance. An

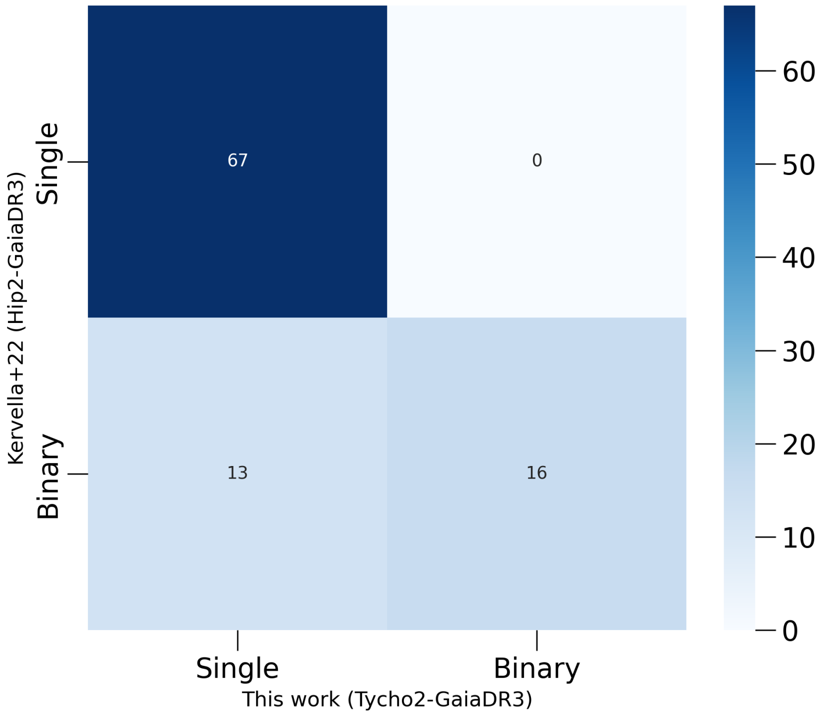

Figure 4.7: Confusion matrix of the astrometric framework benchmark, assuming a detection threshold of $\mathrm{SNR} > 3$. Results are similar, with a slight improve on recall reaching 0.55. This expected considering Figure 4.5, and also positive: the only difference with the more conservative threshold of $SNR = 5$ is that I am decreasing the number of false negatives with no impact on false positives, which remain stably zero. Nonetheless, the more conservative threshold will be adopted in this work to avoid unmitigated and unwanted effects.

example of mass sensitivity curves is given in Figures 4.12 and 4.13, which are associated to non-detection and a detection, respectively.

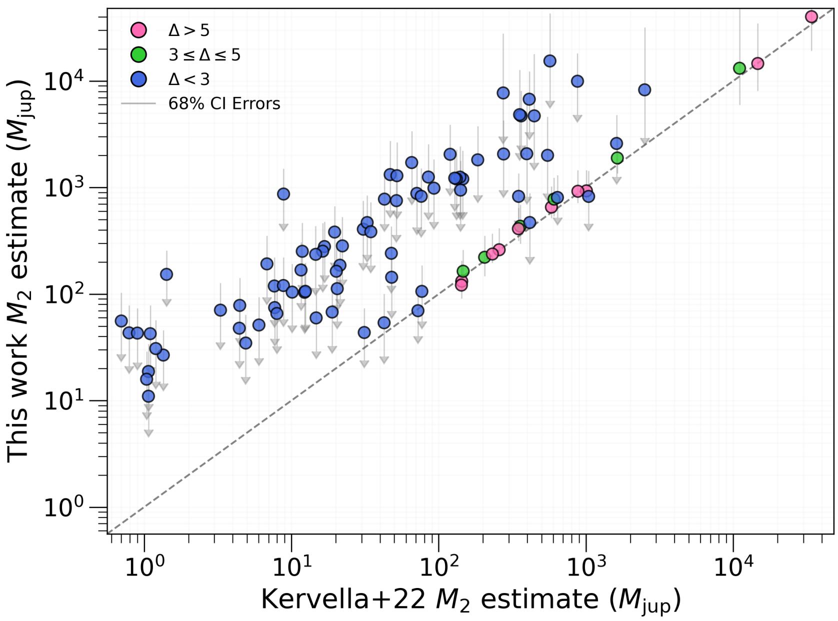

Figure 4.8: Comparison of companion mass determination between this work and Kervella, Arenou & Thévenin (2022) at 3 au. Uncertainties are shown only for the masses computed in this work, due to the unavailability of uncertainties for Kervella, Arenou & Thévenin (2022). Blue dots represent non-detection, and show just an *upper limit* for mass at a distance of 3 au. Green and pink dots show tentative and solid detections, respectively, and they represent the *central value* with its uncertainty. The mass estimates in this latter case are in close alignment with previous literature, as expected for a well behaved code that can associate to a significant PMa signal a value for the companion mass causing it.

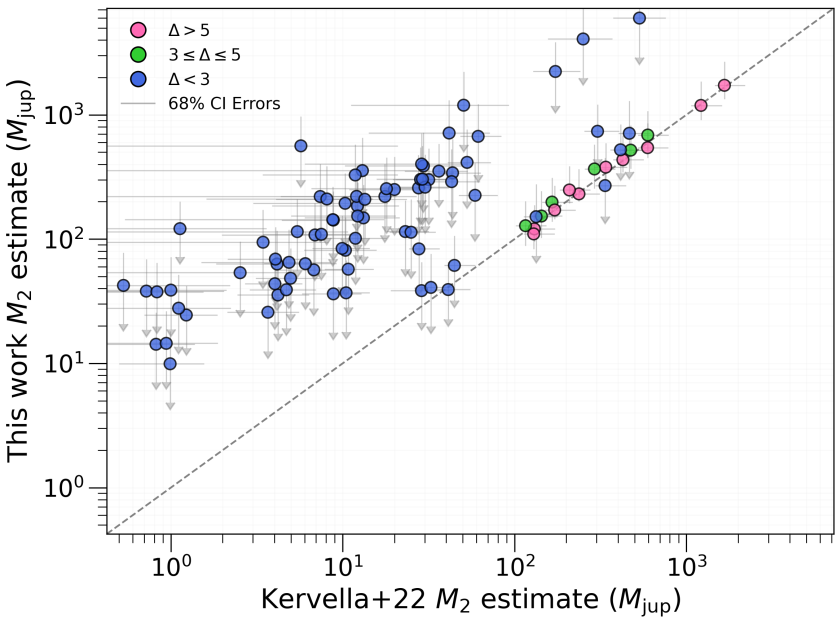

Figure 4.9: Comparison of companion mass determination between this work and Kervella, Arenou & Thévenin (2022) at 5 au. Same as Figure 4.8, but uncertainties are also available for the mass estimates by Kervella, Arenou & Thévenin (2022).

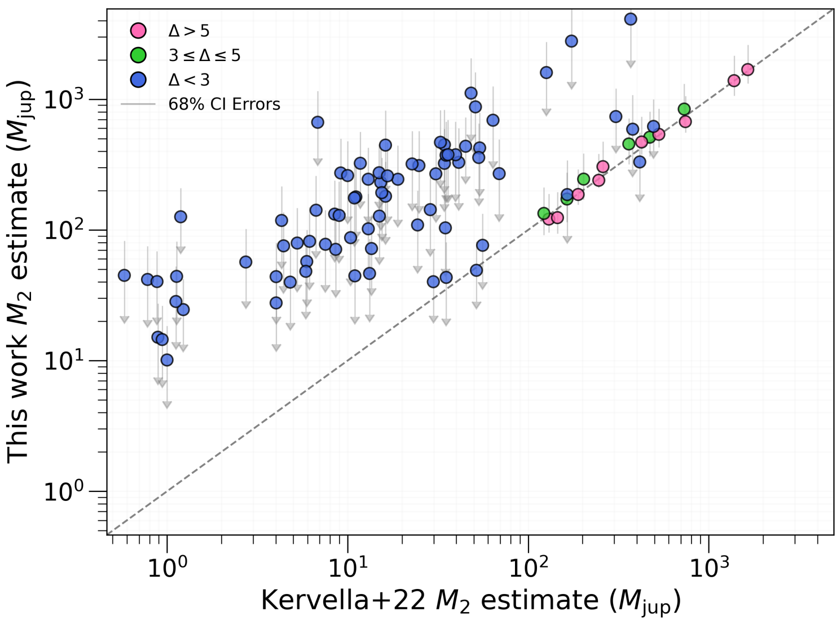

Figure 4.10: Comparison of companion mass determination between this work and Kervella, Arenou & Thévenin (2022) at 10 au. Same as Figure 4.8.

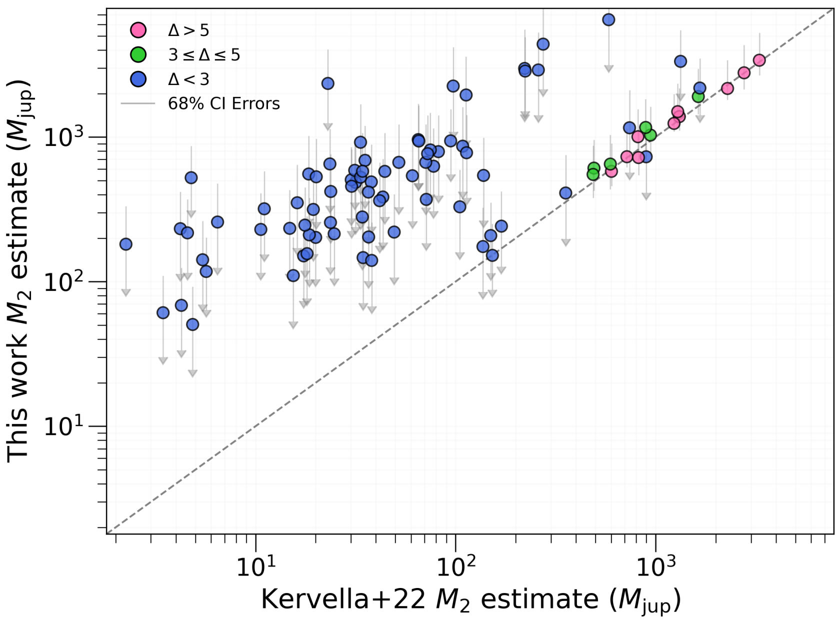

Figure 4.11: Comparison of companion mass determination between this work and Kervella, Arenou & Thévenin (2022) at 30 au. Same as Figure 4.8.

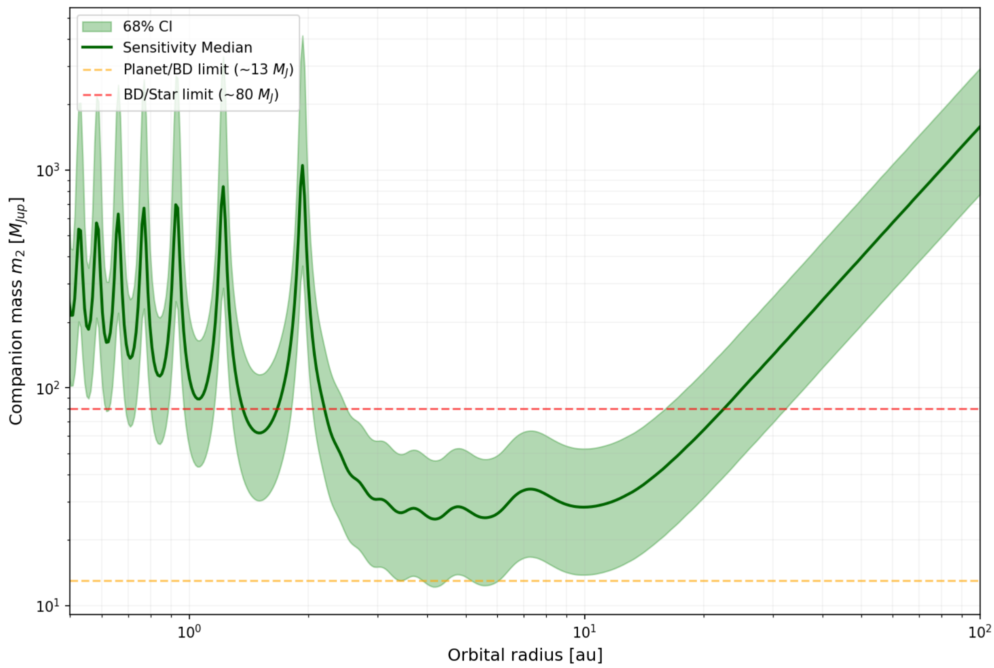

Figure 4.12: Mass sensitivity plot for a PMa non-detection of Gaia DR3 2854774262396590080, or HIP 84. The green curve represents the median value of the mass extracted from Equation (4.15) after the MC analysis of the PMa, while the green shaded area is its 68% confidence interval. The red and yellow dashed line improve the readability of plot, marking the planetary and stellar mass limits, respectively. This represents an upper limit, above which I am able to exclude the presence of companions.

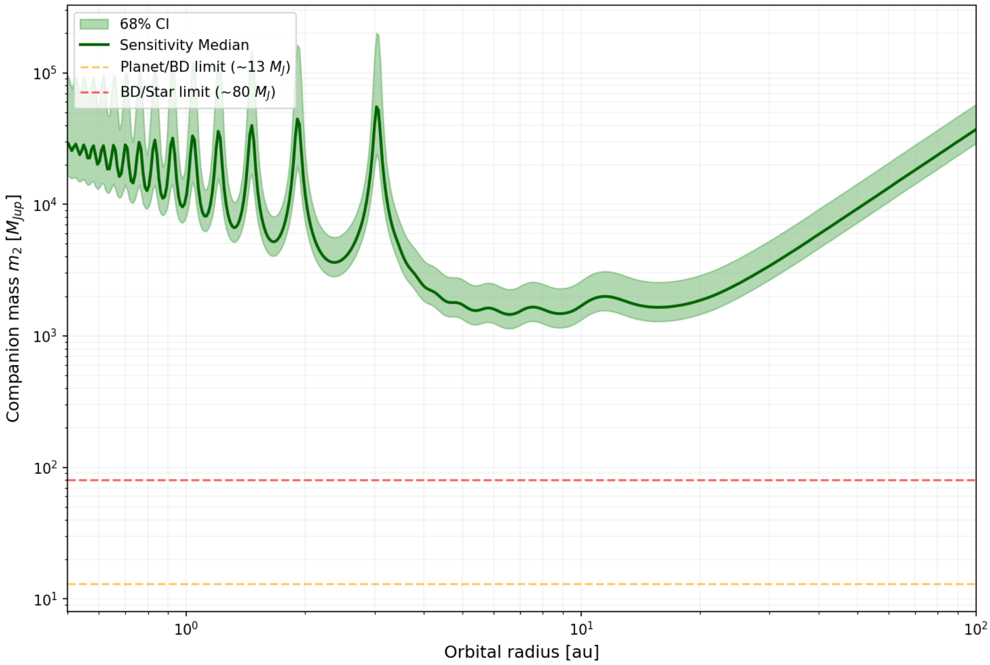

Figure 4.13: Mass sensitivity plot for a PMa detection of Gaia DR3 2773771350992697088, or HIP 78. Same as Figure 4.12, but now the plot represents the space of parameters in which the binary companion, which is present and most likely a star, can exist.

5 A homogeneous and multi-technique analysis

The previous sections provided a brief introduction to exoplanets, and most importantly laid the theoretical and methodological foundations of this work. In this chapter, I will present the statistical analysis of the Rossi et al. (2026) dataset of 32 Neptunian planets[1], basing my discussion on the published properties of the systems, and then thoroughly discuss the possible presence of binaries for each target combining RV, imaging, my original approach to PMa computation, and ten catalogs encompassing astrometry, visual binaries, PMa, and PM acceleration. Two additional planets were included in this analysis, TOI-1135 b (Mallorquín et al. 2024b) and TOI-2374 b (Hacker et al. 2024; Yee et al. 2025), bringing the total to 34. During the final stages of this work, I further included 4 recently published Neptunian planets, namely TOI-622 b (Zak et al. 2025), TOI-837 b (Mantovan et al. 2026b), TOI-1710 A b (Espinoza-Retamal et al. 2026; Mantovan et al. 2026a), and TOI-4495 c (M.-T. Wang et al. 2026). For these systems, the analysis is limited to the discovery papers, bringing the grand total to 38 Neptunian planets with measured true spin-orbit obliquity values. This sample surpasses any currently available collection of Neptunian planets, as similar studies are limited to projected obliquities λ. Projected obliquities offer only partial information regarding this mass regime compared to their more massive Jovian counterparts (Espinoza-Retamal et al. 2024), for which specific trends have been theorized (Dong & Foreman-Mackey 2023) and confirmed (Rossi et al. 2026). A detailed description of the single systems can be found in Chapter A, as their inclusion here would compromise the readability of this section and shift the focus away from the statistical analysis that this thesis is intended to achieve as its primary goal. The following discussion will make use of the largest

[1] https://cdsarc.cds.unistra.fr/viz-bin/cat/J/A+A/705/A142

sample of true spin-orbit obliquities to date created by Rossi et al. (2026), and specifically the largest sample of Neptunian true obliquities therein, to perform the first systematic search for binaries around Neptune-hosting stars. I will also extend the aim of this thesis to exploit the Rossi et al. (2026) Neptunians even more, re-analyzing claims made by recent literature works using a larger sample of planets. Part of the analysis has been performed using the `uncertainties`[2] python package, to ensure a fast, reliable, and mostly analytical error propagation.

5.1 Neptunian sample

In this section, I present the specific outcomes of the investigation conducted on each target host. To ensure a clear and consistent reporting of the findings, the results are organized according to the three primary diagnostic layers developed in this work: high-resolution imaging, the astrometric PMa pipeline, and the systematic crossmatching with established multiplicity catalogs. This structured approach allows for a direct comparison between independent techniques, providing a consensus verdict on the multiplicity of each system while defining robust detection limits where no companion was identified.

Direct imaging The direct imaging analysis was performed on only 22 targets out of 34, due to the lack of measurements in ExoFOP. The details are shown in Table 5.2, including the age of the system (mostly provided by Rossi et al. 2026), its parallax, and the resulting distance (properly corrected according to Section 4.3), along with information about the ExoFOP observation used. These observations consist of either speckle imaging or AO data, conducted using several instruments. Filters are mostly centered on $832\,\mathrm{nm}$ or on the Brγ line at $2159\,\mathrm{nm}$; therefore, the proxies used are the $Gaia$ G_{RP} and the 2MASS K bands, respectively. The mass results, which vary depending on the type of observation, are provided in Table 5.3. No target besides K2-290 B, the first companion of the triple K2-290 system, is detected via imaging (Figures A.6 and A.7).

Radial velocity The RV analysis via DACE software was successfully conducted on 7 out of 34 targets, since 15 lacked RV measurements in DACE, 8 did not have enough datapoints or time coverage to be scientifically meaningful for the goal of this thesis (so the analysis was not conducted), and in 4 cases the fitting algorithm failed to converge (e.g., formally enough measurements and time coverage, but limited to a number of RM series with little to no out-of-RM

[2] https://pypi.org/project/uncertainties/

points). Similarly to imaging, the details are described in Chapter A, while a lookup table is provided in Table 5.1, including the number of datapoints and the time coverage before and after the removal of some outliers.

Proper motion anomaly The astrometric framework was applicable to only 18 out of 34 targets, as 9 of them lacked an entry in Tycho-2, one of which was marked "X" for p_flag, meaning that neither PMs nor mean positions at J2000.0 were available, although the entry was formally included in Tycho-2. Seven more targets were also too faint to be reliably analyzed using Tycho-2 astrometry, having a magnitude close to or beyond the limit of $V_T = 12\,\mathrm{mag}$ (Høg et al. 2000a). The search of the literature papers and on the aforementioned catalogs was performed for each of the 34 targets. Since some of the catalogs (van Leeuwen 2007a; Kervella et al. 2019; Kervella, Arenou & Thévenin 2022; Brandt 2021) are based on $Hipparcos$, it is evident that those targets missing in Tycho-2 will also be missing from these catalogs. This is not the case for $Gaia$ only catalogs (El-Badry, Rix & Heintz 2021). Regarding $Gaia$, I also compiled a list of RUWE values, to obtain information about closer binaries as shown in Figure 3.1. The color dependence of this parameter makes it less obvious for identifying binaries. Only two targets have a RUWE value larger than the threshold of 1.4, but only WASP-131 is ultimately classified as a binary. A summary of these two techniques is provided in Table 5.4. During the final stages of this work, I also confirmed the binaries I found by combining the three techniques of this work (as well as a manual check on the aforementioned catalogs) by comparing them with the Planets in Binary Systems catalog[3] (Thebault & Bonanni 2025). This catalog is provided by `exoplanet.eu` and includes a collection of planets orbiting s-type binaries[4]. Using this catalog, I confirmed all the binaries except for DS Tuc.

Since the goal of this work is to statistically search for a correlation between planetary obliquity and stellar binarity, I report part of the Rossi et al. (2026) catalog in Table 5.5. This table also includes a total of 6 added planets: the whole sample of 38 planets is provided along with projected and true obliquities, eccentricities, effective temperatures, and a flag to distinguish between single stars (1), binaries (2N), wide binaries (2W), and triples (3). The threshold between narrow and wide binarity has been placed at $200-300\,\mathrm{au}$, following the argument by Desidera & Barbieri (2007) on the separation at which planet properties are significantly affected by a stellar companion. It is necessary to point out that the

[3] `https://exoplanet.eu/planets_binary/`

[4] Circumbinary planets are listed in a dedicated catalog available at `https://exoplanet.eu/planets_binary_circum/`. However, this does not apply to this work.

Rossi et al. (2026) catalog did not include orbital eccentricities for the planets; therefore, this work will rely on literature values, which frequently extracted orbital parameters under the reasonable assumption of circular orbits for short-period planets. Recent works have performed a uniform inference of the RM effect without fixing the eccentricity to a zero value (M.-T. Wang et al. 2026), but I preferred to maintain uniformity for each planet and retrieve the orbital parameters of Table 5.5 from the same source when available. Moreover, M.-T. Wang et al. (2026) limited their inference to projected obliquities only.

Table 5.1: Summary of RV datasets and outlier removal process for the Neptunian sample. The table reports the number of data points and temporal coverage before and after the cleaning procedure, along with the detected linear drift. The analysis is inconclusive when the fitting algorithm is unable to converge (e.g., few points, RM series only, etc.), while it is not conducted when the time coverage or the number of measurements is too low.

Target	**N. points**		**Baseline [days]**		**Linear Drift**
	Raw	Cleaned	Raw	Cleaned	[$\mathrm{m\,s^{-1}\,yr^{-1}}$]
AU Mic	478	477	7166	7166	inconclusive
DS Tuc A	218	213	11088	128	not conducted
GJ 436	1124	293	7379	7379	-0.34 ± 0.18
GJ 3470	217	198	5113	5113	-0.25 ± 0.25
HAT-P-11	55	55	1468	1468	11.18 ± 11.16
HD 63433	11	11	5015	5015	not conducted
HD 89345	128	128	122	122	9.78 ± 5.27
HIP 67522	164	164	693	693	not conducted
K2-25	...	...	...	...	...
K2-33	49	49	94	94	not conducted
K2-105	47	46	1742	1742	9.07 ± 4.35
K2-290	46	46	513	513	not conducted
K2-329	78	78	1804	1804	not conducted
Kepler-9	19	19	4290	4290	not conducted
Kepler-25	172	172	4847	4847	0.71 ± 1.42
Kepler-30	...	...	...	...	...
Kepler-63	...	...	...	...	...
Kepler-1656	...	...	...	...	...
TOI-942	...	...	...	...	...
TOI-1135	...	...	...	...	...
TOI-1268	...	...	...	...	...
TOI-1694	...	...	...	...	...
TOI-1759	...	...	...	...	...
TOI-1842	...	...	...	...	...
TOI-2076	...	...	...	...	...
TOI-2364	...	...	...	...	...
TOI-2374	...	...	...	...	...
TOI-3884	2	2	11	11	not conducted
TOI-5398	...	...	...	...	...
WASP-69	116	116	3670	3670	~ 0
WASP-107	221	156	2157	2157	inconclusive
WASP-131	267	232	2604	2163	inconclusive
WASP-148	...	...	...	...	...
WASP-166	589	509	2549	2549	inconclusive

Table 5.2: Summary of high-resolution imaging observations. The table includes the name of the target, as well as its age and distance, the date of the observation and the instrument used in the analysis. It also reports the stellar models used and the proxy filter I employed.

Target	Age[a] [Gyr]	Parallax[b] [mas]	Distance[b] [pc]	Obs. Date	Inst./Filt.	Model[c]	Proxy[d] Filt.
AU Mic	$0.020(3)$	$102.98(2)$	$9.72(1)$	2022-05-18	Zorro/EO832	BHAC15	$G_{\rm RP}$
DS Tuc A	$0.045(4)$	$22.65(2)$	$44.15(3)$	2019-07-14	Zorro/EO832	BHAC15	$G_{\rm RP}$
GJ 436	6^{+4}_{-5}	$102.35(3)$	$9.77(1)$	2019-01-23	NESSI/NB832	BHAC15	$G_{\rm RP}$
HD 63433	$1.5^{+1.6}_{-1.0}$	$44.72(2)$	$22.36(1)$	2020-09-09	NIRC2/Brγ	BHAC15	K
HD 89345	$9.4^{+0.4}_{-1.3}$	$7.65(2)$	$130.77(30)$	2017-12-07	NIRC/Brγ	Mamajek	K
K2-105	N/A	$5.05(2)$	$197.95(60)$	2016-01-21	DSSI/Orange	Mamajek	$G_{\rm RP}$
K2-290	$4.0^{+1.6}_{-0.8}$	$3.75(2)$	$266.84(148)$	2018-03-29	DSSI/Orange	Mamajek	$G_{\rm RP}$
K2-329	$1.8^{+2.2}_{-1.3}$	$4.31(1)$	$231.81(71)$	2017-09-05	NESSI/NB832	BHAC15	$G_{\rm RP}$
Kepler-63	$0.210(45)$	$5.16(1)$	$193.92(36)$	2014-08-10	PHARO/Brγ	BHAC15	K
Kepler-1656	$6.31^{+2.10}_{-2.90}$	$5.39(1)$	$186.92(35)$	2014-07-11	PHARO/Brγ	Mamajek	K
TOI-942	$0.053^{+0.022}_{-0.021}$	$6.63(2)$	$150.88(34)$	2019-10-14	Alopeke/EO832	BHAC15	$G_{\rm RP}$
TOI-1135	$125-1000$	$8.77(1)$	$113.97(15)$	2025-04-14	Alopeke/EO832	BHAC15	$G_{\rm RP}$
TOI-1268	$0.39^{+0.28}_{-0.27}$	$9.10(1)$	$109.85(13)$	2021-02-02	Alopeke/EO832	BHAC15	$G_{\rm RP}$
TOI-1694	$4.3^{+3.5}_{-2.6}$	$8.07(3)$	$123.79(42)$	2021-02-08	Alopeke/EO832	Mamajek	$G_{\rm RP}$
TOI-1759 A	5^{+3}_{-4}	$24.95(1)$	$40.08(2)$	2020-09-09	NIRC2/Brγ	Mamajek	K
TOI-1842	$2.5^{+0.4}_{-0.3}$	$4.45(2)$	$224.63(92)$	2021-06-26	Alopeke/EO832	Mamajek	$G_{\rm RP}$
TOI-2076	$0.338^{+(77)}_{-(56)}$	$23.82(1)$	$41.96(2)$	2021-02-07	Alopeke/EO832	BHAC15	$G_{\rm RP}$
TOI-2364	$3.5^{+4.2}_{-2.4}$	$4.62(2)$	$216.48(87)$	2021-02-24	PHARO/Brγ	Mamajek	K
TOI-3884	$1.0(1.0)$	$23.08(3)$	$43.34(5)$	2022-02-13	PHARO/Brγ	BHAC15	K
TOI-5398	$0.65(15)$	$7.65(2)$	$130.74(24)$	2022-04-17	NESSI/NB832	BHAC15	G_{RP}
WASP-107	$3.4(7)$	$15.56(3)$	$64.29(11)$	2017-06-12	DSSI/Orange	Mamajek	$G_{\rm RP}$
WASP-166	$2.1(9)$	$8.78(2)$	$113.94(18)$	2020-12-07	Alopeke/EO832	BHAC15	$G_{\rm RP}$

Notes:

[a] Stellar ages are reported in Rossi et al. (2026), with the exception of TOI-1135 from Mallorquín et al. (2024b) and K2-105 for which no age estimate is available in the published literature.

[b] Distances are extracted from *Gaia* parallaxes corrected following the prescription of Section 4.3.

[c] BHAC15 refers to age-dependent models by Baraffe et al. (2015), while Mamajek refers to the observational tracks by Pecaut & Mamajek (2013).

[d] G_{RP} refers to the *Gaia* G_{RP} filter centered on 783 nm, while K refers to the 2MASS K filter centered on 2159 nm.

Table 5.3: Summary of companion masses from direct imaging. Mass limits are expressed in M_{Jup} and calculated at fixed physical separations (3, 5, 10, 30, 100, and 300 au) assuming a statistical projection factor of 1.3 (Torres 1999).

Target	*Gaia* DR3 ID	M_{3AU} [$\mathrm{M_{Jup}}$]	M_{5AU} [$\mathrm{M_{Jup}}$]	M_{10AU} [$\mathrm{M_{Jup}}$]	M_{30AU} [$\mathrm{M_{Jup}}$]	M_{50AU} [$\mathrm{M_{Jup}}$]	M_{100AU} [$\mathrm{M_{Jup}}$]	M_{300AU} [$\mathrm{M_{Jup}}$]
AU Mic	6794047652729201024	25.7	20.0	15.0	...	...	...	...
DS Tuc A	6387058411482257536	713.4	282.9	165.2	75.8	53.2	...	...
GJ 436	4017860992519744384	93.7	91.7	79.9	...	...	...	...
HD 63433	875071278432954240	222.4	119.7	87.2	78.6	78.7	79.2	...
HD 89345	3877070590167177344	1219.7	1039.9	590.5	187.6	149.1	124.8	111.6
K2-105	651907079835937280	...	...	840.8	378.5	339.4	260.7	181.2
K2-290	6253844468883543680	1324.4	1324.4	1296.7	619.7	511,1	437.1	365.7
K2-329	2632880927441296640	931.8	931.8	931.8	644.0	283.1	221.6	181.4
Kepler-63	2132628489996257920	1004.4	977.5	910.2	641.2	433.6	164.7	30.9
Kepler-1656	2103392720630278656	1004.3	977.1	909.1	637.0	437.3	193.9	70.2
TOI-942	2974906868489280768	922.2	922.2	685.1	158.8	118.3	64.3	...
TOI-1135	1726858366624544640	1212.5	1114.1	775.1	418.6	290.2	181.3	...
TOI-1268	1675923009431370880	923.7	840.7	415.9	105.0	81.0	60.1	...
TOI-1694	1104269596843209472	829.7	779.5	494.3	178.1	172.8	162.8	...
TOI-1759 A	2216420110788943744	178.3	154.8	78.6	71.1	70.12	70.37	...
TOI-1842	3719927426253118848	1578.8	1578.8	1410.7	614.0	569.1	498.5	211.0
TOI-2076	1490845584382687232	658.4	356.0	249.2	119.1	90.01	...	...
TOI-2364	3022644120017418496	2077.6	1979.5	1734.4	761.4	678.3	228.2	117.5
TOI-3884	3919169687804622336	209.7	140.6	84.2	49.3	42.5	39.6	39.4
TOI-5398	750888548244441344	1158.6	1158.6	1158.6	483.5	404.6	311.8	...
WASP-107	3578638842054261248	632.7	475.5	196.3	156.7	150.0	...	...
WASP-166	5664957444179338240	1193.8	1103.6	772.5	448.9	301.8	150.1	...

Note: Dotted entries indicate that the physical separation was either outside the instrument's field of view (usually large separations in the case of speckle imaging) or too close to the object (usually AO, which is capable of probing larger separations). Although few observations probe separation larger than 300 au, the mass limit beyond this threshold is constant. Hence, it would not be informative to list larger distances in the table (e.g., 500 or 1000 au).

Table 5.4: Consensus summary of binarity evidence for the analyzed sample. This is intended as a lookup table only, as the detailed results of the analysis are reported in Chapter A.

Target	Δ_{G3}[a]	PMa/Acc.[b]	Astro[c]	Surv[d]	Imaging[e]	RUWE	Final Verdict
AU Mic	1.13	×	?	?	×	0.93	Single[1]
DS Tuc	0.53	✓	✓	?	×	0.91	Bound Binary
GJ 436	⊖	×	×	×	×	1.13	Single
GJ 3470	⊖	⊖	×	×	⊖	1.14	Single
HAT-P-11	1.62	✓	×	×	⊖	0.95	Single[2]
HD 63433	0.39	×	×	×	×	0.99	Single
HD 89345	3.49	×	×	×	×	1.08	Single
HIP 67522	1.98	×	×	×	⊖	0.87	Single
K2-25	⊖	⊖	×	×	⊖	1.30	Single[3]
K2-33	⊖	⊖	×	×	⊖	1.22	Single[3]
K2-105	1.32	⊖	×	×	×	0.92	Single
K2-290	0.91	⊖	✓	✓	✓	1.15	Bound triple
K2-329	⊖	⊖	✓	×	×	1.00	Wide binary
Kepler-9	⊖	⊖	×	?	⊖	1.01	Single[4]
Kepler-25	1.13	⊖	✓	?	⊖	1.10	Wide binary
Kepler-30	⊖	⊖	×	×	⊖	1.01	Single[3]
Kepler-63	⊖	⊖	×	×	×	0.75	Single
Kepler-1656	⊖	⊖	×	×	×	0.78	Single
TOI-942	⊖	⊖	×	×	×	1.09	Single
TOI-1135★	1.59	⊖	×	×	×	0.97	Single
TOI-1268	1.45	⊖	×	×	⊖	0.85	Single
TOI-1694	2.51	⊖	×	×	×	1.38	Single
TOI-1759 A	⊖	⊖	✓	✓	×	0.86	Wide binary
TOI-1842	0.33	⊖	×	×	×	0.86	Single
TOI-2076	1.67	⊖	×	×	×	1.67	Single
TOI-2364	⊖	⊖	×	×	×	1.31	Single[3]
TOI-2374★	⊖	⊖	✓	✓	⊖	0.97	Wide binary
TOI-3884	⊖	⊖	×	×	⊖	1.25	Single[3]
TOI-5398	2.29	⊖	×	×	×	0.82	Single
WASP-69	1.44	⊖	×	?	⊖	0.99	Single
WASP-107	⊖	⊖	×	×	×	1.54	Single
WASP-131	2.44	⊖	×	?	⊖	1.94	Bound binary
WASP-148	⊖	⊖	×	×	⊖	0.89	Single
WASP-166	0.88	⊖	×	×	×	0.98	Single

Symbols: ✓ Evidence of binarity; × No evidence (Single star); ? Discordant data; ⊖ Non-detection/Unavailable; ★ not present in Rossi et al. (2026) catalog.

[a] This work PMa significance, binary detection for $\Delta_{G3} > 5$.

[b] Acceleration and PMA catalogs (Section 3.2.a).

[c] Astrometric catalogs (Section 3.2.b).

[d] Dedicated multiplicity surveys (Section 3.2.c).

[e] This work speckle/AO imaging.

(1) Discrepancy arising from mistreated background companion.

(2) Significant PMa caused by a massive planetary companion.

(3) Little to no analysis/information regarding the target.

(4) Unable to confirm possible companion with little to no information.

Table 5.5: Neptunian sample created in this work. It includes information on planetary obliquity, both projected (λ) and true (Ψ), orbital eccentricity e, stellar effective temperature $T_{\rm eff}$, and the result of the binarity analysis conducted throughout this thesis.

Planet	Proj. obliq. λ[a] [deg]	True obliq. Ψ[a] [deg]	Eccentricity e[b]	$T_{\rm eff}$[b] [K]	Binarity[c]
AU Mic b	$-4.7^{+6.8}_{-6.4}$	$14.1^{+10.1}_{-7.3}$	$0.07^{+0.09}_{-0.04}$[(1)]	3540^{+120}_{-110}	1
DS Tuc A b	2.9 ± 0.9	3.2 ± 0.8	0	5660 ± 100	2N
GJ 436 b	114^{+23}_{-17}	$101.0^{+9.6}_{-9.2}$	0.15 ± 0.01	3416 ± 54	1
GJ 3470 b	$101.0^{+29.0}_{-14.0}$	$104.3^{+19.3}_{-14.0}$	0.13 ± 0.02	3622^{+58}_{-55}	1
HAT-P-11 b	$133.9^{+7.1}_{-8.3}$	$110.4^{+5.6}_{-4.9}$	0.264 ± 0.001	4653^{+33}_{-35}	1
HD 63433 b	$8.0^{+33.0}_{-45.0}$	$31.9^{+24.5}_{-15.8}$	0	5640 ± 74	1
HD 89345 b	$74.0^{+34.0}_{-33.0}$	$80.0^{+22.0}_{-23.0}$	0.21 ± 0.04	5499 ± 73	1
HIP 67522 b	$-5.8^{+2.8}_{-5.7}$	$9.5^{+4.6}_{-4.0}$	0	5675 ± 75	1
K2-25 b	3.0 ± 16.0	$14.6^{+10.5}_{-7.9}$	0.43 ± 0.05	3207 ± 58	1
K2-33 b	-10^{+22}_{-24}	$23.2^{+15.5}_{-11.1}$	0	3540 ± 70	1
K2-105 b	-81^{+50}_{-47}	$80^{+36.7}_{-36.1}$	0	5636^{+49}_{-52}	1
K2-290 b	173^{+45}_{-53}	$115.3^{+7.8}_{-16.0}$	0	6302 ± 120	3
K2-329 b	$26.7^{+8.5}_{-8.0}$	$35.8^{+8.4}_{-9.1}$	0.08 ± 0.03	5300 ± 60	2W
Kepler-9 b	-13 ± 16	$27.1^{+13.0}_{-12.7}$	0.064 ± 0.001	5768 ± 25	1
Kepler-25 c	$-0.9^{+7.7}_{-6.4}$	$7.4^{+5.5}_{-4.2}$	$0.006^{+0.005}_{-0.004}$	6270 ± 79	2W
Kepler-30 b	4.0 ± 10.0	$47.3^{+6.2}_{-7.1}$	0.042 ± 0.003	5498 ± 54	1
Kepler-63 b	-110^{+22}_{-14}	$98.3^{+10.9}_{-13.0}$	0[(2)]	5576 ± 50	1
Kepler-1656 b	35^{+15}_{-22}	$37.1^{+15.0}_{-16.2}$	$0.84^{+0.05}_{-0.03}$	5731 ± 60	1
TOI-622 b★★[A]	-4 ± 12	$16.1^{+8.0}_{-9.7}$	0	6400 ± 100	1
TOI-837 b★★[B]	$-18.9^{+2.3}_{-2.5}$	$2.5^{+7.5}_{-6.3}$	0	6000 ± 60	2N
TOI-942 b	$1.0^{+41.0}_{-33.0}$	$29.9^{+24.5}_{-15.3}$	$0.34^{+0.10}_{-0.14}$	4928^{+125}_{-85}	1
TOI-1135 b★[6]	$-68.1^{+7.5}_{-5.3}$	$72.2^{+6.2}_{-6.2}$	$0.06^{+0.12}_{-0.05}$	6320 ± 120	1
TOI-1268 b	$40^{+7.2}_{-9.9}$	$40.1^{+7.8}_{-8.8}$	0.11 ± 0.04[(3)]	5257 ± 40	1
TOI-1694 b	9^{+22}_{-18}	$25.5^{+15.7}_{-13.3}$	0	5135 ± 50	1
TOI-1710 A b ★★[C]	189 ± 19	158^{+11}_{-13}	$0.05^{+0.04}_{-0.02}$	5775 ± 80	2W
TOI-1759 A b	-4^{+19}_{-18}	$25.0^{+12.3}_{-11.8}$	0	3970 ± 40	2W
TOI-1842 b	$-68.1^{+21.2}_{-14.7}$	$70.1^{+11.5}_{-12.8}$	$0.13^{+0.16}_{-0.09}$	6033^{+95}_{-93}	1
TOI-2076 b	-3^{+16}_{-15}	$21.0^{+8.9}_{-9.2}$	0	5201^{+66}_{-61}	1
TOI-2364 b	7^{+10}_{-11}	$21.9^{+6.0}_{-7.0}$	0	5306^{+76}_{-68}	1
TOI-2374 b★[7]	81^{+23}_{-22}	$85.9^{+8.6}_{-9.2}$	0	5002^{+65}_{-64}	2W
TOI-3884 b	75 ± 10	$77.1^{+8.5}_{-9.3}$	$0.06^{+0.06}_{-0.04}$	3180 ± 88	1
TOI-4495 c★★[D]	$-2.3^{+8.3}_{-7.8}$	< 39	$0.023^{+0.043}_{-0.016}$	6210 ± 70	1
TOI-5398 b	$3.0^{+6.8}_{-4.2}$	$20.2^{+4.4\circ}_{-5.1}$	≤ 0.13[(4)]	6000 ± 75	1
WASP-69 b	$0.4^{+2.0}_{-1.9}$	$11.9^{+14.4}_{-8.8}$	0	4700 ± 50	1
WASP-107 b	$-158.0^{+15.0}_{-19.0}$	$103.0^{+2.7}_{-2.8}$	0.09 ± 0.02[(5)]	4425 ± 70	1
WASP-131 b	$162.4^{+1.3}_{-1.2}$	$123.7^{+12.8}_{-8.0}$	0	5990 ± 50	2N
WASP-148 b	-2 ± 8	$18.9^{+14.2}_{-10.1}$	0.22 ± 0.06	5460 ± 130	1
WASP-166 b	-0.7 ± 1.6	$8.9^{+9.7}_{-6.9}$	0	6050 ± 50	1

Notes: ★Not present in Rossi et al. (2026) catalog. Added later and analyzed for binarity according to the techniques described in this work. ★★Not present in Rossi et al. (2026) catalog. Added later and not analyzed. [a]From Rossi et al. (2026). [b]Gathered mostly from the papers from which λ has been retrieved (unpublished part of the catalog by Rossi et al. 2026, following the prescription described therein), unless otherwise noted. A different source may have been chosen as result of a better analysis. [c]1 means single star, 2N bound binary, 2W wide binary, 3 triple.

References: [(1)]Mallorquín et al. (2024a) [(2)]Bourrier et al. (2023), [(3)]Šubjak et al. (2022), [(4)]Mantovan et al. (2024a), [(5)]Wu et al. (2026), [(6)]Dugan et al. (2025), [(7)]Yee et al. (2025), [(A)]Zak et al. (2025), [(B)]Mantovan et al. (2026b), [(C)]Espinoza-Retamal et al. (2026), [(D)]M.-T. Wang et al. (2026)

5.2 Results

Here I will present the most notable results of the analysis. This discussion is not limited only to binarity in Neptunian exoplanetary systems, but encompasses also some of the future analysis that may be undertaken in light of this work, as well as a reanalysis of recent literature results.

5.2.a No new binaries in a larger Neptunian sample

The broad analysis conducted in this work revealed no new stellar companions orbiting Neptune-hosting stars. This first result is not entirely surprising, as the detection of small-sized planets requires a comprehensive understanding of the stellar environment, thus it is unlikely (but not impossible) for a stellar companion to go undetected. This is especially true for WASP, K2, and all the non-TOI systems which have populated the exoplanetary archives for at least a decade. Conversely, recently added Neptunians may require a deeper investigation as in the cases of TOI-622, TOI-4495, although there are instances of recently discovered Neptunians which possess a stellar companion (TOI-837, TOI-4495). To summarize, a deeper and more systematic search may lead to the discovery of new binaries in these systems

- RV searches should not be limited to only a few of databases, namely DACE and SoS, but should be extended to all data available in telescope archives for which the non-disclosure period has expired. New RV observations should be performed over time with medium to high-resolution spectrographs to increase the number of data-points and the temporal coverage. Still, this may happen incrementally as more analyses are performed on the same targets, effectively accomplishing this side goal as a byproduct.
- Similarly, a deeper search in imaging databases and new direct imaging observations can help to probe effectively for companions: only 20 targets out of the 34 analyzed had direct imaging frames available on ExoFOP.
- *Gaia* DR4 will greatly improve astrometric precision, thus allowing for binaries to be directly provided by the *Gaia* DPAC. Moreover, the availability of the astrometric observations will allow astronomers to fit non-single solutions with a degree of customization that has never been possible before.

Regarding the sample, Rossi et al. (2026) presented a sample of 32 Neptunians with computed true obliquities. In this work, I am adding six more planets, bringing the total to 38. This sample does not include recently published Neptunians for which the Ψ value has not been computed due to the unavailability of the stellar rotation period P_{rot}. Since Ψ is a key parameter compared to λ for

Neptunian planets (Espinoza-Retamal et al. 2024), future work will include enlarging the sample to obtain a broader view of this mass regime and mitigate the limitations of small-number statistics (Siegel, Winn & S. H. Albrecht 2023; Rossi et al. 2026). However, I note that 9 systems out of 38 present a binary companion: this is aligned with the observational findings by Fontanive & Bardalez Gagliuffi (2021) who found that roughly a quarter of planet-hosting stars possess a stellar companion.

5.2.b No correlation between obliquity and binarity

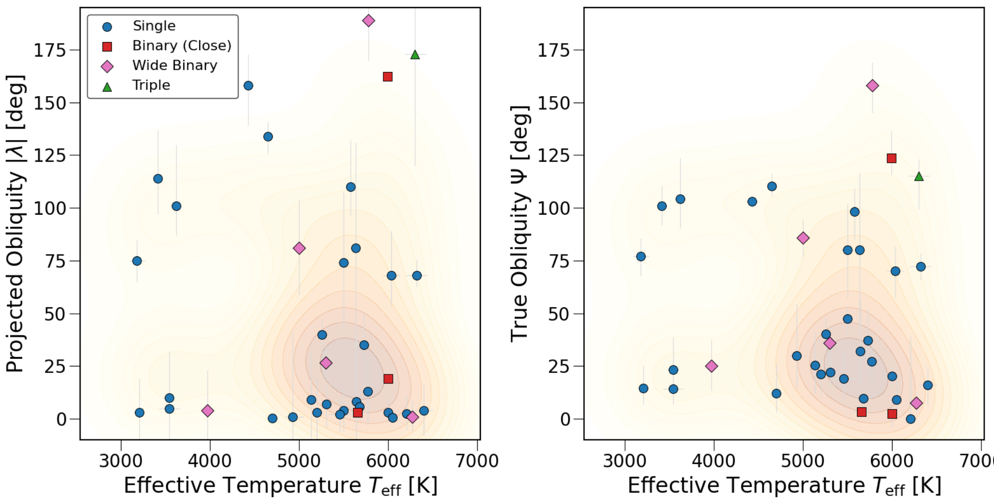

Figure 5.1: Distribution of projected and true obliquities with respect to stellar effective temperature $T_{\rm eff}$. No correlation is present between (mis)alignement and binarity, as proved by the extensive statistical tests. Moreover, a bidimensional KDE shows no peculiar trend in these parameter spaces, besides a clustering of planets around $T_{\rm eff} = 5000 - 6000\,{\rm K}$, most likely arising from an observational bias.

The primary objective of this analysis is to investigate the potential correlation between stellar binarity and planetary obliquity, as the title of this work suggests. No clustering of binary systems is present, with both narrow and wide binaries being scattered across both the $\lambda - T_{\rm eff}$ and the $\Psi - T_{\rm eff}$ parameter spaces fig. 5.1. Following the classification by Desidera & Barbieri (2007), I categorize the nine binaries in my 38 host star sample as either narrow or wide adopting a threshold of $\sim 200 - 300\,{\rm au}$. DS Tuc ($237\,{\rm au}$), TOI-837[5] ($330\,{\rm au}$), and WASP-131 ($36.5\,{\rm au}$) are considered narrow binaries, while, K2-329 ($\sim 8783\,{\rm au}$), Kepler-25 ($\sim 2000\,{\rm au}$), TOI-1710 ($\sim 3610\,{\rm au}$), TOI-1759 A ($\sim 2770\,{\rm au}$), and TOI-2374 ($\sim 3000\,{\rm au}$), are

[5]The difference of $30\,{\rm au}$ still makes this binary target more similar to the narrow population, as the wide is composed of systems with separation above $1000\,{\rm au}$.

considered wide. The edge case of the triple system K2-290, where member B is located at a distance of 109.5 au while member C, the wider, is located at 3030 au is considered narrow because of the dynamical influence of the closer companion. To perform a robust statistical comparison, I grouped the systems into single stars (29), narrow binaries (including the triple system K2-290) (4), and wide binaries (5). Their cumulative distribution functions (CDFs) are compared in Figure 5.2.

Since wide binaries are expected to have a negligible impact on the inner system architecture (e.g., Desidera & Barbieri 2007) I performed a Kolmogorov-Smirnov (KS) (Smirnov 1948; Corder & Foreman 2009) test between the combined population of single stars+wide binaries and narrow binaries (including the triple K2-290). The test returned a p-value of 0.25, which is well above the standard 0.05 significance threshold, thus failing to reject the null hypothesis that these groups are drawn from the same parent distribution. A direct KS test between single stars and wide binaries yielded an even higher p-value of 0.93, further suggesting that these two sub-samples are statistically indistinguishable. Finally, a KS test between singles and non-singles[6] returns a p-value of 0.34, confirming the lack of a clear morphological difference between the distributions. Recognizing that small samples can be prone to statistical flukes, I employed additional non-parametric tests. I performed a Mann-Whitney U (MW) test[7] (H. B. Mann & Whitney 1947) between the distribution of single and non-single stars, in order to maximize the sample size of each group. The resulting p-value of 0.71 does not allow for the rejection of the null hypothesis that the two distributions are drawn from the same population. For further validation, I also implemented a permutation test with 10^5 iterations to test the significance of the difference between the medians. I tested how often I obtained the same difference between the median of two populations, resulting in 27% for single and non singles and 83% for single and narrow binaries. These results consistently demonstrate that no statistical difference exists at the 5% level, and highlight that the inclusion of wide binaries in the non-single sample actually increases the similarity to single stars, reinforcing the idea of their dynamical neutrality. To address the specific question of whether binarity promotes orbital misalignment, I calculated the fraction of planets exceeding the Kozai critical angle of $39.2°$[8] (D.

[6] A combined distribution of narrow binaries, wide binaries, and the triple K2-290.

[7] This non parametric test probes the central tendencies of two distributions, to see if their ranks are randomly mixed or if they show some peculiar clustering (see Appendix of Banerjee et al. 2024, for a deeper description)

[8] I did not explicitly account for the fact the the Kozai effect critically depends on the initial geometry of the system, and also on timescales of single systems. The argument has the only purpose to confirm that the effect is not preponderant in general.

Fabrycky & Tremaine 2007). After 10^5 permutations, I found that: (i) the fraction of misaligned planets in individual systems (0.41) is statistically similar to that in narrow binaries ($0.50, p = 0.76$); (ii) the misalignment ratio in single stars is nearly identical to that of the entire non-single population ($0.44, p = 0.59$).

In conclusion, my analysis indicates that Neptunian planets around single and binary stars are drawn from the same obliquity distribution, regardless of how the binary sample is defined. Nonetheless, this remains a peculiar and intriguing result. While my sample size currently limits the ability to draw definitive conclusions, these findings suggest that stellar binarity may not be the dominant driver for the observed fraction of misaligned Neptunes. Recent results by Y. Liu et al. (2026) have highlighted a broadly applicable mechanism to produce misaligned HJs and Neptunians in the so-called "3+1" systems, in which the star is orbited by a nearby planet, a further perturber (either a cold Jupiter or a BD), and is itself part of a system with a narrow stellar companion. However, its efficiency is highly sensitive to the precise architecture (single or multi-planet systems) and spacing of the components (Y. Liu 2026, private communication). The rarity of known "3+1" systems, with only three confirmed to date despite higher theoretical predictions (Y. Liu et al. 2026, and references therein), underscores the importance of this study in placing observational constraints on such migration pathways.

5.2.c Neptunian alignment in compact systems

Although stellar binarity seems to have little effect on the alignment distribution of Neptunians, it does not imply that the presence of planetary companions has a negligible role. The first statement is supported by the fact that the Kozai mechanism requires an initial misalignment between the planetary and the stellar companion orbits in order to occur. This is not necessarily the case for all planetary systems orbited by an outer companion. Nonetheless, I expanded my analysis to understand whether the presence of other planets in the system may be the driver for a peculiar obliquity distribution. Recently, Radzom et al. (2024) focused specifically on compact Neptunian systems, defined by the authors as being characterized by two consecutive planets with $P_1/P_2 < 4$. Using a sample of 22 projected spin-orbit obliquities λ, the authors noted how compact Neptunian systems tend to be more aligned. The choice of using λ instead of Ψ was due to the limited capability to retrieve Ψ for all the planets, and because recent works had shown that Neptunes orbiting stars cooler than the Kraft break of $T_{\text{eff}} = 6250\,\text{K}$ have just a minor difference between λ and Ψ.

My sample of 38 Neptunians provided Ψ measurements for each target, and it

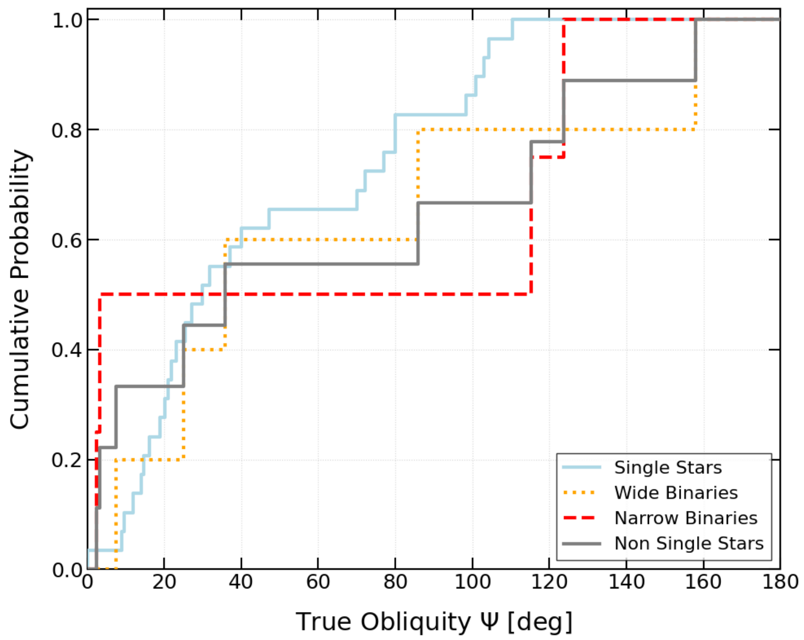

Figure 5.2: CDF of single stars, non single stars, narrow and wide binaries. I define non single stars as the combination of narrow and wide binaries, along with the only triple (K2-290) present in the sample. Statistical tests proved that the populations are statistically indistinguishable, supporting the idea that they are drawn from the same parent distribution, although low statistics can mask the real impact of binarity.

is not strictly confined before the Kraft break[9]. Specifically, using the information available in chapter A I divided the systems into single planets, compact systems if $P_1/P_2 < 4$, and multi-planet system if $P_1/P_2 > 4$. If a planet presents both compact and non-compact companions, it is regarded as compact. To get a comprehensive view, I performed the same analysis detailed in the previous subsection for both λ and Ψ values.

An increase of 73% of the sample size with respect to Radzom et al. (2024) reveals a coherent — and expected — picture for both projected and true obliquities, with only minor differences. Neither of the two quantities correlates with $T_{\rm eff}$ according to a Pearson test, with p-values exceeding 0.5 and thus deemed unable to probe for any correlation. A KS test strongly underscores the results of Radzom et al. (2024) on λ: the population of compact and single planets is statistically different at the 1% level, with compact planets being systematically more aligned, as also shown in Figure 5.3. This is graphically evident also from fig. 5.4. Nonetheless, the p-value rises to 0.10 when the Ψ sample is analyzed.

[9]It is the case for a couple of systems: nonetheless it would not be corrected to make this assumption.

The difference is not dramatic but present. A permutation test with the limit placed on the Kozai threshold reveals similar results: λ values have a probability lower than 0.001 to be aligned by chance, while the value rises to 0.12 when dealing with Ψ. The low sample size can surely play a role, especially when considering that a projected obliquity close to 0° does not necessarily imply such a value of Ψ. Specifically, the larger scatter in the Ψ values may be indicative of some deviations from alignment that, although minimal, are not directly captured by projected obliquities alone. A larger sample may be able to robustly extend Radzom et al. (2024) results also in terms of Ψ distribution.

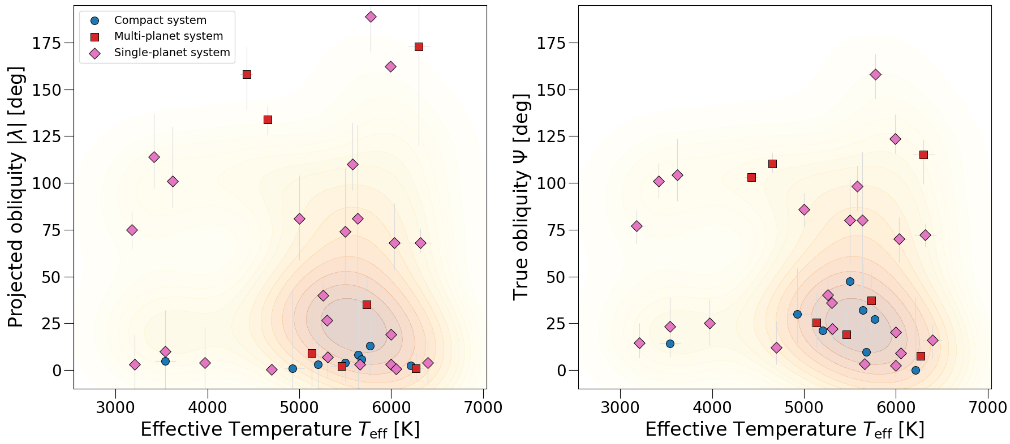

Figure 5.3: Distribution of projected and true obliquities with respect to stellar effective temperature $T_{\rm eff}$, according to system multiplicity. A KS test conducted between compact and single planetary systems confirms that the two are drawn from different populations in the case of λ. In the case of Ψ, the p-value rises to 0.1, likely due to the still limited sample size.

5.2.d A dichotomous Neptunian population?

A secondary goal of this work was to analyze the evolution of the Neptunian population, in order to infer its underlying distribution, although the current sample size is still limited (Rossi et al. 2026, hereafter R26). Indeed, the specific analysis performed in this work yielded the largest collection of Neptunian true obliquities to date as a byproduct, although it may not be complete due to the rapidly evolving observational panorama. I followed the steps of R26 and performed a Hartigan's dip-test[10] (P. M. Hartigan 1985; J. A. Hartigan & P. M. Hartigan 1985) to test for the unimodality of the Neptunian obliquity distribution. The resulting p-values, which are an order of magnitude larger

[10] https://pypi.org/project/diptest/

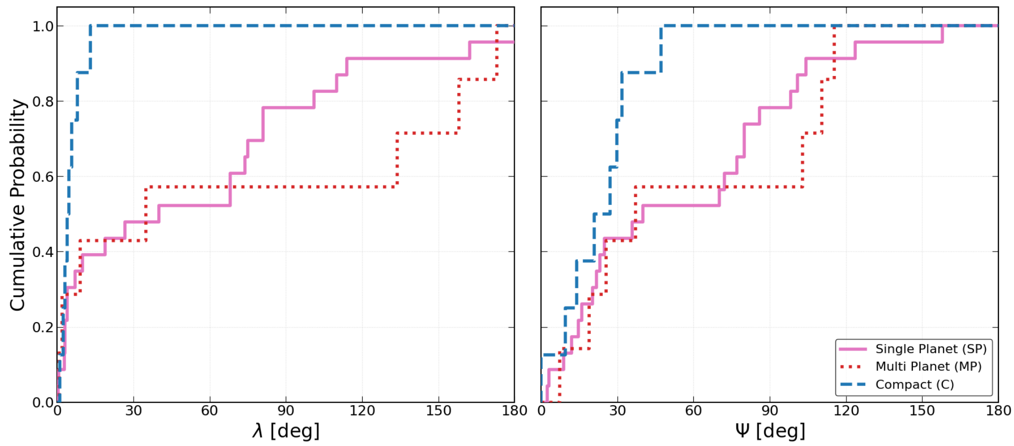

Figure 5.4: CDF of single planet, compact, and multi-planet systems of Figure 5.3.

than the usual threshold of 0.05, suggest that both R26 and my sample (+20% in size) cannot reject the null hypothesis of the distribution being unimodal. As highlighted by R26, this does not constitute definitive proof that Neptunians are unimodal.

I started from the R26 analysis of Neptunian exoplanets to assess whether a deeper statistical analysis with a 20% larger sample (from 32 to 38 planets with measured Ψ) could shed light on the distribution. In order for this to be statistically and methodologically robust, I also reanalyzed the R26 dataset to perform a comparative study. Considering recent literature results, which suggest either a unimodal or bimodal distribution, I employed six distributions[11] that could reasonably fit the data best. Specifically, as unimodal distributions, I picked a Gaussian (hereafter GMM1) and a beta (BETA); as a strongly bimodal distribution, a mixture of two Gaussians with different weights (GMM2) and a mixture of two betas (BETA2). I also chose two distributions that could best fit the current obliquity distribution of exoplanets as a whole, in order to apply them also on the subsample of Neptunes: a mixture of a Gaussian and an isotropic tail, defined as having a uniform distribution in $\sin\Psi$[12] (ISO), and a half-normal centered on $0°$ followed by the above isotropic distribution (ISO_HN). All the parameters describing the distributions were left free across their domains, with minor limitations placed only to avoid numerical instability, as detailed in

[11]The analysis of competing models requires the number of competitors to be reasonably lower than the sample size (Burnham & Anderson 2003). Six models are not a problem for the following inference.

[12]It was constructed according to prescription from Masuda & Winn (2020), Morgan et al. (2024), and Rossi et al. (2026), requiring the distribution to be uniform in $\sin\Psi$, hence isotropic in Ψ.

Table 5.6.

Table 5.6: Configuration of the parameters space for the analyzed models. No hard constraint has been placed on any parameter. k represents the number of parameters associated with the specific model.

Model	Parameter	Search Range	Physical Meaning
GMM1	μ	$[0, 180]$	Mean obliquity (deg)
$(k = 2)$	σ	$[2.0, 100]$	Distribution width (deg)
GMM2	w_1	$[0, 1]$	Relative weight of component 1
$(k = 5)$	$\mu_{1,2}$	$[0, 180]$	Centers of the two populations
	$\sigma_{1,2}$	$[2.0, 60]$	Width of the two populations
ISO	w_{align}	$[0, 1]$	Fraction of aligned planets
$(k = 3)$	μ_{peak}	$[0, 180]$	Peak of the aligned component
	σ_{peak}	$[2.0, 60]$	Width of the aligned component
ISO_HN	w_{align}	$[0, 1]$	Fraction of aligned planets
$(k = 2)$	σ_{hn}	$[2.0, 60]$	Width of the Half-Normal (fixed $\Psi = 0°$)
BETA	α, β	$[0.1, 40]$	Shape parameters (on $x/180$ domain)
$(k = 2)$			
BETA2	w_1	$[0, 1]$	Relative weight of first Beta
$(k = 5)$	$a_{1,2}, b_{1,2}$	$[0.1, 50]$	Shape parameters for both components

I then fitted these distributions to the R26 and my datasets, obtaining the results detailed in Table 5.7. It is possible to note that R26 correctly identified GMM2 as the best fitting model to describe a tentative Neptunian dichotomy. Specifically, GMM2 and BETA2 are equally valid, considering that their differences in AIC and BIC are lower than 2 (Burnham & Anderson 2003; Lubke et al. 2016). Differences greater than 2 provide evidence that a model is disfavored compared to the one with the lower information criterion (IC) value[13]. GMM1 is clearly disfavored by both ICs, however the simplicity of ISO and ISO_HN are favored by BIC, but penalized by AIC due to a poorer fit. A similar fate is followed by the single BETA.

Looking at my current dataset, the picture changes: in terms of AIC, GMM2, ISO, ISO_HN, and BETA are equally favored, with BETA2 being no longer able to fit the data properly, although it was introduced in this comparison as an

[13] Burnham & Anderson (2003) and Lubke et al. (2016) provide an in-depth view over the threshold that define how much a model is disfavored over the winning one. Regarding AIC, a model is considered disfavored if the difference is in the range $2 - 4$, considerably disfavored for $4 - 7$, and extremely disfavored beyond 7. Regarding BIC, the thresholds are slightly different: $2 - 6$ is disfavored, $6 - 10$ considerably disfavored, and extremely disfavored beyond 10. Both teams warn against blindly trusting these estimators, especially when working with small samples due to how the criteria are defined. Assuming k the number of model parameters, AIC penalizes model complexity as $2k$, whereas BIC as $k \ln n$ with n the sample size. Hence, AIC favors the best-fitting model, while BIC tends to avoid overfitting using an unnecessarily complex model.

extremely flexible distribution that could model bimodality. BIC still rewards simpler models by far, with ISO, ISO_HN, and BETA being the clear winners. However, two problems arise now: (i) BIC penalizes model parameters heavily, while AIC is more permissive and unable to differentiate between competing models, (ii) these fits are limited to the obliquities available in the actual sample, and do not account for their individual uncertainties, thus losing both descriptive and predictive power.

Table 5.7: Comparison of information criteria between Rossi et al. (2026) and this work samples. Bold values indicate the preferred model in each sample.

Model	Rossi+26 ($N = 32$)		Current Sample ($N = 38$)	
	AIC	BIC	AIC	BIC
GMM1	313.37	316.30	375.14	378.42
GMM2	**304.48**	**311.81**	371.43	379.61
ISO	308.01	312.40	370.60	375.51
ISO_HN	310.84	313.77	**370.30**	**373.58**
BETA	311.77	314.71	370.79	374.07
BETA2	304.65	311.98	374.30	382.49

To overcome these limitations, I performed a bootstrap of the two datasets, utilizing a splitnormal distribution to model the asymmetric uncertainties[14]. Data were bootstrapped 10^4 times, enough to reduce the error to 1% following the prescription of Shimodaira (2002) and Burnham & Anderson (2003), and then two estimation methods were used:

(A) *Bootstrap-smoothed Akaike weights*. Following Burnham & Anderson (2003), the winning model was chosen for each iteration, and the Akaike weights were computed for each estimator, to assess the strength of preference with respect to the other models for that specific IC. In the end, the mean of the weights was computed. Results for this method (A) are provided in Table 5.8.

(B) *Bootstrap-smoothed Information Criteria*. For each iteration, I computed AIC and BIC for each model. The median of the ICs was then used as a global estimator for the quality of the model throughout the bootstrapping procedure. Median and mean values resulted extremely similar both in absolute and relative terms (relatively to other models), so the median was preferred to avoid the influence of outlying draws during the bootstrapping (Efron 2014; Lubke et al. 2016). Results for this method (B) are provided in Table 5.9.

[14] A skewnormal distribution would have resulted in a distribution resembling the single datapoint, but with a peak shifted with respect to the central value.

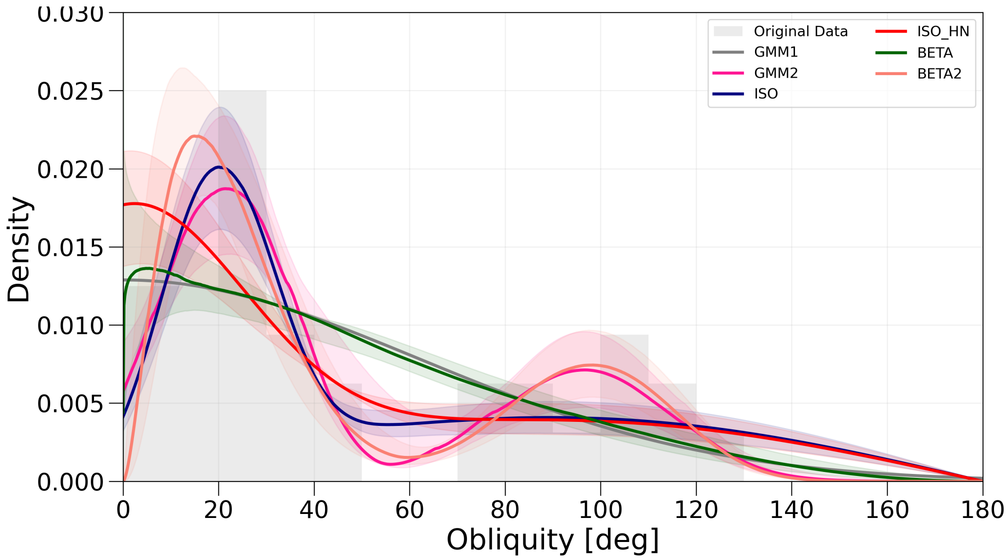

Figure 5.5: Probability density fits for the R26 dataset. The gray histogram is representative of the original obliquity distribution and its included only for visualization purposes. Solid lines show the best-fit models, with shaded regions indicating the 1σ uncertainty intervals derived from the bootstrapping procedure. At this sample size, a dichotomous trend is visible, with GMM2 (magenta) and BETA2 (coral) capturing the two peaks at $\sim 20^\circ$ and $\sim 100^\circ$, as highlighted by Rossi et al. (2026). However, smoother models like BETA (dark green) and ISO_HN (red) already show competitive fits, suggesting that the apparent bimodality might be sensitive to small sample fluctuations.

Bootstrapping is a necessary and critical step to test the limited data at my disposal under stress (e.g., Burnham & Anderson 2003; Lubke et al. 2016), by smoothing the peculiarities that may be inherent in my data. Results of bootstrapping are provided in the aforementioned Tables 5.7 to 5.9, parameters of the distribution can be found in Table 5.10, and their plots in Figures 5.5 and 5.6. Looking at the results for method A for R26, it is evident that GMM2 cannot sustain a stress test, and the data are not robust enough to fit a pronounced dichotomous trend when perturbed. Indeed, smoother distributions win both in terms of winning percentages and weights W_{AIC} and W_{BIC}. There is no possibility to define a winning model at the level of 10% or lower for R26[15], underscoring that R26 data was indeed suggesting a bimodal trend. Conversely, the results of method A on the dataset of this work provide a clearer picture: winning models are the same but with an even stronger preference. I personally

[15]When evaluating competing models, it is statistically sound to aggregate winning frequencies (or weights) for models that share similar physical interpretations (Shimodaira 2002; Burnham & Anderson 2003). In this context, GMM2 and BETA2 represent a strongly dichotomous distribution with a combined winning rate of 31.1%, whereas single-peaked models (ISO, ISO_HN, and BETA) achieve a combined rate of 68.7%. A similar picture can be seen when summing weights.

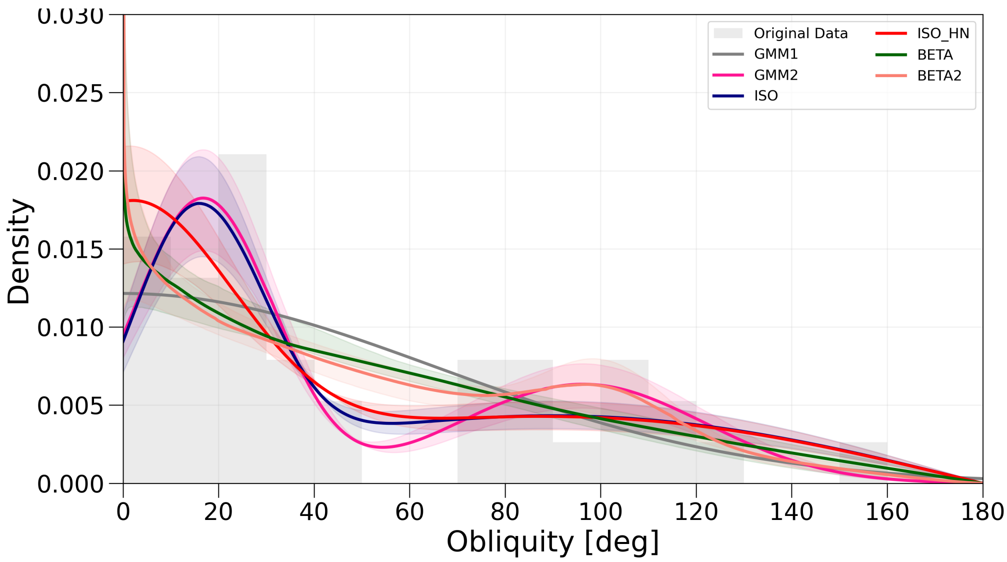

Figure 5.6: Probability density fits for the total updated dataset. As the sample size increases (+20%), the secondary peak at high obliquities becomes less pronounced and more dispersed. The ISO (blue), ISO_HN (red) and BETA (dark green) models now provide the most robust description of the data, as confirmed by the information criteria in Tables 5.8 and 5.9. The complex GMM2 model (magenta) still attempts to fit a bimodal structure, but it is statistically penalized, indicating that a smoother and unimodal distribution with a tail of misalignments is a more probable representation of the Neptunian population.

suggest refraining from using BIC as the sole estimator, although it may seem more definitive, because of the penalty it assigns to more complex models, and to also take into account AIC. Whichever estimator is used, the combined winning rates (or weights) clearly side with a single-peaked model at almost 90% (recall that the only two bimodal distributions are GMM2 and BETA2, which actually could be unimodal depending on the chosen parameters). The isotropicity of these misalignments needs to be better understood with future observations that will place better constraints on the overall distribution. Nonetheless, the idea of a dichotomous distribution for Neptunians is increasingly disfavored.

Looking at the results of method B presented in Table 5.9, we see little difference from before, and the same arguments apply: we cannot unequivocally state the distribution followed by Neptunian planets, but it is hard to believe it is dichotomous, especially looking at AIC. The R26 dataset could either be GMM2, ISO_HN, or BETA, but the addition of six more planets moves the expectations in favor of a single peak. The aforementioned criteria are not fulfilled by the current AIC and BIC values, except for ISO_HN and BETA. The physical interpretation that can be provided is that Neptunians in the current sample exhibit

Table 5.8: Results of the bootstrap-smoothed model selection (Method A) for the R26 and updated datasets. The values are derived from 10^4 bootstrap iterations. WIN_{IC} represents the selection probability (i.e., the frequency with which a model is identified as the best fit for a given IC), while W_{IC} denotes the mean IC weight across all iterations, representing the average relative support for each model. Bold values indicate the most supported models for each dataset.

Model	**Rossi+26 ($N = 32$)**				**Total Updated ($N = 38$)**			
	Selection Prob.		Avg Weight		Selection Prob.		Avg Weight	
	Win_{AIC} (%)	Win_{BIC} (%)	W_{AIC} (%)	W_{BIC} (%)	Win_{AIC} (%)	Win_{BIC} (%)	W_{AIC} (%)	W_{BIC} (%)
GMM1	0.2	0.3	9.1	11.7	6.5	7.4	11.3	13.5
GMM2	12.9	3.8	14.7	5.6	6.0	0.4	7.9	1.6
ISO	9.7	8.4	12.3	11.3	15.5	5.8	18.7	12.7
ISO_HN	26.0	38.6	22.7	31.7	**37.5**	**52.0**	**30.2**	**39.6**
BETA	**33.0**	**41.9**	**25.0**	**32.4**	29.2	32.5	25.2	30.5
BETA2	18.2	7.0	16.2	7.3	5.3	2.0	6.8	2.2

Table 5.9: Results of Method B showing the median information criteria (AIC and BIC) over 10^4 bootstrap iterations. Values represent the median of the IC distribution for each model across all resamples; lower values indicate better model performance and stability. Bold values highlight the best-performing model (minimum IC) for each dataset.

Model	**Rossi+26 ($N = 32$)**		**Total Updated ($N = 38$)**	
	AIC Median	**BIC Median**	**AIC Median**	**BIC Median**
GMM1	314.81	317.74	376.60	379.87
GMM2	314.31	321.64	378.78	386.97
ISO	315.10	319.50	375.94	380.85
ISO_HN	313.45	316.38	**374.64**	**377.91**
BETA	**313.06**	**315.99**	375.39	378.66
BETA2	316.12	323.45	379.56	387.74

a clear preference for aligned orbits, potentially followed by either a smooth beta distribution, (effectively a misalignment tail), or an isotropic distribution of misalignments similarly to HJs and to the global exoplanetary population (Dong & Foreman-Mackey 2023; Espinoza-Retamal et al. 2024; Rossi et al. 2026).

A possible counterargument One could reasonably argue that the observed shift in model preference is primarily driven by the inclusion of TOI-1710 A, whose high obliquity ($\Psi \approx 160°$, see Table 5.5) represents a significant departure from the rest of the sample. To address whether this single target acts as a dominant outlier that artificially biases the global fit, two points must be considered. First, the high obliquity of TOI-1710 A is not a result of an incorrect inference; an independent analysis by Mantovan et al. (2026a) yielded a compatible result, confirming that the planet truly resides on a highly misaligned orbit. Second, I performed a sensitivity check by repeating the entire bootstrapping analysis excluding TOI-1710 A.

The results still disfavor the GMM2 model, although with lower statistical significance (full tables are provided in Chapter C). Specifically, regarding the Method B (bootstrap-smoothed IC), all the models are statistically indistinguishable as $\Delta\mathrm{AIC} < 2$, with the preferred model being BETA. The $\Delta\mathrm{BIC}$ favors BETA once again, while BETA2 and GMM1 exhibit $\Delta\mathrm{BIC} > 2$, indicating they are significantly disfavored. However, looking at winning rates and Akaike weights (Method A) provides further insight: the combined winning rate for single-peaked models is 71% based on AIC, lower than the $\sim 90\%$ obtained with the full sample, but still substantial. Regarding BIC combined victory rates, the percentage rises to 94.1%, lower than before but still well above the 90% threshold. Furthermore, for Method A, the combined weights of single-peaked models are 70.6% for AIC and 91.3% for BIC, lower than before (in line with median AIC and BIC values), but still suggesting a non-dichotomous distribution. Moreover, this thesis does not include several planets recently validated and for which only λ measurements are available. Their addition, along with a larger number of true obliquity measurements over time, will surely help to further characterize the Neptunian population as a whole, as small sample statistics remain the critical point to be addressed.

Nonetheless recent literature proposes various mechanisms to produce misaligned Neptunes, including but not limited to the disk acting as an external perturber for a Kozai mechanism happening during formation (Handley & Batygin 2026), disk-driven resonances in the presence of outer cold Jupiter companions (Petrovich et al. 2020; Louden & Millholland 2024), "3+1" systems (Y. Liu et al. 2026), torques induced by binary companions (Batygin 2012), and planets forming in misaligned disks (Biddle et al. 2025). However, additional observational trends are emerging, such as the tendency for compact Neptunes to be more aligned, and less responsive to tides (see Rossi et al. 2026, and references therein). The picture of Neptunian exoplanets will surely be one of the key studied aspects of exoplanetary architectures, and more statistics is surely needed to fully understand their obliquity distribution.

Table 5.10: Comparison of the estimated best-fit parameters for the R26 and this work datasets. For each model, I report the "master" fit value (obtained from the original data) and the bootstrap results, represented by the median of the distribution and the corresponding standard deviation σ across 10^4 iterations. This comparison illustrates the stability of the parameter estimates and their sensitivity to sample perturbations.

Model	**Param.**	**Rossi+26 ($N = 32$)**		**Total Updated ($N = 38$)**	
		Master	**Bootstrap**	**Master**	**Bootstrap**
GMM1	μ	0.00	0.00 ± 1.37	0.00	0.00 ± 0.94
	σ	62.14	62.16 ± 1.35	66.08	66.10 ± 1.31
GMM2	w_1	0.65	0.67 ± 0.10	0.62	0.59 ± 0.09
	μ_1	21.33	21.36 ± 3.52	16.69	16.71 ± 1.88
	σ_1	12.49	12.78 ± 4.86	14.45	14.48 ± 3.03
	μ_2	96.42	96.42 ± 2.76	96.39	96.38 ± 1.35
	σ_2	16.93	17.06 ± 3.85	25.38	25.40 ± 2.93
ISO	w_{align}	0.57	0.53 ± 0.12	0.55	0.50 ± 0.10
	μ_{peak}	20.05	20.04 ± 3.05	15.29	15.29 ± 1.30
	σ_{peak}	11.31	11.38 ± 3.83	13.74	13.76 ± 2.19
ISO_HN	w_{align}	0.57	0.55 ± 0.11	0.55	0.51 ± 0.10
	σ_{hn}	24.92	24.93 ± 1.75	22.53	22.54 ± 2.31
BETA	α	1.14	1.08 ± 0.19	0.72	0.91 ± 0.16
	β	3.08	3.05 ± 0.59	1.95	1.97 ± 0.59
BETA2	w_1	0.66	0.67 ± 0.09	0.86	0.90 ± 0.08
	a_1	2.76	2.69 ± 0.56	0.68	0.87 ± 0.26
	b_1	18.98	18.92 ± 1.28	2.25	2.26 ± 2.07
	a_2	15.38	15.40 ± 0.82	23.95	23.95 ± 0.22
	b_2	13.22	13.16 ± 1.08	19.11	19.11 ± 0.27

Conclusions

In this work, I have conducted the most systematic search to date for stellar companions around Neptunian host stars, thoroughly analyzing the sample of 32 Neptunian exoplanets from Rossi et al. (2026) (and two additional recently published targets) through a rigorous multi-technique approach. The primary objective was to disentangle the relative roles of internal system dynamics and external stellar perturbations in shaping the true obliquity Ψ of Neptunian exoplanets. The innovative core of this thesis involved the creation of an original PMa pipeline following state-of-the-art prescriptions (Kervella et al. 2019; Brandt 2021; Kervella, Arenou & Thévenin 2022). By cross-calibrating Tycho-2, the historical $Hipparcos$ satellite star mapper, with $Gaia$ DR3, I exploited a 24.5 year temporal lever arm, a baseline that is currently not systematically utilized for exoplanetary hosts outside the $Hipparcos$ main catalog of $100,000$ stars (ESA 1997; M. A. C. Perryman et al. 1997). While acknowledging the inherent precision limits of Tycho-2, whose uncertainties are an order of magnitude larger than those of $Hipparcos$, this approach potentially allows for the investigation of a much larger stellar population of 2.5 million stars. Benchmarking the pipeline on a known sample from Kervella, Arenou & Thévenin (2022) demonstrated that it produced no false positives (unitary precision), confirming that the pipeline is a reliable tool for confirming physical associations, although the recovery rate of known binaries (recall) is naturally constrained by the noise floor of the historical data. To complement the astrometric search and ensure the completeness of the binarity vetting, I performed a high-resolution imaging survey using archival speckle and AO high-resolution imaging observations available on ExoFOP in order to constrain the presence of binaries at smaller separations. The analysis was conducted using both theoretical models (Baraffe et al. 2015) and observational tracks (Pecaut & Mamajek 2013) to account for stellar ages, which are almost always available in the Rossi et al. (2026) catalog. I also employed the DACE database to retrieve and analyze RV observations, searching for linear RV drifts that could suggest the presence of undetected stellar companions. Furthermore, I cross-checked the targets with all the available literature that has previously studied these planets, as well as checking a total of 11 binarity catalogs, to obtain a comprehensive view of the sample. In the final stages of this work, I added four more targets to the Neptunian sample and performed several statistical analyses on the whole sample, finally enlarged by 20%. This combined approach revealed no new stellar companions in the sample of 38 targets, 9 of which already possessed a binary companion, in agreement with previous statistical studies on the occurrence of planets in binary systems (e.g., Desidera & Barbieri 2007; Fontanive & Bardalez Gagliuffi 2021).

The scientific outcomes of this study provide important constraints on Neptunian architectures:

1. The neutral role of binarity. The multi-technique approach confirmed that the sample of 38 targets includes 9 binaries, with no new detections. Crucially, several statistical and permutation tests reveal no significant correlation between the presence of a stellar companion (either narrow or wide) and the obliquity distribution. This finding challenges the common assumption that external stellar perturbers, such as those driving Kozai cycles, are the primary architects of Neptunian misalignments. Instead, it suggests that the dynamical history of these systems is predominantly dictated by internal mechanisms, such as disk-planet interactions or planet-planet scattering, along with other mechanisms that recent literature has proposed and that are detailed in the previous section.

2. Compact Neptunian systems are statistically more aligned. This is especially true for projected obliquities λ, as a KS test strongly confirms that single and compact Neptunian systems are different below the 0.1% level, in alignment with recent results (Radzom et al. 2024). Tentatively different results are found in terms of Ψ, although the limited sample size may be preventing statistical tests from detecting a difference below the 5% level.

3. A tentative paradigm shift in Neptunian obliquity distribution. I analyzed the true obliquity distribution of the 38 planet sample, the largest to date for low-mass exoplanet populations. My analysis reveals that the previously claimed Neptunian dichotomy (e.g., Espinoza-Retamal et al. 2024; Rossi et al. 2026), the sharp division between aligned and perpendicular orbits, is effectively starting to collapse. A bootstrap smoothed model selection through AIC and BIC, and the use of model winning rates and Akaike weights, suggest a transition toward a unimodal distribution, characterized by a strong alignment peak and a tail of misalignments. The shape of this tail is yet to be analyzed with a larger sample. This result is highly robust: sensitivity checks excluding the extremely misaligned target (TOI-1710 A, $\Psi \sim 160°$) did not fundamentally alter the outcome, proving that the shift

away from a dichotomous model is a collective property of the expanding Neptunian sample.

Future prospects

Several possibilities open in light of these results, both directly related and complementary to the specific goal of this work. It is clear that although broadly used and comprehensive, the search on ExoFOP and DACE is rather limited, and a larger and more encompassing search should be performed using raw direct imaging and RV data to shed further light, along with new observations. This could also be aided by *Gaia* imaging detection limits, useful to bridge the inherent gap between AO and speckle observations, and specifically their different sensitivities to separation (Brandeker & Cataldi 2019). Nonetheless, I do not expect a dramatic change in results, with just minor additions to the binary group at best. Similarly, an inference of true obliquities as detailed in Rossi et al. (2026) may provide a more homogeneous sample, with little changes expected in the overall distribution. A medium term goal is surely the extension of this promising framework to the whole Tycho-2 catalog, which although limited in terms of completeness, can provide value even beyond the area of planetary science. On this topic, a thorough analysis of the reliability of the catalog at fainter magnitudes is surely necessary.

The long term goal of increasing the number of true obliquities also depends on the capability to infer them from projected obliquities. Rossi et al. (2026), among others, highlighted how the stellar rotation period $P_{\rm rot}$ was the main limiting factor. Recent literature results are helping to solve this challenge by providing this parameter for TESS stars (Boyle, Bouma & A. W. Mann 2026). In a similar manner, the upcoming PLATO mission, expected to launch in the first quarter of 2027, will provide thousands of new targets that upon analysis will help depict the clearest picture we have ever achieved, conspicuously populating the low-mass planet realm. Furthermore, a major objective is to connect these findings with the primordial stages of planetary systems: combining ALMA observations of protoplanetary disks with spin-orbit obliquity data will help determine whether misalignments are primordial or the result of subsequent dynamical scattering.

Last but not least, we are expected to witness a new flourishing of astrometry thanks to *Gaia* DR4, forthcoming in December 2026. Its unprecedentedly precise data will finally bring us hundreds of astrometrically detected planets. Nonetheless, Tycho-2 can experience a renaissance if a systematic PMa analysis is conducted on its targets, spanning even beyond the exoplanetary science realm. Indeed, this framework represents a valuable asset for the study of binarity as a whole.

A Discussion of individual targets

In this section, I detail the background of the planetary systems included in the Rossi et al. (2026) catalog (with the addition of TOI-1135 b and TOI-2374 b), and I will provide numerical and technical details of the analysis I conducted on each target. Summary tables providing an overview are presented in Chapter 5. To enhance readability, catalogs described in Chapter 3 are referred to using the acronyms listed in Table A.1. Since several of these catalogs were constructed using *Hipparcos*, each target description provides its HIP identifier, if available, as well as its Tycho[1] (TYC) and Gaia DR3 identifiers.

Table A.1: Main astronomical catalogs and their acronyms used in this chapter.

Catalog description	Acronym	Reference
Gaia DR2-*Hipparcos* PMa	K19	Kervella et al. (2019)
Gaia EDR3-*Hipparcos* PMa	K22	Kervella, Arenou & Thévenin (2022)
Tycho Double Star Catalog	TDSC	Fabricius et al. (2002)
Hipparcos new data reduction	Hip2	van Leeuwen (2007b)
Gaia non single stars	NSS	Gaia Collaboration et al. (2023a)
Astrometric accelerations and jerks	MK05	Makarov & Kaplan (2005)
Visual binaries	M06	Malkov et al. (2006)
Hipparcos-*Gaia* Catalog of Accelerations	HGCA	Brandt (2021)
Washington Double Star Catalog	WDS	Mason et al. (2001)
A million *Gaia* binaries	EB21	El-Badry, Rix & Heintz (2021)

To maintain conciseness, not all target discussions include a plot or explicit mentions of every binary catalog listed in Table A.1. However, the analysis was conducted consistently for all targets.

[1]Since Tycho was derived from the star mapper of the *Hipparcos* mission, an absence from Tycho implies an absence from both *Hipparcos* data reductions.

A.1 AU Mic b

Background AU Mic b (Plavchan et al. 2020) is a Neptunian planet with a radius of $R = 4.20 \pm 0.20\,R_\oplus$ (Plavchan et al. 2020) and a mass of $M = 10.2^{+3.9}_{-2.7}\,M_\oplus$. The system also hosts a second Neptunian planet c (Martioli et al. 2021), and a recently confirmed third external member e (Donati et al. 2025). An additional non-transiting companion d has been proposed as a plausible explanation for the observed TTVs (Wittrock et al. 2022; Donati et al. 2025). The system also hosts a bright debris disk with edge-on inclination (e.g., Boccaletti et al. 2018; Addison et al. 2021). It has a projected obliquity of $\lambda = -4.7^{+6.8\circ}_{-6.4}$ (Hirano et al. 2020) and a true obliquity of $\Psi = 14.11^{+10.13\circ}_{-7.3}$ (Rossi et al. 2026). No stellar companions have been found to date, and the target has a low $\mathrm{RUWE} = 0.927$, consistent with a single star scenario.

Update AU Mic (Gaia DR3 6794047652729201024, TYC 7457-641-1, HIP 102409) does not show signs of binarity from my PMa analysis, with a significance of $\Delta_{\mathrm{G3}} = 1.13$. K19 and K22 detected no binarity at either the *Hipparcos* epoch or the Gaia DR2/DR3 epochs. While TDSC suggests the system is a triple, the companion at very wide separation listed in WDS (the close binary AT Mic) is most likely a comoving object part of the young beta Pic moving group, to which these stars belong, rather than a physically bound companion. However, Hip2 indicates this system as a single star, and NSS shows no entry for this target, similarly to MK05, M06, and EB21. HGCA infers no significant acceleration for this target. I analyzed the speckle imaging data collected on 18 May 2022 using the Zorro instrument mounted on Gemini-South in the $832\,\mathrm{nm}$ filter. Using the BHAC15 model at the age most consistent with the system's uncertainties of $0.020 \pm 0.003\,\mathrm{Gyr}$ and Gaia G_{RP} as the magnitude proxy filter, no companion was detected in my frame. Nonetheless, an observation dating to 3 December 2020 with HRCam@SOAR in a slightly redder filter ($879\,\mathrm{nm}$) finds a potential stellar companion in ExoFOP. AU Mic exhibits a high PM according to *Gaia* DR3 of $457\,\mathrm{mas/yr}$, meaning that it would have displaced by $\sim 700\,\mathrm{mas}$ between the two observations. The reported separation is $1.75''$, and the SOAR observation has a PSF three times larger than Zorro. The combined evidence is insufficient to robustly classify AU Mic as a bound binary, as the reported stellar companion is likely a background contaminant. Indeed, *Gaia* DR3 reports 18 targets within $1'$ of AU Mic, with a minimum parallax of $1.97\,\mathrm{mas}$ (compared to AU Mic's $102.9\,\mathrm{mas}$), suggesting that multiple background objects could have crossed the path of the target. DACE includes 478 quality checked RV datapoints, mostly collected by HARPS and ESPRESSO, with a temporal coverage spanning

$3000 - 10000\,\mathrm{BJD}_{2450000}$. I removed one blatant outlier collected by ESPRESSO, located more than a $\mathrm{km\,s^{-1}}$ below the average RV level. I then attempted to model the series by adopting the planetary parameters from Mallorquín et al. (2024a) and Wittrock et al. (2022) in two separate rounds of fitting. In both cases, the algorithm failed to converge. This is likely due to the combination of the planets low and debated semiamplitudes K[2], and the activity of this young M-dwarf which introduces a significant jitter. As a last resort, I tried fitting a linear trend on the raw RV data, which resulted in an extremely high $\chi^2_r > 4000$ and a formal linear drift of $-6.49 \pm 0.07\,\mathrm{m\,s^{-1}}$. These two facts combined suggest that the signal is dominated by unmodeled high frequency variations (induced by both planets and activity), masking any potential long-term trend, and making this inference unreliable, although the formal significance is above 3σ. The high PM, together with the unavailability of precise dates for the observations that compose the WDS, suggests that several other unbound contaminants may have crossed the field of view and been misidentified as companions. It is equivalently possible for the aforementioned possible companion to be a physically unbound, but comoving, companion.

A.2 DS Tuc A b

Background DS Tuc A b (Benatti et al. 2019; Newton et al. 2019) is a Neptunian planet with a radius of $R = 0.50 \pm 0.02\,\mathrm{R_\oplus}$ and a mass upper limit of $M < 14.4\,\mathrm{M_\oplus}$ (Benatti et al. 2021). The system is composed of a G6 star, hosting planet b, and an outer K3 stellar companion DS Tuc B (Benatti et al. 2019). A third stellar M5 member has been noted to be loosely bound (Newton et al. 2019; González-Payo et al. 2024). The planet is on a well-aligned orbit, with $\lambda = 2.9^\circ \pm 0.9^\circ$ (Zhou et al. 2020a) and $\Psi = 3.23^\circ \pm 0.83^\circ$ (Rossi et al. 2026). The presence of stellar companions does not perturb the RUWE indicator, being $\mathrm{RUWE} = 0.913$.

Update DS Tuc A (Gaia DR3 6387058411482257536, TYC 9339-551-1, HIP 116748) shows no sign of binarity from my PMa analysis, with $\Delta_{G3} = 0.533$. K19 confirms this finding, while K22 identifies binarity at the $Gaia$ DR3 epoch ($\Delta_{G3} = 4.65$). Both K22 and WDS find HD222259B (Gaia DR3 6387058411482257280) as the companion, a coeval K3V star aligned with the findings by Newton et al. (2019) and Benatti et al. (2021), and consistent with EB21. Binarity signs are confirmed by Tycho-2, TDSC and Hip2 (which solve the target as a double star system). HGCA also shows a significant

[2]Specifically, the best fit solution from Wittrock et al. (2022) finds all the three members with $K < 1\,\mathrm{m\,s^{-1}}$, while Mallorquín et al. (2024a) has the planet b with $K = 4.7\,\mathrm{m\,s^{-1}}$.

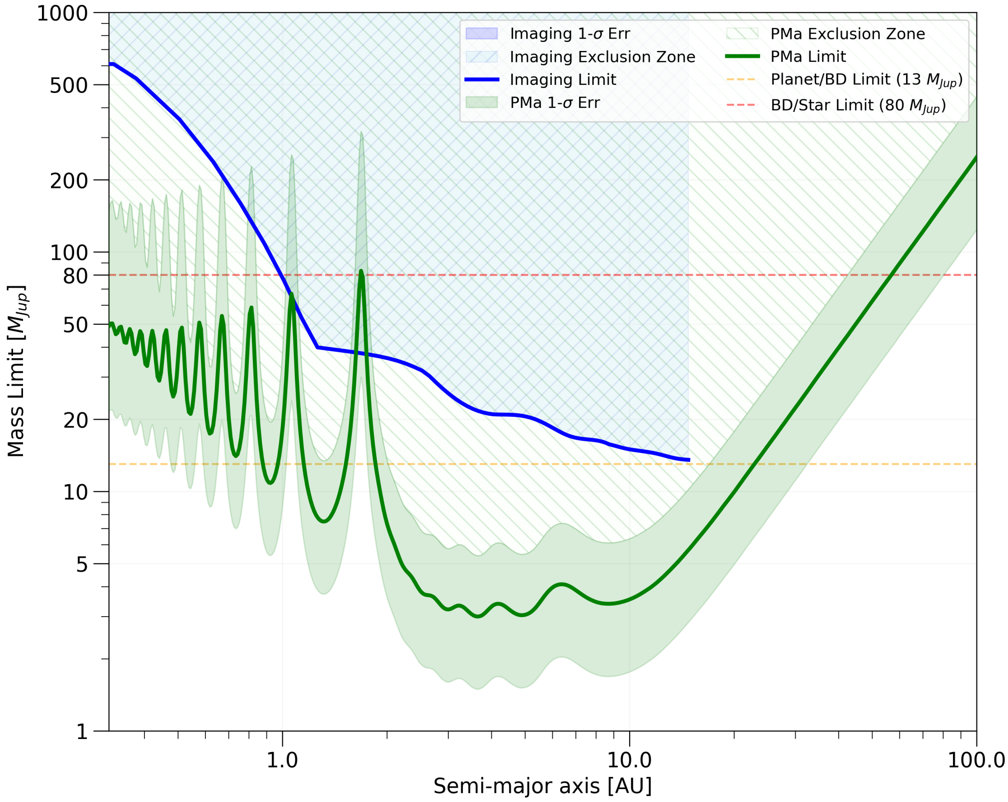

Figure A.1: Sensitivity plot of AU Mic. PMa and imaging lower detection limits are shown in green and blue, respectively. I am able to exclude the presence of companions approximately more massive than BDs.

acceleration for this target. NSS, MK05, and M06 do not include the target. I analyzed the speckle imaging frame observation collected on 14 July 2019 by Zorro@Gemini-South in the $832\,\mathrm{nm}$ filter. The analysis was conducted similarly to the previous target, using BHAC15 models for $0.05\,\mathrm{Gyr}$, reasonably close to the system age of $0.045 \pm 0.004\,\mathrm{Gyr}$. No companion was detected, most likely because of my imaging capabilities being limited to a projected separation of $1.2\,\mathrm{arcsec}$, while the companion is located at $5.4\,\mathrm{arcsec}$, or $237\,\mathrm{au}$, on an aligned orbit with both the primary star and planet b, according to EB21, Newton et al. (2019), Benatti et al. (2021) and references therein. I am unable to confirm the third stellar member of the system due to its distance, hypothetically estimated at $\sim 10^5$ by Newton et al. (2019). I am also unable to confirm it via RV due to the DACE temporal coverage limited to $\sim 130\,\mathrm{JD}$ when 5 outliers are removed. It is worth noting that although my PMa detection is likely a false negative, this does not compromise the robustness of this work for the reasons discussed in

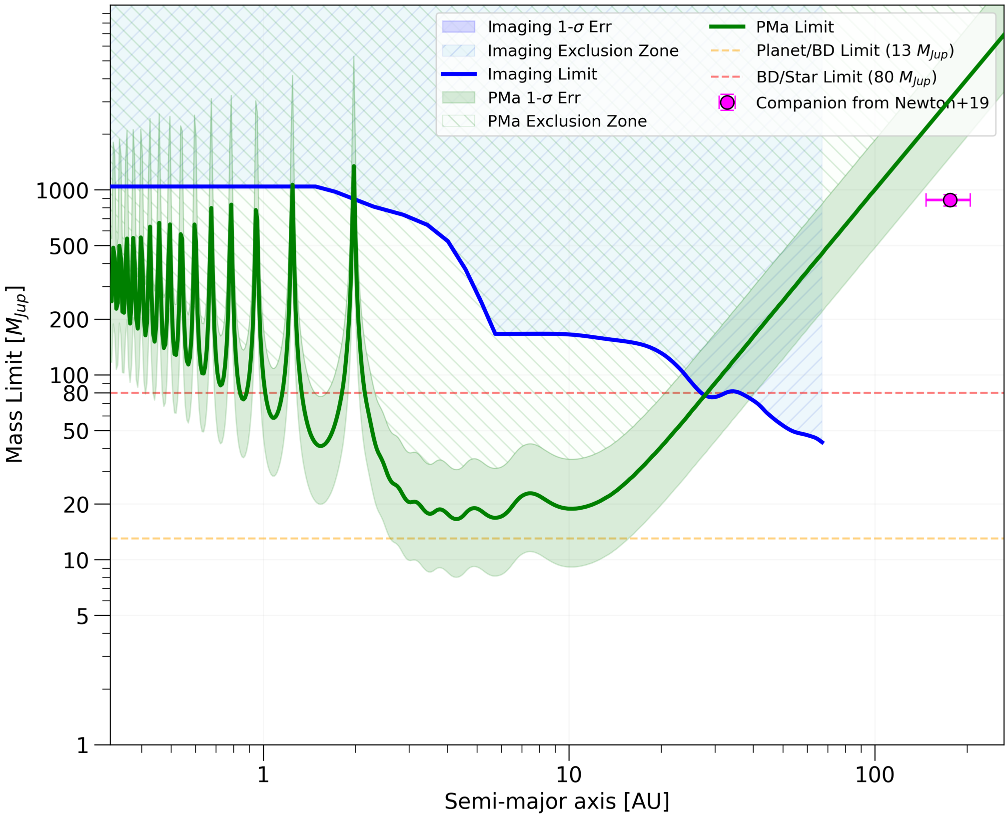

Figure A.2: Sensitivity plot of DS Tuc. Both imaging and PMa are insensitive to the binary companion HD222259B, but my analysis is able to place robust and consistent upper limits on companion mass and physical separation.

Chapter 4: it is expected that K22 is more sensitive to binarity, as the authors employed the *Hipparcos* catalog which is inherently more precise (with lower uncertainties), thus capable of detecting PMas with a larger significance. Most importantly, the mass and distance of the companion are in perfect agreement with the upper limits derived in this study, as shown in Figure A.2.

A.3 GJ 436 b

Background GJ 436 b (Gillon et al. 2007) is a Neptunian planet with a radius of $R = 4.10 \pm 0.16\,\mathrm{R}_\oplus$ and a mass of $M = 25.4^{+2.1}_{-2.0}\,\mathrm{M}_\oplus$ (Lanotte et al. 2014). The existence of a super-Earth planetary companion of $\sim 5 - 10\,\mathrm{M}_\oplus$ has been suggested (e.g., Ribas, Font-Ribera & Beaulieu 2008; Batygin et al. 2009) but never confirmed (Stevenson et al. 2014). Although no planetary or stellar companions are known to date, the non-negligible eccentricity $e \approx 0.16$ of GJ 436 b (Lanotte et al. 2014; Correia, Bourrier & Delisle 2020) and the long-term RV trends (Maness et al. 2007; Demory et al. 2007) may suggest the presence of a binary companion acting via Kozai cycles or spin-driven eccentricity pumping (Correia, Bourrier & Delisle 2020). This is supported by a projected obliquity of $\lambda = 114^{+23°}_{-17}$ and a true obliquity of $\Psi = 103^{+13°}_{-12}$ (Bourrier et al. 2022), in agreement with $\Psi = 101.0^{+9.6°}_{-9.2}$ from Rossi et al. (2026), placing this planet on a blatantly misaligned orbit. The RUWE does not suggest binarity $\mathrm{RUWE} = 1.125$.

Update GJ 436 (Gaia DR3 4017860992519744384, TYC 1984-2613-1, HIP 57087) has no mean position or PMs available in Tycho-2, thus PMa analysis was not conducted. K19, K22, TDSC, Hip2, NSS, MK05, M06, HGCA, EB21 do not suggest the target to be a double star. I derived imaging detection limits using the same models and proxies as for the previous targets, choosing the closest BHAC15 model to the system age of $6^{+4}_{-5}\,\mathrm{Gyr}$ for the observation gathered on 23 January 2019 using NESSI@WIYN with the $832\,\mathrm{nm}$ filter. No stellar ($M \gtrsim 80\,\mathrm{M_{Jup}}$) companion was detected in the range $2 - 15\,\mathrm{au}$. DACE includes 1124 RV observations covering $20.2\,\mathrm{yr}$. I fitted Bourrier et al. (2018) and Bourrier et al. (2023) stellar and planetary parameters to HARPS and ESPRESSO data only[3] (293 points) from which I am able to infer a negligible RV drift of $-0.34 \pm 0.18\,\mathrm{m\,s^{-1}}$. The target is regarded as a single star in this work, in agreement with the recent analysis by Im et al. (2026).

A.4 GJ 3470 b

Background GJ 3470 b (Bonfils et al. 2012) is a Neptunian world with a radius of $R = 4.57 \pm 0.18\,\mathrm{R_{\oplus}}$ and a mass of $M = 13.9 \pm 1.5\,\mathrm{M_{\oplus}}$ (Awiphan et al. 2016), orbiting an M1V star (Stefànsson et al. 2022). Similarly to GJ 436 b, the planet is on a mildly eccentric orbit $e \approx 0.125$ and is located on a perpendicular orbit, with $\lambda = 101^{+29°}_{-14}$ and $\Psi = 97^{+16°}_{-11}$ (Stefànsson et al. 2022), consistent with the Rossi et al. (2026) inference of $\Psi = 104.3^{+19.3°}_{-14.0}$. This can hint at the presence of a still undetected companion, although available observations have not found any evidence of its existence (Demory et al. 2013). Similarly to the previous case, the value of $\mathrm{RUWE} = 1.141$ does not suggest binarity.

Update GJ 3470 (Gaia DR3 654687847820642560) is not included in Tycho-2 and no direct imaging is available on ExoFOP. Since it is not a Tycho target, the majority of the aforementioned catalogs do not contain entries for this target.

[3] The remaining data comes from publications using SOPHIE and HIRES, that introduce an additional degree of complexity in adjusting their offsets.

Those that theoretically could, do not either. DACE provides 217 datapoints, from which I remove all the 14 collected with HIRES and the two collected with ESPRESSO due to being outliers, and an additional 3 outliers collected with HARPS and having a RV hundreds of $\mathrm{m\,s^{-1}}$ below the median RV. I fit the data with planetary and stellar parameters from Stefànsson et al. (2022), consistently with the catalog choice made by Rossi et al. (2026). The resulting $\chi_r^2 = 1.08$ already indicates a consistent fit, as shown in Figure A.3; the addition of a linear drift in RV slightly improves the fit to $\chi_r^2 = 1.04$, with an estimated drift of -0.25 ± 0.25, below the 3σ significance threshold. The addition of an additional stellar jitter, fitted at $\sigma_{\mathrm{jitter}} = 0.85 \pm 1.11$ improves an already consistent fit to $\chi_r^2 = 1.01$. The target is considered a single star.

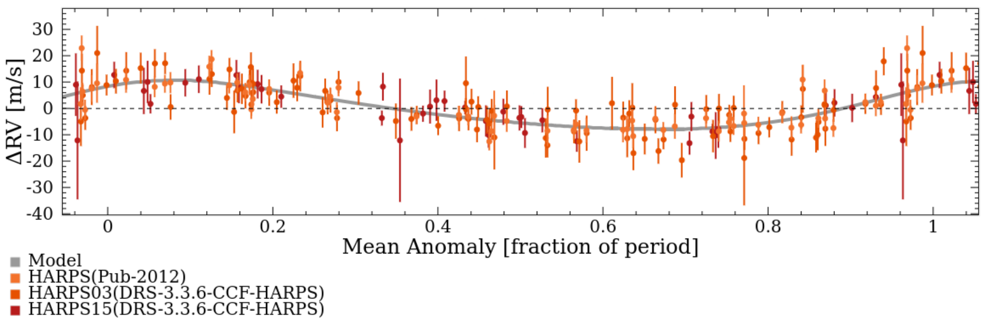

Figure A.3: RV phase-folded plot of GJ 3470. The fit is consistent with having a zero RV drift and an estimated goodness of fit of $\chi_r^2 = 1.04$.

A.5 HAT-P-11 b

Background HAT-P-11 b (Bakos et al. 2010) is a Neptunian planet with a radius of $R = 4.90 \pm 0.07\,\mathrm{R_\oplus}$ and a mass of $M = 25.0 \pm 1.5\,\mathrm{M_\oplus}$ (Basilicata et al. 2024), orbiting a K4 dwarf star (Bakos et al. 2010). Bakos et al. (2010) suggested the presence of a second planet c, which was later confirmed to be an extremely eccentric $e = 0.60 \pm 0.03$ Jupiter companion discovered via RV (Yee et al. 2018). Further measurements have refined this value to $M = 2.68 \pm 0.41\,\mathrm{M_{Jup}}$ located at $4.10 \pm 0.06\,\mathrm{au}$ (An et al. 2025). Similarly to GJ 436 b and GJ 3470 b, planet b resides on a misaligned and eccentric orbit (e.g., Winn et al. 2010; Hirano et al. 2011), which recent characterization works quantify as $\lambda = 133.9^{+7.1°}_{-8.3}$ and $\Psi = 104.9^{+8.6°}_{-9.1}$ (Bourrier et al. 2023), in agreement with $\Psi = 110.4^{+5.6°}_{-4.9}$ from Rossi et al. (2026). Lu et al. (2025) has noted how a simulation of planet-planet scattering followed by Kozai migration can explain the current architecture of the system, although better constraints are needed on other system parameters.

No binarity is suggested by $\mathrm{RUWE} = 0.948$.

Update HAT-P-11 (Gaia DR3 2086512227851023872, TYC 3561-2092-1, HIP 97657) is not a binary target according to my PMa analysis ($\Delta_{G3} = 1.621$). K19 agrees, while K22 noted a clear sign of binarity with $\Delta_{G3} = 4.33$. However, the target is not listed in TDSC, Hip2, NSS, MK05, M06, WDS, and EB21. That said, HGCA lists the target as having a notable acceleration, with a $\chi^2 \approx 42.5$ (the long-term PM differing for more than 6σ from *Gaia* DR3 PM, An et al. 2025) discrepant from a non-accelerating target solution. No imaging data is available on ExoFOP for this target. It is necessary to emphasize that massive planets produce a dynamical effect on the host star, and an anomalous astrometric acceleration is clearly within this dynamical effect; this affects HAT-P-11 directly (J. Zhang et al. 2026), with no stellar companion detected in speckle observations (Howell et al. 2021). The $10\,\mathrm{yr}$ period of planet c fits well within this dynamical discrepancy (An et al. 2025). The RV analysis is conducted using Basilicata et al. (2024) and Bourrier et al. (2023) for stellar and planetary parameters of the b companion, while Yee et al. (2018) is employed for planet c; the three works provide compatible values. The 55 measurements from HIRES and SOPHIE, covering $4\,\mathrm{yr}$ lead to a linear drift of $11.18 \pm 11.16\,\mathrm{m\,s^{-1}}$, with a $\chi^2_r = 3.79$, which improves with the addition of stellar jitter. I conclude that this is not a binary target, and RV analysis further confirms this conclusion, as planet c may have been responsible for unmodeled dynamical effects in past works. I include the PMa plot, which is correctly insensitive to this substellar companion.

A.6 HD 63433 b

Background HD 63433 b (A. W. Mann et al. 2020) is a Neptunian planet with a radius of $R = 2.16^{+0.06}_{-0.05}\,\mathrm{R}_\oplus$ and a mass of $M_p = 37.3 \pm 9.6\,\mathrm{M}_\oplus$ (Polanski et al. 2024). It is the second planet in a three planet system, composed of an inner Earth (d) and two outer Neptunes (b, c) (A. W. Mann et al. 2020; Capistrant et al. 2024). No stellar companion has been detected in *Gaia* DR2 astrometry nor in a 10-years baseline of spectroscopy (A. W. Mann et al. 2020). RV signals show no evidence of a stellar companion (A. W. Mann et al. 2020; Damasso et al. 2023). The planet has a projected spin-orbit inclination of $\lambda = 8^{+33}_{-45}{}^{\circ}$ (A. W. Mann et al. 2020) and a true obliquity of $\Psi = 31.9^{+24.54}_{-15.84}{}^{\circ}$ (Rossi et al. 2026). Once again, there is no indication of binarity by $\mathrm{RUWE} = 0.991$.

Update HD 63433 (Gaia DR3 875071278432954240, TYC 1933-747-1, HIP 38228) does not have a binary companion ($\Delta_{G3} = 0.386$) according to my PMa analysis.

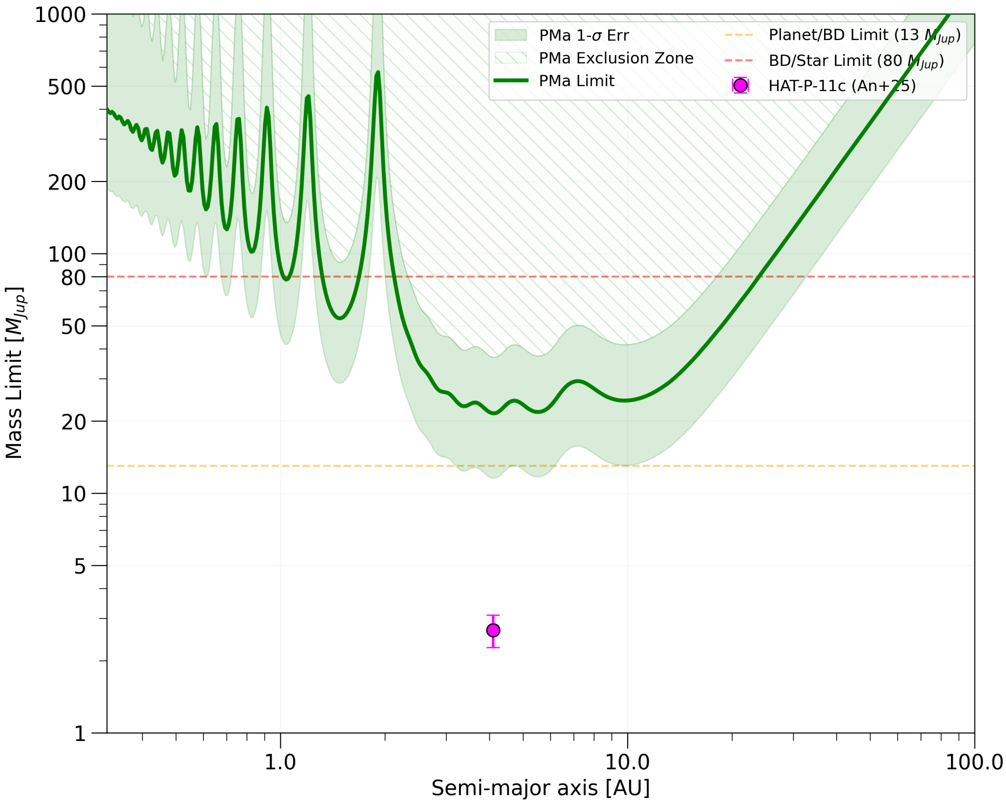

Figure A.4: Sensitivity plot of HAT-P-11. Same as Figure A.2, but the companion I am unsensitive to is substellar.

No catalog suggests the presence of stellar companions. Imaging was performed using the observations collected on 9 September 2020 using NIRC2@Keck2 with the Brγ filter. I chose the 2MASS K filter as a proxy and applied BHAC15 models for a target age of $2\,\mathrm{Gyr}$, the closest to the actual system age of $1.5^{+1.6}_{-1.0}\,\mathrm{Gyr}$ (Rossi et al. 2026). I am able to exclude stellar mass companions in the range $10-115\,\mathrm{au}$, while having less sensitivity to closer distances. However, the analysis by A. W. Mann et al. (2020) already excludes such close companions. The RV analysis cannot be conducted as only 11 datapoints in a range of $\sim 5000\,\mathrm{JD}$ are present. Interestingly, my PMa analysis is able to exclude down to a minimum mass of $\sim 6.3^{+5.3}_{-3.2}\,\mathrm{M_{Jup}}$ at both 5 and 10 au. Although this limit is not as low as the threshold from K22, it still indicates that Tycho-2 can provide valuable insights even in the planetary regime.

A.7 HD 89345 b

Background HD 89345 b (Van Eylen et al. 2018) is a relatively understudied Neptunian planet with a radius of $R = 7.40^{+0.31}_{-0.34}\,\mathrm{R}_\oplus$ and a mass of $M = 34.96^{+5.4}_{-5.72}\,\mathrm{M}_\oplus$ (Yu et al. 2018). It is the only planet orbiting its G5 star (Bourrier et al. 2023) on an eccentric orbit $e \approx 0.2$ (Van Eylen et al. 2018; Yu et al. 2018; Bourrier et al. 2023). No other planets have been found with an $\mathrm{SNR} > 4.5$ (Van Eylen et al. 2018). Both Van Eylen et al. (2018) and Bourrier et al. (2023) noted RMS values larger than the corresponding median RV errors and a RV drift, which may be linked to an outer planetary companion. Stellar companions are not suggested by the low $\mathrm{RUWE} = 1.079$. The planet is on a misaligned orbit with $\lambda = 74^{+34}_{-33}{}^\circ$ (Bourrier et al. 2023) and $\Psi = 80^{+22}_{-23}{}^\circ$ (Bourrier et al. 2023).

Update HD 89345 (Gaia DR3 3877070590167177344, TYC 840-840-1, HIP 50496) shows no binary companion, although the signal is moderate ($\Delta_{G3} = 3.49$). However, the nominally more sensitive *Gaia-Hipparcos* PMa is not significant (with a SNR of 1.46 in K22). No stellar companion is detected across the catalogs. The imaging observation I analyzed was collected on 27 December 2017 with NIRC2@KECK2 in the Brγ filter. The star is clearly a main sequence star, with an age of $9.4^{+0.4}_{-1.3}\,\mathrm{Gyr}$, consequently, I used Mamajek models with the 2MASS K filter as a proxy. Unlike BHAC15 models, these require the use of color indexes to compute the magnitude in the desired filter, as they do not provide separate tables for different filters. Due to the large distance of the target, imaging can exclude companions with a minimum mass of $\sim 100\,\mathrm{M_{Jup}}$ beyond $\sim 30\,\mathrm{au}$, while allowing for larger masses at inner separations. However, no additional companion is present in the analyzed image. Regarding RV, I analyzed 128 datapoints collected in a time span of $122\,\mathrm{JD}$. Although such a short baseline is rather inconclusive for the search of binary companions, I performed the analysis as previous works noted a RV trend using less datapoints (Section 3 and Fig. 4 of Bourrier et al. 2023). Using the same stellar and planetary parameters, which are 1σ consistent with other characterization efforts performed on this planet (Yu et al. 2018; Van Eylen et al. 2018), I am able to retrieve a Keplerian fit which is, itself, consistent with the literature. Most importantly, a $\chi^2_r = 4.84$ estimates the goodness of this fit, improving to $\chi^2_r = 1.12$ by fitting a linear RV drift of $9.78 \pm 5.27\,\mathrm{m\,s^{-1}}$ and a stellar jitter of $\sigma_{\mathrm{jitter}} = 2.16 \pm 0.20\,\mathrm{m\,s^{-1}\,yr^{-1}}$. These results, shown in Figure A.5 are fully consistent with previous research on HD 89345, and it can be explained by solar-like oscillations. The significance threshold is not met, hence I consider this target as single in the statistical analysis

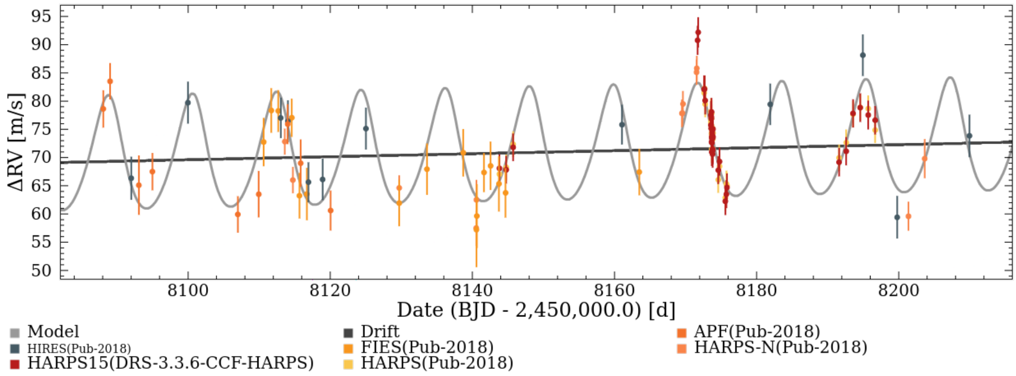

Figure A.5: RV plot of HD 89345. The linear drift is a notable effect across the 132 JD of datapoints, as reported in previous literature with a lower sample.

A.8 HIP 67522 b

Background HIP 67522 (Rizzuto et al. 2020) is a Neptunian planet with a radius of $R = 9.76^{+0.49}_{-0.50}\,\mathrm{R}_{\oplus}$ and a mass of $M < 20\,\mathrm{M}_{\oplus}$ (Thao et al. 2024). The planetary system also comprises a planet c close to a 2:1 MMR (Barber et al. 2024). Speckle imaging combined with *Gaia* DR2 astrometry excludes the presence of stellar companions closer than 3″ to the primary source (Rizzuto et al. 2020). Its orbit is near circular, while being aligned with $\lambda = -5.8^{+2.8°}_{-5.7}$ and $\Psi = 20.2^{+10.3°}_{-8.7}$ (Heitzmann et al. 2021), slightly more misaligned compared to $\Psi = 9.5^{+4.6}_{-4.0}$ from Rossi et al. (2026). No binarity is suggested by $\mathrm{RUWE} = 0.869$

Update HIP 67522 (Gaia DR3 6113920619134019456, TYC 7794-2268-1) shows no signs of binarity from PMa analysis with $\Delta_{G3} = 1.98$. The star is confirmed to be single after checking K19, K22, WDS, EB21, Hip2, TDSC, NSS, MK05, M06, HGCA (astrometric acceleration compatible with a single star). No imaging frames are available on ExoFOP. The RV temporal coverage in DACE is limited to approximately a year, so no analysis is performed. The target is a single star.

A.9 K2-25 b

Background K2-25 b (A. W. Mann et al. 2016a) is a Neptunian planet with a radius of $R = 3.44 \pm 0.12\,\mathrm{R}_{\oplus}$ and a mass of $M = 24.5^{+5.7}_{-5.2}\,\mathrm{M}_{\oplus}$ (Stefansson et al. 2020). It is the only planet orbiting its M4V host in the Hyades cluster (A. W. Mann et al. 2016a). However, a larger RV error than expected has been noted, hinting at the possible presence of an unseen companion (A. W. Mann et al. 2016a). It is also worth noting that the planet resides on a curiously aligned ($\lambda = 3^\circ \pm 16^\circ$, $\Psi = 17^{+11}_{-8}{}^\circ$) but very eccentric ($e = 0.43 \pm 0.05$) orbit (Stefansson et al. 2020). This inclination is in full agreement with the value of $14.6^{+10.5}_{-7.9}{}^\circ$ inferred by Rossi et al. (2026). On this topic, TTVs analyses rule out the possibility of an unseen resonant planetary companion, but the high e might suggest that the orbital eccentricity is being actively excited by companions at longer periods (Kain et al. 2020). Thao et al. (2020) noted how *Gaia* DR2 astrometric excess noise and RUWE rule out the possibility of a stellar companion ($\mathrm{RUWE} = 1.303$). Stefansson et al. (2020) noted how Kozai can produce planets with high eccentricities and low obliquities, giving a plausible explanation for the peculiar architecture of this system, also excluding at 99.7% confidence a planetary companion with a period between 0.5 and $50\,\mathrm{d}$ with a mass larger than $82\,\mathrm{M}_\oplus$. However, they specify how continued and precise RV monitoring is required to confidently detect or exclude such a companion.

Update K2-25 (Gaia DR3 3311804515502788352) has no Tycho entry and no imaging data on ExoFOP, for this reason I am unable to perform any dedicated analysis beside gathering results from catalogs. NSS, MK05, M06, EB21 do not mark this target as binary. I am also unable to perform RV analysis as no data is available on DACE. Considering also the literature associated with this star, the target is considered single.

A.10 K2-33 b

Background K2-33 b (A. W. Mann et al. 2016b) is a Neptunian planet with a radius of $R = 5.04^{+0.34}_{-0.37}\,\mathrm{R}_\oplus$ (A. W. Mann et al. 2016b) and a still uncertain mass $M < 70\,\mathrm{M}_\oplus$ (David et al. 2016), which according to the Stevens & Gaudi (2013) classification places it in the Neptunian realm. A. W. Mann et al. (2016b) ruled out the possibility of a stellar companion or a debris disk. Conversely, David et al. (2016) noted the presence of a cool circumstellar disk, best fitted by a dust component at $122\,\mathrm{K}$ having an inner edge at $2\,\mathrm{au}$. The orbital eccentricity is fully compatible with 0 (A. W. Mann et al. 2016b; David et al. 2016). This, combined with a projected obliquity of $\lambda = -10^{+22}_{-24}{}^\circ$ (Hirano et al. 2024) and a true obliquity of $\Psi = 23.2^{+15.5}_{-11.1}{}^\circ$ (Rossi et al. 2026), as well as a $\mathrm{RUWE} = 1.216$, strongly disfavors the presence of a binary companion.

Update K2-33 (Gaia DR3 6245758900889486720) similarly to K2-25 has no information regarding PMa, imaging or catalogs. This is logical as K2 targets were observed along the galactic plane, a region which due to its high extinction was loosely surveyed[4] by the *Hipparcos* mission (Turon et al. 1992a; Turon et al. 1992b, and references therein). The limited temporal coverage of 94 JD prevents conducting any reliable RV analysis. From the available data, the target is a single star.

A.11 K2-105 b

Background K2-105 b (Narita et al. 2017) is a little studied Neptunian planet with a radius of $R = 3.59^{+0.44}_{-0.39}\,\mathrm{R}_{\oplus}$ and a mass of $M = 30 \pm 19\,\mathrm{M}_{\oplus}$ (Narita et al. 2017). Bourrier et al. (2023) noted a significantly misaligned orbit — with $\lambda = -81^{+50°}_{-47}$ — further confirmed by a true obliquity of $\Psi = 80^{+36.7°}_{-36.1}$ (Rossi et al. 2026). This blatant misalignment supports the potential existence of a planetary companion (Bourrier et al. 2023). However, the low astrometric excess noise and low RUWE value (0.923) apparently disfavor the presence of a companion.

Update K2-105 (Gaia DR3 651907079835937280, TYC 807-1019-1) shows no signs of binarity from a PMa analysis, with a $\Delta_{G3} = 1.319$. The star is not a *Hipparcos* target, and no catalog lists this star as a binary. No age estimate is available in the literature, as discussed by Rossi et al. (2026). Considering that the target is a main sequence star, I used Mamajek tracks (with G_{RP} as proxy filter) to obtain a mass sensitivity curve from the observation collected on 21 January 2016 using DSSI@Gemini equipped with the orange filter (880 nm). Due to the large distance of the target ~ 200 pc, I am able to put constraints on the presence of binary targets only beyond 10 au at a mass of $840.8\,\mathrm{M_{Jup}}$. Considering the literature regarding this target, and its status as a main sequence star, I would expect a companion to be of a comparable age and detectable in a red filter. DACE includes 47 datapoints covering 4.77 yr, 40 of which collected with ESPRESSO, one with HARPS, and 6 more with SOPHIE. I exclude one ESPRESSO datapoint located above $100\,\mathrm{m\,s^{-1}}$ above the median RV and I then use Howard et al. (2025) and Bourrier et al. (2023) for stellar and planetary parameters, respectively. The fitting algorithm is not able to converge unless e and ω are set as free parameters. Doing this allows convergence with a $\sigma_{\mathrm{jitter}} = 5.04 \pm 0.57\ \mathrm{m\,s^{-1}}$, $\chi^2_r = 1.21$ and with a RV drift of $9.07 \pm 4.35\,\mathrm{m\,s^{-1}\,yr^{-1}}$. Removing the stellar jitter results in a lower drift uncertainty of $1.03\,\mathrm{m\,s^{-1}}$, clearly trying to compensate the unmodeled stellar noise. Datapoints are too few to infer definitive conclusions via RV; hence, I conclude this is a single target.

[4] A generic threshold that describes most of the *Hipparcos* star visible magnitudes is a function of the galactic latitude, and in general no stars fainter than $V = 13$ are included. Exceptions exists, and they are fully detailed in the printed copy of the mission guide.

A.12 K2-290 b

Background K2-290 b (Hjorth et al. 2019) is a Neptunian planet with a radius of $R = 3.06 \pm 0.16\,\mathrm{R}_{\oplus}$ and a mass limit of $M < 21.1\,\mathrm{M}_{\oplus}$ (Narita et al. 2017). It resides in a well studied system, composed of a primary late-type F star K2-290A, hosting planet b and a Jupiter c, and two more M dwarfs K2-290B and K2-290C orbiting at $113 \pm 2\,\mathrm{au}$ and $2467^{+177}_{-155}\,\mathrm{au}$ from the planet-hosting star, respectively, according to *Gaia* DR2 (Hjorth et al. 2019; Hjorth et al. 2021). Both planets are misaligned: K2-290b has an obliquity of $\lambda_b = 173^{+45}_{-53}{}^{\circ}$ (Hjorth et al. 2021) and $\Psi_b = 115.3^{+7.8}_{-16.0}{}^{\circ}$ (Rossi et al. 2026), whereas K2-290c has an obliquity of $\lambda_c = 153 \pm 8^{\circ}$ and $\Psi_c = 124 \pm 6^{\circ}$ (Hjorth et al. 2021). Best & Petrovich (2022) demonstrated how the strong misalignment of both planets is a chaotic behavior induced by the presence of two stellar companions. This reinforces the goal of this work to systematically search for binary companions to shed light on certain peculiar planetary obliquities.

Update K2-290 (Gaia DR3 6253844468883543680, TYC 6193-663-1) does not show binarity from a PMa analysis, with a $\Delta_{G3} = 0.909$. It is not a $Hipparcos$ target, and it is not listed in TDSC, NSS, WDS, MK05, M06. It is however noted as a binary in EB21. The companion Gaia DR3 253844464585162880 is located at $3030\,\mathrm{au}$, and it actually corresponds to K2-290C noted by Hjorth et al. (2019).

I derived the detection limits from speckle observations taken on 29 March 2018 with DSSI@Gemini using the orange filter ($880\,\mathrm{nm}$) using Mamajek tracks with $Gaia\ G_{RP}$ as a proxy filter. The close companion is clearly visible (Figure A.7), although the PMa analysis is not conclusive; I used `ds9` to perform 30 iterations of centroiding to find the optimal position for the centroids of K2-290A and K2-290B. The angular separation of the two targets is $0.398''$, resulting in a distance of $109.5\,\mathrm{au}$, slightly lower than the $113 \pm 2\,\mathrm{au}$ declared by Hjorth et al. (2019) after analyzing an IRCS@Subaru observation in the H band ($16.23\,\mu\mathrm{m}$), resulting in an angular separation of 0.389 ± 0.008. I speculate that the discrepancy between the two measurements may arise from several possible factors: (i) H band observations are able to better resolve the stellar companion B compared to the DSSI orange filter as shown in Hjorth et al. (2019)[5]; (ii) Hjorth et al. (2019) did not correct the parallax according to Lindegren et al. (2021a) and Lindegren et al. (2021b), declaring a parallax of $3.64 \pm 0.05\,\mathrm{mas}$ instead of the corrected value of $3.75 \pm 0.02\,\mathrm{mas}$. A lower parallax immediately results in larger angular separations; (iii) a latter observational epoch may have accumulated some

[5] Specifically, the target is brighter and although it is partially blended with the primary star, an algorithmic determination of two photocenters is based on a higher photon count.

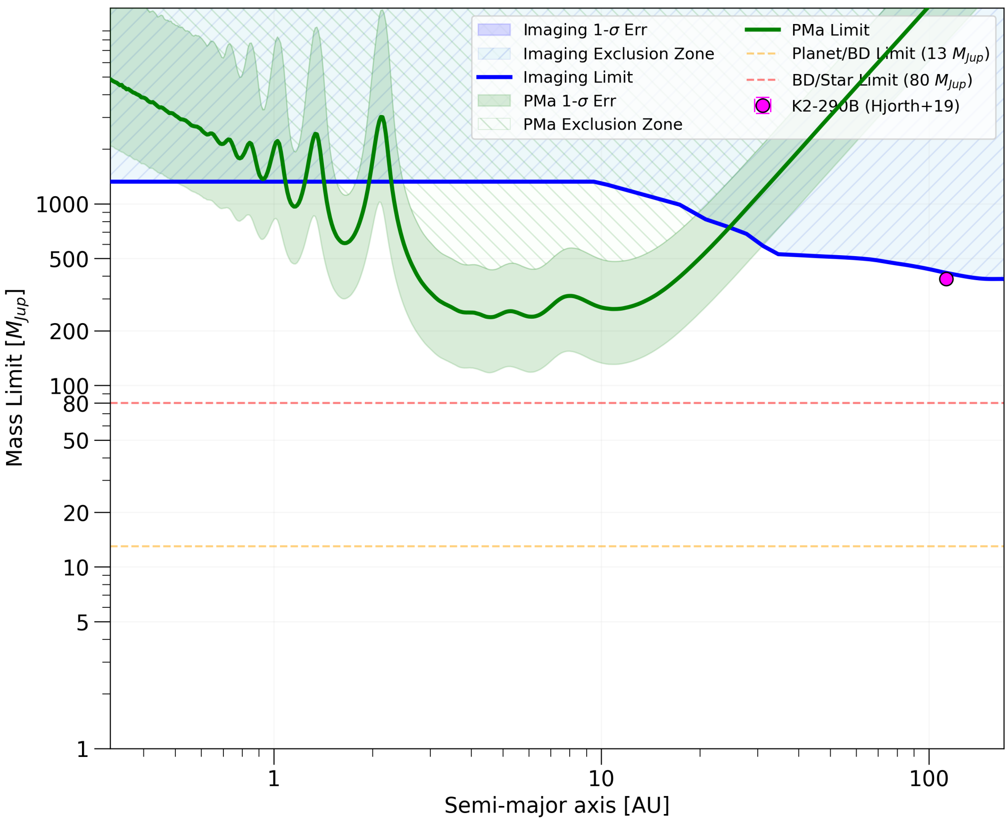

Figure A.6: Mass-separation plot of K2-290. The mass and separation of K2-290B are fully compatible with my PMa upper limits and it is detectable via speckle imaging.

additional orbital motion. However, it is necessary to point out that a deeper analysis is required to confirm any of these hypotheses. Nonetheless, my sensitivity analysis is able to detect the stellar companion B, being limited at $110\,\mathrm{au}$ to $\sim 0.38\,\mathrm{M}_\odot$ compared to the true value of $M_B = 0.368\,\mathrm{M}_\odot$.

The projected separation of K2-290C is $2467^{+177}_{-155}\,\mathrm{au}$ according to Hjorth et al. (2019), making this target the same one detected by EB21. The target is a bound triple system. RV analysis cannot be performed as the 27 HARPS datapoints in DACE have a temporal coverage limited to $196\,\mathrm{JD}$, that combined with 19 RM points from ESPRESSO cover $513\,\mathrm{JD}$ only.

A.13 K2-329 b

Background K2-329 b is a Neptunian planet with a radius of $R = 8.68^{+0.29}_{-0.27}\,\mathrm{R}_\oplus$ and a mass of $M = 82.6^{+6.4}_{-7.0}\,\mathrm{M}_\oplus$ orbiting a G dwarf (Sha et al. 2021). The only

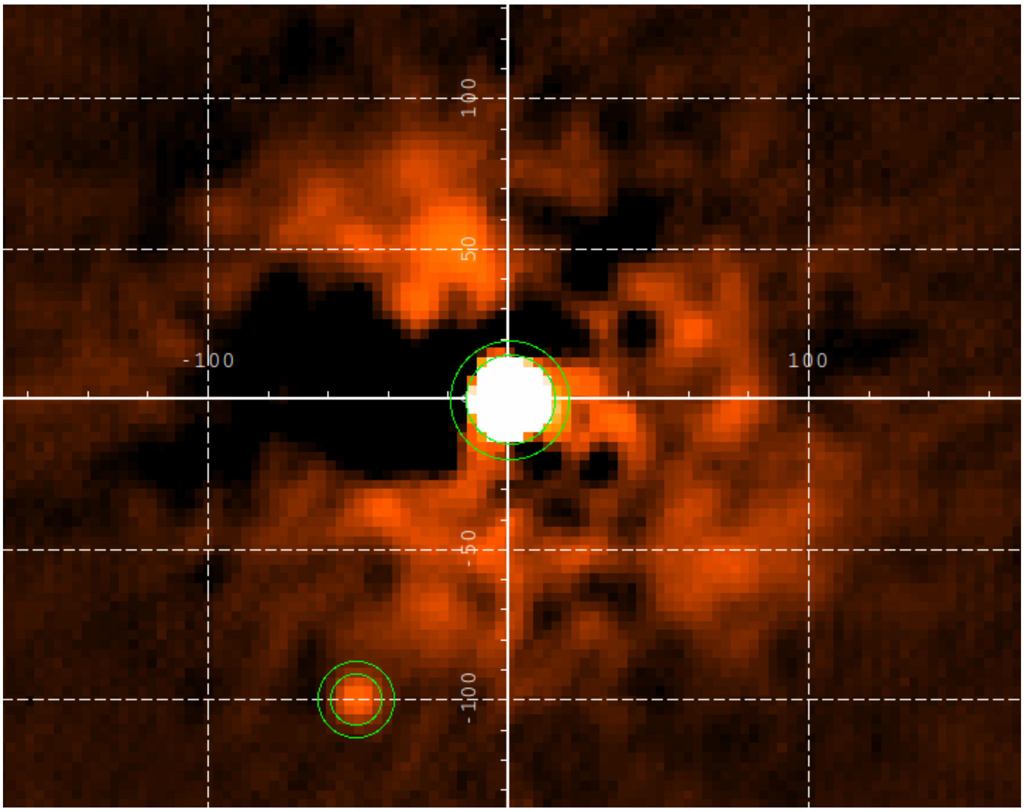

Figure A.7: Speckle imaging of K2-290. The companion K2-290B is clearly visible and it is located at a separation of $109.5\,\mathrm{au}$, in slight disagreement with literature results but compatible at the level of 2σ. The axes represent separation in au.

planet in the system is on a mildly aligned orbit with $\lambda = 26.7^{+8.5\circ}_{-8.0}$, $\Psi = 33.3^{+7.9\circ}_{-8.3}$ (Espinoza-Retamal et al. 2025) (or $\Psi = 35.8^{+8.4\circ}_{-9.1}$ according to Rossi et al. (2026)), and is weakly eccentric $e = 0.08 \pm 0.03$ (Espinoza-Retamal et al. 2025). (Sha et al. 2021) noted that the tidal realignment timescale for this planet is comparable to the age of the universe. The low $\mathrm{RUWE} = 1.003$ does not hint at the presence of a binary companion.

Update K2-329 (Gaia DR3 2632880927441296640) has no Tycho-2 entry, so no PMa analysis was conducted. No entry is found in WDS, NSS, MK05, M06. However, it has been classified as a binary by EB21, which suggests the binary companion Gaia DR3 2632880991865749376 is located at a distance of $\sim 8783\,\mathrm{au}$. Hwang, Ting & Zakamska (2022) determined it to be an extremely eccentric system $e = 0.99^{+0.01}_{-0.38}$. I derived the imaging detection limits using the observations collected on 14 August 2017 using NESSI@WIYN equipped with the $832\,\mathrm{nm}$ filter, employing BHAC15 models for an age of $2\,\mathrm{Gyr}$, reasonably close to the system age of $1.8^{+2.2}_{-1.3}$ Gyr. No companion was detected, and I am able to place an upper limit on the presence of close-in companions with masses in the range $50-300$ au. The wide and eccentric companion is detected in imaging by Polanski & Clark (2025), but no ExoFOP entry is provided for the observation. It is unclear to which extent this wide companion may influence K2-329 b. Once again, the low temporal coverage of 307 JD of HARPS measurements, together with two more RM measured with ESPRESSO, makes this target unfeasible for a RV analysis.

A.14 Kepler-9 b

Background Kepler-9 b (Holman et al. 2010) is a Neptunian planet with a radius of $R = 8.29^{+0.54}_{-0.43}\,\mathrm{R}_\oplus$ and a mass of $M = 43.4^{+1.6}_{-2.0}\,\mathrm{M}_\oplus$ (Borsato et al. 2019) orbiting a G2 dwarf (Holman et al. 2010). The system is also populated by an outer Neptune c in a 2:1 MMR with b (Holman et al. 2010) and an inner super-Earth d (Holman et al. 2010; Torres et al. 2010). Planet b resides on a mildly aligned orbit with $\lambda = -13 \pm 16°$ (S. Wang et al. 2018) and $\Psi = 27.1^{+13.0°}_{-12.7}$ (Rossi et al. 2026). No binarity is suggested by the $\mathrm{RUWE} = 1.011$.

Update Kepler-9 (Gaia DR3 2099925719951103872) is not in the Tycho catalog and no imaging is available on ExoFOP. 19 RV points on DACE make this target unfavorable for further analysis. NSS, MK05, M06, EB21 have no entry for this target, however WDS lists it as a binary. Specifically, three companions (B, C, D) are proposed, at separations of $2.8''$, $6.10''$, and $8.00''$, respectively. Their magnitudes were collected in the Johnson R or I bands for B and C[6], being $20.90\,\mathrm{mag}$ and $18.90\,\mathrm{mag}$, while D has its magnitude measured in the K band (or redder IR bands) with a value of $19.20\,\mathrm{mag}$. Furlan et al. (2017), in their work aiming to systematically detect contaminants nearby KOI targets, suggested the existence of a contaminant B located at $2.854''$. In the K-band, Kepler-9 (hereafter A), has a magnitude of $12.34\,\mathrm{mag}$ according to the Kepler Input Catalog[7] (KIC, Kepler Mission Team 2009), reasonably matching the one reported by WDS. Furlan et al. (2017) reported a magnitude difference of $6.80\,\mathrm{mag}$ between A and B, making B a $19.14\,\mathrm{mag}$ target in K. WDS declares a R-band magnitude of $20.90\,\mathrm{mag}$.

The color index $K - R$ is extracted for A via WDS and is 1.5, while the color index for A is computed using KIC values as $K - r = 1.4$. Extinction is neglected

[6]Recall that WDS is a collection of inhomogeneous measurements, and information on magnitudes is provided with extremely generic notes about the used filters.

[7]https://cdsarc.cds.unistra.fr/viz-bin/cat/V/133

as the color indexes are computed always for the same target. The r and R filters are used as proxies for one another due to their similarity. The colors are compatible, suggesting a system composed of two similar stars. Moreover, using both KIC and WDS at the same time, $K_B - K_A = 6.84$ while $R_B - R_A = 7.1$, making B fainter than A, hence concluding the two catalogs are reasonably detecting the same star for the B companion.

I queried *Gaia* around Kepler-9 in a radius of $8.5''$ to understand whether the catalog was suggesting the presence of the four stars detected by WDS. With no possibility to move from *Gaia* bands to WDS bands, I resorted to projected separations. *Gaia* detects Gaia DR3 2099925750013898112 at a projected separation of $6.11''$, making it compatible with WDS' target C, and Gaia DR3 2099925719948694400, compatible with WDS' D. However the difference in parallax, namely $1.58''$ for A, $0.26''$ for C (Gaia DR3 2099925750013898112), and $0.14''$ for D (Gaia DR3 2099925750013898112) makes them clearly separated with no possibility of a quadruple system[8]. Moreover, their PMs are incompatible with each other at the level of several σ: underscoring the conclusion that C and D are background contaminants and not bound to A. No candidate B is detected by querying *Gaia*, which might be due to its magnitude being close to the detection capability of the satellite roughly at $G \sim 20$ (Gaia Collaboration et al. 2021). Additionally, assuming the unknown candidate B to be located at the same distance as Kepler-9, its projected separation would locate it $\sim 1800\,\mathrm{au}$ away. Since Furlan et al. (2017) was a systematic search for contaminants, and WDS is a visual survey, there is insufficient information to conclude that this is a binary system, hence I will follow the literature and classify this as a single star.

A.15 Kepler-25 c

Background Kepler-25 c (Steffen et al. 2012) is a Neptunian planet with a radius of $R = 5.22 \pm 0.07\,\mathrm{R}_\oplus$ and a mass of $M = 15.2^{+1.3}_{-1.6}\,\mathrm{M}_\oplus$ (Mills et al. 2019) orbiting an F8 dwarf (Bourrier et al. 2023). The system is composed of an inner Earth b — almost in a 2:1 MMR with planet c — (Steffen et al. 2012; Migaszewski & Goździewski 2018), and an outer non-transiting Neptune d (G. W. Marcy et al. 2014) (according to the mass-based classification by Stevens & Gaudi (2013), since the radius is not yet characterized). These planets are orbiting the primary star, which part of a binary configuration with Kepler-25B, with Kepler-25C being a background contaminant (Michel & Mugrauer 2024). Planet c is on

[8] For the sake of completeness, a parallax estimation was conducted following the methodology described in Section 4.3.b. Although parallax errors are larger than 10%, it is reasonable to assume that a direct parallax inversion instead of a Bayesian computation of distance may not change the conclusions drawn for Kepler-9's supposed binary companions C and D

a near-circular ($e = 0.006^{+0.005}_{-0.004}$, Mills et al. 2019) mildly aligned orbit with $\lambda = -0.9^{+7.7\circ}_{-6.4}$ and $\Psi = 24.1^{+9.2\circ}_{-9.3}$ (Bourrier et al. 2023), in slight disagreement with the $\Psi = 7.4^{+5.5\circ}_{-4.2}$ reported by Rossi et al. (2026). There is a slight presence of excess astrometric noise and a RUWE of 1.096.

Update Kepler-25 (Gaia DR3 2100451630105041152, TYC 3124-1264-1) does not show binarity from a PMa analysis ($\Delta_{G3} = 1.13$). It is not a *Hipparcos* target. No entry for this star is present in TDSC, as well as MK05, or M06. NSS shows an accelerating solution for Gaia DR3 2100450771111569408, that due to its large separation ($\sim 120''$, or $\sim 28800\,\mathrm{au}$), as well as a significantly different parallax and PM, is unlikely to be part of the system. No imaging frames are available on ExoFOP; however, WDS includes two companions (B and C), both located at a separation of $8.4''$, but at very different position angles. The C companion is shown to be a background object from *Gaia* DR3 astrometric parameters. Following a similar argument to the Kepler-9 case, I conclude that Kepler-25 has a single stellar companion (Gaia DR3 2100451630105040256 or KOI-1803), with a similar parallax and PM. This corresponds to the companion reported by Michel & Mugrauer (2024) and it is further confirmed by EB21. RV analysis on 172 datapoints covering a time span of $13.3\,\mathrm{yr}$ infers a non-significant drift, following the procedure detailed for other targets above. The system is thus a wide binary ($\sim 2000\,\mathrm{au}$) and the results are fully compatible with the upper limit placed by my mass sensitivity curve. The system is a wide binary.

A.16 Kepler-30 b

Background Kepler-30 b (D. C. Fabrycky et al. 2012) is a Neptunian planet with a radius of $R = 3.9 \pm 0.2\,\mathrm{R}_\oplus$ and a mass of $M = 11.44 \pm 1.27\,\mathrm{M}_\oplus$ (Sanchis-Ojeda et al. 2012). The system also includes a Jupiter companion c and a further Neptunian planet d, all of them orbiting in nearly coplanar orbits (Sanchis-Ojeda et al. 2012; Sanchis-Ojeda, Winn & D. C. Fabrycky 2013; Panichi et al. 2018) a G dwarf star (de Freitas et al. 2021). Planet b and c are close to a 2:1 MMR (Hadden & Lithwick 2017; Panichi et al. 2018), while c and d are close to a higher resonant state (e.g., 17:7 or 7:3 Panichi et al. 2018). Planet b is on a similarly misaligned orbit, with $\lambda = 4.0^\circ \pm 10.0^\circ$ (Sanchis-Ojeda et al. 2012) and $\Psi = 47.3^{+6.2\circ}_{-7.1}$ (Rossi et al. 2026). Astrometric excess noise is not reported in *Gaia* DR3, while $\mathrm{RUWE} = 1.011$. Two further planets KOI-806.04 and KOI-806.05 have been proposed within the system but remain unconfirmed.

Update Kepler-30 (Gaia DR3 2100243616248608896) is not a Tycho-2 target, has no imaging available on ExoFOP, and no RV data on DACE. Catalogs, along with the imaging performed by Furlan et al. (2017), confirm Kepler-30 as a single star.

A.17 Kepler-63 b

Background Kepler-63 b (Sanchis-Ojeda et al. 2013) is a Neptunian planet with a radius of $R = 6.11 \pm 0.20\,\mathrm{R}_\oplus$ and a mass of $M < 120\,\mathrm{M}_\oplus$, orbiting a G-type MS star (Sagynbayeva & Farr 2026). Renormalized unit weight error is low $\mathrm{RUWE} = 0.752$. The planet has been found to be on a blatantly misaligned orbit $\lambda = -110^{+22}_{-14}{}^\circ$, $\Psi = 104^{+9}_{-14}{}^\circ$ (Sanchis-Ojeda et al. 2013) — further confirmed by other studies (Bourrier et al. 2023; Rossi et al. 2026; Sagynbayeva & Farr 2026) — with a non-negligible eccentricity $e < 0.45$ at 3σ (Sanchis-Ojeda et al. 2013). Bourrier et al. (2023) argued that improperly managed stellar variability affected the inference of the orbital parameters, the eccentricity in particular, which the team then fixes to 0. Nonetheless, the obliquity values of the two teams are in agreement. No stellar companions have been found, but their presence cannot be excluded (Sanchis-Ojeda et al. 2013).

Update Kepler-63 (Gaia DR3 2132628489996257920, TYC 3550-458-1) shows a tentative sign of binarity with a $\Delta_{G3} = 3.04$ arising from a PMa analysis. It is not an $Hipparcos$ target, and TDSC, NSS, MK05, M06, WDS have no entry for it, while Furlan et al. (2017) confirms it to be a single. It is worth noting that its faintness ($V_T = 12.06$) is beyond the photometric completeness threshold of Tycho-2 (Høg et al. 2000a), hence the signal is not scientifically meaningful. High uncertainties on the astrometric solution, along with a backpropagation, may dramatically hinder the inference of my framework. Imaging was performed using the frames collected on 10 August 2024 by PHARO@Palomar in the Brγ band, with BHAC15 models at $0.2\,\mathrm{Gyr}$, closely matching the system age of $0.210 \pm 0.045\,\mathrm{Gyr}$, with 2MASS K as proxy filter. I am able to exclude companions more massive than $\sim 1\,\mathrm{M}_\odot$ within $10\,\mathrm{au}$, dropping to $\sim 0.6\,\mathrm{M}_\odot$ at $30\,\mathrm{au}$. No RV datapoints are included in DACE. The target is a single star.

A.18 Kepler-1656 b

Background Kepler-1656 b (Brady et al. 2018) is a Neptunian planet with a radius of $R = 5.02 \pm 0.53\,\mathrm{R}_\oplus$ (Brady et al. 2018) and a mass of $M = 47.8^{+6.2}_{-3.3}\,\mathrm{M}_\oplus$ (Angelo et al. 2022). The system also hosts a wide and eccentric $e \approx 0.53$ Jovian companion c, with a period of $P_{orb,c} \approx 1920\,\mathrm{d}$ (Angelo et al. 2022). Planet b is on an aligned $\lambda = 35^{+15°}_{-22}$ (Rubenzahl et al. 2024), $\Psi = 37.1^{+15.0°}_{-16.2}$ (Rossi et al. 2026) but highly eccentric orbit $e \approx 0.84$ (Brady et al. 2018; Angelo et al. 2022). Similarly to the previous case, there is a low $\mathrm{RUWE} = 0.782$. Brady et al. (2018), using *Gaia* DR2 data, excluded any companion earlier than M4 further than $18\,\mathrm{au}$. However, Angelo et al. (2022) noted how a distant companion could be the driver for such a peculiar system.

Update Kepler-1656 (Gaia DR3 2103392720630278656, TYC 3123-1355-1) shows a tentative sign of binarity ($\Delta_{G3} = 3.24$) similarly to the previous case, most probably due to its faintness ($V_T = 11.7\,\mathrm{mag}$). It is not a $Hipparcos$ target and no RV data is available on DACE. Imaging was performed with Mamajek models, due to the maturity of the star, on the observations collected on 11 July 2014 with PHARO@Palomar, following the same methodology as Kepler-63. Results and their justification are broadly similar to Kepler-63, the target is thus considered a single star. Specifically, the planet Kepler-1656 c proposed by Angelo et al. (2022) has a minimum mass of $M_c \sin i = 0.337 \pm 0.032\,\mathrm{M_{Jup}}$ and it is located at $\sim 3\,\mathrm{au}$. It is broadly compatible with the upper limit placed by my PMa analysis of $300\,\mathrm{M_{Jup}}$, and the combination of the two serves as a powerful constraint for the possible mass of the planet.

A.19 TOI-942 b

Background TOI-942 b (Zhou et al. 2020b; Carleo et al. 2021) is a Neptunian planet with a radius of $R = 4.24^{+0.38}_{-0.31}\,\mathrm{R_\oplus}$ and a mass upper limit of $M < 14\,\mathrm{M_\oplus}$ (Carleo et al. 2021). The K-type host star is also orbited by an outer Neptunian planet c (Zhou et al. 2020b; Carleo et al. 2021). I note a low value of $\mathrm{RUWE} = 1.089$. Zhou et al. (2020b) excluded the presence of binaries with $\Delta M < 4$ within $\sim 0.''2$ via high resolution speckle imaging and within $2''$ using $Gaia$. Carleo et al. (2021) further excluded companions even within a $50''$ aperture using *Gaia* DR2. The team also thoroughly discussed the probable dynamical history of the system, considering the non negligible eccentricities of $e_b \circ 0.285$ and $e_c \approx 0.175$, as well as the near-equatorial orbit of planet b $\lambda = 1.0^{+41.0°}_{-33.0}$ and $\Psi = 2.0^{+27.0°}_{-23.0}$ (Wirth et al. 2021). The large uncertainties place the planet on a mildly aligned orbit, as further emphasized by Rossi et al. (2026), who inferred a true obliquity of $\Psi = 29.9^{+24.5°}_{-15.3}$ Other planetary companions are also excluded (Wirth et al. 2021).

Update TOI-942 (Gaia DR3 2974906868489280768, TYC 5909-319-1) shows no sign of binarity from my PMa analysis ($\Delta_{G3} = 2.06$, despite the faintness

$V_T = 12.07\,\mathrm{mag}$). It is not a *Hipparcos* target. No RV data is available on DACE. Imaging was performed on frames gathered in the $832\,\mathrm{nm}$ filter using Alopeke@Gemini on 14 October 2019; these were analyzed using *Gaia* G_{RP} as the proxy filter, and BHAC15 models assuming a central age estimation of $0.05 \pm 0.02\,\mathrm{Gyr}$. No companion was detected, neither via imaging nor by consulting other catalogs. The target is a single star.

A.20 TOI-1135 b

Background TOI-1135 b (Mallorquín et al. 2024b) is a relatively understudied, puffy Neptunian planet with a radius of $R = 9.92 \pm 0.31\,\mathrm{R}_\oplus$ and a mass of $M = 26.4 \pm 16.2\,\mathrm{M}_\oplus$, with an upper limit of $M < 58.8\,\mathrm{M}_\oplus$ at 3σ (Dugan et al. 2025). The orbit of this single-planet system is mildly eccentric $e = 0.062^{+0.12}_{-0.045}$ and dramatically misaligned, with $\lambda = -68.1^{+7.5°}_{-5.3}$ and $\Psi = 72.2^{+6.2°}_{-6.2}$ (Dugan et al. 2025). Mallorquín et al. (2024b) detected a companion $5.39\,\mathrm{mag}$ fainter at a separation of $0.973''$ via NESSI speckle imaging (Scott et al. 2018). The team also reported the non-detection of stellar companions brighter than $\Delta I_c = 4.8\,\mathrm{mag}$ and $7.2\,\mathrm{mag}$ at separations of $0.25''$ and $1.0''$, respectively, using SAI speckle imaging (Safonov, Lysenko & Dodin 2017). No wide companions were found by the team using the *Gaia* DR3 catalog. No planetary companions are detected (Mallorquín et al. 2024b; Dugan et al. 2025). Consistent with these findings, I also note a low $\mathrm{RUWE} = 0.974$.

Update TOI-1135 (Gaia DR3 1726858366624544640, TYC 4637-60-1, HIP 62908) shows no sign of binarity from my analysis $\Delta_{G3} = 1.59$. No catalog suggests binarity and no RV data is available on DACE. Imaging frames were not available on ExoFOP. The target is a single star.

A.21 TOI-1268 b

Background TOI-1268 b (Dong et al. 2022) is a young Neptune ($0.39^{+0.28}_{-0.27}\,\mathrm{Gyr}$) with a radius of $9.1 \pm 0.6\,\mathrm{R}_\oplus$ and a mass of $M = 96.4^{+8.2}_{-8.3}\,\mathrm{M}_\oplus$, orbiting a K dwarf (Šubjak et al. 2022). The orbit of the only known planet in this system is mildly eccentric $e \approx 0.1$ (Dong et al. 2022; Šubjak et al. 2022) and slightly misaligned $\lambda = 40^{+7.2°}_{-9.9}$ (Dong et al. 2022) $\Psi = 40.1^{+7.8°}_{-8.8}$ (Rossi et al. 2026). No stellar companions have been detected from *Gaia* EDR3 data within $10''$ of the host star (Dong et al. 2022), and no diluting sources were found closer than the *Gaia* separation limit of $0.4''$ (Šubjak et al. 2022). The $\mathrm{RUWE} = 0.851$ does not indicate binarity.

Update TOI-1268 (Gaia DR3 1675923009431370880, TYC 4163-44-1) shows no sign of binarity from my PMa analysis with $\Delta_{G3} = 1.45$. Neither imaging nor entries in binarity catalogs are available, as well as no RV data on DACE. The target, also considering the extensive discussion by Šubjak et al. (2022), is a single star.

A.22 TOI-1694 b

Background TOI-1694 b (Mistry et al. 2023) is a Neptunian world with a radius of $R = 5.5 \pm 0.5\,\mathrm{R}_\oplus$ and a mass of $M = 26.1 \pm 2.2\,\mathrm{M}_\oplus$ (Handley et al. 2025). The early K dwarf TOI-1694 also hosts an outer, eccentric ($e \approx 0.18$) Jupiter companion c (Van Zandt et al. 2023). The inner Neptune b is on an aligned orbit $\lambda = 9^{+22°}_{-18}$ (Handley et al. 2025), $\Psi = 25.5^{+15.7°}_{-13.3}$ (Rossi et al. 2026) that is consistent with being circular (Van Zandt et al. 2023). I note a relatively high $\mathrm{RUWE} = 1.383$.

Update TOI-1694 (Gaia DR3 1104269596843209472, TYC 4108-1434-1) shows no sign of binarity from my PMa analysis with a $\Delta_{G3} = 2.51$, although it is extremely close to the Tycho-2 limiting magnitude, having $V_T = 11.53\,\mathrm{mag}$. No RV data is available on DACE. No entry is available for this target in binarity catalogs; moreover, it is flagged as a star with a dubious reference star in the Tycho-1 catalog, casting even more doubt on the correctness of the PMa inference in the first place. Imaging was performed as detailed using Mamajek models and $Gaia\ G_{RP}$ on the frame collected on 8 February 2021 using Alopeke@Gemini equipped with the 832nm filter. Although the RUWE is close to the Lindegren et al. (2021b) limit of 1.4, a search in the $Gaia$ DR3 archive reveals no $Gaia$ sources within $2'$ with a compatible parallax that could justify this RUWE value.

A.23 TOI-1759 A b

Background TOI-1759 A b is a Neptunian planet with a radius of $R = 3.14 \pm 0.10\,\mathrm{R}_\oplus$ and a mass of $M = 10.8 \pm 1.5\,\mathrm{M}_\oplus$ (Espinoza et al. 2022) orbiting an M0V star (Martioli et al. 2022). (Martioli et al. 2022) in their work set upper limits against the presence of a stellar binary companion. However, Polanski et al. (2025) suggest the presence of a stellar companion B using the TESS Input Catalog. The $\mathrm{RUWE} = 0.858$ is not high enough to suggest binarity. Planet b has no outer or inner planetary companions, and it resides on a circular and aligned orbit ($\lambda = -4^{+19°}_{-18}$, $\Psi = 25.0^{+12.3°}_{-11.8}$; Polanski et al. 2025; Rossi et al. 2026, respectively).

Update TOI-1759 A (Gaia DR3 2216420110788943744, TYC 4266-736-1) shows no sign of binarity according to PMa ($\Delta_{G3} = 1.66$, with $V_T = 11.93\,\mathrm{mag}$). No RV data is available on DACE. Imaging was performed on NIRC2@Keck observations collected in the Brγ filter and analyzed using Mamajek models and 2MASS K as the proxy filter. I am able to set upper limits of $\sim 80\,\mathrm{M_{Jup}}$ in the range $10 - 200\,\mathrm{au}$. No companion is detected nearby; however, EB21 noted that Gaia DR3 2216420969782393472, located $\sim 2770\,\mathrm{au}$ away from TOI-1759 A, has a compatible PM and parallax that make this system statistically and physically bound in a Keplerian orbit (refer to El-Badry, Rix & Heintz 2021, for further details on their analysis). This is further confirmed by WDS, identifying a likely physically bound companion at $69''$, corresponding to the same physical distance as EB21. This confirms the findings of Polanski et al. (2025), making this a wide binary system.

A.24 TOI-1842 b

Background TOI-1842 b (Wittenmyer et al. 2022) is a Neptunian planet with a radius of $R = 11.9^{+0.8}_{-0.7}\,\mathrm{R}_\oplus$ and a mass of $M = 60^{+19}_{-13}\,\mathrm{M}_\oplus$ (Hixenbaugh et al. 2023). No additional planets orbit the host star, and the planetary orbit is a slightly eccentric $e = 0.13^{+0.16}_{-0.09}$ and clearly misaligned ($\lambda = -68.1^{+21.2}_{-14.7}{}^\circ$, $\Psi = 73.3^{+16.3}_{-12.9}{}^\circ$) orbit (Hixenbaugh et al. 2023), a result further confirmed by $\Psi = 70.1^{+11.5}_{-12.8}{}^\circ$ (Rossi et al. 2026). I note a low $\mathrm{RUWE} = 0.857$, with published literature reporting no information regarding stellar companions.

Update TOI-1842 (Gaia DR3 3719927426253118848, TYC 892-28-1) is not a binary target according to my PMa analysis ($\Delta_{G3} = 0.33$). Tycho-1 conducted a binarity analysis with no results. No indication of binarity is found either in catalogs or in the imaging frames I analyzed. No RV data is available on DACE. The star is a single star.

A.25 TOI-2076 b

Background TOI-2076 b (Hedges et al. 2021) is a Neptunian planet with a radius of $R = 2.77^{+0.14}_{-0.10}\,\mathrm{R}_\oplus$ and a mass of $M = 16.1^{+8.3}_{-8.2}$ (Polanski et al. 2024). No stellar companion has been reported for the young ($\sim 200\,\mathrm{Myr}$) K3 host, which is part of a comoving group (Hedges et al. 2021). The system is also composed of two outer Neptunes c and d, where b and c are close to a 2:1 MMR and c and d are close to a 5:3 MMR (Osborn et al. 2022). The eccentricity of planet b is — reasonably — fixed to 0 and its orbit is aligned $\lambda = -3^{+16}_{-15}{}^\circ$, $\Psi = 18^{+10}_{-9}{}^\circ$ (Frazier et al. 2023) (or $\Psi = 21.0^{+8.9°}_{-9.2}$). RVs of the system show a linear trend (Hedges et al. 2021; Osborn et al. 2022; Damasso et al. 2024). Barber et al. (2025) found evidence of an inner small sized planet e, and suggest the presence of another outer planet f, awaiting further confirmation. I note a negligible $\mathrm{RUWE} = 0.976$.

Update TOI-2076 (Gaia DR3 1490845584382687232, TYC 3036-481-1) is not a binary target according to my PMa analysis ($\Delta_{G3} = 1.67$). Results are broadly similar to those of TOI-1842 for astrometry, RV, and imaging, thus the target is a single.

A.26 TOI-2364 b

Background TOI-2364 b is a Neptunian planet with a radius of $R = 8.61^{+0.26}_{-0.20}\,\mathrm{R}_\oplus$ and a mass of $M = 71.5^{+13.7}_{-15.6}\,\mathrm{M}_\oplus$ (Yee et al. 2023). It is the only known planet orbiting its K dwarf host, with an eccentricity fixed to 0 (Yee et al. 2023; Tamburo et al. 2025) and an aligned orbit $\lambda = 7^{+10°}_{-11}$, $\Psi = 15.6^{+7.7°}_{-7.3}$ (Tamburo et al. 2025) (consistent with $\Psi = 21.9^{+6.0°}_{-7.0}$ from Rossi et al. (2026). I note a non-negligible $\mathrm{RUWE} = 1.308$.

Update TOI-2364 (Gaia DR3 3022644120017418496) does not have a binary entry in any catalog, despite its considerable RUWE, although it remains below the 1.4 threshold. No RV data is available on DACE. Imaging was performed using the observations collected on 24 February 2021 in the Brγ filter using PHARO@Palomar, with Mamajek models and 2MASS K as a proxy filter. The target is a single star.

A.27 TOI-2374 b

Background TOI-2374 b is a little studied Neptunian planet with a radius of $R = 6.81 \pm 0.30\,\mathrm{R}_\oplus$ and a mass of $M = 56.64^{+3.49}_{-4.27}\,\mathrm{M}_\oplus$ orbiting a K5V host (Hacker et al. 2024). The planet, which was not included in the Rossi et al. (2026) dataset, presents a misaligned orbit $\lambda = 81^{+23°}_{-22}$, $\Psi = 85.9^{+8.6°}_{-9.2}$ (Yee et al. 2025). No significant RV trends are detected (Hacker et al. 2024), and $\mathrm{RUWE} = 0.972$. However, Yee et al. (2025) identified HD 202673 as its binary companion, using the El-Badry, Rix & Heintz (2021) catalog of binary stars developed from *Gaia* EDR3 data.

Update TOI-2374 (Gaia DR3 6828814283414902912) is listed only in the WDS as having a companion with a $\sim 22''$ separation. This is in agreement with the findings of Yee et al. (2025), as HD 202673 (Gaia DR3 6828814283414902784) has a similar parallax ($7.33\,\mathrm{mas}$, with TOI-2374 having $7.35\,\mathrm{mas}$) and a similar proper motion. The system is indeed a wide binary, with a separation of $\sim 3000\,\mathrm{au}$. No imaging frames are available for this target, as well as no RV data on DACE.

A.28 TOI-3884 b

Background TOI-3884 b (Almenara et al. 2022b) is a Neptunian planet $R = 6.43 \pm 0.20\,\mathrm{R}_{\oplus}$ and a mass of $M = 32.59^{+7.31}_{-7.38}\,\mathrm{M}_{\oplus}$, orbiting a mid-M dwarf (Libby-Roberts et al. 2023). The only planet in this system is on a slightly eccentric $e = 0.06^{+0.06}_{-0.04}$ and misaligned orbit $\lambda = 75 \pm 10^{\circ}$ (Libby-Roberts et al. 2023), with $\Psi = 77.1^{+8.5^{\circ}}_{-9.3}$ (Rossi et al. 2026). Almenara et al. (2022b) and Libby-Roberts et al. (2023) report that the *Gaia* DR3 $\mathrm{RUWE} = 1.252$ suggests the absence of stellar companions, and several other works noted how the conspicuous presence of starspots plays a crucial role in modeling this transit (Almenara et al. 2022b; Libby-Roberts et al. 2023; Chakraborty et al. 2025; Mori et al. 2025).

Update TOI-3884 (Gaia DR3 3919169687804622336) has no entry in any catalog. Only two ESPRESSO datapoints are available on DACE. Imaging was performed on the observations collected on 13 February 2022 with PHARO. The analysis conducted is equivalent to TOI-2374 (except for the use of BHAC15 models). I am able to tightly constrain the presence of stellar companions, starting from limits of $209\,\mathrm{M_{Jup}}$ at a distance of $3\,\mathrm{au}$, and reaching $50\,\mathrm{M_{Jup}}$ beyond $30\,\mathrm{au}$. The target is a single star.

A.29 TOI-5398 b

Background TOI-5398 b is a recently confirmed Neptune world with a radius of $R = 10.3 \pm 0.4\,\mathrm{R}_{\oplus}$ and a mass of $M = 58.7^{+5.7}_{-5.6}\,\mathrm{M}_{\oplus}$, orbiting a two-planet system with an inner sub-Neptune c (Mantovan et al. 2024b). The discovery paper did not find evidence of a stellar companion closer than $\rho = 0.25''$ and $\rho = 1.0''$ brighter than $\Delta I_c = 4.0$ and $6.8\,\mathrm{mag}$, respectively. Observations performed with HARPS-N (Cosentino et al. 2012) at the TNG found a projected spin-orbit obliquity of $\lambda = 3.0^{+6.8^{\circ}}_{-4.2}$ and a true obliquity of $\Psi = 13.2^{\circ} \pm 8.2^{\circ}$ (Mantovan et al. 2024a), in agreement with the value of $\Psi = 20.2^{+4.4^{\circ}}_{-5.1}$ found by Rossi et al. (2026). There is no immediate indication of binarity, with $\mathrm{RUWE} = 0.817$

Update TOI-5398 (Gaia DR3 7508885482444441344, TYC 2518-317-1) has a low $\Delta_{G3} = 2.292$ suggesting no binarity from a PMa analysis. No RV data is available on DACE. Imaging was performed on observations collected on 17 April 2022 using NESSI in the $832\,\mathrm{nm}$ band, using BHAC15 models. I set an upper limit of $1158\,\mathrm{M_{Jup}}$ up to $\sim 10\,\mathrm{au}$, lowering the limit to $484\,\mathrm{M_{Jup}}$ beyond $30\,\mathrm{au}$. Considering that no catalog lists this star, this target is considered single.

A.30 WASP-69 b

Background WASP-69 b is a bloated Neptunian planet orbiting a $\sim 1\,\mathrm{Gyr}$ mid-K dwarf (Anderson et al. 2014), with a radius of $R = 11.85 \pm 0.19\,\mathrm{R_\oplus}$ and a mass of $M = 82.64 \pm 5.88\,\mathrm{M_\oplus}$ (Casasayas-Barris et al. 2017). No stellar or planetary companions have been detected, and the system exhibits a $\mathrm{RUWE} = 0.993$. The only planet in this system is on a mildly aligned orbit with $\lambda = 0.4^{+2.0}_{-1.9}{}^\circ$ (Casasayas-Barris et al. 2017) and $\Psi = 11.92^{+14.41}_{-8.82}{}^\circ$ (Rossi et al. 2026), which is compatible with the result from Allart et al. (2025) obtained via RMR $\Psi = 29.2^{+6.1}_{-5.0}{}^\circ$.

Update WASP-69 (Gaia DR3 6910753016653587840, TYC 5200-1560-1) is not a binary target according to my PMa analysis ($\Delta_{G3} = 1.44$). No imaging data are available. The RV coverage on DACE is 3670 JD, consisting of 116 measurements of two RM effects. Although Mallorquín et al. (2024a) data is able to properly fit these measurements, no convergence can be reached if linear drift or stellar jitter are added. However, the two RM series reasonable match each other when phase folded, suggesting that no drift is present over time. WDS suggests the presence of three stellar companions, located at a projected separation of $7.4''$ (B), $15.0''$ (C), $17.0''$ (D), with magnitudes of 18.3, 19.7, and 19.7, respectively, in the Johnson-R or I filters. In the same bands, the primary has a magnitude of $9.58\,\mathrm{mag}$. I queried *Gaia* DR3 in a conservative $20''$ circle, but no star with a compatible parallax was found. Consequently, they are most likely visual contaminants, and this target is classified as a single star.

A.31 WASP-107 b

Background WASP-107 b (Dai & Winn 2017) is a puffy Neptunian planet orbiting a K6 star in the Virgo constellation (Anderson et al. 2017), with a radius of $R = 0.94 \pm 0.02\,\mathrm{R_{Jup}}$ (Anderson et al. 2017) and a mass of $M = 30.5 \pm 1.6\,\mathrm{M_\oplus}$ (Piaulet et al. 2021). The absence of statistically significant TTVs or transit duration variations (TDVs) excludes the presence of close-in massive planets (Močnik et al. 2017). Conversely, Piaulet et al. (2021) detected an external Jupiter-sized planetary companion $M_c = M \sin i_{orb,c} = 115 \pm 13\,\mathrm{M_\oplus}$ on an eccentric $e_c = 0.28 \pm 0.07$

and distant $P_c \sim 1100\,\mathrm{d}$ orbit. Planet b is on a mildly eccentric $e_b = 0.06 \pm 0.04$ (Piaulet et al. 2021) and on a retrograde and misaligned $\lambda = -158.0^{+15.0°}_{-19.0}$, $\Psi = 103.5^{+1.7°}_{-1.8}$ orbit (Bourrier et al. 2023), in full agreement with the value of $\Psi = 103.0^{+2.7°}_{-2.8}$ from Rossi et al. (2026). The formation processes and dynamical history of this planet need further investigation (Bourrier et al. 2023). I note a significant astrometric excess noise with a high $\mathrm{RUWE} = 1.540$.

Update WASP-107 (Gaia DR3 3578638842054261248, TYC 5530-1795-1) shows tentative signs of binarity with $\Delta_{G3} = 4.54$ from my PMa analysis. However, it is important to note that its magnitude is $V_T = 11.94$, making it a dubious Tycho-2 entry. Imaging performed on frames collected on 12 June 2017 using the orange filter on DSSI places strict constraints on the maximum mass allowed nearby this star, which is limited to $632.74\,\mathrm{M_{Jup}}$ at $3\,\mathrm{au}$. However, I do not detect any star in the analyzed frame. DACE has a temporal coverage of $5.9\,\mathrm{yr}$, including three RM measurements and an ESPRESSO observing run of 65 outlying points, scattered throughout $\sim 1\,\mathrm{km\,s^{-1}}$, that I remove as outliers. The algorithm is unable to converge on the remaining RM datapoints; however, a visual inspection of data reveals no trend other than an offset that is able to overlap the measurements. However, the HARPS measurement included in Trifonov et al. (2020) only, that have been found in the later stages of this work and have not been thoroughly analyzed, show an apparent and visual RV drift. Although no catalog lists this target, the high RUWE value, together with a tentative detection of binarity, suggests that this target might be orbited by another companion. Nonetheless, a query on *Gaia* DR3 within $4'$ of WASP-107, returned only HD 109249 (Gaia DR3 3578615232618520448) as a target with a roughly similar parallax. The line-of-sight separation between the two is still too large to speculate on their physical association ($3.42\,\mathrm{pc}$). Hence, the target is considered a single star, although a deeper analysis on the reasons behind such a high RUWE could be of interest[9].

A.32 WASP-131 b

Background WASP-131 b is a bloated Neptunian planet orbiting a G0 star (Hellier et al. 2017), with a radius of $R = 13.74 \pm 0.41\,\mathrm{R_\oplus}$ and a mass of $M = 86.8 \pm 6.0\,\mathrm{M_\oplus}$ (Doyle et al. 2023). Bohn et al. (2020) noted a candidate stellar companion with a separation of $0.189'' \pm 0.003''$ with a mass of $0.62^{+0.05}_{-0.04}\,\mathrm{M_\odot}$, confirmed in a subsequent companion work (Southworth et al. 2020). Planet b, the only known

[9]This thesis does not focus on the scientific meaning of the RUWE value. Although interesting, its proper interpretation goes far beyond the threshold 1.4, having some more complex dependencies that need to be accounted for to extract scientifically robust information (e.g., stellar color).

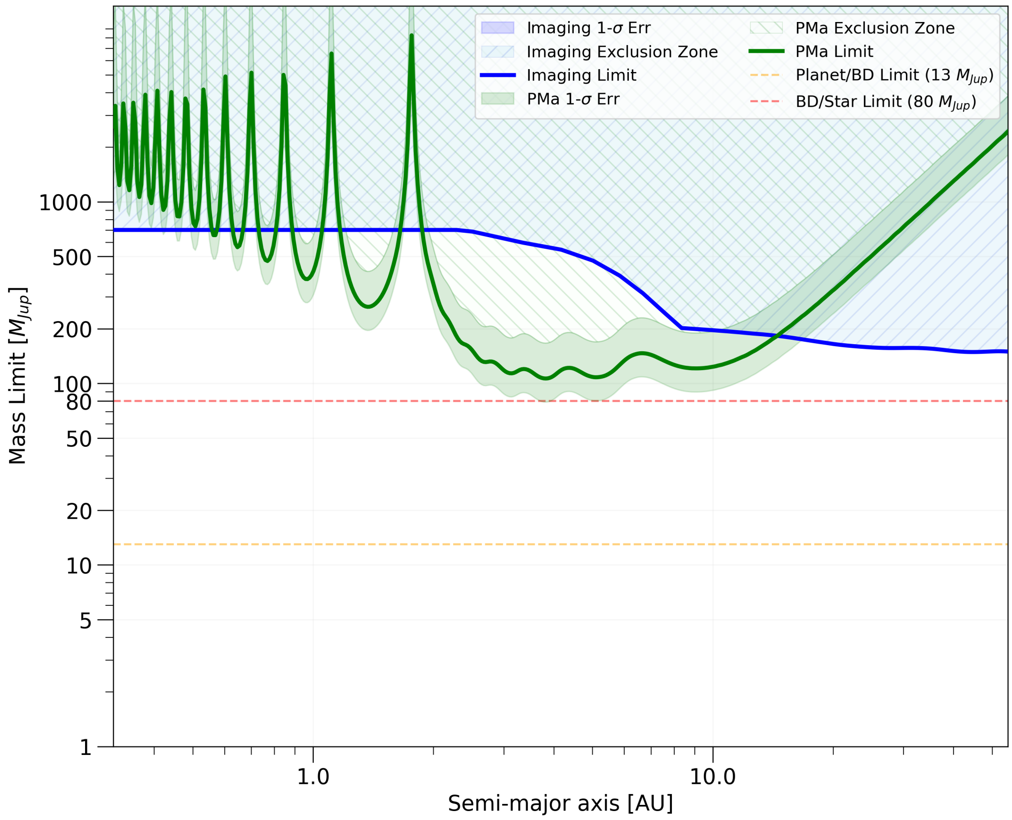

Figure A.8: Mass-separation plot of WASP-107. No companion is detected by my PMa analysis, and very stringent limits are placed on the possible masses of a companion, although I cannot exclude its existence without deeper analysis.

element populating this system, is on a circular but misaligned ($\lambda = 162.4^{+1.3°}_{-1.2}$, $\Psi = 123.7^{+12.8°}_{-8.0}$) orbit (Doyle et al. 2023). Indeed, Doyle et al. (2023) consider the companion as a plausible cause for this dramatic misalignment. Similar results, both for orbital parameters and conclusions, have been found by Zak et al. (2024). This result was expected, as the astrometric solution from *Gaia* DR3 presents a high and significant astrometric excess noise along with a $\mathrm{RUWE} = 1.939$.

Update WASP-131 (Gaia DR3 6173451477191225984, TYC 7280-548-1) shows no sign of binarity from my PMa analysis with a $\Delta_{G3} = 2.44$. No imaging is available on ExoFOP. DACE includes 267 RV measurements, from which I exclude the 34 outlying measurements from CORALIE07, along with an additional point from CORALIE14. The remaining datapoints consist of two RM, that the algorithm is unable to fit using stellar and planetary parameters from Doyle et al. (2023). No catalog besides WDS lists this target, that according to WDS may have a B companion located $10.0''$ away and a C component with a projected separation of $24.9''$. Indeed *Gaia* DR3 shows two objects that match the separations and magnitudes reported in WDS; however, the significant difference in parallaxes makes them unlikely to be a physical triple (or quadruple, if we consider the one confirmed by Southworth et al. (2020)). The system is a binary system following Southworth et al. (2020) and Zak et al. (2024), with a physical separation of $36.5\,\mathrm{au}$ and a mass of $0.27 \pm 0.02\,\mathrm{M}_\odot$[10].

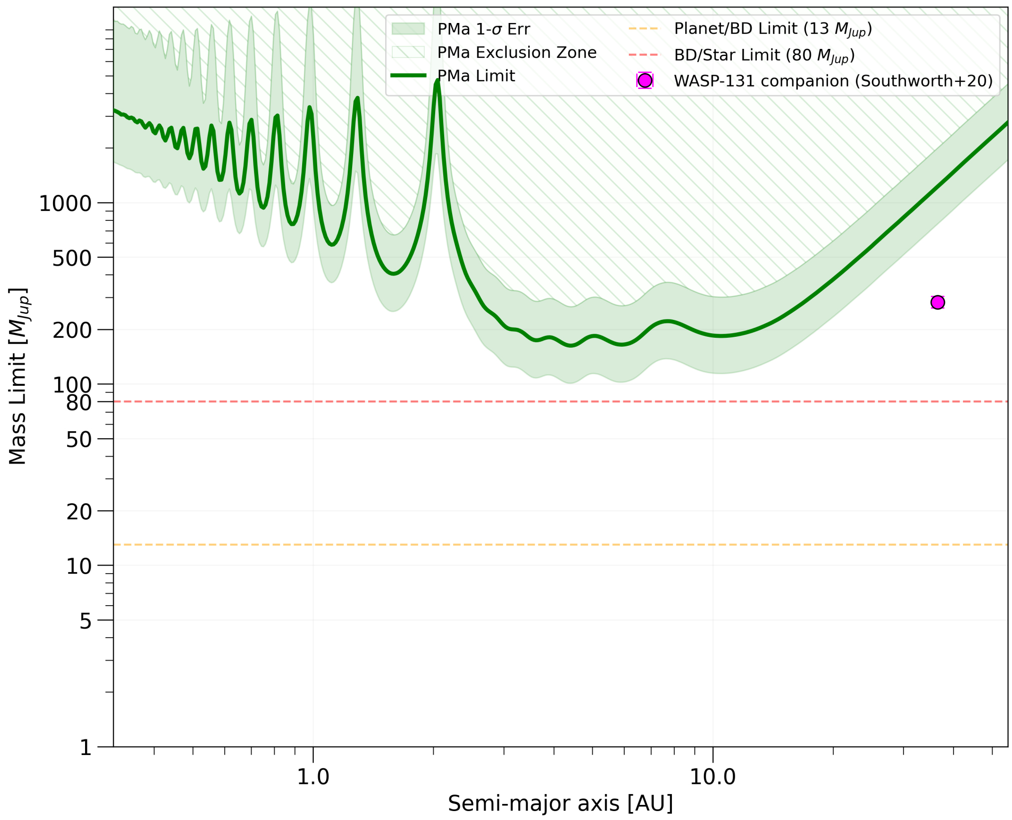

Figure A.9: Mass-separation plot of WASP-131. The companion detected by Southworth et al. (2020), marked in pink, is fully compatible with my PMa non-detection.

[10]The discrepancy between the masses declared by the two consecutive papers of Bohn et al. (2020) and Southworth et al. (2020) arises from the more detailed observations available in the latter work. Indeed, Bohn et al. (2020) declare that more observations were needed to properly constrain the object in orbit around WASP-131.

A.33 WASP-148 b

Background WASP-148 b is a Neptunian planet orbiting a late-G dwarf (Hébrard et al. 2020), with a radius of $R = 8.1 \pm 0.7\,\mathrm{R}_\oplus$ and a mass of $M = 92 \pm 10\,\mathrm{M}_\oplus$ (Knudstrup et al. 2024). The system also hosts an outer, non transiting planet — causing TTVs — that according to Stevens & Gaudi (2013) is a Jupiter, close to a 4:1 MMR (Hébrard et al. 2020). Hébrard et al. (2020) also suggested a possible third planet with a period of $\sim 150\,\mathrm{d}$ and a minimum mass of $0.25\,\mathrm{M}_\mathrm{Jup}$, which was never confirmed. The inner planet b is eccentric $e = 0.29 \pm 0.03$ and aligned $\lambda = -2 \pm 8°$, $\Psi = 21^{+9}_{-17}{}^\circ$ (Knudstrup et al. 2024), consistent with previous measurements from X.-Y. Wang et al. (2022) and with subsequent inferences of $\Psi = 18.9^{+14.2°}_{-10.1}$ (Rossi et al. 2026). The outer planet has no obliquity measurement available, but it is on a very eccentric orbit $e_c = 0.36 \pm 0.09$ (Hébrard et al. 2020). No companion object is visible via imaging within 6″ of the host star (Hébrard et al. 2020). It is disputed whether the two confirmed planets have a low (Maciejewski et al. 2020) or high (Almenara et al. 2022a) mutual inclination. I note a low $\mathrm{RUWE} = 0.886$.

Update WASP-148 (Gaia DR3 1358355738906114816, TYC 3083-295-1) shows binarity from my PMa analysis ($\Delta_{G3} = 10.56$). Considering that (i) no imaging is available (besides the fact that the imaging analyzed by other teams has already dismissed the presence of binary companions nearby); (ii) no catalog lists this well-studied planet-hosting star, that its magnitude is above $V_T = 12.0$; (iii) the predicted mass of the companion object is $\sim 1\,\mathrm{M}_\odot$ in the range $3 - 10\,\mathrm{au}$ (a disruptive companion for the very existence of the planet), I consider this detection an artifact from Tycho-2 catalog positions or PMs. No RV data is available on DACE. The target is considered single.

A.34 WASP-166 b

Background WASP-166 b is a bloated Neptunian planet with a radius of $R = 7.1 \pm 0.3\,\mathrm{R}_\oplus$ and a mass of $M = 32.1 \pm 1.6\,\mathrm{M}_\oplus$ orbiting an F9V star (Hellier et al. 2019). The planetary orbit is compatible with a very low eccentricity, and is most probably aligned, with $\lambda = -0.7 \pm 1.6°$ and $\Psi < 56.2°$ (Bourrier et al. 2023), inferred with higher precision as $\Psi = 8.9^{+9.7°}_{-6.9}$ in subsequent works (Rossi et al. 2026). Published literature does not discuss the possible presence of a binary companion. I note a low $\mathrm{RUWE} = 0.979$.

Update WASP-166 (Gaia DR3 5664957444179338240, TYC 6055-537-1) shows no sign of binarity with $\Delta_{G3} = 0.88$. Tycho-1 carried out multiplicity search with a negative result; no catalog lists this target. Imaging was performed on 7 December 2020 observations collected using the $832\,\mathrm{nm}$ filter mounted on Alopeke, using BHAC15 models and the $Gaia$ G_{RP} filter as a proxy: no companion is detected. DACE includes a total of 589 measurements covering $6.98\,\mathrm{yr}$, from which I exclude 80 points collected using CORALIE14 with the DRS versions 0.3.8 and 3.3.12, as a systematic offset is present and affects the measurement points differently: the temporal coverage is unchanged by this drop and the loss of data is limited to 80 measurements. I fit stellar and planetary parameters from Hellier et al. (2019) (compatible with parameters inferred by Bourrier et al. (2023)), in continuity with Rossi et al. (2026) work. The remaining datapoints do not allow for a convergence, as they consist of two RM collected with ESPRESSO and two more with HARPS (with little to no points outside the RM effect). Hence, the target is considered a single star.

B Gaia DR3 zero-point correction

Here I report the code from Cantat-Gaudin & Brandt (2021) to correct for the reference frame alignment. A description is provided in Section 4.3.e, while a thorough description is given in their work.

```
def edr3ToICRF(pmra, pmdec, ra, dec, G):
    """
    Input: source position, coordinates,
    and G magnitude from Gaia EDR3.
    Output: corrected proper motion.
    """
    if G >= 13:
        return pmra, pmdec

    import numpy as np

    def sind(x):
        return np.sin(np.radians(x))

    def cosd(x):
        return np.cos(np.radians(x))

    table1=""" 0.0    9.0     18.4  33.8   -11.3
               9.0    9.5     14.0  30.7   -19.4
               9.5    10.0    12.8  31.4   -11.8
               10.0   10.5    13.6  35.7   -10.5
               10.5   11.0    16.2  50.0     2.1
               11.0   11.5    19.4  59.9     0.2
               11.5   11.75   21.8  64.2     1.0
               11.75  12.0    17.7  65.6    -1.9
               12.0   12.25   21.3  74.8     2.1
               12.25  12.5    25.7  73.6     1.0
               12.5   12.75   27.3  76.6     0.5
```

```
                12.75 13.0   34.9  68.9   -2.9 """

    table1 = np.fromstring(table1, sep=' ').reshape((12, 5)).T
    Gmin = table1[0]
    Gmax = table1[1]

    # pick the appropriate omegaXYZ for the source's magnitude:
    omegaX = table1[2][(Gmin <= G) & (Gmax > G)][0]
    omegaY = table1[3][(Gmin <= G) & (Gmax > G)][0]
    omegaZ = table1[4][(Gmin <= G) & (Gmax > G)][0]

    pmraCorr = -1*sind(dec)*cosd(ra)*omegaX - sind(dec)*sind(ra)*
   omegaY + cosd(dec)*omegaZ
    pmdecCorr = sind(ra)*omegaX - cosd(ra)*omegaY

    return pmra - pmraCorr / 1000., pmdec - pmdecCorr / 1000.
```

Listing B.1: Python implementation of the frame rotation correction (Cantat-Gaudin & Brandt 2021).

C Sensitivity analysis: exclusion of TOI-1710 A

Table C.1: Results of the bootstrap-smoothed model selection (Method A) for the sample excluding TOI-1710 A ($N = 37$). $\mathrm{Win}_{\mathrm{IC}}$ represents the selection probability, while W_{IC} denotes the mean (Mn) and median (Md) weights across 10^4 iterations. Bold values indicate the most supported model.

Model	**Selection Prob.**		**Relative Weights**	
	Win_{AIC} (%)	Win_{BIC} (%)	$W_{AIC,Mn}$ (%)	$W_{BIC,Mn}$ (%)
GMM1	2.4	3.4	10.7	14.5
GMM2	15.6	4.4	15.2	5.1
ISO	8.4	3.9	12.1	9.4
ISO_HN	21.6	35.0	19.9	29.4
BETA	**39.1**	**51.8**	**28.1**	**38.1**
BETA2	12.9	1.5	14.2	3.6

Table C.2: Results of Method B showing the median information criteria over 10^4 bootstrap iterations for the sample excluding TOI-1710 A ($N = 37$). Bold values highlight the best-performing model.

Model	**AIC Median**	**BIC Median**
GMM1	362.19	365.42
GMM2	362.83	370.89
ISO	362.96	367.79
ISO_HN	361.59	364.81
BETA	**360.61**	**363.83**
BETA2	361.89	369.95

Acronyms

AAPS Anglo-Australian Planet Search.
AL along-scan.
AO Adaptive optics.
BD brown dwarf.
CDF cumulative distribution function.
DACE Data Analysis Center for Exoplanets.
Dec declination.
DOF degrees of freedom.
ExoFOP Exoplanet Follow-up Observing Program.
HGCA Hipparcos-Gaia Catalog of Accelerations.
HJ hot Jupiter.
HZ habitable zone.
IC information criterion.
ICRF International Celestial Reference Frame.
KS Kolmogorov-Smirnov.
MC Monte Carlo.
MCMC Markov Chain Monte Carlo.
MMR mean-motion resonance.
MS main sequence.
MW Mann-Whitney U.
PM proper motion.
PMa proper motion anomaly.
RA right ascension.
RM Rossiter–McLaughlin.
RMR Rossiter–McLaughlin revolutions.
RRM reloaded Rossiter–McLaughlin.
RUWE renormalized unit weight error.
RV radial velocity.
SNR signal-to-noise ratio.
SoS Survey of Surveys.
SVO FPS Spanish virtual observatory filter profile service.
TDSC Tycho Double Star Catalog.
TDV transit duration variation.
TESS Transiting Exoplanet Satellite Survey.
TTV transit time variation.

References

Abril-Pla, O. et al. 2023. "PyMC: A Modern and Comprehensive Probabilistic Programming Framework in Python". In: *PeerJ Computer Science* 9.

Addison, B. C. et al. 2021. "The Youngest Planet to Have a Spin-Orbit Alignment Measurement AU Mic b". In: *AJ* 162, 137.

Agol, E., R. Luger & D. Foreman-Mackey 2020. "Analytic Planetary Transit Light Curves and Derivatives for Stars with Polynomial Limb Darkening". In: *AJ* 159, 123.

Albrecht, S. et al. 2009. "Misaligned spin and orbital axes cause the anomalous precession of DI Herculis". In: *Nature* 461, 373–376.

Albrecht, S. et al. 2012. "OBLIQUITIES OF HOT JUPITER HOST STARS: EVIDENCE FOR TIDAL INTERACTIONS AND PRIMORDIAL MISALIGNMENTS*". In: *ApJ* 757, 18.

Albrecht, S. H., R. I. Dawson & J. N. Winn 2022. "Stellar Obliquities in Exoplanetary Systems". In: *PASP* 134, 082001.

Albrecht, S. H. et al. 2021. "A Preponderance of Perpendicular Planets". In: *ApJL* 916, L1.

Allart, R. et al. 2025. "NIRPS detection of delayed atmospheric escape from the warm and misaligned Saturn-mass exoplanet WASP-69 b". In: *A&A* 700, A7.

Almenara, J. M. et al. 2022a. "Photodynamical analysis of the nearly resonant planetary system WASP-148. Accurate transit-timing variations and mutual orbital inclination". In: *A&A* 663, A134.

Almenara, J. M. et al. 2022b. "TOI-3884 b: A rare 6-R_E planet that transits a low-mass star with a giant and likely polar spot". In: *A&A* 667, L11.

An, Q. et al. 2025. "Significant Mutual Inclinations Between the Stellar Spin and the Orbits of Both Planets in the HAT-P-11 System". In: *AJ* 169, 22.

Anderson, D. R. et al. 2014. "Three newly discovered sub-Jupiter-mass planets: WASP-69b and WASP-84b transit active K dwarfs and WASP-70Ab transits the evolved primary of a G4+K3 binary". In: *MNRAS* 445, 1114–1129.

Anderson, D. R. et al. 2017. "The discoveries of WASP-91b, WASP-105b and WASP-107b: Two warm Jupiters and a planet in the transition region between ice giants and gas giants". In: *A&A* 604, A110.

Angelo, I. et al. 2022. "Kepler-1656b's Extreme Eccentricity: Signature of a Gentle Giant". In: *AJ* 163, 227.

Arenou, F. et al. 2018. "Gaia Data Release 2. Catalogue validation". In: *A&A* 616, A17.

Astropy Collaboration et al. 2013. "Astropy: A community Python package for astronomy". In: *A&A* 558, A33.

Atek, H. et al. 2024. *Euclid: Early Release Observations – A preview of the Euclid era through a galaxy cluster magnifying lens*.

Autiwa 2010. *Rossiter-McLaughlin effect*. URL: https://commons.wikimedia.org/wiki/File:Rossiter-McLaughlin_effect.svg.

Awiphan, S. et al. 2016. "Transit timing variation and transmission spectroscopy analyses of the hot Neptune GJ3470b". In: *MNRAS* 463, 2574–2582.

El-Badry, K. 2024. "Gaia's binary star renaissance". In: *New Astronomy Reviews* 98, 101694.

El-Badry, K., H.-W. Rix & T. M. Heintz 2021. "A million binaries from Gaia eDR3: sample selection and validation of Gaia parallax uncertainties". In: *MNRAS* 506, 2269–2295.

Bailer-Jones, C. A. L. et al. 2021. "Estimating Distances from Parallaxes. V. Geometric and Photogeometric Distances to 1.47 Billion Stars in Gaia Early Data Release 3". In: *AJ* 161, 147.

Bakos, G. Á. et al. 2010. "HAT-P-11b: A Super-Neptune Planet Transiting a Bright K Star in the Kepler Field". In: *ApJ* 710, 1724–1745.

Banerjee, B. et al. 2024. "Host-star Properties of Hot, Warm, and Cold Jupiters in the Solar Neighborhood from Gaia Data Release 3: Clues to Formation Pathways". In: *AJ* 168, 7.

Baraffe, I. et al. 2015. "New evolutionary models for pre-main sequence and main sequence low-mass stars down to the hydrogen-burning limit". In: *A&A* 577, A42.

Barber, M. G. et al. 2024. "TESS Investigation—Demographics of Young Exoplanets (TI-DYE). II. A Second Giant Planet in the 17 Myr System HIP 67522". In: *ApJL* 973, L30.

Barber, M. G. et al. 2025. "TESS Investigation—Demographics of Young Exoplanets (TI-DYE). III. An Inner Super-Earth in TOI 2076". In: *AJ* 170, 32.

Barnard, E. E. 1916. "A small star with large proper-motion". In: *AJ* 29, 181–183.

Basant, R. et al. 2025. "Four Sub-Earth Planets Orbiting Barnard's Star from MAROON-X and ESPRESSO". In: *ApJL* 982, L1.

Basilicata, M. et al. 2024. "The GAPS Programme at TNG. LV. Multiple molecular species in the atmosphere of HAT-P-11 b and review of the HAT-P-11 planetary system". In: *A&A* 686, A127.

Batygin, K. 2012. "A primordial origin for misalignments between stellar spin axes and planetary orbits". In: *Nature* 491, 418–420.

Batygin, K. et al. 2009. "A Quasi-stationary Solution to Gliese 436b's Eccentricity". In: *ApJ* 699, 23–30.

Beck, J. G. & P. Giles 2005. "Helioseismic Determination of the Solar Rotation Axis". In: *ApJ* 621, L153.

Becklin, E. E. & B. Zuckerman 1988. "A low-temperature companion to a white dwarf star". In: *Nature* 336, 656–658.

Benatti, S. et al. 2019. "A possibly inflated planet around the bright young star DS Tucanae A". In: *A&A* 630, A81.

Benatti, S. et al. 2021. "Constraints on the mass and on the atmospheric composition and evolution of the low-density young planet DS Tucanae A b". In: *A&A* 650, A66.

Bernstein, G. M., J. A. Tyson & C. S. Kochanek 1993. "A large arc in the gravitational lens system 0957 + 561". In: *AJ* 105, 816.

Best, S. & C. Petrovich 2022. "The Chaotic History of the Retrograde Multi-planet System in K2-290A Driven by Distant Stars". In: *ApJL* 925, L5.

Beuzit, J.-L. et al. 2019. "SPHERE: the exoplanet imager for the Very Large Telescope". In: *A&A* 631, A155.

Bi, J. et al. 2020. "GW Ori: Interactions between a Triple-star System and Its Circumtriple Disk in Action". In: *ApJL* 895, L18.

Biddle, L. I. et al. 2025. "One-third of Sun-like stars are born with misaligned planet-forming disks". In: *Nature* 644, 356–361.

Boccaletti, A. et al. 2018. "Observations of fast-moving features in the debris disk of AU Mic on a three-year timescale: Confirmation and new discoveries". In: *A&A* 614, A52.

Bohn, A. J. et al. 2020. "A multiplicity study of transiting exoplanet host stars. I. High-contrast imaging with VLT/SPHERE". In: *A&A* 635, A73.

Bonfils, X. et al. 2012. "A hot Uranus transiting the nearby M dwarf GJ 3470. Detected with HARPS velocimetry. Captured in transit with TRAPPIST photometry". In: *A&A* 546, A27.

Borsato, L. et al. 2019. "HARPS-N radial velocities confirm the low densities of the Kepler-9 planets". In: *MNRAS* 484, 3233–3243.

Borsato, L. et al. 2014. "TRADES: A new software to derive orbital parameters from observed transit times and radial velocities. Revisiting Kepler-11 and Kepler-9". In: *A&A* 571, A38.

Borucki, W. J. 2018. "Space Missions for Exoplanet Science: Kepler/K2". In: *Handbook of Exoplanets*. Ed. by H. J. Deeg & J. A. Belmonte. Cham: Springer International Publishing, pp. 1159–1178.

Borucki, W. J. et al. 2010. "Kepler Planet-Detection Mission: Introduction and First Results". In: *Science* 327, 977.

Bourrier, V. et al. 2021. "The Rossiter-McLaughlin effect revolutions: an ultra-short period planet and a warm mini-Neptune on perpendicular orbits". In: *A&A* 654, A152.

Bourrier, V. et al. 2022. "The polar orbit of the warm Neptune GJ 436b seen with VLT/ESPRESSO". In: *A&A* 663, A160.

Bourrier, V. et al. 2023. “DREAM: I. Orbital architecture orrery”. In: *A&A* 669, A63.
Bourrier, V. et al. 2018. “Orbital misalignment of the Neptune-mass exoplanet GJ 436b with the spin of its cool star”. In: *Nature* 553, 477–480.
Bowler, B. P. 2016. “Imaging Extrasolar Giant Planets”. In: *PASP* 128, 102001.
Bowler, B. P. et al. 2023. “Rotation Periods, Inclinations, and Obliquities of Cool Stars Hosting Directly Imaged Substellar Companions: Spin-Orbit Misalignments Are Common”. In: *AJ* 165, 164.
Boyle, A. W., L. G. Bouma & A. W. Mann 2026. “The TESS All-Sky Rotation Survey: Periods for 1,046,317 Stars within 500 pc”. In: *ApJS* 284, 75.
Brady, M. T. et al. 2018. “Kepler-1656b: A Dense Sub-Saturn with an Extreme Eccentricity”. In: *AJ* 156, 147.
Brandeker, A. & G. Cataldi 2019. “Contrast sensitivities in the Gaia Data Release 2”. In: *A&A* 621, A86.
Brandt, T. D. 2018. “The Hipparcos-Gaia Catalog of Accelerations”. In: *ApJS* 239, 31.
— 2021. “The Hipparcos-Gaia Catalog of Accelerations: Gaia EDR3 Edition”. In: *ApJS* 254, 42.
Briot, D. & J. Schneider 2018. “Prehistory of Transit Searches”. In: *Handbook of Exoplanets*. Ed. by H. J. Deeg & J. A. Belmonte, p. 169.
Brown, D. J. A. et al. 2012. “Analysis of Spin-Orbit Alignment in the WASP-32, WASP-38, and HAT-P-27/WASP-40 Systems”. In: *ApJ* 760, 139.
Burnham, K. P. & D. R. Anderson 2003. “Model selection and multimodel inference : a practical information-theoretic approach”. In: *Journal of Wildlife Management* 67, 655.
Butkevich, A. G. & L. Lindegren 2014. “Rigorous treatment of barycentric stellar motion. Perspective and light-time effects in astrometric and radial velocity data”. In: *A&A* 570, A62.
Campbell, B., G. A. H. Walker & S. Yang 1988. “A Search for Substellar Companions to Solar-type Stars”. In: *ApJ* 331, 902.
Cantat-Gaudin, T. & T. D. Brandt 2021. “Characterizing and correcting the proper motion bias of the bright Gaia EDR3 sources”. In: *A&A* 649, A124.
Capistrant, B. K. et al. 2024. “TESS Hunt for Young and Maturing Exoplanets (THYME). XI. An Earth-sized Planet Orbiting a Nearby, Solar-like Host in the 400 Myr Ursa Major Moving Group”. In: *AJ* 167, 54.
Carleo, I. et al. 2021. “The GAPS Programme at TNG. XXVIII. A pair of hot-Neptunes orbiting the young star TOI-942”. In: *A&A* 645, A71.
Casasayas-Barris, N. et al. 2017. “Detection of sodium in the atmosphere of WASP-69b”. In: *A&A* 608, A135.
Cegla, H. M. et al. 2016. “The Rossiter-McLaughlin effect reloaded: Probing the 3D spin-orbit geometry, differential stellar rotation, and the spatially-resolved stellar spectrum of star-planet systems”. In: *A&A* 588, A127.
Chakraborty, H. et al. 2025. “The changing transit shape of TOI-3884 b”. In: *A&A* 702, A100.
Charbonneau, D. et al. 1999. “Detection of Planetary Transits Across a Sun-like Star”. In: *ApJ* 529, L45.
Chatterjee, S. et al. 2008. “Dynamical Outcomes of Planet-Planet Scattering”. In: *ApJ* 686, 580–602.
Chauvin, G. et al. 2004. “A giant planet candidate near a young brown dwarf. Direct VLT/NACO observations using IR wavefront sensing”. In: *A&A* 425, L29–L32.
Christiansen, J. L. et al. 2025. “The NASA Exoplanet Archive and Exoplanet Follow-up Observing Program: Data, Tools, and Usage”. In: *PSJ* 6, 186.
Cloutier, R. 2026. “Exoplanet demographics: Physical and orbital properties”. In: *Encyclopedia of Astrophysics, Volume 1*. Vol. 1, pp. 288–306.
Cloutier, R. & A. H. M. J. Triaud 2016. “Prospects for detecting the Rossiter–McLaughlin effect of Earth-like planets: the test case of TRAPPIST-1b and c”. In: *MNRAS* 462, 4018–4027.
Cohen, J. 1960. “A Coefficient of Agreement for Nominal Scales”. In: *Educational and Psychological Measurement* 20, 37–46.
Corder, G. W. & D. I. Foreman 2009. *Nonparametric Statistics for Non-Statisticians: A Step-by-Step Approach*. Wiley.
Correia, A. C. M., V. Bourrier & J.-B. Delisle 2020. “Why do warm Neptunes present nonzero eccentricity?” In: *A&A* 635, A37.
Cosentino, R. et al. 2012. “Harps-N: the new planet hunter at TNG”. In: *Ground-based and Airborne Instrumentation for Astronomy IV*. Ed. by I. S. McLean, S. K. Ramsay & H. Takami. Vol. 8446. Society of Photo-Optical Instrumentation Engineers (SPIE) Conference Series, 84461V.
Dai, F. & J. N. Winn 2017. “The Oblique Orbit of WASP-107b from K2 Photometry”. In: *AJ* 153, 205.
Damasso, M. et al. 2023. “The GAPS Programme at TNG. XLII. A characterisation study of the multi-planet system around the 400 Myr-old star HD 63433 (TOI-1726)”. In: *A&A* 672, A126.
Damasso, M. et al. 2024. “The GAPS Programme at TNG: LIX. Characterisation study of the $\sim$300 Myr-old multi-planetary system orbiting the star BD+40 2790 (TOI-2076)”. In: *A&A* 690, A235.

David, T. J. et al. 2016. “A Neptune-sized transiting planet closely orbiting a 5-10-million-year-old star”. In: *Nature* 534, 658–661.

Dawson, R. I. & J. A. Johnson 2018. “Origins of Hot Jupiters”. In: *ARA&A* 56, 175–221.

de Freitas, D. B. et al. 2021. “Multiscale behaviour of stellar activity and rotation of the planet host Kepler-30”. In: *A&A* 650, A40.

Deleuil, M. & M. Fridlund 2018. “CoRoT: The First Space-Based Transit Survey to Explore the Close-in Planet Population”. In: *Handbook of Exoplanets*. Ed. by H. J. Deeg & J. A. Belmonte. Cham: Springer International Publishing, pp. 1135–1158.

Demory, B.-O. et al. 2007. “Characterization of the hot Neptune GJ 436 b with Spitzer and ground-based observations”. In: *A&A* 475, 1125–1129.

Demory, B.-O. et al. 2013. “Spitzer Observations of GJ 3470 b: A Very Low-density Neptune-size Planet Orbiting a Metal-rich M Dwarf”. In: *ApJ* 768, 154.

Desidera, S. & M. Barbieri 2007. “Properties of planets in binary systems. The role of binary separation”. In: *A&A* 462, 345–353.

Dick, S. J. 1982. *Plurality of words*. Cambridge University Press.

Dommanget, J. & O. Nys 1995. “Catalogue of the components of double and multiple stars (CCDM)- First edition, June 1994”. In: *Bulletin d’Information du Centre de Donnees Stellaires* 46, 3.

Donati, J.-F. et al. 2025. “Six-year SPIRou monitoring of the young planet-host AU Mic”. In: *A&A* 700, A227.

Dong, J. & D. Foreman-Mackey 2023. “A Hierarchical Bayesian Framework for Inferring the Stellar Obliquity Distribution”. In: *AJ* 166, 112.

Dong, J. et al. 2022. “NEID Rossiter–McLaughlin Measurement of TOI-1268b: A Young Warm Saturn Aligned with Its Cool Host Star”. In: *ApJL* 926, L7.

Doyle, L. et al. 2023. “WASP-131 b with ESPRESSO - I. A bloated sub-Saturn on a polar orbit around a differentially rotating solar-type star”. In: *MNRAS* 522, 4499–4514.

Dugan, E. et al. 2025. “Early Evidence for Polar Orbits of Sub-Saturns around Hot Stars”. In: *ApJL* 994, L23.

Dupuy, T. J. & M. C. Liu 2011. “On the Distribution of Orbital Eccentricities for Very Low-mass Binaries”. In: *ApJ* 733, 122.

Duquennoy, A., M. Mayor & J.-L. Halbwachs 1991. “Multiplicity among solar type stars in the solar neighbourhood. I. CORAVEL radial velocity observations of 291 stars.” In: *A&AS* 88, 281–324.

Dyson, F. W., A. S. Eddington & D. C. 1920. “IX. A determination of the deflection of light by the sun’s gravitational field, from observations made at the total eclipse of May 29, 1919”. In: *Philosophical Transactions of the Royal Society of London. Series A, Containing Papers of a Mathematical or Physical Character* 220, 291–333.

Efron, B. 2014. “Estimation and Accuracy After Model Selection”. In: *Journal of the American Statistical Association* 109, 991–1007.

ESA, ed. 1997. *The HIPPARCOS and TYCHO catalogues. Astrometric and photometric star catalogues derived from the ESA HIPPARCOS Space Astrometry Mission*. Vol. 1200. ESA Special Publication.

Espinoza, N. & A. Jordán 2015. “Limb darkening and exoplanets: testing stellar model atmospheres and identifying biases in transit parameters”. In: *MNRAS* 450, 1879–1899.

Espinoza, N. et al. 2022. “A Transiting, Temperate Mini-Neptune Orbiting the M Dwarf TOI-1759 Unveiled by TESS”. In: *AJ* 163, 133.

Espinoza-Retamal, J. I. et al. 2024. “HATS-38 b and WASP-139 b Join a Growing Group of Hot Neptunes on Polar Orbits*”. In: *AJ* 168, 185.

Espinoza-Retamal, J. I. et al. 2025. “The Spin–Orbit Alignment of Eight Warm Gas Giant Systems”. In: *AJ* 170, 70.

Espinoza-Retamal, J. I. et al. 2026. “POSEIDON II: The Anti-Aligned Orbit of the Warm Neptune TOI-1710 A b”. In: *ApJL accepted*, arXiv:2604.03364.

European Space Agency (ESA) & DPAC Consortium 2022. *Gaia DR3*.

Fabricius, C. et al. 2002. “The Tycho double star catalogue”. In: *A&A* 384, 180–189.

Fabrycky, D. & S. Tremaine 2007. “Shrinking Binary and Planetary Orbits by Kozai Cycles with Tidal Friction*”. In: *ApJ* 669, 1298.

Fabrycky, D. C. & J. N. Winn 2009. “EXOPLANETARY SPIN–ORBIT ALIGNMENT: RESULTS FROM THE ENSEMBLE OF ROSSITER–MCLAUGHLIN OBSERVATIONS”. In: *ApJ* 696, 1230.

Fabrycky, D. C. et al. 2012. “Transit Timing Observations from Kepler. IV. Confirmation of Four Multiple-planet Systems by Simple Physical Models”. In: *ApJ* 750, 114.

Facchini, S., G. Lodato & D. J. Price 2013. “Wave-like warp propagation in circumbinary discs - I. Analytic theory and numerical simulations”. In: *MNRAS* 433, 2142–2156.

Feinberg, L. et al. 2024. “The Habitable Worlds Observatory engineering view: status, plans, and opportunities”. In: *Space Telescopes and Instrumentation 2024: Optical, Infrared, and Millimeter Wave*. Ed. by L. E. Coyle, S. Matsuura & M. D. Perrin. Vol. 13092. SPIE Conference Series, 130921N.
Feng, F. 2026. “Astrometric detection of exoplanets”. In: *Encyclopedia of Astrophysics, Volume 1*. Vol. 1, pp. 419–428.
Feng, F. et al. 2022. “3D Selection of 167 Substellar Companions to Nearby Stars”. In: *ApJS* 262, 21.
Fischer, D. A. & G. W. Marcy 1992. “Multiplicity among M Dwarfs”. In: *ApJ* 396, 178.
Fischer, D. A. et al. 2008. “Five Planets Orbiting 55 Cancri”. In: *ApJ* 675, 790–801.
Fontanive, C. et al. 2019. “A high binary fraction for the most massive close-in giant planets and brown dwarf desert members”. In: *MNRAS* 485, 4967–4996.
Fontanive, C. & D. Bardalez Gagliuffi 2021. “The Census of Exoplanets in Visual Binaries: Population Trends from a Volume-Limited Gaia DR2 and Literature Search”. In: *Frontiers in Astronomy and Space Sciences* Volume 8 - 2021.
Ford, E. B. & F. A. Rasio 2006. “On the Relation between Hot Jupiters and the Roche Limit”. In: *ApJ* 638, L45.
Foreman-Mackey, D. et al. 2013. “emcee: The MCMC Hammer”. In: *PASP* 125, 306.
Foucart, F. & D. Lai 2013. “Assembly of Protoplanetary Disks and Inclinations of Circumbinary Planets”. In: *ApJ* 764, 106.
Frazier, R. C. et al. 2023. “NEID Reveals That the Young Warm Neptune TOI-2076 b Has a Low Obliquity”. In: *ApJL* 944, L41.
Furlan, E. et al. 2017. “The Kepler Follow-up Observation Program. I. A Catalog of Companions to Kepler Stars from High-Resolution Imaging”. In: *AJ* 153, 71.
Gaia Collaboration et al. 2016. “The Gaia mission”. In: *A&A* 595, A1.
Gaia Collaboration et al. 2021. “Gaia Early Data Release 3. Summary of the contents and survey properties”. In: *A&A* 649, A1.
Gaia Collaboration et al. 2022. “Gaia Early Data Release 3. The celestial reference frame (Gaia-CRF3)”. In: *A&A* 667, A148.
Gaia Collaboration et al. 2023a. “Gaia Data Release 3. Stellar multiplicity, a teaser for the hidden treasure”. In: *A&A* 674, A34.
Gaia Collaboration et al. 2023b. “Gaia Data Release 3. Summary of the content and survey properties”. In: *A&A* 674, A1.
Gatewood, G. & H. Eichhorn 1973. “An unsuccessful search for a planetary companion of Barnard’s star BD +4 3561.” In: *AJ* 78, 769–776.
Gaudi, B. S. 2010. *Exoplanetary Microlensing*.
— 2012. “Microlensing Surveys for Exoplanets”. In: *ARA&A* 50, 411–453.
Gillon, M. et al. 2007. “Detection of transits of the nearby hot Neptune GJ 436 b”. In: *A&A* 472, L13–L16.
Gillon, M. et al. 2017. “Seven temperate terrestrial planets around the nearby ultracool dwarf star TRAPPIST-1”. In: *Nature* 542, 456–460.
Ginsburg, A. et al. 2019. “astroquery: An Astronomical Web-querying Package in Python”. In: *AJ* 157, 98.
González Hernández, J. I. et al. 2024. “A sub-Earth-mass planet orbiting Barnard’s star”. In: *A&A* 690, A79.
González-Payo, J. et al. 2024. “Multiplicity of stars with planets in the solar neighbourhood”. In: *A&A* 689, A302.
Gysembergh, V., P. J. Williams & E. Zingg 2022. “New evidence for Hipparchus’ Star Catalogue revealed by multispectral imaging”. In: *Journal for the History of Astronomy* 53, 383–393.
Hacker, A. et al. 2024. “TOI-2374 b and TOI-3071 b: two metal-rich sub-Saturns well within the Neptunian desert”. In: *MNRAS* 532, 1612–1634.
Hadden, S. & Y. Lithwick 2017. “Kepler Planet Masses and Eccentricities from TTV Analysis”. In: *AJ* 154, 5.
Handley, L. B. & K. Batygin 2026. “Secular Excitation of Polar Neptune Orbits in Pure Disk-Planet Systems”. In: *ApJ* 998, 324.
Handley, L. B. et al. 2025. “An Obliquity Measurement of the Hot Neptune TOI-1694b”. In: *AJ* 169, 212.
Handley, L. B. et al. 2026. “The KPF-SLOPE Survey - Small, Compact Multi-Planet Systems Appear Spin-Orbit Aligned”. In: *ApJ, under review*, arXiv:2603.23713.
Hartigan, J. A. & P. M. Hartigan 1985. “The Dip Test of Unimodality”. In: *The Annals of Statistics* 13, 70–84.
Hartigan, P. M. 1985. “Computation of the Dip Statistic to Test for Unimodality”. In: *Journal of the Royal Statistical Society Series C: Applied Statistics* 34, 320–325.
Hatzes, A. P. 2016. “The Radial Velocity Method for the Detection of Exoplanets”. In: *Methods of Detecting Exoplanets: 1st Advanced School on Exoplanetary Science*. Ed. by V. Bozza, L. Mancini & A. Sozzetti.

Hayward, T. L. et al. 2001. “PHARO: A Near-Infrared Camera for the Palomar Adaptive Optics System”. In: *PASP* 113, 105–118.
Hébrard, G. et al. 2020. “Discovery and characterization of the exoplanets WASP-148b and c. A transiting system with two interacting giant planets”. In: *A&A* 640, A32.
Hedges, C. et al. 2021. “TOI-2076 and TOI-1807: Two Young, Comoving Planetary Systems within 50 pc Identified by TESS that are Ideal Candidates for Further Follow Up”. In: *AJ* 162, 54.
Heitzmann, A. et al. 2021. “The Obliquity of HIP 67522 b: A 17 Myr Old Transiting Hot, Jupiter-sized Planet”. In: *ApJL* 922, L1.
Hellier, C. et al. 2017. “WASP-South transiting exoplanets: WASP-130b, WASP-131b, WASP-132b, WASP-139b, WASP-140b, WASP-141b and WASP-142b”. In: *MNRAS* 465, 3693–3707.
Hellier, C. et al. 2019. “WASP-166b: a bloated super-Neptune transiting a V = 9 star”. In: *MNRAS* 488, 3067–3075.
Helmi, A. et al. 2018. “The merger that led to the formation of the Milky Way’s inner stellar halo and thick disk”. In: *Nature* 563, 85–88.
Hirano, T. et al. 2011. “A Possible Tilted Orbit of the Super-Neptune HAT-P-11b”. In: *PASJ* 63, 531.
Hirano, T. et al. 2020. “Evidence for Spin-Orbit Alignment in the TRAPPIST-1 System”. In: *ApJL* 890, L27.
Hirano, T. et al. 2024. “Transit spectroscopy of K2-33b with subaru/IRD: Spin-Orbit alignment and tentative atmospheric helium”. In: *MNRAS* 530, 3117–3126.
Hixenbaugh, K. et al. 2023. “The Spin–Orbit Misalignment of TOI-1842b: The First Measurement of the Rossiter–McLaughlin Effect for a Warm Sub-Saturn around a Massive Star”. In: *ApJL* 949, L35.
Hjorth, M. et al. 2019. “K2-290: a warm Jupiter and a mini-Neptune in a triple-star system”. In: *MNRAS* 484, 3522–3536.
Hjorth, M. et al. 2021. “A backward-spinning star with two coplanar planets”. In: *Proceedings of the National Academy of Science* 118, e2017418118.
Ho, P. 2000. *Li, Qi and Shu: An Introduction to Science and Civilization in China*. Dover Publications.
Høg, E. et al. 1997. “The TYCHO Catalogue”. In: *A&A* 323, L57–L60.
Høg, E. et al. 1998. “The TYCHO Reference Catalogue”. In: *A&A* 335, L65–L68.
Høg, E. et al. 2000a. “Construction and verification of the Tycho-2 Catalogue”. In: *A&A* 357, 367–386.
Høg, E. et al. 2000b. “The Tycho-2 catalogue of the 2.5 million brightest stars”. In: *A&A* 355, L27–L30.
Holczer, T. et al. 2016. “Transit Timing Observations from Kepler. IX. Catalog of the Full Long-cadence Data Set”. In: *ApJS* 225, 9.
Holman, M. J. & N. W. Murray 2005. “The Use of Transit Timing to Detect Terrestrial-Mass Extrasolar Planets”. In: *Science* 307, 1288–1291.
Holman, M. J. et al. 2010. “Kepler-9: A System of Multiple Planets Transiting a Sun-Like Star, Confirmed by Timing Variations”. In: *Science* 330, 51–54.
Holt, J. R. 1893. “Spectroscopic Determination of Stellar Rotation”. In: *A&A (formerly The Sidereal Messenger)* 12, 646.
Howard, A. W. et al. 2025. “Planet Masses, Radii, and Orbits from NASA’s K2 Mission”. In: *ApJS* 278, 52.
Howell, S. B. et al. 2014. “The K2 Mission: Characterization and Early Results”. In: *PASP* 126, 398.
Howell, S. B. et al. 2021. “Speckle Observations of TESS Exoplanet Host Stars: Understanding the Binary Exoplanet Host Star Orbital Period Distribution”. In: *AJ* 161, 164.
Hwang, H.-C., Y.-S. Ting & N. L. Zakamska 2022. “The eccentricity distribution of wide binaries and their individual measurements”. In: *MNRAS* 512, 3383–3399.
Im, H. et al. 2026. “Observational and Dynamical Constraints on an Unseen Outer Perturber in the GJ 436 Hot Neptune System”. In: *ApJ* 1003, 84.
Innes, R. T. A. 1907. “Secular perturbations, the computation of”. In: *MNRAS* 67, 427.
Jeffers, H. M., W. H. van den Bos & F. M. Greeby 1963. *Index Catalogue of Visual Double Stars, 1961.0*.
Kain, I. J. et al. 2020. “The Young Planetary System K2-25: Constraints on Companions and Starspots”. In: *AJ* 159, 83.
Kepler Mission Team 2009. *VizieR Online Data Catalog: Kepler Input Catalog (Kepler Mission Team, 2009)*.
Kervella, P., F. Arenou & F. Thévenin 2022. “Stellar and substellar companions from Gaia EDR3. Proper-motion anomaly and resolved common proper-motion pairs”. In: *A&A* 657, A7.
Kervella, P. et al. 2019. “Stellar and substellar companions of nearby stars from Gaia DR2. Binarity from proper motion anomaly”. In: *A&A* 623, A72.
Kley, W. & R. P. Nelson 2012. “Planet-Disk Interaction and Orbital Evolution”. In: *ARA&A* 50, 211–249.

Knudstrup, E. et al. 2024. "Obliquities of exoplanet host stars: Nineteen new and updated measurements, and trends in the sample of 205 measurements". In: *A&A* 690, A379.

Knutson, H. A. et al. 2014. "Friends of Hot Jupiters. I. A Radial Velocity Search for Massive, Long-period Companions to Close-in Gas Giant Planets". In: *ApJ* 785, 126.

Kozai, Y. 1962. "Secular perturbations of asteroids with high inclination and eccentricity". In: *AJ* 67, 591–598.

Kraft, R. P. 1967. "Studies of Stellar Rotation. V. The Dependence of Rotation on Age among Solar-Type Stars". In: *ApJ* 150, 551.

Kreidberg, L. 2015. "batman: BAsic Transit Model cAlculatioN in Python". In: *PASP* 127, 1161.

Lai, D., F. Foucart & D. N. C. Lin 2011. "Evolution of spin direction of accreting magnetic protostars and spin-orbit misalignment in exoplanetary systems". In: *MNRAS* 412, 2790–2798.

Lanotte, A. A. et al. 2014. "A global analysis of Spitzer and new HARPS data confirms the loneliness and metal-richness of GJ 436 b". In: *A&A* 572, A73.

Latham, D. W. et al. 1989. "The unseen companion of HD114762: a probable brown dwarf". In: *Nature* 339, 38–40.

Léger, A. et al. 2009. "Transiting exoplanets from the CoRoT space mission. VIII. CoRoT-7b: the first super-Earth with measured radius". In: *A&A* 506, 287–302.

Libby-Roberts, J. E. et al. 2023. "An In-depth Look at TOI-3884b: A Super-Neptune Transiting an M4Dwarf with Persistent Starspot Crossings". In: *AJ* 165, 249.

Lidov, M. L. 1962. "The evolution of orbits of artificial satellites of planets under the action of gravitational perturbations of external bodies". In: *Planet. Space Sci.* 9, 719–759.

Lindegren, L. & M. A. C. Perryman 1996. "GAIA: Global astrometric interferometer for astrophysics." In: *A&AS* 116, 579–595.

Lindegren, L. et al. 2018. "Gaia Data Release 2. The astrometric solution". In: *A&A* 616, A2.

Lindegren, L. et al. 2021a. "Gaia Early Data Release 3. Parallax bias versus magnitude, colour, and position". In: *A&A* 649, A4.

Lindegren, L. et al. 2021b. "Gaia Early Data Release 3. The astrometric solution". In: *A&A* 649, A2.

Lissauer, J. J. 1993. "Planet formation." In: *ARA&A* 31, 129–174.

Lissauer, J. J. et al. 2012. "Almost All of Kepler's Multiple-planet Candidates Are Planets". In: *ApJ* 750, 112.

Lissauer, J. J. et al. 2014. "Validation of Kepler's Multiple Planet Candidates. II. Refined Statistical Framework and Descriptions of Systems of Special Interest". In: *ApJ* 784, 44.

Lithwick, Y., J. Xie & Y. Wu 2012. "Extracting Planet Mass and Eccentricity from TTV Data". In: *ApJ* 761, 122.

Liu, Y. et al. 2026. "High-Eccentricity Tidal Migration Driven by Secular Chaos in Wide-Binary Systems". In: *ApJ under review*, arXiv:2606.17344.

Louden, E. M. & S. C. Millholland 2024. "Polar Neptunes Are Stable to Tides". In: *ApJ* 974, 304.

Lovis, C. & D. Fischer 2010. "Radial Velocity Techniques for Exoplanets". In: *Exoplanets*. Ed. by S. Seager, pp. 27–53.

Lu, T. et al. 2025. "Planet–Planet Scattering and Von Zeipel–Lidov–Kozai Migration—The Dynamical History of HAT-P-11". In: *ApJ* 979, 218.

Lubke, G. H. et al. 2016. "Assessing Model Selection Uncertainty Using a Bootstrap Approach: An Update". In: *Structural Equation Modeling: A Multidisciplinary Journal* 24, 230–245.

Luger, R. et al. 2017. "A seven-planet resonant chain in TRAPPIST-1". In: *Nat. Astron.* 1, 0129.

Luri, X. et al. 2018. "Gaia Data Release 2. Using Gaia parallaxes". In: *A&A* 616, A9.

Maciejewski, G. et al. 2020. "A Newtonian Model for the WASP-148 Exoplanetary System Enhanced with TESS and Ground-based Photometric Observations". In: *Acta Astron.* 70, 203–217.

Maciejewski, G. 2026. "Detection of periodic transit timing variations in the warm sub-Saturn planet HD 332231 b". In: *A&A* 708, A285.

Macintosh, B. et al. 2006. "The Gemini Planet Imager". In: *Advances in Adaptive Optics II*. Ed. by B. L. Ellerbroek & D. Bonaccini Calia. Vol. 6272. Society of Photo-Optical Instrumentation Engineers (SPIE) Conference Series, 62720L.

Macintosh, B. et al. 2014. "First light of the Gemini Planet Imager". In: *Proceedings of the National Academy of Science* 111, 12661–12666.

Mahalanobis, P. C. 1936. "On the generalized distance in statistics". In: *Proceedings of the National Institute of Sciences (Calcutta)* 2, 49–55.

Makarov, V. V. & G. H. Kaplan 2005. "Statistical Constraints for Astrometric Binaries with Nonlinear Motion". In: *AJ* 129, 2420–2427.

Malkov, O. Y. et al. 2006. "A catalogue of eclipsing variables". In: *A&A* 446, 785–789.

Mallorquín, M. et al. 2024a. "Revisiting the dynamical masses of the transiting planets in the young AU Mic system: Potential AU Mic b inflation at 20 Myr". In: *A&A* 689, A132.

Mallorquín, M. et al. 2024b. "TOI-1135 b: A young hot Saturn-size planet orbiting a solar-type star". In: *A&A* 685, A90.

Maness, H. L. et al. 2007. "The M Dwarf GJ 436 and its Neptune-Mass Planet". In: *PASP* 119, 90–101.

Mann, A. W. et al. 2016a. "ZODIACAL EXOPLANETS IN TIME (ZEIT). I. A NEPTUNE-SIZED PLANET ORBITING AN M4.5 DWARF IN THE HYADES STAR CLUSTER". In: *ApJ* 818, 46.

Mann, A. W. et al. 2016b. "ZODIACAL EXOPLANETS IN TIME (ZEIT). III. A SHORT-PERIOD PLANET ORBITING A PRE-MAIN-SEQUENCE STAR IN THE UPPER SCORPIUS OB ASSOCIATION". In: *AJ* 152, 61.

Mann, A. W. et al. 2020. "TESS Hunt for Young and Maturing Exoplanets (THYME). III. A Two-planet System in the 400 Myr Ursa Major Group". In: *AJ* 160, 179.

Mann, H. B. & D. R. Whitney 1947. "On a Test of Whether one of Two Random Variables is Stochastically Larger than the Other". In: *The Annals of Mathematical Statistics* 18, 50–60.

Mantovan, G. et al. 2024a. "Orbital obliquity of the young planet TOI-5398 b and the evolutionary history of the system". In: *A&A* 684, L17.

Mantovan, G. et al. 2024b. "The GAPS programme at TNG. XLIX. TOI-5398, the youngest compact multi-planet system composed of an inner sub-Neptune and an outer warm Saturn". In: *A&A* 682, A129.

Mantovan, G. et al. 2026a. "A tidally detached super Neptune on a strongly misaligned retrograde orbit". In: *A&A* 709, L15.

Mantovan, G. et al. 2026b. "The 35-Myr old infant planet TOI-837 b has a mildly misaligned orbit". In: *A&A accepted*, arXiv:2606.12010.

Marconi, A. et al. 2022. "ANDES, the high resolution spectrograph for the ELT: science case, baseline design and path to construction". In: *Ground-based and Airborne Instrumentation for Astronomy IX*. Ed. by C. J. Evans, J. J. Bryant & K. Motohara. Vol. 12184. Society of Photo-Optical Instrumentation Engineers (SPIE) Conference Series, 1218424.

Marcy, G. et al. 2000. "Extrasolar Planets Around Main Sequence Stars". In: *Bioastronomy 99*. Ed. by G. Lemarchand & K. Meech. Vol. 213. ASP Conf. Ser. P. 85.

Marcy, G. W. et al. 2001. "A Pair of Resonant Planets Orbiting GJ 876". In: *ApJ* 556, 296–301.

Marcy, G. W. et al. 2014. "Masses, Radii, and Orbits of Small Kepler Planets: The Transition from Gaseous to Rocky Planets". In: *ApJS* 210, 20.

Marois, C. et al. 2008. "Direct Imaging of Multiple Planets Orbiting the Star HR 8799". In: *Science* 322, 1348.

Marois, C. et al. 2010. "Images of a fourth planet orbiting HR 8799". In: *Nature* 468, 1080–1083.

Martioli, E. et al. 2021. "New constraints on the planetary system around the young active star AU Mic. Two transiting warm Neptunes near mean-motion resonance". In: *A&A* 649, A177.

Martioli, E. et al. 2022. "TOI-1759 b: A transiting sub-Neptune around a low mass star characterized with SPIRou and TESS". In: *A&A* 660, A86.

Mason, B. D. et al. 2001. "The 2001 US Naval Observatory Double Star CD-ROM. I. The Washington Double Star Catalog". In: *AJ* 122, 3466–3471.

Masuda, K. & J. N. Winn 2020. "On the Inference of a Star's Inclination Angle from its Rotation Velocity and Projected Rotation Velocity". In: *AJ* 159, 81.

Mayor, M. & D. Queloz 1995. "A Jupiter-mass companion to a solar-type star". In: *Nature* 378, 355–359.

Mayor, M. et al. 2003. "Setting New Standards with HARPS". In: *The Messenger* 114, 20–24.

McLaughlin, D. B. 1924. "Some results of a spectrographic study of the Algol system." In: *ApJ* 60, 22–31.

Michalik, D. et al. 2014. "Joint astrometric solution of HIPPARCOS and Gaia. A recipe for the Hundred Thousand Proper Motions project". In: *A&A* 571, A85.

Michel, K.-U. & M. Mugrauer 2024. "Gaia search for (sub)stellar companions of exoplanet hosts". In: *MNRAS* 527, 3183–3195.

Migaszewski, C. & K. Goździewski 2018. "A periodic configuration of the Kepler-25 planetary system". In: *MNRAS* 480, 1767–1777.

Miglio, A. et al. 2017. "PLATO as it is : A legacy mission for Galactic archaeology". In: *Astronomische Nachrichten* 338, 644–661.

Miller, G. R. M. et al. 2010. "The Doppler shadow of WASP-3b. A tomographic analysis of Rossiter-McLaughlin observations". In: *A&A* 523, A52.

Mills, S. M. et al. 2019. "Long-period Giant Companions to Three Compact, Multiplanet Systems". In: *AJ* 157, 145.

Mistry, P. et al. 2023. “VaTEST. II. Statistical Validation of 11 TESS-detected Exoplanets Orbiting K-type Stars”. In: *AJ* 166, 9.

Močnik, T. et al. 2017. “Starspots on WASP-107 and pulsations of WASP-118”. In: *MNRAS* 469, 1622–1629.

Moe, M. & R. Di Stefano 2017. “Mind Your Ps and Qs: The Interrelation between Period (P) and Mass-ratio (Q) Distributions of Binary Stars”. In: *ApJS* 230, 15.

Montet, B. T. et al. 2014. “The TRENDS High-contrast Imaging Survey. IV. The Occurrence Rate of Giant Planets around M Dwarfs”. In: *ApJ* 781, 28.

Morgan, M. et al. 2024. “Signs of Similar Stellar Obliquity Distributions for Hot and Warm Jupiters Orbiting Cool Stars”. In: *AJ* 167, 48.

Mori, M. et al. 2025. “Multiband, Multiepoch Photometry of the Spot-crossing System TOI-3884: Refined System Geometry and Spot Properties”. In: *AJ* 170, 204.

Morton, T. D. et al. 2016. “False Positive Probabilities for all Kepler Objects of Interest: 1284 Newly Validated Planets and 428 Likely False Positives”. In: *ApJ* 822, 86.

Mugnai, L. V. et al. 2020. “ArielRad: the Ariel radiometric model”. In: *Exp. Astron.* 50, 303–328.

Naponiello, L. 2026. “A homogeneous transit-timing-variation investigation of all TESS systems with a confirmed single-transiting planet”. In: *A&A* 705, A5.

Narita, N. et al. 2017. “The K2-ESPRINT project. VI. K2-105 b, a hot Neptune around a metal-rich G-dwarf”. In: *PASJ* 69, 29.

NASA Exoplanet Science Institute 2020. *Planetary Systems Table*.

Nascimbeni, V. et al. 2022. “The PLATO field selection process. I. Identification and content of the long-pointing fields”. In: *A&A* 658, A31.

Nascimbeni, V. et al. 2025. “The PLATO field selection process: II. Characterization of LOPS2, the first long-pointing field”. In: *A&A* 694, A313.

Nature Astronomy editorial 2025. “From one exoplanet to six thousand”. In: *Nat. Astron.* 9, 1581–1581.

Newton, E. R. et al. 2019. “TESS Hunt for Young and Maturing Exoplanets (THYME): A Planet in the 45 Myr Tucana-Horologium Association”. In: *ApJL* 880, L17.

NExScI 2022. *Exoplanet Follow-up Observing Program web service*.

Ochsenbein, F., P. Bauer & J. Marcout 2000. “The VizieR database of astronomical catalogues”. In: *A&AS* 143, 23–32.

Ochsenbein, F. 1996. *The VizieR database of astronomical catalogues*.

Ohta, Y., A. Taruya & Y. Suto 2005. “The Rossiter-McLaughlin Effect and Analytic Radial Velocity Curves for Transiting Extrasolar Planetary Systems”. In: *ApJ* 622, 1118.

Osborn, H. P. et al. 2022. “Uncovering the true periods of the young sub-Neptunes orbiting TOI-2076”. In: *A&A* 664, A156.

Panichi, F. et al. 2018. “The architecture and formation of the Kepler-30 planetary system”. In: *MNRAS* 478, 2480–2494.

Parviainen, H. 2015. “PYTRANSIT: fast and easy exoplanet transit modelling in PYTHON”. In: *MNRAS* 450, 3233–3238.

Pecaut, M. J. & E. E. Mamajek 2013. “Intrinsic Colors, Temperatures, and Bolometric Corrections of Pre-main-sequence Stars”. In: *ApJS* 208, 9.

Pepe, F. et al. 2002. “The CORALIE survey for southern extra-solar planets VII. Two short-period Saturnian companions to HD 108147 and HD 168746”. In: *A&A* 388, 632–638.

Pepe, F. et al. 2021. “ESPRESSO at VLT. On-sky performance and first results”. In: *A&A* 645, A96.

Perryman, M. A. C. 2000. “Extra-solar planets”. In: *Reports on Progress in Physics* 63, 1209–1272.

Perryman, M. A. C. et al. 1997. “The HIPPARCOS Catalogue”. In: *A&A* 323, L49–L52.

Perryman, M. 2018. *The Exoplanet Handbook*. Cambridge University Press.

Perryman, M. et al. 2014. “Astrometric Exoplanet Detection with Gaia”. In: *ApJ* 797, 14.

Petrovich, C. 2015. “HOT JUPITERS FROM COPLANAR HIGH-ECCENTRICITY MIGRATION”. In: *ApJ* 805, 75.

Petrovich, C. et al. 2020. “A Disk-driven Resonance as the Origin of High Inclinations of Close-in Planets”. In: *ApJL* 902, L5.

Piaulet, C. et al. 2021. “WASP-107b’s Density Is Even Lower: A Case Study for the Physics of Planetary Gas Envelope Accretion and Orbital Migration”. In: *AJ* 161, 70.

Plavchan, P. et al. 2020. “A planet within the debris disk around the pre-main-sequence star AU Microscopii”. In: *Nature* 582, 497–500.

Polanski, A. S. & C. A. Clark 2025. "An Inventory of Resolved Stellar Companions in the Ariel Target List". In: *Research Notes of the American Astronomical Society* 9, 291.

Polanski, A. S. et al. 2024. "The TESS-Keck Survey. XX. 15 New TESS Planets and a Uniform RV Analysis of All Survey Targets". In: *ApJS* 272, 32.

Polanski, A. S. et al. 2025. "An Aligned Sub-Neptune Revealed with MAROON-X and a Tendency Toward Alignment for Small Planets". In: *AJ* 170, 182.

Puig, L. et al. 2018. "The Phase A study of the ESA M4 mission candidate ARIEL". In: *Exp. Astron.* 46, 211–239.

Quanz, S. P. et al. 2022. "Large Interferometer For Exoplanets (LIFE). I. Improved exoplanet detection yield estimates for a large mid-infrared space-interferometer mission". In: *A&A* 664, A21.

Queloz, D. et al. 2000a. "Detection of a spectroscopic transit by the planet orbiting the star HD209458". In: *A&A* 359, L13–L17.

Queloz, D. et al. 2000b. "The CORALIE survey for southern extra-solar planets. I. A planet orbiting the star Gliese 86". In: *A&A* 354, 99–102.

Quirrenbach, A. 2010. "Astrometric Detection and Characterization of Exoplanets". In: *Exoplanets*. Ed. by S. Seager, pp. 157–174.

Radzom, B. T. et al. 2024. "Evidence for Primordial Alignment: Insights from Stellar Obliquity Measurements for Compact Sub-Saturn Systems". In: *AJ* 168, 116.

Rasio, F. A. & E. B. Ford 1996. "Dynamical instabilities and the formation of extrasolar planetary systems". In: *Science* 274, 954–956.

Rauer, H. et al. 2014. "The PLATO 2.0 mission". In: *Exp. Astron.* 38, 249–330.

Rauer, H. et al. 2025. "The PLATO mission". In: *Exp. Astron.* 59, 26.

Ribas, I. et al. 2018. "A candidate super-Earth planet orbiting near the snow line of Barnard's star". In: *Nature* 563, 365–368.

Ribas, I., A. Font-Ribera & J.-P. Beaulieu 2008. "A $\sim$5 $M_\oplus$ Super-Earth Orbiting GJ 436? The Power of Near-Grazing Transits". In: *ApJL* 677, L59.

Ricker, G. R. et al. 2014. "Transiting Exoplanet Survey Satellite". In: *Journal of Astronomical Telescopes, Instruments, and Systems* 1, 014003.

Riello, M. et al. 2021. "Gaia Early Data Release 3. Photometric content and validation". In: *A&A* 649, A3.

Rizzuto, A. C. et al. 2020. "TESS Hunt for Young and Maturing Exoplanets (THYME). II. A 17 Myr Old Transiting Hot Jupiter in the Sco-Cen Association". In: *AJ* 160, 33.

Rossi, A. M. et al. 2026. "True spin-orbit obliquity distribution: Data-driven confirmation of no clustering of misaligned planets". In: *A&A* 705, A142.

Rossiter, R. A. 1924. "On the detection of an effect of rotation during eclipse in the velocity of the brighter component of beta Lyrae, and on the constancy of velocity of this system." In: *ApJ* 60, 15–21.

Rowe, J. F. et al. 2014. "Validation of Kepler's Multiple Planet Candidates. III. Light Curve Analysis and Announcement of Hundreds of New Multi-planet Systems". In: *ApJ* 784, 45.

Rubenzahl, R. A. et al. 2024. "Obliquity Constraints for the Extremely Eccentric Sub-Saturn Kepler-1656 b". In: *ApJL* 971, L40.

Safonov, B. S., P. A. Lysenko & A. V. Dodin 2017. "The speckle polarimeter of the 2.5-m telescope: Design and calibration". In: *Astronomy Letters* 43, 344–364.

Sagynbayeva, S. & W. M. Farr 2026. "Polka-dotted Stars. II. Starspots and Obliquities of Kepler-17 and Kepler-63". In: *ApJ* 997, 297.

Saha, P. et al. 2024. *Essentials of strong gravitational lensing*.

Sahlmann, J. et al. 2011. "Search for brown-dwarf companions of stars". In: *A&A* 525, A95.

Sanchis-Ojeda, R., J. N. Winn & D. C. Fabrycky 2013. "Starspots and spin-orbit alignment for Kepler cool host stars". In: *Astronomische Nachrichten* 334, 180–183.

Sanchis-Ojeda, R. et al. 2012. "Alignment of the stellar spin with the orbits of a three-planet system". In: *Nature* 487, 449–453.

Sanchis-Ojeda, R. et al. 2013. "KEPLER-63b: A GIANT PLANET IN A POLAR ORBIT AROUND A YOUNG SUN-LIKE STAR". In: *ApJ* 775, 54.

Schneider, J. et al. 2011. "Defining and cataloging exoplanets: the exoplanet.eu database". In: *A&A* 532, A79.

Scott, N. J. & S. B. Howell 2018. "NESSI and 'Alopeke: two new dual-channel speckle imaging instruments". In: *Optical and Infrared Interferometry and Imaging VI*. Ed. by M. J. Creech-Eakman, P. G. Tuthill & A. Mérand. Vol. 10701. Society of Photo-Optical Instrumentation Engineers (SPIE) Conference Series, 107010G.

Scott, N. J. et al. 2018. "The NN-explore Exoplanet Stellar Speckle Imager: Instrument Description and Preliminary Results". In: *PASP* 130, 054502.

Scott, N. J. 2019. "'Alopeke, Zorro, and NESSI: Three dual-channel speckle imaging instruments at Gemini-North, Gemini-South, and the WIYN telescopes." In: *AAS/Division for Extreme Solar Systems Abstracts*. Vol. 51, 330.15.

Sha, L. et al. 2021. "TOI-954 b and K2-329 b: Short-period Saturn-mass Planets that Test whether Irradiation Leads to Inflation". In: *AJ* 161, 82.

Shimodaira, H. 2002. "An Approximately Unbiased Test of Phylogenetic Tree Selection". In: *Systematic Biology* 51. Ed. by N. Goldman, 492–508.

Siegel, J. C., J. N. Winn & S. H. Albrecht 2023. "Ponderings on the Possible Preponderance of Perpendicular Planets". In: *ApJL* 950, L2.

Smirnov, N. 1948. "Table for Estimating the Goodness of Fit of Empirical Distributions". In: *The Annals of Mathematical Statistics* 19, 279–281.

Snellen, I. A. G. & A. G. A. Brown 2018. "The mass of the young planet Beta Pictoris b through the astrometric motion of its host star". In: *Nature Astronomy* 2, 883–886.

Southworth, J. et al. 2020. "A multiplicity study of transiting exoplanet host stars. II. Revised properties of transiting planetary systems with companions". In: *A&A* 635, A74.

Southworth, J. 2011. "Homogeneous studies of transiting extrasolar planets - IV. Thirty systems with space-based light curves". In: *MNRAS* 417, 2166–2196.

— 2026. "TEPCat: The Transiting Extrasolar Planet Catalogue". In: *Universe* 12, 62.

Sozzetti, A. et al. 2014. "Astrometric detection of giant planets around nearby M dwarfs: the Gaia potential". In: *MNRAS* 437, 497–509.

Sozzetti, A. et al. 2016. "Gaia: The Astrometry Revolution". In: *Young Stars & Planets Near the Sun*. Ed. by J. H. Kastner, B. Stelzer & S. A. Metchev. Vol. 314. IAU Symposium, pp. 264–269.

Sozzetti, A. 2005. "Astrometric Methods and Instrumentation to Identify and Characterize Extrasolar Planets: A Review". In: *PASP* 117, 1021–1048.

Spejcher, B. et al. 2025. "The EBLM Project XVIII. 3D Obliquities of Five Low-Mass Eclipsing Binaries". In: *arXiv e-prints*, arXiv:2511.23430.

Stefanov, A. K. et al. 2025. "A sub-Earth-mass planet orbiting Barnard's star - No evidence of transits in TESS photometry". In: *A&A* 693, L3.

Stefansson, G. et al. 2020. "The Habitable Zone Planet Finder Reveals a High Mass and Low Obliquity for the Young Neptune K2-25b". In: *AJ* 160, 192.

Stefànsson, G. et al. 2022. "The Warm Neptune GJ 3470b Has a Polar Orbit". In: *ApJL* 931, L15.

Steffen, J. H. et al. 2012. "Transit timing observations from Kepler - III. Confirmation of four multiple planet systems by a Fourier-domain study of anticorrelated transit timing variations". In: *MNRAS* 421, 2342–2354.

Stevens, D. J. & B. S. Gaudi 2013. "A Posteriori Transit Probabilities". In: *PASP* 125, 933.

Stevenson, K. B. et al. 2014. "A Hubble Space Telescope Search for a Sub-Earth-sized Exoplanet in the GJ 436 System". In: *ApJ* 796, 32.

Struve, O. 1952. "Proposal for a project of high-precision stellar radial velocity work". In: *The Observatory* 72, 199–200.

Šubjak, J. et al. 2022. "TOI-1268b: The youngest hot Saturn-mass transiting exoplanet". In: *A&A* 662, A107.

Tamburo, P. et al. 2025. "The True Stellar Obliquity of a Sub-Saturn Planet from the Tierras Observatory and the Keck Planet Finder". In: *AJ* 170, 34.

Tamuz, O. et al. 2008. "The CORALIE survey for southern extra-solar planets. XV. Discovery of two eccentric planets orbiting HD 4113 and HD 156846". In: *A&A* 480, L33–L36.

Thao, P. C. et al. 2020. "Zodiacal Exoplanets in Time (ZEIT). IX. A Flat Transmission Spectrum and a Highly Eccentric Orbit for the Young Neptune K2-25b as Revealed by Spitzer". In: *AJ* 159, 32.

Thao, P. C. et al. 2024. "The Featherweight Giant: Unraveling the Atmosphere of a 17 Myr Planet with JWST". In: *AJ* 168, 297.

Thebault, P. & D. Bonanni 2025. "A complete census of planet-hosting binaries". In: *A&A* 700, A106.

Thiele, T. N. 1883. "Neue Methode zur Berechung von Doppelsternbahnen". In: *Astronomische Nachrichten* 104, 245.

Tinetti, G. et al. 2018. "A chemical survey of exoplanets with ARIEL". In: *Exp. Astron.* 46, 135–209.

Tinetti, G. et al. 2022. "Ariel: Enabling planetary science across light-years". In: *European Planetary Science Congress*, EPSC2022-1114.

Tokovinin, A. & O. Kiyaeva 2016. "Eccentricity distribution of wide binaries". In: *MNRAS* 456, 2070–2079.

Torres, G. 1999. "Substellar Companion Masses from Minimal Radial Velocity or Astrometric Information: a Monte Carlo Approach". In: *PASP* 111, 169–176.

Torres, G. et al. 2010. “MODELING KEPLER TRANSIT LIGHT CURVES AS FALSE POSITIVES: REJECTION OF BLEND SCENARIOS FOR KEPLER-9, AND VALIDATION OF KEPLER-9 d, A SUPER-EARTH-SIZE PLANET IN A MULTIPLE SYSTEM”. In: *ApJ* 727, 24.

Traub, W. A. & B. R. Oppenheimer 2010. “Direct Imaging of Exoplanets”. In: *Exoplanets*. Ed. by S. Seager, pp. 111–156.

Triaud, A. H. M. J. et al. 2013. “The EBLM project. I. Physical and orbital parameters, including spin-orbit angles, of two low-mass eclipsing binaries on opposite sides of the brown dwarf limit”. In: *A&A* 549, A18.

Triaud, A. H. M. J. 2018. “The Rossiter-McLaughlin Effect in Exoplanet Research”. In: *Handbook of Exoplanets*. Ed. by H. J. Deeg & J. A. Belmonte, p. 2.

Triaud, A. H. M. J. et al. 2017. “The EBLM Project. IV. Spectroscopic orbits of over 100 eclipsing M dwarfs masquerading as transiting hot Jupiters”. In: *A&A* 608, A129.

Trifonov, T. 2026. “Radial velocity technique”. In: *Encyclopedia of Astrophysics, Volume 1*, pp. 320–341.

Trifonov, T. et al. 2020. “Public HARPS radial velocity database corrected for systematic errors”. In: *A&A* 636, A74.

Tsantaki, M. et al. 2022. “Survey of Surveys. I. The largest compilation of radial velocities for the Galaxy”. In: *A&A* 659, A95.

Turchi, A. et al. 2025. “Survey of Surveys: II. Stellar parameters for 23 million stars”. In: *A&A* 700, A195.

Turon, C. et al. 1992a. “The Hipparcos input catalogue”. In: *Bulletin d'Information du Centre de Donnees Stellaires* 41, 9.

Turon, C. et al. 1992b. *The Hipparcos Input Catalogue. Volumes 1 - 7.*

Udry, S. & N. C. Santos 2007. “Statistical Properties of Exoplanets”. In: *ARA&A* 45, 397–439.

Unwin, S. C. et al. 2008. “Taking the Measure of the Universe: Precision Astrometry with SIM PlanetQuest”. In: *PASP* 120, 38.

Urban, S. E. et al. 1998. “The AC 2000: The Astrographic Catalogue on the System Defined by the HIPPARCOS Catalogue”. In: *AJ* 115, 1212–1223.

Van de Kamp, P. 1963. “Astrometric study of Barnard's star from plates taken with the 24-inch Sproul refractor.” In: *AJ* 68, 515–521.

— 1982. “The planetary system of Barnard's star”. In: *Vistas in Astronomy* 26, 141–157.

Van Eylen, V. et al. 2018. “HD 89345: a bright oscillating star hosting a transiting warm Saturn-sized planet observed by K2”. In: *MNRAS* 478, 4866–4880.

van Leeuwen, F. 2007a. “Validation of the new Hipparcos reduction”. In: *A&A* 474, 653–664.

van Leeuwen, F. 2007b. *Hipparcos, the New Reduction of the Raw Data*. Vol. 350.

Van Zandt, J. et al. 2023. “TESS-Keck Survey. XIV. Two Giant Exoplanets from the Distant Giants Survey”. In: *AJ* 165, 60.

von Zeipel, H. 1910. “Sur l'application des séries de M. Lindstedt à l'étude du mouvement des comètes périodiques”. In: *Astron. Nachr.* 183, 345.

Wang, S. et al. 2018. “Stellar Spin–Orbit Alignment for Kepler-9, a Multi-transiting Planetary System with Two Outer Planets Near 2:1 Resonance”. In: *AJ* 155, 70.

Wang, M.-T. et al. 2026. “TOI-4495: A Pair of Aligned, Near-resonant Sub-Neptunes That Likely Experienced Overstable Migration”. In: *AJ* 171, 135.

Wang, X.-Y. et al. 2022. “The Aligned Orbit of WASP-148b, the Only Known Hot Jupiter with a nearby Warm Jupiter Companion, from NEID and HIRES”. In: *ApJL* 926, L8.

Weidenschilling, S. J. & F. Marzari 1996. “Gravitational scattering as a possible origin for giant planets at small stellar distances”. In: *Nature* 384, 619–621.

Wenger, M. et al. 2000. “The SIMBAD astronomical database: The CDS reference database for astronomical objects”. In: *A&AS* 143, 9–22.

Winn, J. N. 2010. “Exoplanet Transits and Occultations”. In: *Exoplanets*. Ed. by S. Seager, pp. 55–77.

Winn, J. N. 2024. “The Transiting Exoplanet Survey Satellite”. In: *arXiv e-prints*, arXiv:2410.12905.

Winn, J. N. et al. 2005. “Measurement of Spin-Orbit Alignment in an Extrasolar Planetary System”. In: *ApJ* 631, 1215–1226.

Winn, J. N. et al. 2010. “Hot Stars with Hot Jupiters Have High Obliquities”. In: *ApJL* 718, L145–L149.

Wirth, C. P. et al. 2021. “TOI-942b: A Prograde Neptune in a 60 Myr Old Multi-transiting System*”. In: *ApJL* 917, L34.

Wittenmyer, R. A. et al. 2020. “Cool Jupiters greatly outnumber their toasty siblings: occurrence rates from the Anglo-Australian Planet Search”. In: *MNRAS* 492, 377–383.

Wittenmyer, R. A. et al. 2022. “TOI-1842b: A Transiting Warm Saturn Undergoing Reinflation around an Evolving Subgiant”. In: *AJ* 163, 82.
Wittrock, J. M. et al. 2022. “Transit Timing Variations for AU Microscopii b and c”. In: *AJ* 164, 27.
Wolszczan, A. & D. A. Frail 1992. “A planetary system around the millisecond pulsar PSR1257 + 12”. In: *Nature* 355, 145–147.
Wright, J. T. & A. W. Howard 2009. “Efficient Fitting of Multiplanet Keplerian Models to Radial Velocity and Astrometry Data”. In: *ApJS* 182, 205–215.
Wright, J. T. 2018. “Radial Velocities as an Exoplanet Discovery Method”. In: *Handbook of Exoplanets*. Ed. by H. J. Deeg & J. A. Belmonte, p. 4.
Wu, Y. & Y. Lithwick 2011. “Secular Chaos and the Production of Hot Jupiters”. In: *ApJ* 735, 109.
Wu, Y. et al. 2026. “Evidence for a Nonzero Eccentricity Superpuff Exoplanet WASP-107 b Using JWST Occultation Observation”. In: *ApJL* 996, L28.
Xuan, W. J. et al. 2018. “Characterizing the Performance of the NIRC2 Vortex Coronagraph at W. M. Keck Observatory”. In: *AJ* 156, 156.
Yee, S. W. et al. 2018. “HAT-P-11: Discovery of a Second Planet and a Clue to Understanding Exoplanet Obliquities”. In: *AJ* 155, 255.
Yee, S. W. et al. 2023. “The TESS Grand Unified Hot Jupiter Survey. II. Twenty New Giant Planets*”. In: *ApJS* 265.
Yee, S. W. et al. 2025. “The Polar Orbit of TOI-2374 b, a Planet in the Neptunian Ridge”. In: *AJ* 170, 275.
Yu, L. et al. 2018. “Two Warm, Low-density Sub-Jovian Planets Orbiting Bright Stars in K2 Campaigns 13 and 14”. In: *AJ* 156, 127.
Zak, J. et al. 2024. “Stellar obliquity measurements of six gas giants. Orbital misalignment of WASP-101b and WASP-131b”. In: *A&A* 686, A147.
Zak, J. et al. 2025. “PLATOSpec’s first results: Planets WASP-35b and TOI-622b are on aligned orbits, and K2-237b is on a polar orbit”. In: *A&A* 702, A266.
Zanazzi, J. J. & D. Lai 2018. “Planet formation in discs with inclined binary companions: can primordial spin-orbit misalignment be produced?” In: *MNRAS* 478, 835–851.
Zellem, R. T. et al. 2019. “Constraining Exoplanet Metallicities and Aerosols with the Contribution to ARIEL Spectroscopy of Exoplanets (CASE)”. In: *PASP* 131, 094401.
Zhang, J. et al. 2026. “Dynamical Architectures of S-type Transiting Planets in Binaries. II. A Dichotomy in Orbital Alignment of Small Planets in Close Binary Systems”. In: *AJ* 171, 77.
Zhang, Y. et al. 2022. “Echelle Grating Spectroscopic Technology for High-Resolution and Broadband Spectral Measurement”. In: *Applied Sciences* 12.
Zhou, G. et al. 2020a. “A Well-aligned Orbit for the 45 Myr-old Transiting Neptune DS Tuc Ab”. In: *ApJL* 892, L21.
Zhou, G. et al. 2020b. “Two Young Planetary Systems around Field Stars with Ages between 20 and 320 Myr from TESS”. In: *AJ* 161, 2.
Ziegler, C. et al. 2020. “SOAR TESS Survey. I. Sculpting of TESS Planetary Systems by Stellar Companions”. In: *AJ* 159, 19.
Zingales, T. et al. 2018. “The ARIEL mission reference sample”. In: *Exp. Astron.* 46, 67–100.

List of Figures

1.1 Barnard's star yearly mean positions from Van de Kamp (1963) . . 2
1.2 Stevens & Gaudi (2013) classification of exoplanets according to their mass. 4
1.3 "Perryman Tree" plot of exoplanet detection methods. 6
1.4 Sketch of the RV method. 8
1.5 Illustration of the stellar flux varying according to transits and occultations. 9
1.6 Light curve of HD 209458 from the discovery paper by Charbonneau et al. (1999). 10
1.7 Cumulative histogram of discovered planet, by year. 15
1.8 Artist's impressions of the *Hipparcos* and *Gaia* satellites. 16
1.9 Plot of microlensing of an exoplanetary system 19
1.10 Three-panel diagnostic plot for TTV candidates 20

2.1 Simplified model of a counterclockwise-rotating star with a planet orbiting it. 22
2.2 Two sequences of RV measurements of HD 209458 from Queloz et al. (2000a). 23
2.3 The RM effect on the HJs HD 189733A b and WASP-8A b. 24
2.4 Tridimensional visualization of vectors and angles showing the RM geometry. 25
2.5 Coordinate systems for theoretical description of RM effect. . . . 26
2.6 Dichotomous distribution of exoplanetary obliquities according to S. H. Albrecht et al. (2021). 30
2.7 HBA probing the obliquity trend of the exoplanetary population. 31

2.8 True obliquity distribution of Neptunian exoplanets from Rossi et al. (2026) dataset. 32

3.1 Discovery space for binary star detection methods. 36
3.2 Pictures of imaged planets within 100 au 37
3.3 ExoFOP direct imaging entry 38
3.4 Example of imaging contrast curve 40
3.5 Example of imaging mass sensitivity plot 41

4.1 Principle of PMa determination. 49
4.2 Efficiency function ζ as a function of the orbital period normalized to the observational baseline. 52
4.3 Probability density distribution of the geometric projection factor η. 53
4.4 DOF bug plaguing *Gaia* DR2 58
4.5 Benchmarking of the PMa framework. 66
4.6 Confusion matrix of the astrometric framework benchmark, assuming a detection threshold of $\mathrm{SNR} > 5$ 68
4.7 Confusion matrix of the astrometric framework benchmark, assuming a detection threshold of $\mathrm{SNR} > 3$ 69
4.8 Comparison of companion mass determination between this work and Kervella, Arenou & Thévenin (2022) at 3 au. 70
4.9 Comparison of companion mass determination between this work and Kervella, Arenou & Thévenin (2022) at 5 au. 71
4.10 Comparison of companion mass determination between this work and Kervella, Arenou & Thévenin (2022) at 10 au. 71
4.11 Comparison of companion mass determination between this work and Kervella, Arenou & Thévenin (2022) at 30 au. 72
4.12 Mass sensitivity plot for a PMa non-detection 73
4.13 Mass sensitivity plot for a PMa detection 74

5.1 Distribution of projected and true obliquities with respect to stellar effective temperature T_{eff} 85
5.2 CDF of single stars, non single stars, narrow and wide binaries. . 88
5.3 Distribution of projected and true obliquities with respect to stellar effective temperature T_{eff}, according to system multiplicity . . 89
5.4 CDF of single planet, compact, and multi-planet systems. 90
5.5 Probability density fits for the R26 dataset. 93
5.6 Probability density fits for the total updated dataset. 94

A.1 Sensitivity plot of AU Mic 106
A.2 Sensitivity plot of DS Tuc 107

A.3 RV phase-folded plot of GJ 3470 109
A.4 Sensitivity plot of HAT-P-11 111
A.5 RV plot of HD 89345 113
A.6 Mass-separation plot of K2-290 117
A.7 Speckle imaging of K2-290 118
A.8 Mass-separation plot of WASP-107 131
A.9 Mass-separation plot of WASP-131 132

List of Tables

5.1 Summary of RV datasets and outlier removal process for the Neptunian sample. 79
5.2 Summary of high-resolution imaging observations 80
5.3 Summary of companion masses from direct imaging 81
5.4 Consensus summary of binarity evidence for the analyzed sample 82
5.5 Neptunian sample created in this work. 83
5.6 Configuration of the parameters space for the analyzed models . 91
5.7 Comparison of information criteria between Rossi et al. (2026) and this work samples. Bold values indicate the preferred model in each sample. 92
5.8 Results of method A after bootstrapping R26 and my datasets 10^4 times. 95
5.9 Results of Method B showing the median information criteria (AIC and BIC) over 10^4 bootstrap iterations. 95
5.10 Comparison of the estimated best-fit parameters for the R26 and this work datasets. 97

A.1 Main astronomical catalogs and their acronyms used in this chapter. 103

C.1 Selection probabilities and weights for the sample excluding TOI-1710 A. 137
C.2 Median information criteria for the sample excluding TOI-1710 A. 137

Acknowledgments

I would like to express my deepest gratitude to my supervisors, Prof. Malavolta, Drs. Borsa, Desidera, and Rainer, for their constant support and availability to discuss every aspect of this thesis, while allowing me to explore the scientific aspects I was most drawn to. Without their guidance, this work would have never been possible.

I thank Juan I. Espinoza-Retamal, Luke Handley, and Yurou Liu for the insightful conversations regarding their research in the context of Neptunian exoplanets, Moreno Monticelli for his brilliant suggestions concerning statistical analyses, Tong Bao and Michele Frangiamore for stimulating conversations and for providing valuable feedback on parts of this work.

My immeasurable gratitude and love go to my mother and my father, who allowed me to pursue my dreams from the very beginning. They have supported me every step of the way, and it is difficult to express in words how much this means to me.

A final, loving thank you goes to Greta. She stands by my side unconditionally, sparking joy in every moment. Without her, this path I am pursuing would not have the same meaning.

This work has made use of the Transiting ExoPlanet Catalogue (TEPCat) by John Southworth, Keele University, UK (Southworth 2011; Southworth 2026).
This research has made use of the SIMBAD database, operated at CDS, Strasbourg, France (Wenger et al. 2000).
This research has made use of the VizieR catalogue access tool, CDS, Strasbourg, France (Ochsenbein 1996). The original description of the VizieR service was published in Ochsenbein, Bauer & Marcout (2000).
This research has made use of the NASA Exoplanet Archive, which is operated by the California Institute of Technology, under contract with the National Aeronautics and Space Administration under the Exoplanet Exploration Program (NASA Exoplanet Science Institute 2020).
This research has made use of the Astrophysics Data System, funded by NASA under Cooperative Agreement 80NSSC21M00561.
This research has made use of data obtained from or tools provided by the portal exoplanet.eu of The Extrasolar Planets Encyclopaedia.
This work has made use of data from the European Space Agency (ESA) mission Gaia (`https://www.cosmos.esa.int/gaia`), processed by the Gaia Data Processing and Analysis Consortium (DPAC, `https://www.cosmos.esa.int/web/gaia/dpac/consortium`). Funding for the DPAC has been provided by national institutions, in particular the institutions participating in the Gaia Multilateral Agreement (European Space Agency (ESA) & DPAC Consortium 2022).
This research has made use of the Exoplanet Follow-up Observation Program (NExScI 2022; Christiansen et al. 2025) website, which is operated by the California Institute of Technology, under contract with the National Aeronautics and Space Administration under the Exoplanet Exploration Program.S
Part of this work is based on archival data, software or online services provided by the Space Science Data Center - ASI. In particular, the GaiaPortal access tool was used for this research (`http://gaiaportal.ssdc.asi.it`).
This publication makes use of The Data & Analysis Center for Exoplanets (DACE), which is a facility based at the University of Geneva (CH) dedicated to extrasolar planets data visualisation, exchange and analysis. DACE is a platform of the Swiss National Centre of Competence in Research (NCCR) PlanetS, federating the Swiss expertise in Exoplanet research. The DACE platform is available at `https://dace.unige.ch`.